Antenna Design for On-Skin UHF and 5G RFID Tags

Jack Dylan Hughes

A thesis submitted for the degree of

Doctor of Philosophy in Electronic Engineering

School of Engineering

University of Kent

September, 2022

"You know, I'm something of a scientist myself."

<div style="text-align: right;">Norman Osborn</div>

Abstract

This thesis presents RFID solutions for healthcare applications, using the battery-less (passive) communication link, in an attempt to provide medical facilities and individuals alike unrestricted access to well-being information. Through this technology, improvements can be made in early detection and illness prevention, as well as tracking and analysing recovery progress. To achieve this goal, an RFID tag must be designed to function on the body, a challenging task owing to the difficult electro-magnetic (EM) properties and variability of the human body. In discussing the challenges of the communication link, the first step is to consider dedicated frequency bands allocated for their controlled operation in public spaces, which for long-range RFID communication has been predominantly UHF (860 MHz). This wavelength parameter of the communication link is important as it has implications on the size and structure of the antenna to provide an efficient communication link. To this effect, this thesis has also considered the possibility of higher frequency 5G bands for RFID to potentially expand into, in order to reduce the operational wavelength, but also incorporate the many desirable qualities of a 5G network, foremost being its fast data rate, low-latency, and wide availability. The thesis is organised as to initially introduce RFID technology, discuss the current state of research around designing RFID tags for placement on the body. Going on to introduce a Directional Discontinuity Ring Radiator (DDRR) antenna as a novel application in the UHF RFID tag system for live streaming data, presenting 1.2 m range of consistent streaming, then up to 3.6 m maximum read range with dropouts. The thesis will then go into the design process for 5G RFID, adopting the grid-array antenna for its simple structure, high gain for the on-body environment, and potential for improved breathability. Since no RFID IC packages exist for 5G, and creating comparable circuitry is into itself a challenge, technological assumptions are taken from UHF to assess the quality these antennas obtain. The studies found the low-end frequency band for 5G (3.6 GHz) is comparable to UHF in terms of achievable radiation performance, but suffers the same structural limitations as UHF antennas, suggesting higher frequency 5G bands are required to produce a high performing epidermal antenna.

Acknowledgements

I would like to express utmost gratitude to my supervisor Professor John Batchelor for his constant guidance, support and advice throughout my PhD. I am also grateful to Professor Cecilia Occhiuzzi, Professor Gaetano Marrocco, and the whole of the University of Rome Tor Vergata 'Pervasive Electromagnetics' laboratory for their support, guidance, and friendship in our collaborative work during my research visit. Thank you also to Doctor Robert Horne, Doctor Paul Taylor, and Nathan Brabon for their assistance and advice on antennas, fabrication, measurement techniques, general communication systems and electromagnetic simulators.

I would also like to express my thanks to Antonio Mendoza, Jason Morris, Joanna Scamp, and the rest of the university technical staff who have provided excellent assistance in resources, technical advice, and measurement assistance both throughout my PhD, as well as through my undergraduate studies.

Thank you also to the EPSRC, for funding my PhD work.

Finally, thank you to my parents, family and friends who encouraged me to throughout this journey, in whose council, support and occasional beer has made this a joyful experience.

<div align="right">

Jack Dylan Hughes, September 2022

</div>

Publications

(1) - J. D. Hughes, C. Occhiuzzi, J. Batchelor and G. Marrocco, "Wearable Soft Grid Array Antenna for S-band 5G Communication," 2020 XXXIIIrd General Assembly and Scientific Symposium of the International Union of Radio Science, Rome, Italy, 2020, pp. 1-4. doi: 10.23919/URSIGASS49373.2020.9232249

(2) - J. D. Hughes, C. Occhiuzzi, J. Batchelor and G. Marrocco, "Miniaturized Grid Array Antenna for Body-centric RFID Communications in 5G S-band," 2020 50th European Microwave Conference (EuMC), Utrecht, Netherlands, 2021, pp. 796-799. doi: 10.23919/EuMC48046.2021.9338030

(3) - J. D. Hughes, C. Occhiuzzi, J. Batchelor and G. Marrocco, "Twin-Grid Array as 3.6 GHz Epidermal Antenna for Potential Backscattering 5G Communication," in IEEE Antennas and Wireless Propagation Letters, vol. 19, no. 12, pp. 2092-2096, Dec. 2020. doi: 10.1109/LAWP.2020.3023291

(4) - J. D. Hughes, C. Occhiuzzi, J. Batchelor and G. Marrocco, "Folded Comb-line Array for Healthcare 5G-RFID-based IoT applications," 2021 IEEE International Conference on RFID (RFID), Atlanta, GA, USA, 2021, pp. 1-5. doi: 10.1109/R-FID52461.2021.9477309

(5) - C. Occhiuzzi, J. D. Hughes, F. R. Venturi, J. Batchelor and G. Marrocco, "Folded Comb-line Array for Backscattering-based Bodycentric Communications in the 5G sub-6 GHz Band," in IEEE Transactions on Antennas and Propagation. (2022). doi: 10.1109/TAP.2022.3161287

(6) - J. D. Hughes, R. J. Horne, N. K. Brabon, J. C. Batchelor, "An On-Body UHF RFID Tag with DDRR Antenna for Healthcare Data Streaming Applications", submitted to IEEE RFID, 2022.

Contents

List of Acronyms

RFID	Radio Frequency Identification
EM	Electromagnetic
UHF	Ultra-High Frequency
5G	Fifth-Generation
DDRR	Directional Discontinuity Ring Radiator
IC	Integrated Circuit
EPSRC	Engineering and Physical Sciences Research Council
NFC	Near-Field Communication
RADAR	Radio Detection and Ranging
EAS	Electronic Article Surveillance
EPC	Electronic Product Code
CMOS	Complementary Metal-Oxide-Semiconductor
RAIN	RAdio frequency IdentificatioN
ERP	Effective Radiated Power
EIRP	Effective Isotropic Radiated Power
ISO	International Standardisation Organisation
ISM	Industrial, Scientific, and Medical
ASK	Amplitude Shift Keying
BMI	Body Mass Index
EES	Epidermal Electronic System
ASIC	Application-Specific Integrated Circuit

ADC	Analogue Digital Converter
EEC	Electroencephalograph
BCG	Ballistocardiography
CP	Circularly Polarized
AC	Alternating Current
WBAN	Wireless Body Area Network
QoS	Quality of Service
D2D	Device to Device
IoT	Internet of Things
M2M	Machine to Machine
EWS	Early Warning Scores
PIFA	Planar Inverted-F Antenna
FDTD	Finite-Difference Time-Domain
EPDM	Ethylene Propylene Diene Monomer
MCU	Microcontroller Unit
RAM	Random-Access Memory
PCB	Printed Circuit Board
SPI	Serial Peripheral Interface
SDK	Software Development Kit
RSSI	Received Signal Strength Indicator
RoM	Range of Motion
BFM	Beam Forming Network
GAA	Grid-Array Antenna

CAD   Computer Animated Design

VNA   Vector Network Analyser

SMA   Sub-Miniature Version A

BA   Breathable Area

BW   Bandwidth

H-IoT   Healthcare Internet-of-Things

MIMO   Multiple-Input Multiple-Output

PAN   Personal Area Network

Chapter 1

Introductory Material

1.1 Introduction

Radio frequency identification (RFID) is a wireless communication technology originally designed for unique identification of tagged objects. RFID has the potential to replace bar-codes, allowing identification of objects from a distance, without requiring line-of-sight, and capable of storing significantly more identifying data [1]. Since the innovation of RFID, adoption has become increasingly wide-spread, used in industries such as transport, maritime, aviation, pharmaceuticals, banking, construction, security and many more, to the point RFID technology could be considered ubiquitous in modern life [2]. Between 2012 and 2020, the world RFID market had an increased from estimated \$6.7B to \$12.1B, with projections for growth to continue to over \$20B by 2032 [3].

RFID tags have many characteristics by which they are categorised, the standard highest-level defining factor is usually whether an RFID tag is *active* or *passive*. These refer to whether the RFID functions with the use of a power supply, or not, whereby active tags utilize a battery and passive tags rely on only the reflected RF power supplied by an external reader. Where passive tags are much more limited in what they can communicate, active tags use the additional energy for continual broadcasting of more complex data. However active tags are bulkier,

limited in lifespan, and a more potent polluter than passive tags, whose functionality is only limited by the quality of the material it is shaped from, so for these reasons this thesis is focused on maximising the potential of passive RFID. Another fundamental design approach to an RFID is whether the tag is designed to communicate through magnetic-induction or electro-magnetic (EM) waves. RFID tags using induction are known as near-field communication (NFC) tags, owing to the functional read distance only working in the near-field, whilst EM tags, operate in the far-field. As such EM tags offer a much longer read range, which for the applications pursued in this thesis, make this category of tags the focus of the discussion. The frequency band popularised by the incentive to provide longer read range to RFID is 'ultra-high frequency' (UHF). At this frequency an RFID tag has potential for a long enough read range to cover any standard room size, combined with the sufficient data rate for live data streaming. In addition, with the introduction of a new microwave 5G band at 3.6 GHz and mmWave 5G bands at 24 GHz and also 64 GHz for RFID to adopt, there is still more potential for development of RFID with faster data-rates, lower-latencies, and a more widely interconnected system. However, the integrated circuit (IC) packages, referred to as RFID chips, that allow RFID to seamlessly function at UHF are yet to exist for the newer 5G frequency bands. When recreating these devices through equivalent components it is difficult to accurately predict the characteristic impedance, which is essential for the antenna design and operation, so their development remains theoretical.

Within this multi-billion dollar industry, interest into increasing the RFID capabilities have spurred significant research, with one such direction being the incorporation of sensor networks into passive RFID tags for data collection. Passive RFID tags with sensors could revolutionise many industries, owing to the low-profile, robust, long life-span, and potential for mass-production. The area of interest in this thesis is healthcare, in which passive RFID could provide a low cost solution to holding patient information, transmitting live sensor data, or long-term vitals tracking through an amalgamation of sensors. Granting people access to live well-being information either within a medical facility or even from their own home,

could be a critically required advancement for the medical industries who deal with excessive patient counts, but also struggle to track patient follow-through [4, 5]. For this thesis, the design and fabrication of on-body RFID tags are discussed, beginning with an overview of the RFID systems, fundamental technical language, an insight into the current state-of-the-art developments, then delving into tag antenna designs.

1.2   RFID History

World War II is considered to be the earliest recording of RFID, extending off the work produced in RADAR technology invented some years prior. German forces discovered it was possible to more easily identify their own aircraft by changing the reflected radar signal by rolling the aeroplane. Allied British forces caught on and further developed the idea, introducing an additional transmitter to their own aircraft, which would receive the signal from the radar stations and broadcast a signal back to identify themselves as friendly. This culminated into a foundational RFID paper called "Communication by Means of Reflected Power" by H. Stockman, published 1948 in [6].

Post-WW2 the research and development of radar and RFID continued alongside substantial investment into remote identification [7–9]. Outside of military use, early applications of RFID technology were for anti-theft, producing what is known as 'Electronic Article Surveillance' (EAS). During the 70s developers, investors, companies, academic institutions, and government laboratories actively worked on RFID showing achievements mainly in animal tracking, vehicle tracking, and factory automation. Los Alamos Scientific Laboratory contributed a great deal to RFID research in this period with papers such as "Short-Range Radio-telemetry for Electronic Identification Using Modulated Backscatter," by A. Koelle, S. Depp, and R. Freyman [10]. Government agencies explored introducing the technology to new use cases, such as transportation, where vehicles and items they carried were tracked by placing transponder chips onto the vehicle,

through which receivers placed at the gates of secure locations could identify e.g. shipping ports. Later becoming the same technology behind future automated toll collection booths. Livestock tracking and identification was also considered, primarily achieved through UHF radio-waves. Tracking both the cow position, as well as medicines and hormones they required to make sure each cow received the right dosage and not accidental excessive medicines [11].

Moving toward 1990, progress in CMOS technology aided RFID systems, allowing reduced power requirements and increased functionality. Developments in micro-electronics also expanded the functionality as well as wide scale deployment of RFID in other sectors, such as toll collections, railway cars, access control and many other applications. In this time period IBM engineers patented the first ultra-high frequency (UHF) RFID system, offering 20 feet read range under good conditions and fast data transfer [12].

By then end of the 20th Century, an MIT consortium of 120 global corporations and university labs invented the Electronic Product Code (EPC), a universal identifier for every physical object anywhere in the world and managed under the 'EPCglobal' standard. Now objects that needed uniquely identifying just needed a physical label. 21st Century developments saw the first small microwave tag built using a single custom CMOS integrated circuit and an antenna. Tags could now be built as sticky labels and easily attached to objects and data could be collectively shared.

Today, organisations such as the RAIN alliance are promoting the global adoption of UHF RFID technology, much as other bodies have promoted standards ubiquitous with modern life today, such as Wifi, Bluetooth, and NFC. RAIN promotes RFID beyond just identification, symbolising the possible synergy between RFID and cloud computing [13].

1.3 RFID Standards and Regulations

RFID communication data networks are standardised for the benefit of the end user with regards to security, privacy and application. These regulations and standards are governed by varying bodies worldwide, meaning the laws that apply to the RFID tag designer are dependent on geographical location. These country specific regulators specify the allowed field strength and power levels at carrier frequencies, for example the UK regulations and standards are governed by the Office of Communications (Ofcom), whereas in the US by the Federal Communications Commission (FCC) [14, 15]. Whilst most countries abide by the same regulations there are differences highlighted by Table 1.1 sourced from the GS1 allocation database [16].

TABLE 1.1: UHF RFID Operating Regulations from [16].

Location	Frequency Bands (MHz)	ERP (W)
UK	865.6 - 867.6	2
	915 - 921	4
Europe	865.6 - 867.6	2
	916.1 - 918.9	4
US	902 - 928	4
Japan	916.7 - 920.9	4
Korea	917 - 920.8	4
China	920.5 - 924.5	2

Effective radiated power (ERP) represents the directional radio frequency power emitted by a radio transmitter. It is the total power in Watts that would have to be radiated by a half-wave dipole antenna to give the same radiation intensity as the actual source at a distance receiver located in the direction of the main lobe of the radiation pattern. ERP measures the combination of the power emitted by the transmitter and the ability of the antenna to direct that power in a given

direction. More commonly, ERP is quoted with respect to an isotropic radiator. Effective isotropic radiated power (EIRP) is the total power that would have to be radiated by a hypothetical isotropic antenna to give the same signal strength at the source in the direction of the antennas strongest beam/lobe. The difference between ERP and EIRP is a half-wave dipole antenna gain of 1.64 (or 2.15 dB) compared to an isotropic radiator of gain 1 (0 dB).

The International Standardisation Organisation (ISO) is an independent body that acts as a link between national regulators to facilitate coordination and unification of industrial standards. At UHF, one such standard is the 'ISO 18000-6' which defines the air interface for RFID devices to operate in the 860MHz to 960MHz industrial, scientific and medical (ISM) band. What is more commonly seen today is the EPC Gen2 protocol, this is an application of ISO 18000-6 standard and ties the RFID system to the 'EPCglobal' initiative [17, 18]. Although very close, a slight difference between EPC Gen 2 and ISO standard exists in a few identifier bits in the transponder memory mapping [19].

1.4 RFID Advantages

RFID tags in their most basic form are often compared to a 'barcode scanning', another common object identification system. RFID systems have a multitude of advantages over barcode, foremost being RFID systems do not operate in serial process unless specifically programmed to do so, allowing by default the ability to read multiple tags simultaneously. Barcode scanning also requires the scanner to be within line-of-sight of the barcode intended to be identified, RFID readers do not have this limitation, not requiring an optical path. Alongside these aspects the speed at which RFID can read tags is significantly faster than barcode scanning, reducing the amount of work required to identify a larger number of tags. In supply chains, efficient coordination of stock allows businesses to reduce storage inventory sizes as products may be moved from production to end user more freely. If applied correctly, RFID scanning has a high enough accuracy to

outperform barcode in both first time pass rate as well as the number of retries required for a successful read [20]. A particularly useful trait for access control, reducing delays usually onset by required security validation. Speed is especially important considering emergency situations where an automated system would need to allow fast access for potential entrance or exit. Items or people can be tagged for tracking, tracing and locating, in the supply chain this could refer to managing stock supply, deciphering where issues may be caused within the movement of the item, but could also apply to patients entering a medical facility. Beyond tracking, RFID has the capability to include passive sensor systems, such as when an item or person has fallen over, which can, for example, be critical for example businesses with expensive fragile items such as computer parts, or providing quick assistance. To which, such RFID system information can then be returned to the appropriate managers for analysis to be used for discussion into beneficial changes. The supply chain process is reported to have a 95% increase in efficiency [21], and it is believed to be equally efficacious for the healthcare system locally, and globally.

1.5   RFID Challenges

Implementation of RFID systems into any industry has an upfront integration cost, not only due to the high RFID reader price, but also the adoption of the backend systems, replacing current systems which require training and maintenance. This can be a cascading problem, as those not willing to meet such upfront costs when adopting RFID technology can then be detrimental to the entire RFID architecture, as the goal is to have the technology ubiquitous. Whilst supply chains using RFID run worldwide, standards by which RFID is maintained are not aligned globally, therefore RFID tags are either required to cover the entire bands, or be sold in specific areas which may result in confusion. Additionally, a threat to global adoption stems from the manufacturers of RFID systems, some of such businesses use proprietary technology to corner markets in given regions which prevents integration into networks.

RFID systems ease of use comes with the cost of vulnerability to environmental factors, such as possible inference from background noise, which is a common issue, often overcome through careful control over the reader environment. Most issues stem from RFID reader collisions or tag collisions, whereby RFID signals can potentially overlap preventing tags from being read. Alternatively, signal convergence may cause a tag to be read multiple times. High density RFID tag environments could cause simultaneous energising of tags from multiple readers, which could overload the reader and interrupt other simultaneous operations. Being easily readable also comes with security and privacy concerns, as barriers to entry on the stored data are limited, for example, a healthcare application could potentially put at risk sensitive patient information. RFID readers are becoming more readily available and portable, information stored on RFID tags do not delineate between interrogating readers and provide a long enough read range for many to be considered highly susceptible.

Application issues aside, an RFID tags ability to communicate comes down to the ability of the antenna to perform, which can be heavily hampered by the environment in which it is placed. Notably difficult areas are often the most desirable application location, such as on-metal, liquid containers and living tissue.

1.6 RFID Technical Fundamentals

A top-level description of a passive backscatter RFID communication system is described in Fig. 1.1, showing primarily the communication link between an RFID tag and RFID reader, which then funnels back the received data to a collection point. Whilst Fig. 1.1 describes the communication link with a single tag, an RFID system can operate seamlessly with many tags within the readers emitted field, simultaneously communicating with each, which can then be uniquely identifiable thanks to the unique code provided by the RFID IC manufacturer.

In a truly passive system, the RFID tag is the combination of an antenna and an RFID IC, however, there also exists a middle ground between passive and
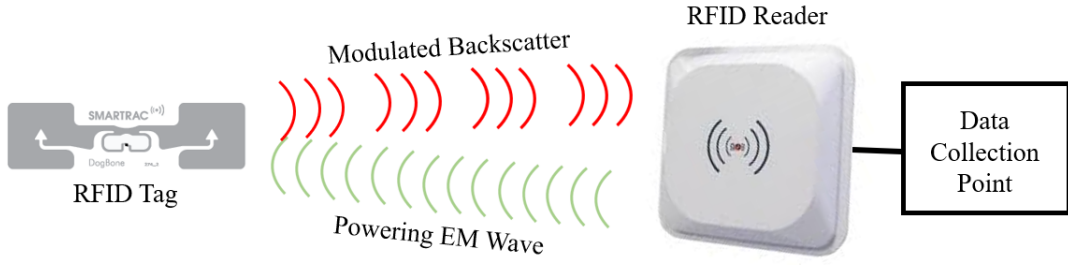
FIGURE 1.1: Top-Level RFID System.

active called semi-active. A semi-active system employs a battery for more complex on-board functions, such as processing sensors, whilst still utilizing a passive communication link. In either of these systems employing a backscattering communication link, the RFID tag IC operates as a transponder, applying amplitude shift keying (ASK) to the reflecting EM wave [22].

To achieve a strong communication link, the tag antenna needs to have a conjugately matched impedance to that of the IC, to allow for efficient power transfer. The quantifiable result of a efficient tag antenna is assessed by the resultant maximum read range, described by the Friis Equation (1) [23].

$$r = \frac{\lambda}{4\pi} \sqrt{\frac{EIRP \cdot G_{tag} \cdot \tau}{P_{th}}} \tag{1}$$

Where λ is the operational wavelength of the antenna, EIRP is the combination of the reader antenna gain and transmitted power (controlled by government regulatory bodies), G_{tag} is the gain of the tag antenna, τ is the power transmission coefficient, and P_{th} is the threshold power required to turn on the tag. The τ component being the result of the conjugate match between the antenna and IC, described by the equation (2).

$$\tau = 1 - |\Gamma^2| = \frac{4R_a R_c}{|Z_c + Z_a|^2} \quad (0 \geq \tau \geq 1) \tag{2}$$

Where Γ is the reflection coefficient of the tag antenna, $Z_c = R_c - jX_c$ is the complex impedance of the RFID IC, and $Z_a = R_a + jX_a$ is the complex antenna

impedance. The IC impedance is capacitive owing to the presence of an internal solid state switch, requiring the antenna impedance to be equal in inductive reactance.

1.7   Research Aims and Objectives

The aim of the research in this thesis is to develop an efficient passive-RFID tag antenna for on-body applications. To achieve this goal, our objectives were to progressively examine increasingly challenging technological evolutions of RFID and evaluate the performance at each stage. The objectives are as such:

1. Design and fabricate a UHF RFID antenna resilient to the on-body environment. As UHF is the current RFID standard operational frequency, investigate new possible antenna topologies, then prototype with off-the-shelf RFID components. In doing so, attempt to improve the communication link read range, whilst making the antenna as small and comfortable for wearing as possible.

2. Investigate the feasibility of 5G RFID antenna designs for on-body applications, at 3.6 GHz. Since the 5G allocated bands are still relatively new, the technology to drive such an antenna is yet to exist. Using the UHF RFID fundamentals as guidance, employ EM simulation tools and physical antenna measurements where possible to assess the achievable 5G RFID performances.

3. Explore the potential performance of the 3.6 GHz antenna designs at the higher 5G frequencies of 24 GHz or 64 GHz. Attempt to utilize the reflective properties of the skin at the higher frequency to completely remove the ground plane, whilst maintaining performance.

1.8   Thesis Organisation

The organisation of the thesis is as follows:

Chapter 2 presents an overview of the on-body RFID tag antenna field, firstly, using literature to frame the challenge of placing an antenna on the body. Then, going on to consider the techniques other researchers have used to overcome these challenges, prominently at UHF, finding where there has been success but also deciphering in which areas there is potential for new developments. Finally, using the literature to discuss incorporating sensor networks into RFID tags and the potential advantages moving to 5G could have for RFID.

Chapter 3 on-wards presents the technological research of the thesis, beginning with the design and fabrication of a UHF RFID tag for live data-streaming through a Direct Driven Resonant Radiator (DDRR) antenna. Since the operational frequency in this case is the standard UHF, this chapter presents a complete, operational system that has potential for direct healthcare application.

Chapter 4 is the start of the evolutionary process of designing a 5G RFID antenna, utilising a monolithic array antenna called the grid-array antenna. This chapter defines the traditional topology of the antenna structure, going on to provide insight into how the structure performs on the body, at the newly allocated 5G C-band at 3.6 GHz. This chapter is used to provide the foundational description of simulation and measurement methods that subsequent chapters will reference.

Chapter 5 continues the evolution of the grid-array antenna, by acknowledging the short-comings of the original structure, this chapter presents research into two variations of the grid-array to overcome inherent issues. The first structural iteration providing a potential solution for the relative large size of the original structure, through miniaturization. The second iteration proving a potential solution for the issue of the large obstructing ground plane, blocking access of potential sensors from connecting with the skin.

Chapter 6 presents an antenna design tangential to the grid-array antenna, in the comb-line antenna. Whilst both antenna structures share the same fundamental antenna operation, the comb-line is shown to offer greater miniaturisation potential, both in surface area reduction achievable and the resultant radiation performance. Showing that as the antenna is miniaturised, previously unexploited conductor can be employed to enhance the radiation performance.

Chapter 7 utilizes the knowledge gained from the previous chapters and attempts to deploy the grid-array antenna at 24 GHz. Since the operational wavelength at this frequency is significantly smaller than the previously used 3.6 GHz, here the antenna structure returns to the traditional topology, but utilizes the reflective EM properties of the skin to remove the obstructing rear-ground plane.

Chapter 8 provides conclusions on the research, offering thoughts and ideas on the successes and failures of the presented work, before going on to suggest potential future work avenues.

1.9 Contributions of This Work

The contributions to research from this thesis are:

(1) Development of a UHF RFID tag system for live data streaming for healthcare applications through novel adoption of a DDRR antenna.

(2) Investigating into the performance of a grid-array antenna as a 5G RFID tag antenna, for the on-body environment.

(3) Evaluation of the performance of a miniaturised grid-array array antenna for the on-body environment.

(4) Evaluation of the effects reducing the ground plane of the grid-array antenna has, for possible integration of sensor networks to have direct access to the skin.

(5) Investigation into the comb-line array antenna, a highly miniaturised and efficient variation of the grid-array antenna.

(6) Analysing the possibility of utilizing higher frequency 5G bands and utilising the reflective properties of the body in place of a ground plane.

The respective publication for each contribution has been presented in the following section. Contribution (6) is currently unique to this thesis, having no associated publication.

Chapter 2

Literature Review

2.1 Introduction

Electronics as a diagnostic tool has long been accepted for our homes, automobiles, and industry, but as of yet the best diagnostic tools for our body remains the clinics operated by healthcare professionals. With increasing population numbers and ever increasing pressure on the healthcare system to look after those in need of care [24], an ideological push has been made towards self-care. Self-care refers to a capability of allowing people to track and manage their own well-being from their own homes [25]. Much as a modern day car can have over 200 sensors to track the well-being of the mechanical components of the vehicle, showing warning or hazard lights on the dashboard, we too must now look to apply this system to our body to achieve well-being maintenance and illness prevention. To realise this for the human body, technological advancement needs to be made to allow for information to be gathered from a person's body through the utilisation of sensors, into robust and inexpensive packages [26]. Physiological measurements that require interfacing with the skin have been prominent since the early 20th century, yet the devices in question have mostly remained unchanged [27], such as using bulk electrodes, attached to the skin with adhesives, clamps, straps, needles or sometimes conductive gels. The devices come in many shapes and sizes but

generally the data taken from the body by sensors are received by a separately housed rigid circuit board, requiring its own power supplies and communication modules. In order to advance these measurement tools a certain standard of device needs to be met for successful adoption of the technology [28]. An example of this is seen today through the adoption rates of hearing-aids, whereby those who require audio assistance do not wear the device under what is deemed a combination of poor-comfort, low quality, and associated stigma [29]. Combating poor-comfort, less than optimal quality, the stigma of requiring electronic device assistance, and stimulating the interest in improving these devices, comes at a time electronics is seeing a movement towards what is being called 'soft electronics'. Electronics that can be worn comfortably and function even under the most extreme effects of contortion, allow engineers to be rid of typical rigid housing materials and, instead, interface the electronics tightly with a mounting surface, without gaps and unwanted loss of contact area [30, 31].

With the physiological measurements, one clear step forward that is required in the evolution is a shift to a wireless communication link [32]. When a device can be made wireless, the user is freed and the information processing can be offloaded to cloud based services [33]. As a community, RF engineers are working together to find the best possible wireless communication solution for each telemetry scenario. A goal which all those concerned hope to achieve is an optimum communication link, through efficient antenna operation. This thesis investigates the field of on-body, wearable, and epidermal antenna designs. The designs considered throughout this thesis will be on the subject of antenna designs external to the body, also known as non-invasive, meaning implanted designs will be omitted from discussion. As discussed in the introduction, the on-body environment is a formidable challenge for antenna operation, which is an especial problem for antennas mounted directly on skin. When considering on-body antenna design, what is found is that a balance must be made between the desired structural performance and the radiation performance. If we were to conceive of an ideal antenna for the on-body environment, the antenna structure would be a comfortable, skin-like material, and low-profile to the point of complete unobtrusiveness. This ideal

structure has been dubbed 'epidermal' electronics, referring to the idea of electronics being as close to skin-like (epidermis) as possible [34]. However, due to the problems arising from the body, the RF capabilities of such devices suffer most severely in terms of read range performance, since the losses are prevalent to an antenna without protection from the body. More traditional antenna designs for the on-body environment overcome losses by introducing separation between the body and the antenna, be it low-loss rigid materials or additional EBG structures. In a more general sense, these designs would be considered 'wearable' antennas. Hence, the current state of the field suggests on-body antennas looking to achieve longer read distances therefore must compromise on structural characteristics for performance. Using the literature available, this section will explore what other authors have used to define an epidermal antenna, then go on to consider the wider field of wearable antenna types. The advantages and disadvantages of each and comparing performance capabilities both in terms of radiation capability and wearability is then discussed.

Another aspect of the communication link which needs to be discussed is the frequency of operation. Whilst the antenna design is the focus of discussion here, it is just one factor in a multi-system operation to pass data from one device to another. The two main communication bands for discussion are Ultra-High Frequency (UHF) and Fifth-Generation (5G). These are of particular interest since they have the most well supported back-ends, meaning that the setup, operation, and maintenance of such systems is more easily and simply achieved, therefore being more likely to be adopted. The literature of the current state-of-the-art will be discussed in each case.

2.2 Human Body Impact on Antennas

Before discussing the devices developed in the current state-of-the-art, it is worth exploring the literature on the effects the human body can have on RF electronics, especially when attached to the body.

Since the onset of communications devices becoming suitably small enough to be carried on the person, research has been carried out into the effect that radiation has on the body and the effect the body has on the radiation. In one of these early studies by Krupka, a whip antenna (monopole) was used in the HF and VHF frequency bands to analyse radiation performance in close proximity to the body, shown in Fig.2.1. In this study, the body is described as acting as a radiating element itself, surrounded by a dielectric medium applying a strong "dissipative resistance" [35]. Situating the whip antenna in close proximity to such an element (the human body) seems to cause a coupling arise. Through this coupling, Krupka describes the human body acting as a director at lower frequencies then eventually a reflector at the higher frequencies.

FIGURE 2.1: Measurement of pocket-sized communication system properties [35].

Studies were further continued by King, for the first time exploring the effects of the body in the UHF band [36, 37]. King first described the deleterious effects of the antenna due to body absorption, body position, head and arm movements, clothing, and fabrication materials. Then, in a similar fashion to Krupka, they studied the effect of a dipole in close vicinity to the body. They reported one particularly prominent effect, that, as the operating frequency increases, the greater the shadowing effect the body has on the dipole radiation field. What these works describe is the consequences of the electrical nature of our bodies. This phenomenon has continued to be shown in literature when studying various antenna topology types and materials for the on-body environment [38–40].

In more recent times, tools have been developed capable of measuring tissue conductivity, with the results accumulated in publicly available tables such as the IT'IS foundation databases [41]. Oyeka uses one such tool to provide an in-depth analysis of the skin conductivity and how this parameter can vary from person to person [42]. As well as a strong frequency dependence, the electrical properties of the body are defined by factors such as the skin thickness, density of underlying fat tissues, muscles, and bone, all of which are influenced by environment and ethnicity. Using BMI as a differentiating parameter, the paper searches for conductivity trends between a diverse population in the UHF band. It concludes that such a trend is visible for people with low muscle density, but less clear for people with a higher muscle mass. In general, what is shown is a strong correlation between tissue permittivity and conductivity with read range, represented through the correlation between BMI and read range, Fig.2.2.

The importance of analysing diversity arises in conjunction with the nature of the dielectric effect on antennas [43]. That is, the antenna is strongly affected by the properties of the platform it is mounted on, making it challenging to create antennas that function well on a range of different body types.
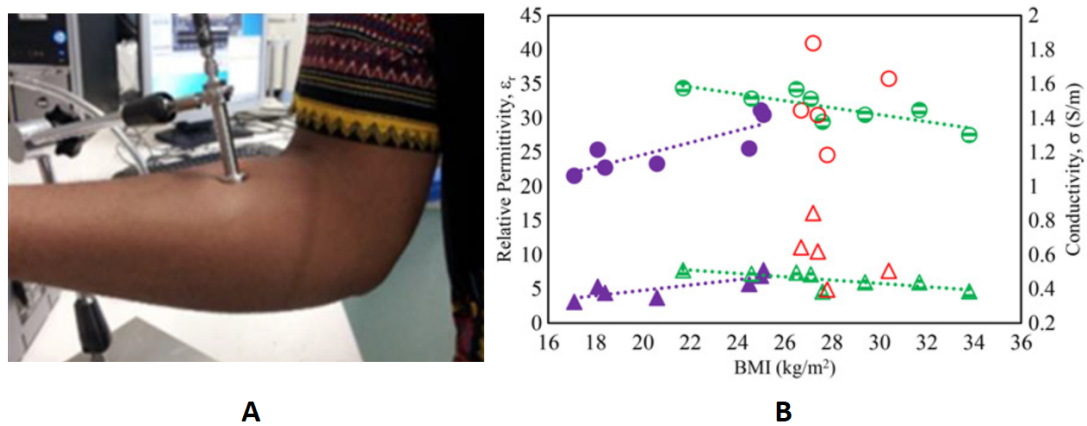
FIGURE 2.2: (A) Measurement of body dielectric parameters. (B) Effect of BMI on body dielectric properties at 867 MHz. Circles: ϵ_r, Triangles: σ. Solid: women, strip: men (low muscle mass), hollow: men (high muscle mass) [42].

Miozzi [44], is one such example of attempting to cope with the challenging diversity problem when considering a single antenna use for a wide variety of users. The system is composed of an open-loop UHF-RFID antenna, enveloping a two-way discrete (four states) tuning circuit, shown in Fig. 2.3. The operation would then allow for detection of frequency shifting, then correction through up/down shifting for the operating frequency to restore performance capabilities.

FIGURE 2.3: Prototype of the epidermal board with two-way discrete impedance tuning and its application on the skin by 5 μm polyurethane film [44].

Another example of overcoming the body diversity issue comes from Makarovaite [45], in which the proposed design features a breathable polyurethane polymer, which when either layered singularly or doubled-up can provide a suitable frequency shift for possible correction mitigation of the body diversity variations,

shown in Fig. 2.4. When measuring the relative permittivity of a persons skin, if they were in the range less than 30, a single polyurethane layer could be employed, but over 30, there was a requirement to increase substrate thickness in order to maintain the resonant frequency in the intended band.
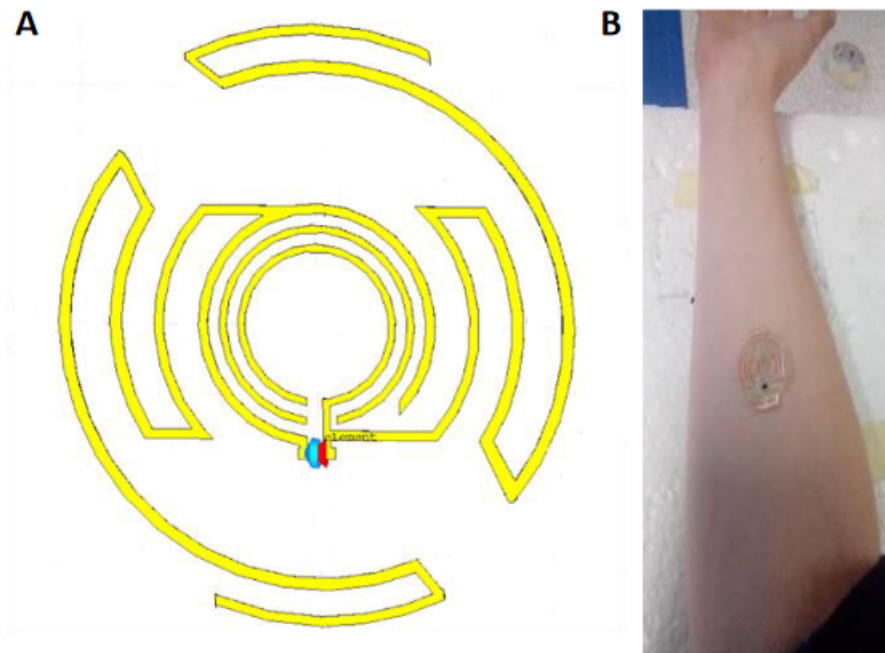

FIGURE 2.4: Figure 1. A) Topology of the on-skin antenna sticker design with the Higgs-3 IC; B) Copper etched tag on mylar with a polyurethane layer and skin [45].

2.3 On-Body Antennas

2.3.1 Epidermal Antennas

First coined by Kim et al. in [34], the epidermal electronics term in this paper sets the goal-posts for engineers attempting to achieve electrical integration between the human body and wider world.
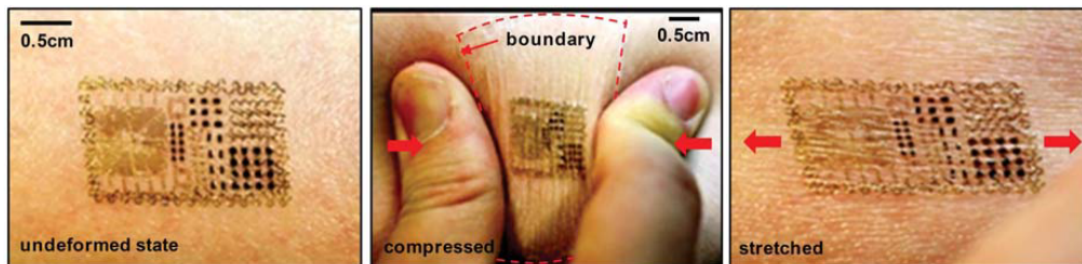

FIGURE 2.5: Multi-functional EES on skin: undeformed (left), compressed (middle), and stretched (right) [34].

Whilst not specific to antennas, this paper introduces a new approach to electrodes, electronics, sensors, power supply and communication components, to package them into an ultra-thin, low-modulus, lightweight, stretchable "skin-like" device that is capable of conforming to the skin surface by soft contact. This was achieved by way of utilising multi-functional sensors, wireless power coils, and radio frequency communications integrated into a thin 30μm, gas-permeable, elastomeric sheet based on modified polyester, shown in Fig. 2.5. The gold conductor embedded in polyester is capable of matching the skins mechanophysiology in strains that cause the face of the skin to wrinkle, crease, and pit producing altitudes ranging from 40μm to 1000μm. An alternative adhesion technique is provided in the integration of the electronics into a commercially available transfer-tattoo, acting as both a mounting tool as well as concealment device, shown in Fig. 2.6. Through these characteristics described, Kim et al. declare this technology as an 'epidermal electronic system' (EES). Regarding the RF communication capabilities, it is noted the RF components were able to achieve resonance, however the expected deformation of the device in correlation with the skin causes a considerable detuning, quoting a 30% change in frequency from only a 12% tensile strain. Antenna

detuning occurs with deformation (e.g. bending or stretching) owing mostly to the change in electrical length of the antenna under strain, however, this deformation also impacts the material properties of the antenna is placed upon, making characterising and predicting the response to strain difficult [46].
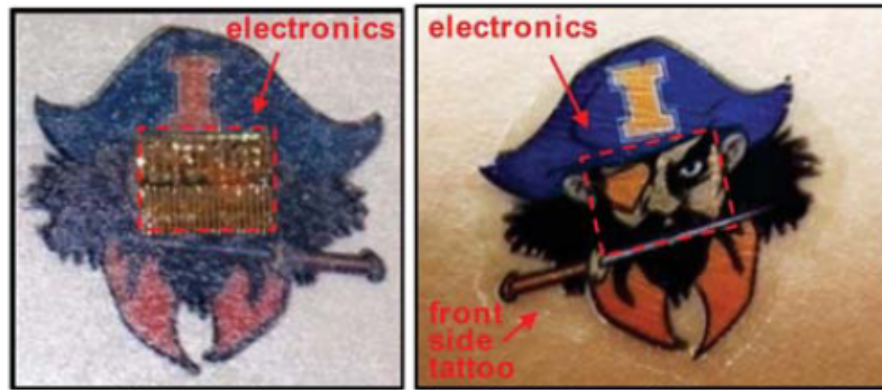

FIGURE 2.6: Commercial temporary transfer tattoo provides an alternative to polyester/PVA for the substrate; in this case, the system includes an adhesive to improve bonding to the skin. Images are of the back-side of a tattoo (left), electronics integrated onto this surface (right) [34].

Deformation of the antenna is a major challenge with on-body antennas, since one major aim of the ultimate design is a low-profile structure, therefore curvature with the body profile is unavoidable. Song [47] provides an analysis of the impact of bending a patch antenna, specifically for wearable applications. The authors conclude the frequency shift of caused by bending any typical antenna topology is expected, and future research should be made into a standard formula for expected frequency shift with bending.

Published at a similar time as Kim (2011), the transfer tattoo technique was being considered with the antenna as the major focus in Ziai (2011) [48]. This time exploiting passive RFID for the communication link, with the application aim on identifying and tracking people in work environments. Specifically, UHF RFID is employed for the communication link, since the use of relatively high gain antennas and EM wave propagation as a coupling mechanism provides a greater identification distance of up to 10m.
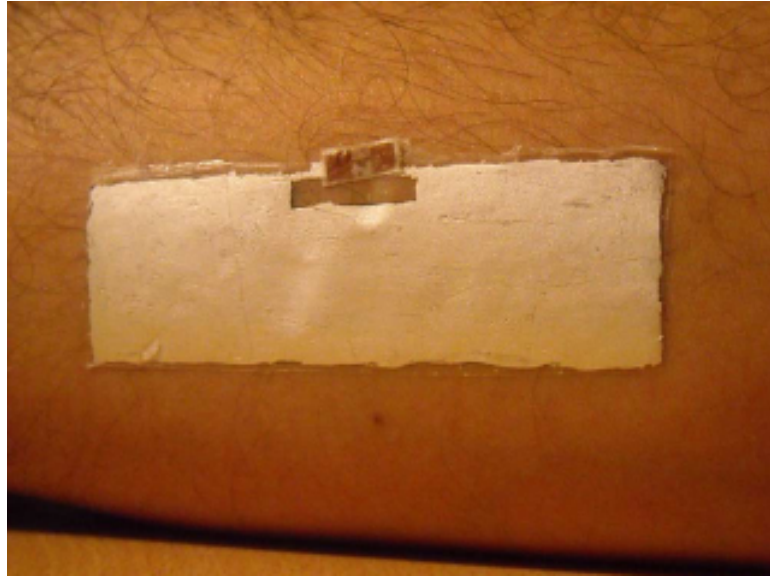
FIGURE 2.7: Tattoo transfer tag mounted on volunteer arm. Conducting paint separated from skin by a 10 micrometer layer [48].

As shown in Fig. 2.7, the antenna topology utilised is a form of slotted-patch antenna. Chosen for being a low-profile antenna formed from only a single conducting layer and therefore requiring no vertical via connections. The RFID ASIC feeding the antenna is conntected across the slot, such to induce an electric field in the slot, hence causing electric current to flow around it. This loop provides the inductance to match to the RFID ASIC, allowing the rest of the patch aperture to radiate the energy. The conductive material is applied straight onto the skin with transfer tattoo mechanisms, separated from the skin by the transfer tattoo adhesive polyurethane material a few microns thick. Ultimately, the read range performance of the antenna is between 80 cm and 120 cm depending on the placement of the antenna upon the body. Whilst an appreciable distance, the intended application would require the user to come into close proximity of the reader, for example in a doorway or turnstile. Expecting the tag to read in over large unconstrained areas consistently would be too unreliable, especially passively.

In more recent developments, Miozzi presents a general-purpose small RFID epidermal data logger for continuous human skin monitoring in mobility [49]. A 3 cm by 3 cm flexible kapton layer hosts a miniaturized open-loop antenna, a microchip with internal ADC and pads for interconnecting external sensors and a battery

for data-logging mode. The open-loop antenna operates at multiple global RFID bands through the design of two structural sections; a tapered track at the input to match to the RFID chip impedance (with an additional tuning inductor for control of the operational frequency), and a meander line portion to correctly align the current distribution over the loop. Whilst the antenna itself is not directly bound with the skin, separated by the 50 μm kapton layer, the package utilizes the space inside the loop to allow for sensors to interact with the body through the Kapton layer. Whilst titled 'epidermal', the Kapton material would not fall under the description of an EES system described by Kim (2011) [34], since it lacks the epidermis-like characteristics, but it is still a very thin laminate capable of flexing around any part of the body. In a more focused consideration of the antenna on the epidermis and an insight into the durability of epidermal tags, Miozzi again adopts the open-loop antenna topology in Miozzi (2020) [50]. However, in this approach the antenna is made with a thin copper wire and a conductive yarn attached onto an elastic membrane. In the first case where a copper wire had been laid onto the membrane, the radiation saw the best performance (G = -14 dB), but durability and longevity of the antenna was at its weakest, with only a day of use before breaking through wear and tear. Additionally, it was seen the bandwidth of the copper wire antenna could be improved by increasing the width of the wire, although the more rigid structure was more vulnerable to breaking. The second design using conductive yarn was far more durable lasting several days before any noticeable damage, but consistently measured a slightly poorer radiation performance (G = -16 dB). Tests performed on volunteers with different body-mass indexes demonstrated that it is possible to guarantee a read distance of at least 75 cm in 90% of cases, when positioned favourably on the body. Furthermore, if placed onto the abdomen, the epidermal tag can even be read from up to 2 metres.
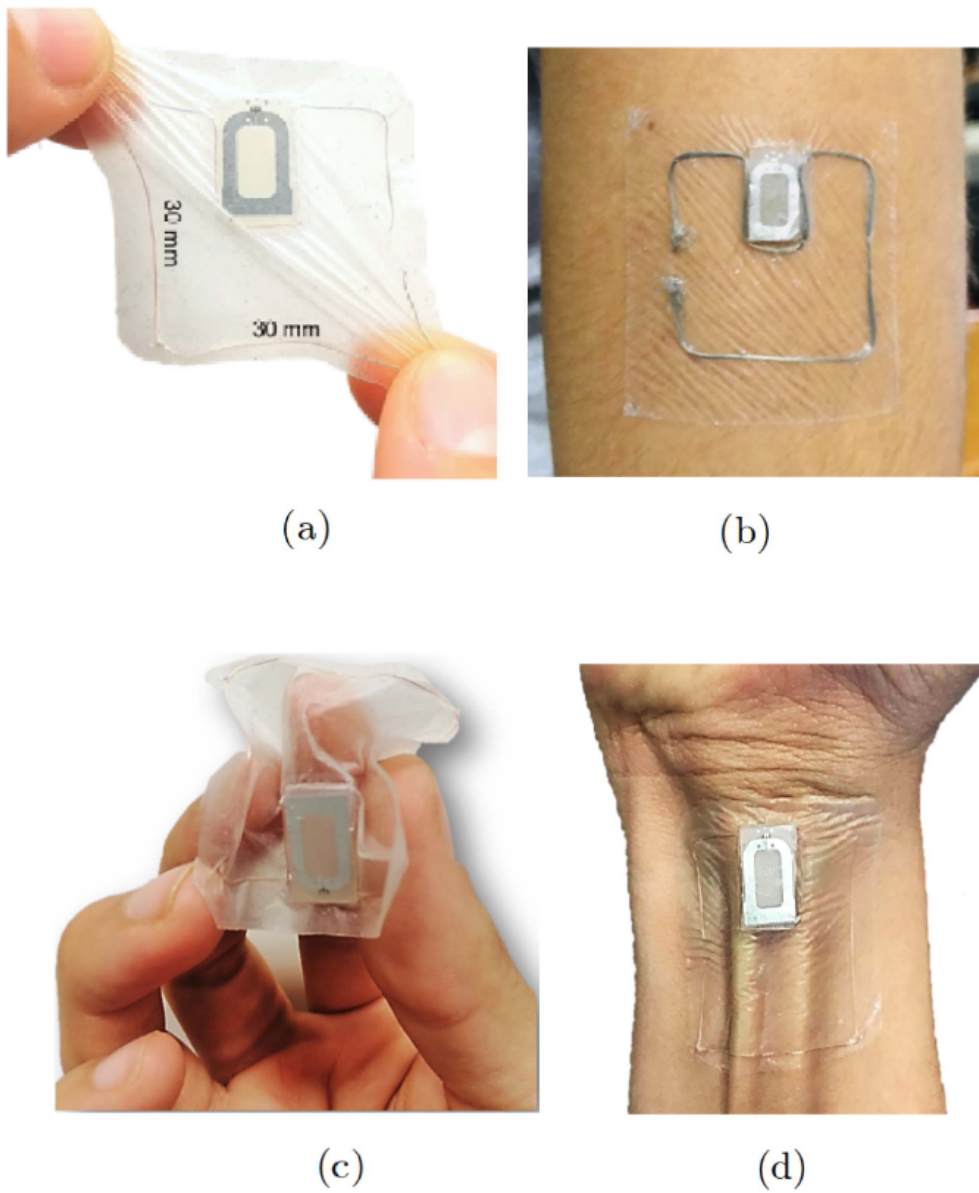
FIGURE 2.8: Prototypes of the epidermal tags made by (a) copper wire and (b) conductive yarn. They are (c) soft and (d) conform to body discontinuities (forearm tendons) [50].

2.3.2 Printed Electronics

An exciting new trend is occurring through adopting printed electronics as the fabrication technique [51]. Printing has shown to allow for an effective fabrication solution for low-profile and intricate designs, offering inexpensive options (dependent on the ink utilized), and allows for manufacturing in large quantities, in the kilometers scale, for mass-production [52]. Printing also offers a potential 'green' avenue for moving electronics toward a sustainable future [53]. Whilst printed electronics is an expansive field of research, it does not imply that the electronics are flexible, such as in Sharif (2019) [54] describing antenna design for healthcare applications on rigid substrates. Such flexibility is a key component in the realm of wearable electronics, the following publications reflect how printed electronics can be a powerful tool to aid electronics for the on-body environment.

Amendola [55] pursues ink-jet printing of epidermal RFID antennas by utilizing a self-sintering conductive ink. Self-sintering is a relatively new ink technology whereby the ink can dry at room temperature and form an instantly conductive layer, without the need of time-consuming thermal sintering. These sintering-free inks are both inexpensive and simple to deposit on a flexible substrate by using consumer-grade, low-cost, inkjet printers. The antenna topology employed is the meandered-rectangular loop, connected to a EM4325 RFID microchip, shown in Fig. 2.9.
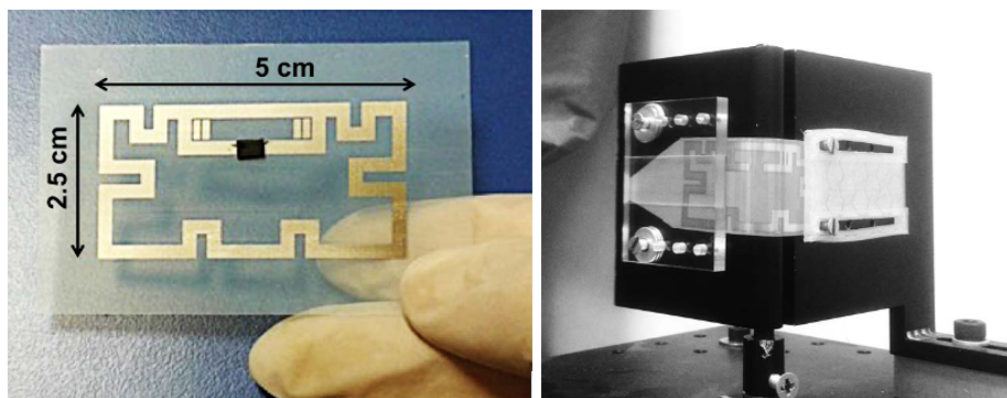

FIGURE 2.9: (A) Inkjet-printed meandered-loop epidermal antenna over PET substrate. (B) Inkjet-printed antenna mounted over a hinge setup for the bending fatigue test [55].

Experimental practice showed whilst printing could perform within the same bounds as typically used bulk copper, however achieving such a feat requires multiple layers (threefold) of ink to be deposited [55].

In recent years graphene has been a much sought after material for research, as an ultra-thin, single atom wide, and flexible alternative to traditional conductors such as copper [56]. Leng attempts to utilise this material for Low-Cost RFID and Sensing Applications [57]. A flexible graphene nanoflake printed meandered-line dipole antenna is presented, showing acceptable return loss, gain, bandwidth, and radiation patterns for mid and short-range RFID, and sensing applications.
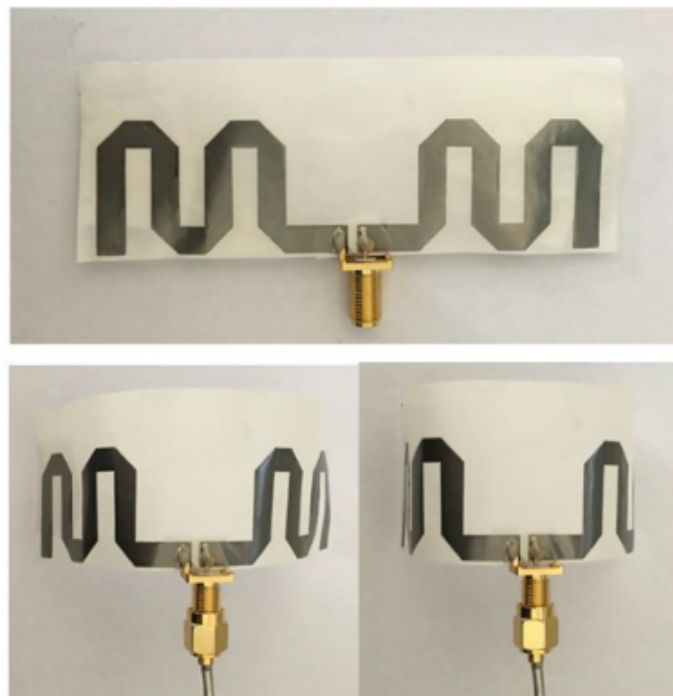

FIGURE 2.10: Photograph of the printed graphene antenna on paper, without bending, with mild bending, with extreme bending [57].

Considering printed electronics in the more general sense, Jacob (2018) [58] employs printed electrodes for use of electroencephalography (EEC) and ballistocardiography (BCG) by way of behind-the-ear measurements. Standard electrodes for these measurements have a central conductive disc for sensing, which is encompassed by a large area of adhesive material, a non-contributor to the signal collection. The ink-jet printed electrodes presented consist of a silver nano-particle layer on a conformal substrate with adhesive film placed over the electrode, thus

providing the bond to the skin and allowing for a much larger sensing area than standard electrodes, Fig. 2.11.
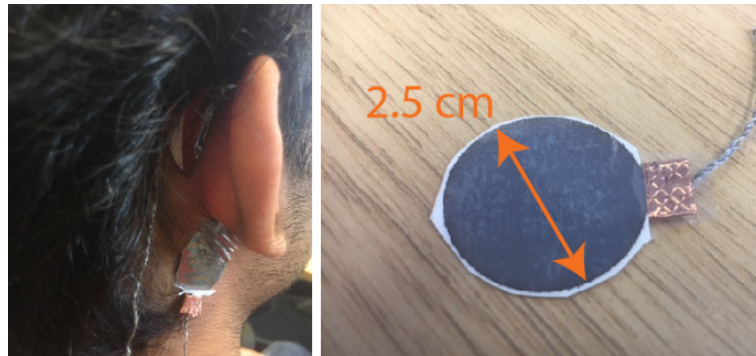
FIGURE 2.11: Illustration of the electrode placement behind the right ear [58].

Another printing technique comes by way of 3D-printing, allowing for entire sophisticated and flexible devices to be constructed through printing alone [59–61]. Thus, 3D-printing would circumvent the traditional multi-stage fabrication methods which require expensive equipment. Although, currently 3D- printing is a slow manufacturing process, the technique is mostly favoured for prototyping, rather than full scale fabrication, such as roll-to-roll printing [62].

2.3.3 Wearable Antennas

Whereas epidermally mounted structures are by definition always directly on the skin, wearable devices function on or close to the body with the goal of communicating wirelessly to an off-body device. This would even include the term 'wearables' in the mainstream, more often that not these devices separate themselves from the body significantly by use of encasement or housing, such as a smartwatch, head-mounted displays, fitness trackers, and communication devices embedded into clothing. However, there is considerable research space between the 'wearables' in use today and the epidermal devices we envision as part of this work.

Exemplifying this, Dubok presents a robust UHF RFID antenna for use on perishable goods and human bodies in Dubok (2014) [63]. Introducing a balanced-slot antenna design, structured with the RFID chip centrally feeding a dipole of tapered tracks. This dipole structure utilizes the induced electric fields of the adjacent, symmetrical, slots to match to the chip impedance. The resultant radiation occurs at the end of these central dipole tracks, either end of the antenna. The balanced-slot antenna is constructed on FR-4, a rigid inflexible material, backed by a ground plane. The application for this antenna is intended only for identification and the 'wearability' of the design leaves much to be desired. However, in having poor structural properties for the body, the radiation capabilities appear well-performing for a passive tag, in a range of non-ideal UHF-RFID antenna scenarios such as on perishable meat, on a water containers, and on the body.
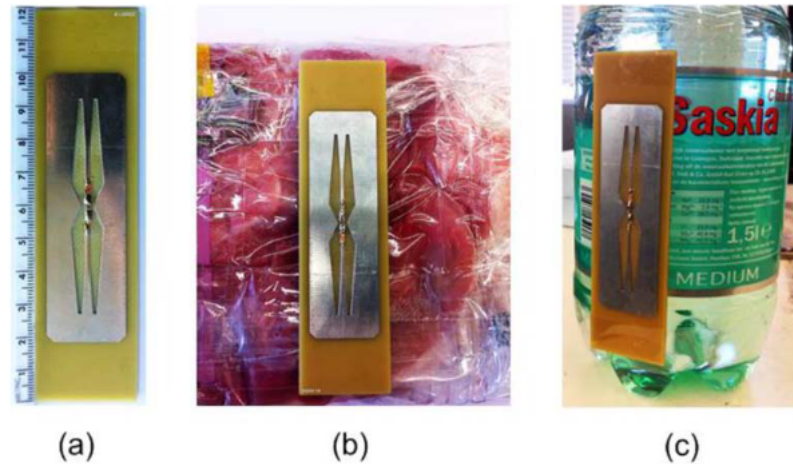
FIGURE 2.12: Robustness experiments of the antenna on various environments: (a) air; (b) meat; (c) water [63].

Similarly, Casula [64] presents a robust printed antenna for UHF wearable applications. Much like with Dubok's design, Casula presents a balanced-slot structure, employing symmetrical elliptical slots in close proximity and breaking the track between them at the center to place the RFID chip. However, this design develops the slots with 'teeth' adaptions to produce a grid-like pattern, focusing the radiation of the antenna closer to the center of the design (hence reducing the distance to the RFID chip), for improved radiation performance. Going on to show the capability of the singular antenna design to be compatible to several commercial chips. Not only robust when being attached to the body, but also tolerant of being up to 40 mm from of the body and still functioning. As with the prior design, this antenna again opts for a 'copper shield' to insulate against the coupling effects of the body.

An example of a wearable antenna approaching the requirements for epidermal electronics is presented by Taylor, in his design of a finger-worn UHF far-field RFID tag antenna [65]. The operating theory is that the single turn loop small-antenna (circumference $< 0.1(\lambda)$) behaves as an inductor that can be made resonant through the addition of a tuning capacitance, forming a high-Q parallel tuned circuit. Neatly, this wavelength of UHF closely resembles the circumference of an adult finger or toe. Three prototype finger ring tags were designed and fabricated; the first being placed on 2 mm foam, the second 1 mm foam, and the third on 0.1

mm thick 80 gsm standard office paper substrate. Results showed relative gain performances of -6, -7.8, and -13.8 dB, respectively, showing that between the thickest foam and the paper substrates there is a 7 dB performance improvement in favour of the thicker material. These gain values equate to a 2 m read range for the paper substrate, and a 5 m read range for the thick foam. In this context we can see the difference in performance is as a result of the difference in application capability, whether a reader antenna is required to be in relative close proximity or if the read distance can be achieved within a standard room size, so to be more seamlessly integrated into the environment.
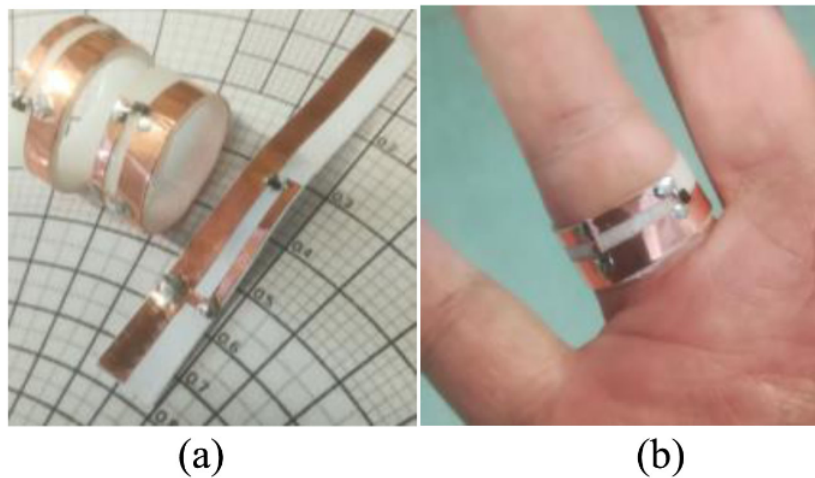

FIGURE 2.13: (a) Three constructed prototype rings. (b) 22 mm version being worn [65].

One key component in all mainstream devices is the power source. As far as batteries have come in the past decade, they still remain an unavoidably large component in any electronic device. Whilst passive RFID communication removes the need for a battery, the amount data a passive link is capable of passing is limited, thus power supplies are required to increase the complexity of the data being processed, and in-turn increase the intelligence of the device.

In Caccami (2018) [66], the separation between antenna and body is utilised for an ultra-low profile local power source, required for beyond just identification in the additional capability of data-logging. Employing the same slotted patch antenna as presented in [48], by Batchelor. This is achieved by fashioning the negative electrode of the battery (anode) also as the RFID tag antenna, and by coating

the tag with a conductive polymer anode material, Fig. 2.14. One challenge this design must overcome is dealing with the material properties of a discharging battery. As the battery discharges the dielectric properties of the material changes, which must be accounted for to stabilise the chosen resonant frequency, which in this case is via UHF. Measurements of the antenna take place when positioned on a person's forearm, quoting read range distances between 1.3 m - 3 m based off of the measured gain performance.
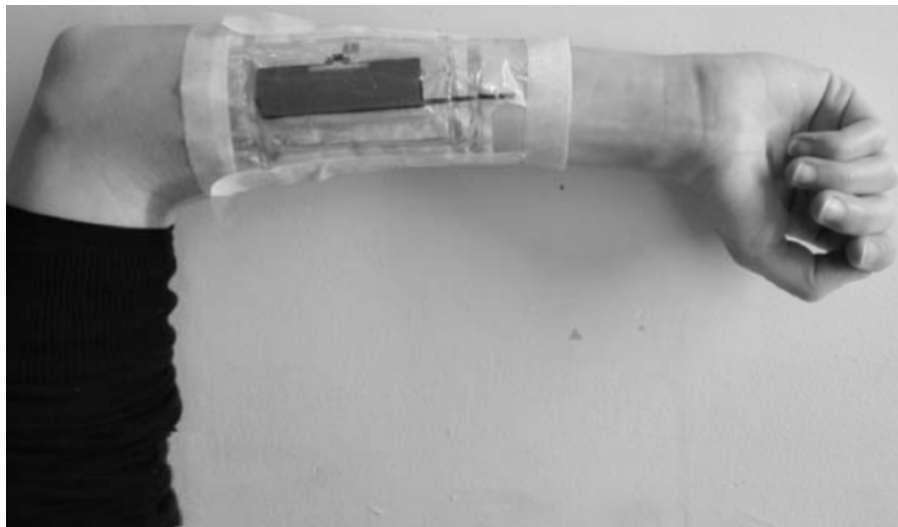

FIGURE 2.14: Prototype of the tightly integrated multi-layer battery antenna [66].

Another point of interest on the antenna design is the radiation polarity, which for the most part is decided by the application requirements. The antennas considered so far for extended read range in the UHF-RFID band have been linearly polarized. This is opted for in part due to linear antennas obtaining a simpler antenna topology, making them more easily prototyped. There is also an additional advantage through a 3 dB gain from reader antenna, should a linearly polarised reader be used in combination with a linearly polarised tag antenna, allowing for a slightly extended read-range. Working with linear polarisation, the orientation of the tag needs to be aligned with the reader antenna for proper functioning, any misalignment in this polarity between the tag and reader would result in large loss of performance proportional to the 'Propagation Loss Factor' (PLF).

Alternatively, circularly polarised antennas could be employed, allowing for the alignment to not be as much a factor in performance capability. For many applications based on the on-body environment, this would be ideal since the orientation of an antenna worn on the person may not always be predictable, for example physiotherapeutic applications would require the antenna to be tracked as the body moves in all directions. However, relative to the linear polarisation reader and tag setup, introducing a circularly polarised reader would result in a 3 dB loss in gain, due to the fundamental operation of the circular antenna being two orthongal linear polarized waves 90 degrees out of phase, hence resulting in a permanent polarization mismatch loss of 0.5 (-3 dB). This avenue is pursued in Le (2021) [67], fabricating a passive UHF RFID tag based on a circularly polarised (CP) patch antenna, connected to the body by a low-permittivity textile. This is achieved by applying a combination of cross and L-shaped slots into the radiating patch, producing surface current patterns in the vertical, horizontal, and median space for right hand circular polarization. This structure is made in conjunction with asymmetrical truncating of the corners of the square patch, applied for a more efficient antenna and optimal axial ratio.

2.4   RFID Sensors Networks

A common pursuit to advance the field has been to take RFID communication beyond identification. Generally speaking, the industry has adopted RFID sensor networks for many applications including: infrastructure structural health [68], integrity of pipelines [69], concrete integrity [70], AC currents [71], corrosion affects [72], pressure sensing [73], strain sensing [74], humidity sensing [75], food quality monitoring [76], and many more. More closely related to the on-body environment, there have also been some attempts at integrating RFID into the medical field with applications such as checking blood pressure [77] and glucose [78].

Within the on-body realm this thesis is investigating, Horne exemplifies an application in Horne (2019) [79], a UHF sensor network is employed as an inexpensive method for tracking therapeutic movements aiding clinicians and patients in post-surgery physiotherapy. As the focus of Horne's publication is on data collection and processing, the antenna opted for is a simple dipole.

FIGURE 2.15: Sensor locations for Xsens and RFID units [79].

Further to this, using the same acceleration measurement system, Horne advanced the back-end to transmit real-time data through UHF RFID at data rates of up to 5.2 KBps, with 99.99% data integrity, up to a read distance of 2.4 m with use of a ultra-low power supply on the tag [80]. This would allow for on-body data

transmission to offline or even supplementary computing power units in real-time, whilst presenting performance comparable to the industry standard.

Colella presents a similar idea in Colella (2021) [81], however the form factor of the system is large (13.3 x 6.8 cm^2), rigid (owing to the FR-4 substrate), whilst not providing as much data-rate (25 samples per second) as cited in Horne (2020) [80].

Within this aspect of research, utilisation of the RFID-tag antenna has found as much interest as the sensor itself, as well as a communication link. Occhiuzzi presents a passive respiratory monitoring technology using epidermal sensors in the form of shaped dipoles and loop structured around the nasal cavity [82].

FIGURE 2.16: Experimental setup for epidermal tags characterization and breath detection by the help of some volunteers [82].

Employing an RFID IC with an embedded temperature sensor, the rationale being that the idea relies on the temperature gradient that is established between the inhaled ambient air and the exhaled air warmed-up by the respiratory system. The detected change in temperature data is then conveyed over the communication link. Multiple topologies were tested, with all layouts offering read distances greater than 0.8 m in a fully passive mode [83]. The study suggests that instead of the

embedded temperature sensor, a graphene-oxide (GO) electrode is proposed for measuring the moisture emitted during inhalation and exhalation.

Chipless RFID sensor networks are explored in Behera (2022) [84], who explores wearable sensors designed and fabricated using fabrics and flexible substrates which can be more suitable for wearable and WBAN applications. Chipless RFID sensors are also explored in Fathi (2020) [85], though Fathi considers them for the application of food packaging, as it provides a good explanation of the chipless limitations in involving inaccurate readings, short reading range, reduced data capacity, and lack of multi-parameter sensing capabilities. Comprehensive studies are required to investigate EM response of tags if they become conformal, in addition printing issues and reproducibility also need to be addressed in fabrication.

2.5 5G Systems

5G wireless communication is currently being adopted for the high data rates (typically of Gbps order), lower latency, and staunch commitment to increasing base station capacity, resulting in an improvement in quality of service (QoS) for network users. This, in combination with prolific smart phones, watches and tablets adoption, is providing ample opportunity for application of the network down to the personal level [86]. Beyond increasing capacity, operating in such a ubiquitous network of devices has allowed for further communication frameworks, such as 'Device to Device' (D2D), 'Internet of Things' (IoT), and 'Machine to Machine' (M2M) to reduce latency and increase connectivity. Whereby, through the utilisation of nearby communicating devices, users have increased ease of access through short-range communications for maintenance of the proximity-based services and improve the performance of networks [87].
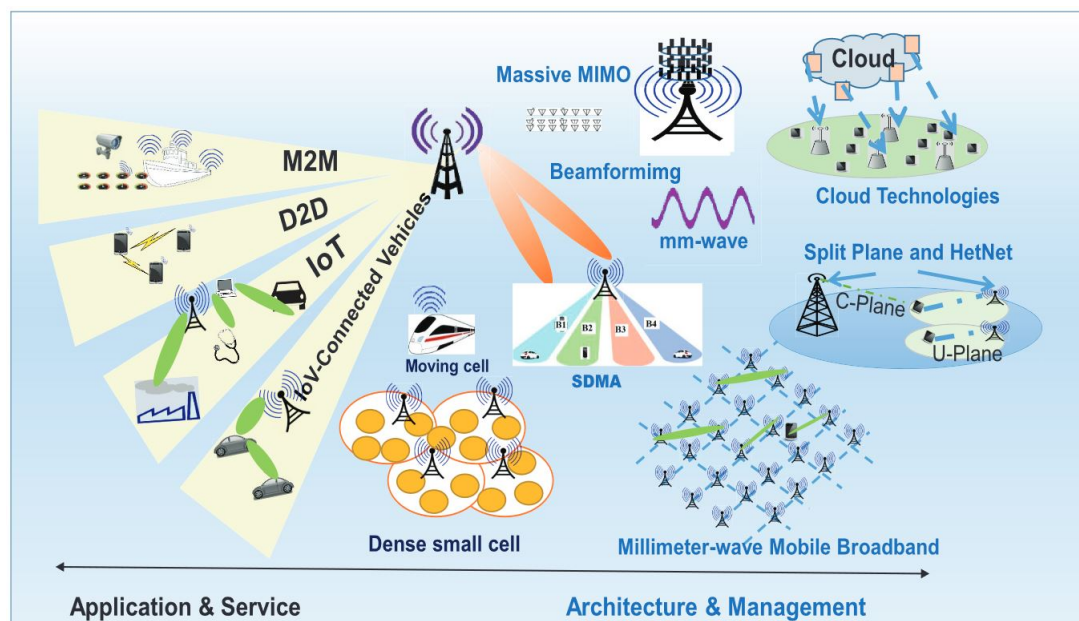

FIGURE 2.17: Schematic Diagram of Next Generation 5G Wireless Networks [86].

Considering the role 5G will play in health-care, interest is already being perpetuated in continuous tracking of our health provided by the wealth of popular mobile devices with sensors, such as the Apple Watch, Garmin Smart Watch, and FitBit [88–90]. Taking these technologies a step closer to acceptance within the medical

field would be advantageous for 'Early Warning Scores' (EWS), a physiological track-and-trigger systems which uses a multi-parameter or aggregate weighted scoring system that assist in detecting physiological changes, and thereby identify patients at risk for further deterioration [91]. However, the standard which the medical field requires for professional application [92] is not currently met by the aforementioned popular devices [93]. That said, the development described by Horne (2020) [80] far surpasses this requirement, even at UHF, suggesting that 5G communications are viable, given further development.

Taking these ideas and looking to the future for global 5G healthcare systems, Amato (2019) [94] discusses the role 5G will play in RFID epidermal systems. The study looks at the effects of the human skin on the link budget, through numerical simulation of dipoles at microwave and mmWave frequencies on the body. In the same vein, Soldani (2019) [95] presents two examples of use cases for healthcare: healthcare: 1. Using robotic platforms enabled by ultra reliable low latency communications in wireless tele surgery, and, 2. Wireless service robots for tele health and tele care services which require the deployment of 5G wireless.

Chapter 3

An On-Body UHF RFID Tag with DDRR Antenna for Healthcare Data Streaming Applications

This chapter describes the development of a Direct Driven Resonant Radiator (DDRR) antenna for an ultra-low power UHF RFID tag system, integrating an accelerometer for movement tracking.

3.1 Introduction

In recent years, Radio-frequency identification (RFID) tags have helped make opportunities such as wireless-health monitoring obtainable in a cost-effective manner [96]. In doing so, they have propelled interest in on-body sensor networks for medical, military, and leisure applications [97]. While various mobile and wearable platforms have been developed, obtaining reliable low power data from devices placed directly on the skin remains an open challenge owing to the significant losses the body introduces. One such major factor in this research is the necessity to improve read range from an antenna on-skin. When considering on-body antenna design, a balance must be made between the desired structural performance and the radiation performance. Epidermal Electronics [34], originally proposed moving external electronics and sensors from items such as clothing, directly to the skin and set a standard to offer seamless communication from a completely unobtrusive and comfortable device. However, the RF capabilities of such devices suffer poor read range performance, since the losses are so prevalent for an antenna without shielding from the body. Outside of epidermal electronics, more traditional designs for on-body antennas overcome losses by introducing separation between the body and the antenna, low-loss rigid materials, or ground plane EBG structures [98]. Hence, the current state of the field suggests on-body antennas looking to achieve longer read distances, must compromise on structural characteristics for performance. Typically, for RFID communication at UHF and higher bands, the antennas employed include loops, slots, and other horizontally polarized antennas [48–50, 63, 65, 66]. The designers of these antennas have opted for these antenna types for on-body communication due to their simple and low-profile structure. However, since these antennas run adjacent to the skin, at close proximity to the body these antennas suffer from an overwhelming and uniform loss, imparted by influence of the body tissues resulting in low efficiency. Demonstrating this, Chowdhury explores the effects the human body has on the performance of a wire antenna as the proximity between them is reduced in [99]. What is shown is that in the separation region of $\lambda < 0.5$, between the body and antenna, a steep gain

improvement is made with any increase in separation. Acknowledging this, it would be pertinent to consider antennas that are perpendicular to the body, such to reduce the effects the proximity inflicts on the performance of the antenna, as the radiating element will stretch away from the body.

In this chapter, the antenna considered is a variation of a top-loaded monopole, the DDRR antenna [100]. The DDRR is vertically polarized with a miniaturised vertical radiating element connected directly to a matching transmission line element. For on-body, the DDRR is more appealing than alternatives such as typical top loaded antennas and PIFA antennas, owing to the simple feed network, critical for tuning to the high permittivity on-body antenna application. The DDRR was originally designed for HF, finding applications on maritime vessels as well with amateur radio enthusiasts. Here, we employ it at UHF for its low-profile vertical radiating element, to run perpendicular to the body and reduce the induced losses. As well as the novel application of the antenna design to on-body, this paper will also demonstrate a new RFID communication package incorporating a framework capable of sending data over 1 kB/s, suitable for applications requiring fast and real-time updates, in this case using accelerometer data [80].

3.2 Human Body Simulation at UHF

First, the body tissues need to be numerically defined for the FDTD simulation tool, CST studio suite. For the following simulations in this section a 250×250 mm^2 3-layers body phantom is devised with the parameters as shown in Table 4.1. The electrical properties of the tissues have been sourced from the 'IT'IS Foundation' tissue property database [41].

TABLE 3.1: Permittivity and conductivity values for numerical body models at the 866 MHz UHF ISM band [41].

Layers		866 (MHz)
Skin (1mm)	ε_r	41.6
	σ (S/m)	0.85
Fat (3mm)	ε_r	11.3
	σ (S/m)	0.11
Muscle (31mm)	ε_r	55.1
	σ (S/m)	0.93

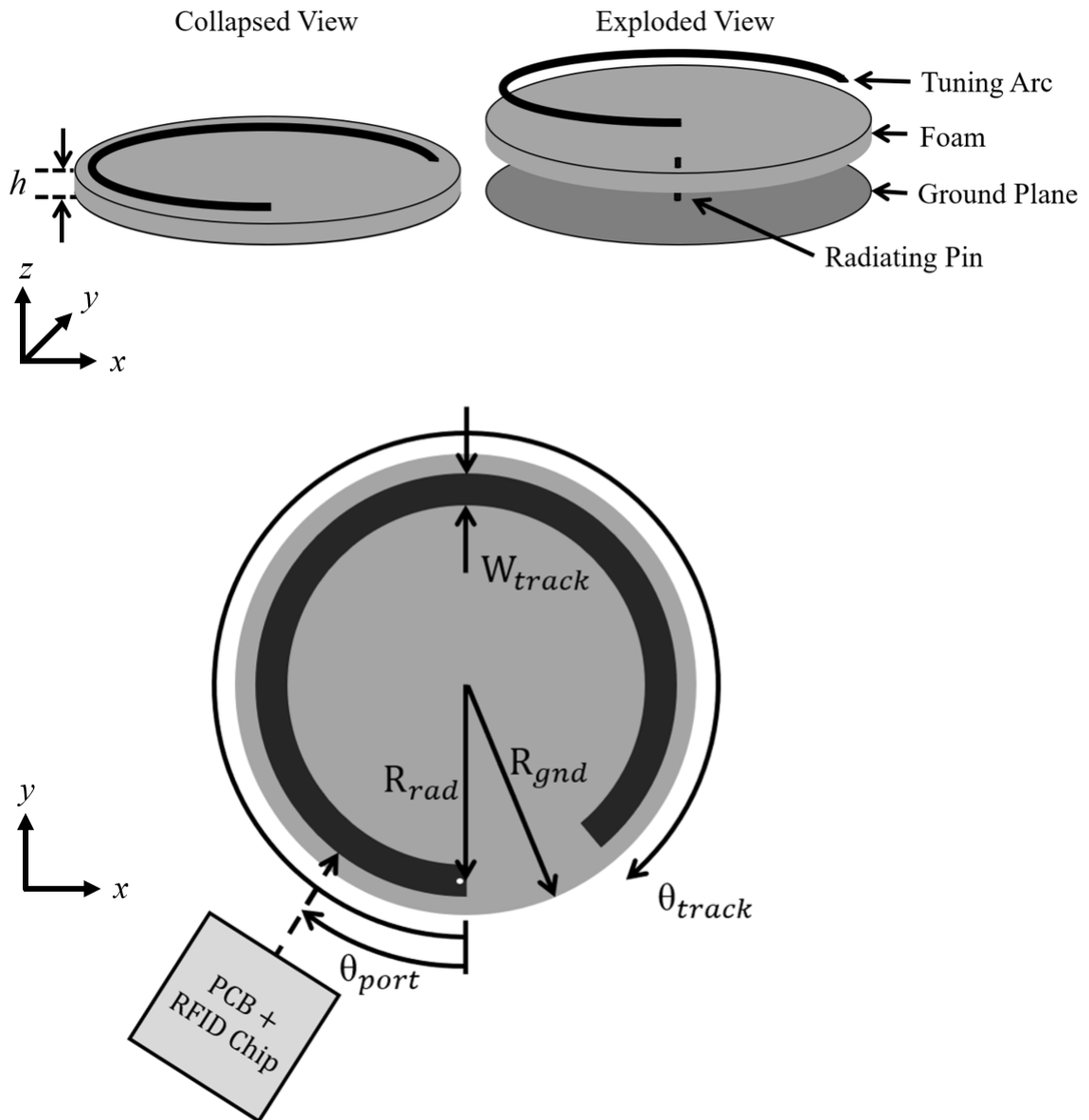## 3.3   Antenna design and parametric analysis

FIGURE 3.1: DDRR Structure: Top transmission line tuning element, EPDM
foam layer, ground plane, and a radiating element threading through the foam
connecting the top element to the ground plane.

Fig. 3.1 shows the DDRR structure made up of a ground plane, substrate separator, radiating pin, and transmission line tuning stub of length θ_{port}. The substrate is a low permittivity foam mounted on a circular ground plane. The height is determined by the foam thickness, thus determining the length of the radiating pin. The arc transmission line and radiating pin (h) combined length is a quarter-wave length, where the arc circumvents the foam perimeter, acting as a the tuning

element ($\frac{\lambda}{4} - h$ mm). The radius of the antenna would hence be derived by the location of the vertical radiating element, relative to the centre of the ground plane. There is no significant radiation from the arc transmission line which is parallel and close to the ground plane, meaning the primary radiation element is the vertical feed pin. The resulting structure is low profile, vertically linearly polarised, and orthogonal to the lossy body.

The RFID chip is the EM4325, chosen for its ability to send custom data at a high data rate over an RFID communication link. It was run in battery assisted mode with an input impedance of 7.4 - j122 Ω, in the microwave simulation environment CST Studio and represented by a discrete port of 7.4 Ω in series with a capacitor of 1.52 pF. All simulations took place on a human body phantom described in Table 3.1.

To obtain a conjugate match between the DDRR and the chosen RFID IC, the controlling parameters are: the arc length (θ_{track}) and width (W_{track}), radiator pin radius (R_{rad}), ground radius (R_{gnd}), and stub length (θ_{port}). Simulation showed that as the surface area of the capacitive matching element (described by W_{track} and θ_{track}) increased, so did the efficiency. However, since these parameters are factors in determining the antenna match, the resultant efficiency is limited by the ability to tune to 866 MHz. Fig. 3.2 shows that as W_{track} increases from 6 mm, to 8 mm, to 10 mm the ability to match to the RFID chip is lost, as the θ_{track} cannot extend further without overlapping with the start of the loop. Whilst Fig. 3.2 shows a suitable match for $W_{track} = 10$ mm, it was determined $W_{track} = 8$ mm would be more appropriate as this allows for unaccounted for losses arising in fabrication. Therefore, the matched structure had the following dimensions, shown in Table 3.2. Resulting in an antenna efficiency and gain of η = -9.5 dBi and G = -7.5 dBi. The radiation pattern is shown in Fig. 3.3.

TABLE 3.2: Final Simulated DDRR Parameters (lengths in mm).

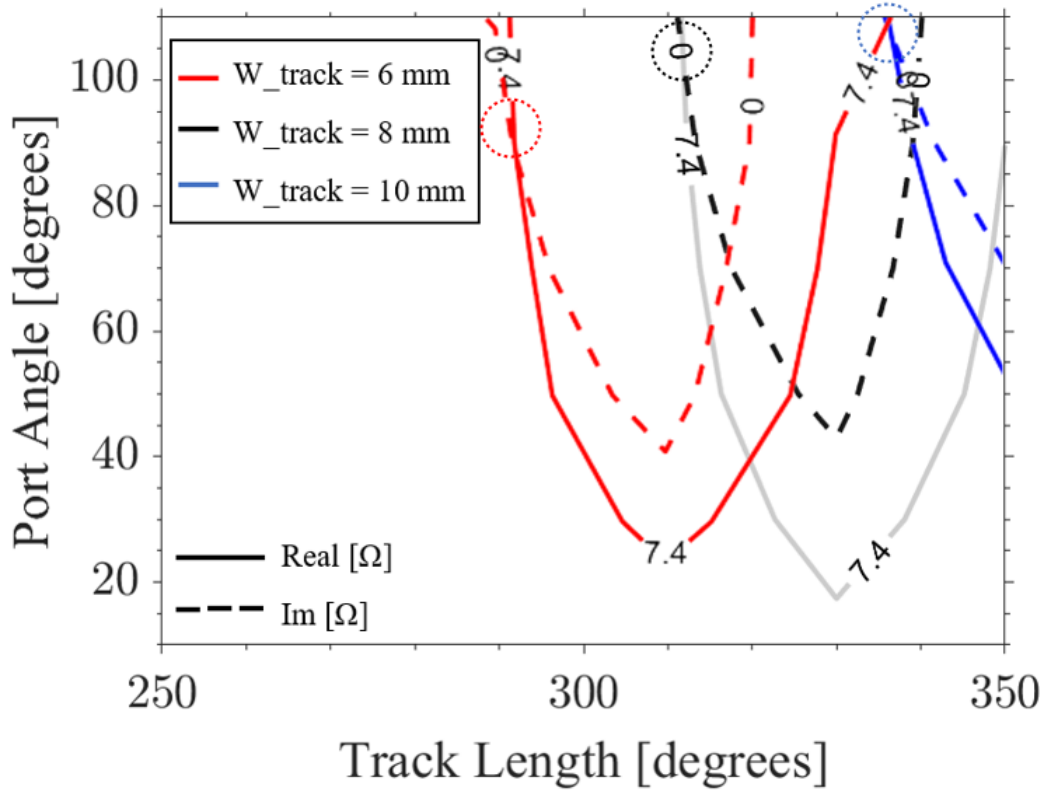| h	W_{track}	R_{rad}	R_{gnd}	θ_{port}	θ_{track}
1	8	14	20	70°	321°

FIGURE 3.2: Contour map describing the conjugate match possibilities (highlighted by dotted circles) of the DDRR antenna to the RFID IC through parameters θ_{port} and θ_{track}, at W_{track} = 6 mm, 8 mm, and 10 mm.

Resulting in an antenna efficiency and gain of η = -9.5 dBi and G = -7.5 dBi. Further adjustments post-fabrication could be applied to the port angle and arc length, for fine-tune control over the input impedance. The efficiency is proportional to the size of the capacitive tuning element. By keeping the vertical radiating element central to the transmission line tuning element, the vertical element could in theory be moved inwards to maximise the transmission line width for improvement in efficiency. However, this change also results in the reduction of the capability to match the antenna to the chip impedance. Moving the vertical radiating element away from the centre only appears detrimental to the radiation performance. Therefore, the structural parameters described above offer the optimal balance between antenna performance with the matching capabilities.
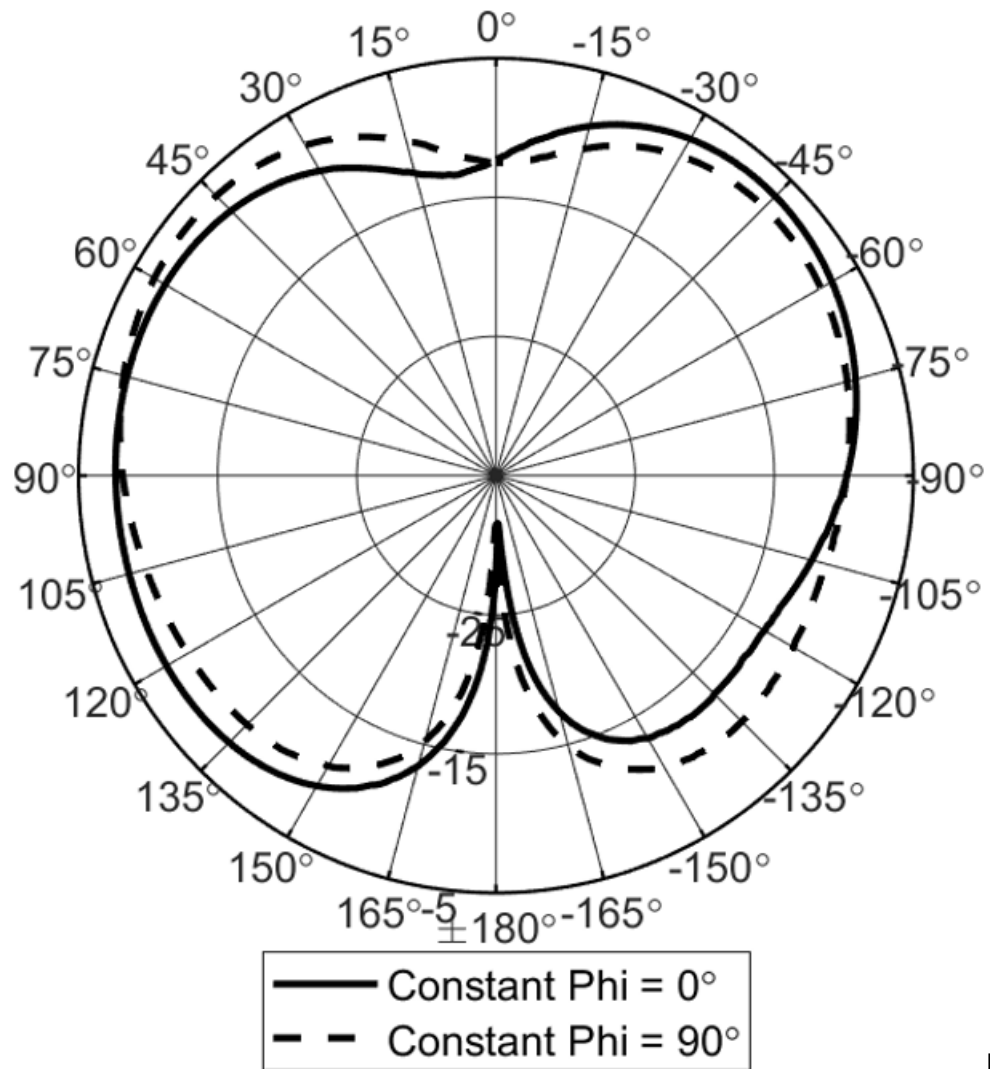
FIGURE 3.3: DDRR simulated radiation pattern on the horizontal (Phi = 0°) and vertical plane (Phi = 90°).

3.3.1 Height Analysis

Having defined the antenna topology, the height can be adjusted to analyse the possible vertical miniaturisation and the relative radiation performance. The height of the antenna is equal to the foam substrate thickness and determines the length of the radiating pin.
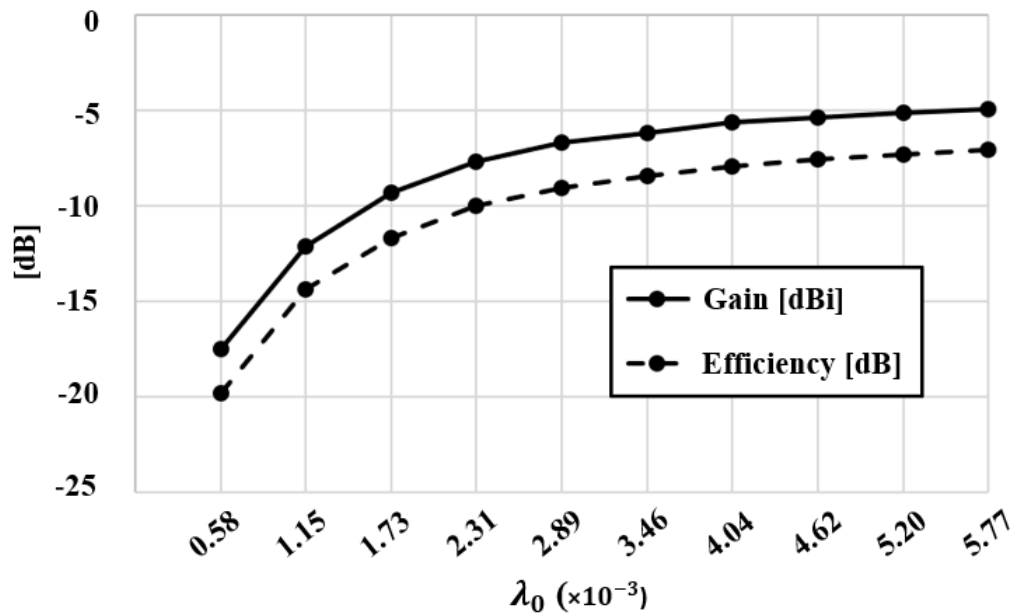

FIGURE 3.4: Simulated DDRR antenna height versus and radiation performance described by gain (solid line) and radiation efficiency (dashed line).

Fig. 3.4, shows how the gain and radiation efficiency change with respect to the DDRR height. Thinner thicknesses show very poor performance capabilities, improving with increased separation until a lower gradient appears from, $h = 1$ mm. Since the ideal antenna for on-body applications would be as low-profile as possible, a verdict must be made on what level of performance is acceptable for the application. Balancing antenna thickness with performance, hence, $h = 1$ mm was deemed an acceptable length reducing the gain by 3 dBi from the maximum.

3.3.2 Bending Analysis

The antenna matching simulations were carried out on a flat human-body model. In real applications, the antenna must be flexible to conform with the body. In this section, we assess the ability of the DDRR to bend around a curve, representative of human limbs, whilst maintaining acceptable radiation performance.
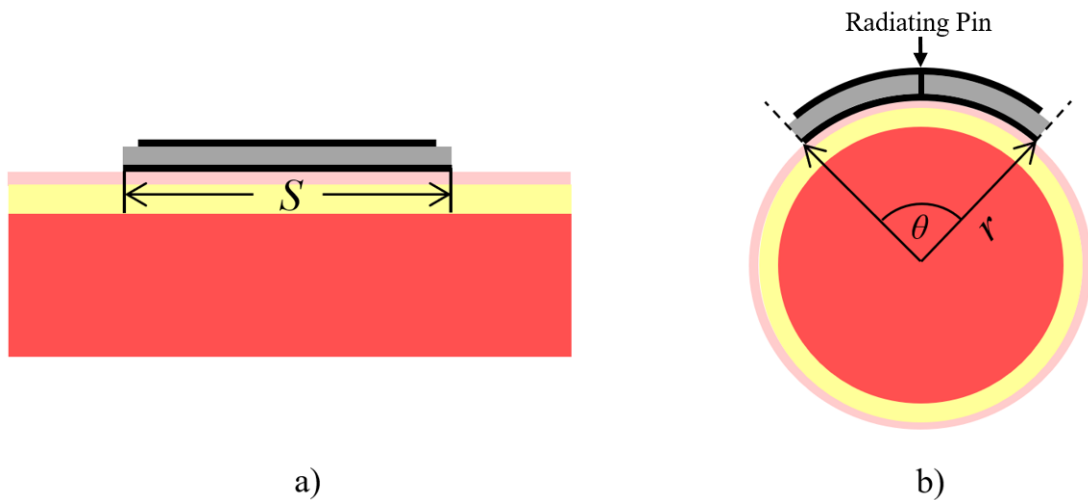

FIGURE 3.5: DDRR antenna simulated structures and 3-layer body model made of skin (pink), fat (yellow), and muscle (red). a) DDRR antenna planar with a flat body model b) DDRR antenna curved around a cylindrical body model.

The major affect of bending on the antenna is the detuning of the resonant frequency. Since the DDRR is a narrow-band antenna, this affect could be significant to the performance within the ISM UHF band. The antenna bending has been characterized by the bending angle described in (3.1). The arc angle theta is defined by bending the DDRR over a cylinder with a radius of 'r', relative to 'S' representing the diameter of the ground plane.

$$S = \theta \cdot r \tag{3.1}$$

The acceptable performance limit of the antenna under bending is defined by a realized gain reduction of 3 dB with respect to the flat antenna. The flat version saw a realised gain performance of -7.6 dBi, thus, a self-applied realized gain limit of -10.6 dBi is set.
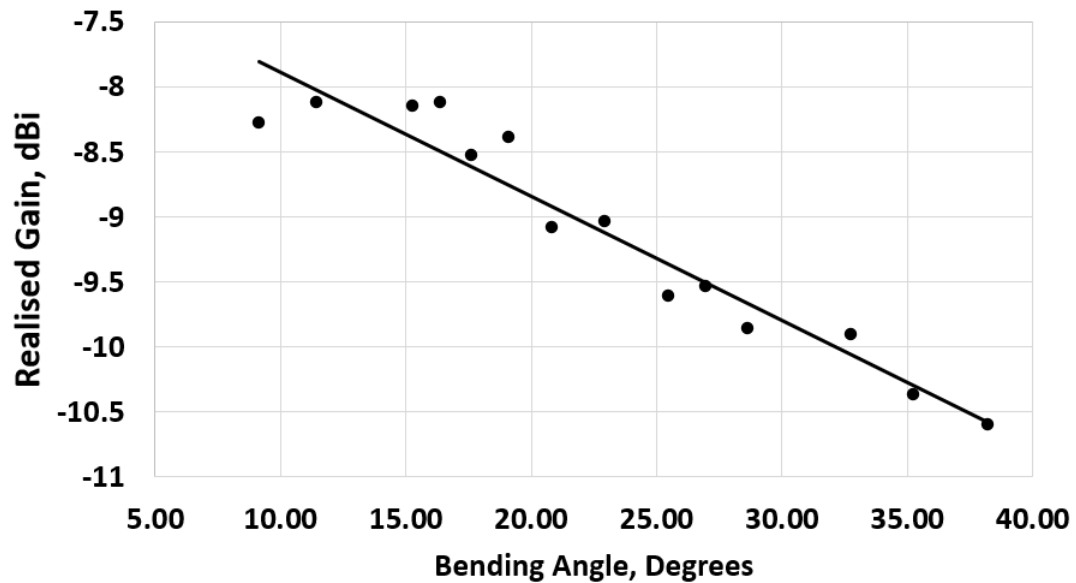
FIGURE 3.6: Simulated DDRR antenna realized gain performance over simu-
lated bending angles until reduced below the lower limit of -10.6 dBi.

Through CST simulation, the realised gain is seen to decline steadily as bending angle increases (Fig. 3.6). Using a linear regression line, it can be seen the -10.6 dBi limit is surpassed after 38-degrees of curvature. As expected, the tolerance for curvature is small owing to the narrow bandwidth. However, the body features many acceptable areas that are within the range of this 38-degree 'maximum bend' threshold, such as the side of the arm, back of the hand, thighs, back, torso, and forehead. The bending causes a respective S_{11} detuning of about 4 MHz and causes the on-frequency (866 MHz) reflection coefficient value to be about -5 dB (Fig. 3.7).
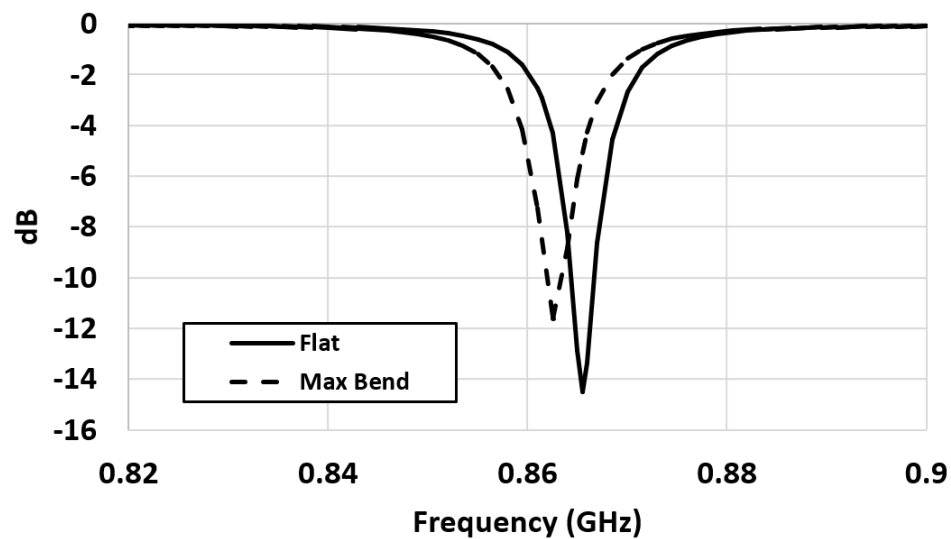
FIGURE 3.7: S11 characteristics, solid line describing the DDRR antenna on the flat body-model, dashed line describing the detuning effect of the maximum allowed bending.

The performance and system factors simulated and adopted for this paper are compared with other on-body designs from the literature in Table 3.3. To fairly compare this diverse range of antenna topologies are considered charecteristics include substrate, surface area, thickness, radiation properties and RFID chip choice. Some authors have taken advantage of material dielectrics to reduce the operational wavelength, utilizing materials such as FR-4 or Rogers substrates to allow for a reduction in the size of the antenna at the cost of being rigid materials. Other authors have attempted to maximise radiation performance whilst limiting themselves to the 'epidermal' definition, choosing groundless topologies with ultra-thin substrates, such as polyurethane. Relatively speaking, the thicker and more obtrusive the substrate is, the greater the performance gain, and the lower the profile and more body conformal the antenna is, the worse the radiation performance. The DDRR parameters are selected between the extremes and in comparison to the antennas in Table 3.3, the design does not obtain the smallest area or thinnest thickness, such of that of [50] or [65], but the radiation performance achieved relative to the size, with being on a flexible material, does provide improvements in gain and efficiency over alternatives such as [67], and the EPDM versions of [65].

TABLE 3.3: SIMULATED RADIATION PERFORMANCE OF ON-BODY UHF RFID ANTENNAS IN LITERATURE.

	Antenna Topology	Substrate	Flexible (Y/N)	Area (mm^2)	Thickness (λ)	η (dBi)	Gain (dBi)	RFID Chip
[67]	CP Patch	EPDM	N	50x50	0.014λ	-13.8	-7.1	NXP G2iL
[64]	Slotted Patch	Rogers RT/Duroid 6010LM	N	90x42	0.0116λ	-7	-	Various
[50]	Wire	Polyurethane	Y	30x30	0.00003λ	-	-13	Magnus S3
[49]	Loop (Battery Assisted)	Kapton	Y	30x30	0.00014λ	-	-16.5	AMS-SL900A
[48]	Nested-Slotline	Tattoo	Y	65x20	0λ	-20.7	-16.5	NXP G2X
[65]	Loop	EPDM	Y	23x23*	0.0056λ	-10	-8.7	Alien Higgs 3
[65]	"	"	"	22x22*	0.0028λ	-11	-9.7	"
[65]	"	Paper	"	21x21*	0.00028λ	-16	-14	"
[63]	Slotted Patch	FR-4	N	120x30	0.00434λ	-4.3	-	NXP G2XL
[66]	Nested-Slotline	Mylar	Y	105x20	0.00017λ	-	-16	EM4325
This work	DDRR	Foam	Y	40x40*	0.0028λ	-9	-7.5	EM4325

3.4 Tag Prototyping

3.4.1 DDRR Antenna Prototype

The DDRR was prototyped using a 'Cricut' die cutter. Using adhesive copper tape, the two sides of the DDRR antenna were cut to size, producing the tuning circuit and ground plane. For the substrate, foam (ROHACELL® HF) was utilised for the soft and flexible structural properties with a dielectric closely resembling air [101]. Once the copper layers were adhered to the foam, a 0.2 mm diameter wire is slotted through a pin hole, soldered, then trimmed to size for the radiating element. The resultant structure is shown in Fig. 3.8.
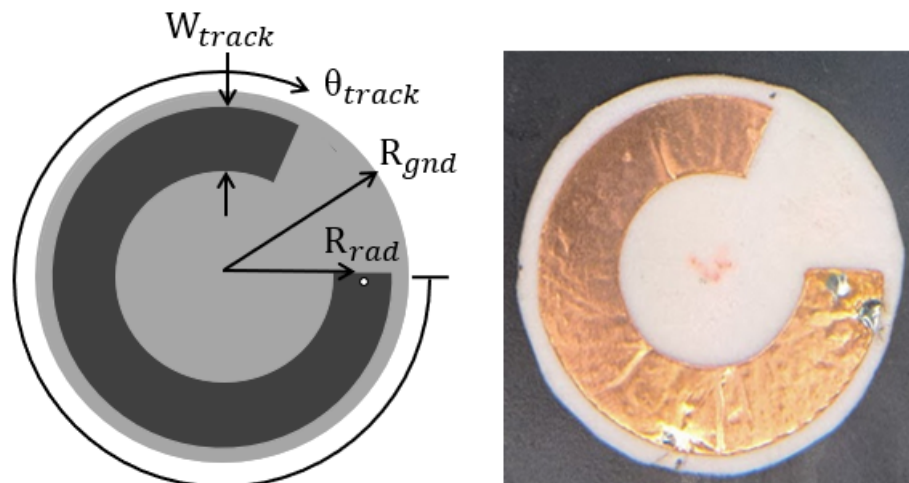

FIGURE 3.8: DDRR antenna line drawing and prototype, dimensions given in Table 3.2.
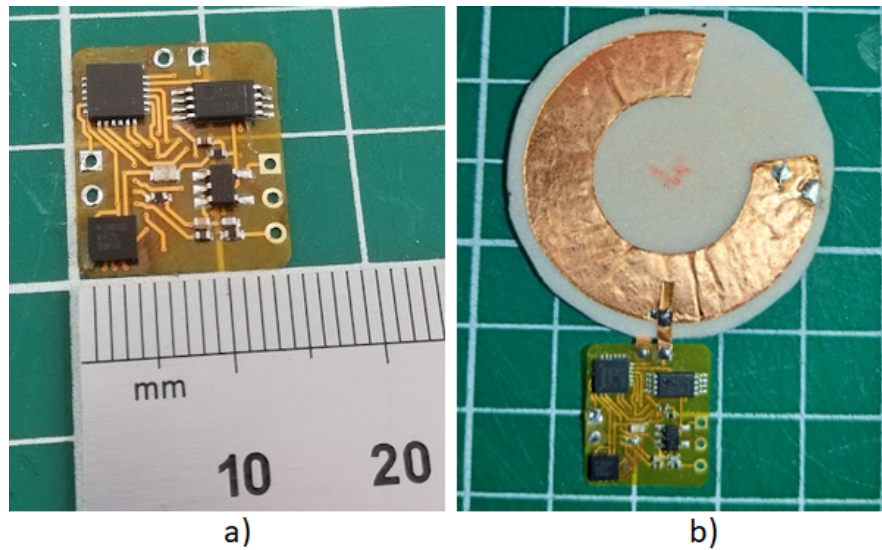
3.4.2 Kapton PCB

FIGURE 3.9: Kapton PCB a) size b) connection to DDRR antenna via short copper tracks at θ_{port}, given in Table 3.2.

The Kapton PCB designed for this system (Fig. 3.9 and 3.10) is an application specific flexible board for the power and size constrained domain of sending data to a host PC via UHF RFID. One of the main requirements of the board is ultra-low power operation for battery longevity. To achieve this, the MSP430FR2433 microcontroller unit (MCU) from Texas Instruments is employed together with the EM4325 RFID transponder and the low power ADXL363 accelerometer from Analog Devices. The latter provides relative orientation to 'x, y, z' axes. In addition to the accelerometer data, the MCU has been coded to increment an integer with each RFID IC interruption by the RFID reader (between 0 and to 255 before resetting). Thus, when a data packet fails to send, the integer value increments to indicate data has been lost. In operation, the EM4325's auxiliary pin is used by the MCU as an interrupt to schedule loading the data into the EM4325's RAM register, allowing for high speed read out communication with minimal corruption. The complete system interconnections from the components on the PCB communicating through the antenna are shown in Fig. 3.11.

Voltage Regulator

Accelerometer

Battery Terminals

RFID Chip

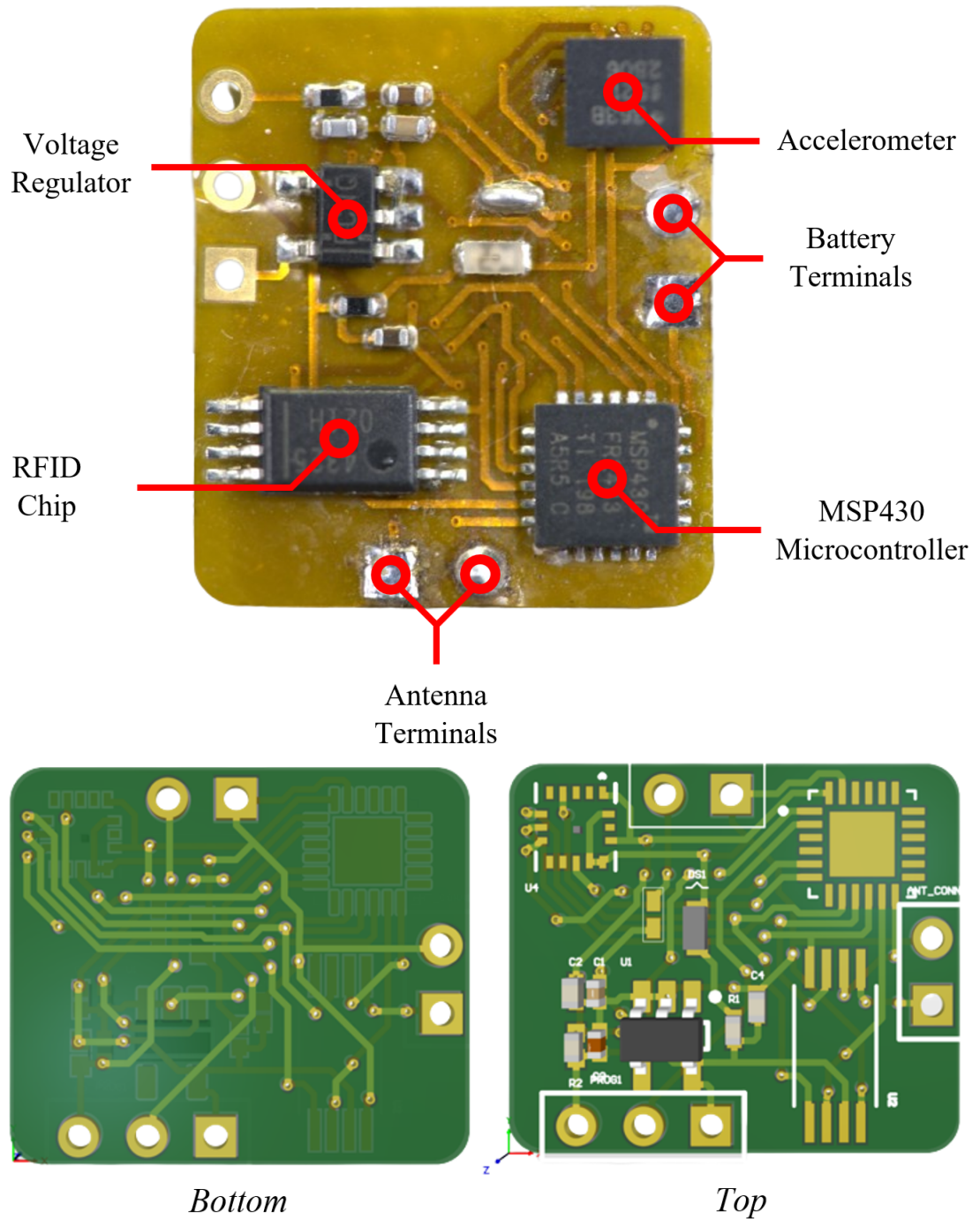MSP430 Microcontroller

Antenna Terminals

Bottom

Top

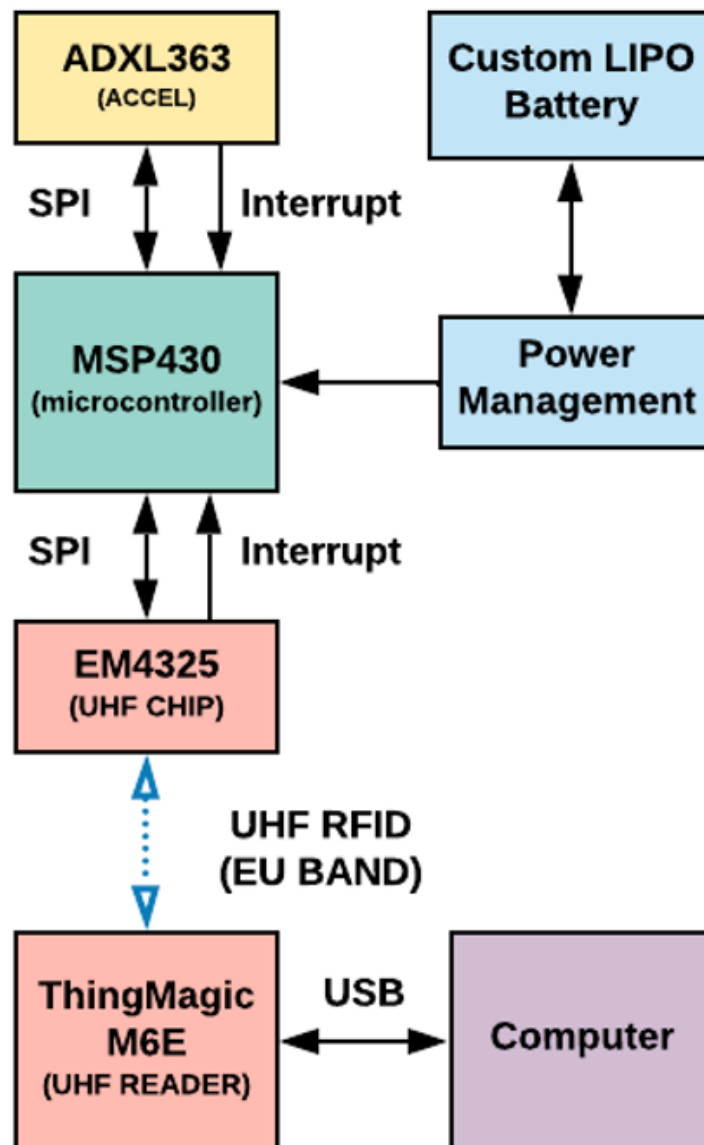FIGURE 3.10: Kaptop PCB layout.

FIGURE 3.11: System component interconnection and communication flowchart.

3.4.3 Tag Construction

Using the simulation dimensions as a guide, short copper foil tracks were soldered between the kapton PCB and antenna linking the tuning track and ground plane to define the angle, θ_{port} (Fig. 3.9 b). Adjusting θ_{port} in combination with trimming the length θ_{track} with a scalpel, the antenna could be tuned for optimum performance at 866 MHz. To determine the frequency response and gauge performance between adjustments, a Voyantic Tagformance Pro was utilised using the read range measurement setting. The DDRR tag was attached to the upper right arm with microporous surgical tape, Fig. 3.12 shows the arm mounted tag on double-sided adhesive tape to more clearly display structure, the surgical tape is more straightforward to remove from the skin. Once mounted, the tag was positioned at a calibrated distance of 30 cm from the Voyantic reader antenna, so the frequency response could be measured, as shown in Fig. 3.13. Alternative reader positions directly above and below the arm were also tested, however the most prominent beam was clearly pointing broadside to the tag antenna. After some trial and error tuning of the matching element, through incremental adjustment of the parameters θ_{port} and θ_{track}, the final tuned prototype DDRR parameters are shown in Table 3.4.

TABLE 3.4: Final Prototype DDRR Parameters (lengths in mm).

h	W_{track}	R_{rad}	R_{gnd}	θ_{port}	θ_{track}
1	8	14	20	85°	210°

As can be seen in Fig. 3.14, the operating frequency is centred on 866 MHz. The Voyantic response shows considerably greater theoretical read range than expected for on-body UHF. A complete link budget is the combination of the forward and reverse communication links, in this case, the reverse link is the bottleneck of the system, as seen in Fig. 3.15, thus the forward link is used only for frequency tuning and the resultant read range will be recorded through practical measurements.

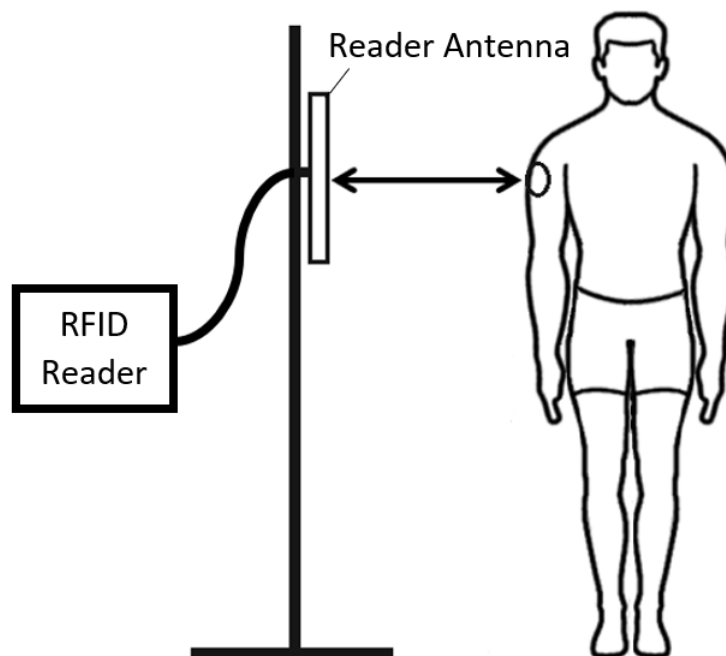FIGURE 3.12: DDRR tag placement on the upper right arm attached via double sided tape.

FIGURE 3.13: DDRR tag performance measurement with RFID reader setup.
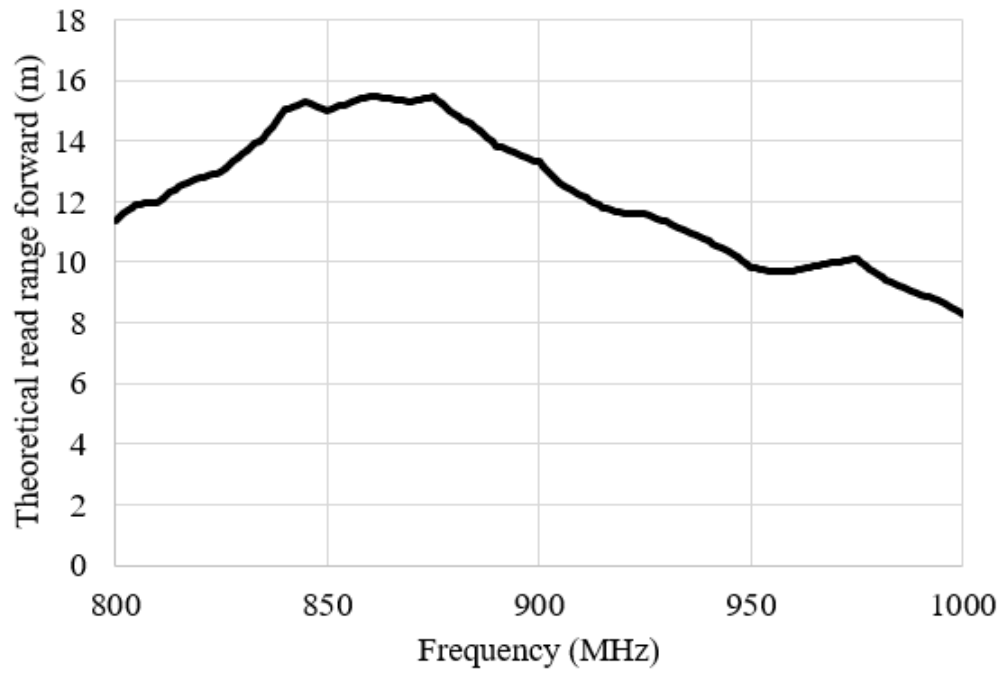
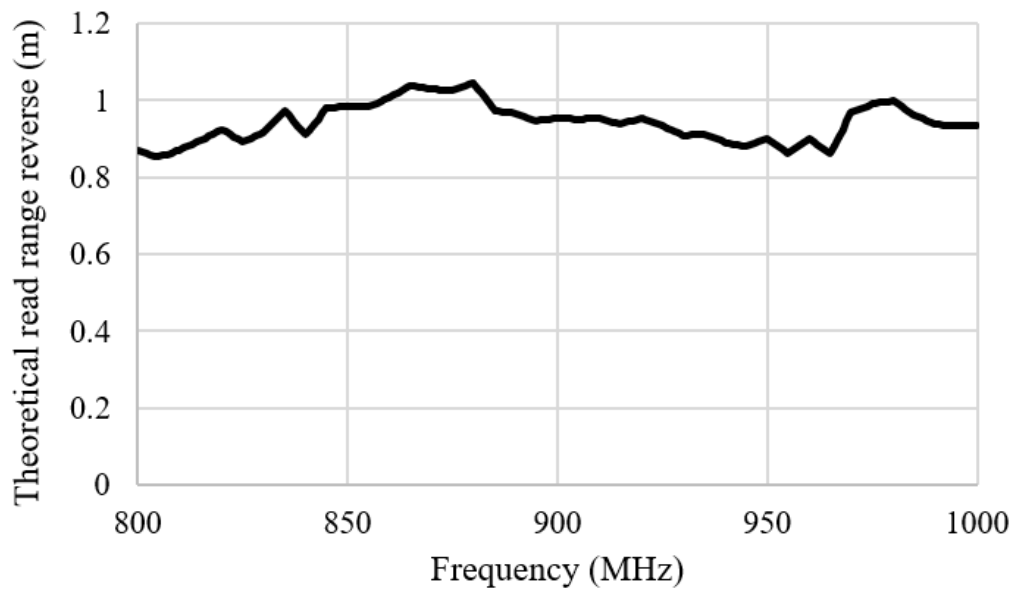FIGURE 3.14: Voyantic Tagformance theoretical forward read range measurement.

FIGURE 3.15: Voyantic Tagformance theoretical reverse read range measurement.

3.5 Tag Performance Measurements

The radiation pattern cannot be measured in a conventional manner since the antenna complex impedance would require a matching network which effects the radiation performance, therefore retuning the DDRR to 50 Ω would not be comparable to the RFID matched performance. Instead, the antenna radiation performance and radiation pattern are assessed practically, through the quality of the communication link relative to body position. The attachment of the tag to the body plays a role in how the orientation of the radiation beam will be received by the circularly polarized reader antenna. For ease of use, the orientation of the tag was kept such that the kapton PCB and battery were always aligned along the arm as shown in Fig. 3.12. Measurements were performed using the 'ThingMagic M6e' RFID reader, chosen for the fast read rate, intuitive software development kit (SDK), and availability.

For initial measurements, the worn DDRR tag was moved away from the reader antenna in 5 cm increments, maintaining a 'static' body position as described by Fig. 3.13, until the maximum read distance was found, and the results are presented in Fig. 3.16. In this application, 32 bits of data are being passed over the communication link, 24 bits for the accelerometer data (8 bits per axis) and 8 bits for the counter. As such, when communicating at full speed, over 250 reads per second, the data rate is 8 kbps (250 reads $\cdot$ 32 bits), equating to 1 kBps.

Data dropouts are observed between 2.1 m and 3 m, are likely caused by channel effects including constructive and destructive interference in a complex echoic environment. Although reads are obtainable at 180, 300, 350, and 380 cm, in practice the maximum read range is 120 cm. Further investigation using antenna diversity at the reader could help extend the read range. The speed of the tag data appears proportional with the read distance, suffering a 30 reads per second decrease between the closest and furthest functional read ranges. However, the grey area representing the minimum acceptable sample rate for medical application (60 Hz), shows the speed is well within acceptance, up to the 2.1 m drop out [79]. The gradient of the unfolded dashed line describes the data rate decreasing

at a rate of ∼0.09 reads per second/cm, or ∼1 read/s is lost every 10 cm, when not in a null.

Using the information obtained in the 'static' measurements, the performance of the tag was then considered as the wearer moved, at distances where performance was achieved, namely 50 cm, 100 cm, 200 cm, and 350 cm.

The movements undertaken were designed to best describe the limitations of the antenna with respect to a single reader antenna and be representative of possible therapeutic exercises the tag could be adopted for, described by Fig. 3.17. For all movements, measurements were taken as before, with respect to the reader antenna, broadside to the tag. In movement cases where a reasonable level of performance was achieved and measurements were taken with the person facing the antenna, as shown in Fig. 3.18.
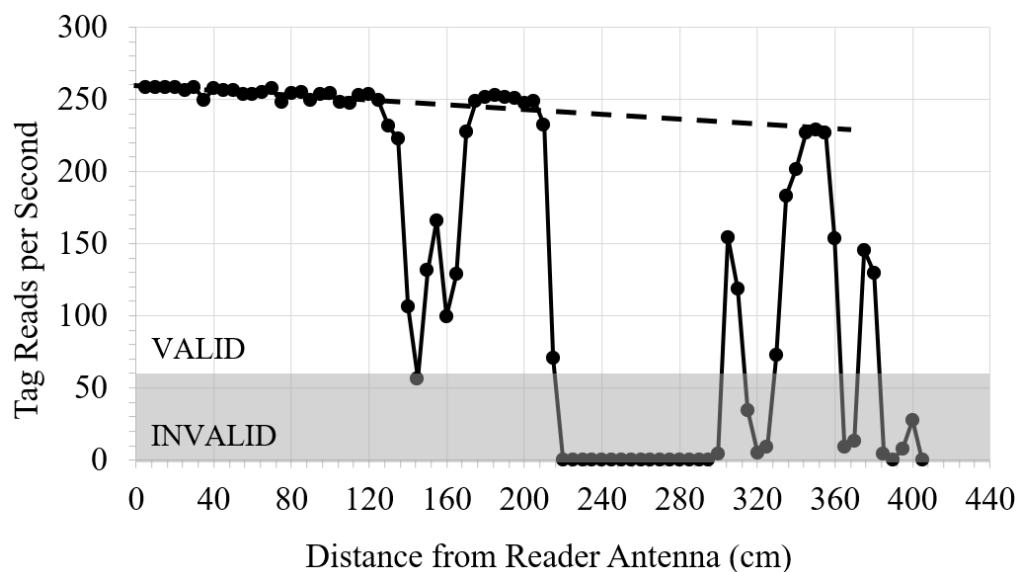

FIGURE 3.16: Data rate measurements taken in 5cm increments from the reader antenna, dashed line represents data fall off with distance for the unfaded signal. Grey area indicated unacceptable data rate.

The communication link performance has been tested through controlling the data output of the tag. That is, each time the tag is interrogated, the MCU will attempt to send the accelerometer data and a counter, which when received by the host PC, will be timestamped and provide the correlating 'Received Signal Strength Indicator' (RSSI) value of when the data was received, as shown in Table 3.5.

Rotation

Lateral Bending

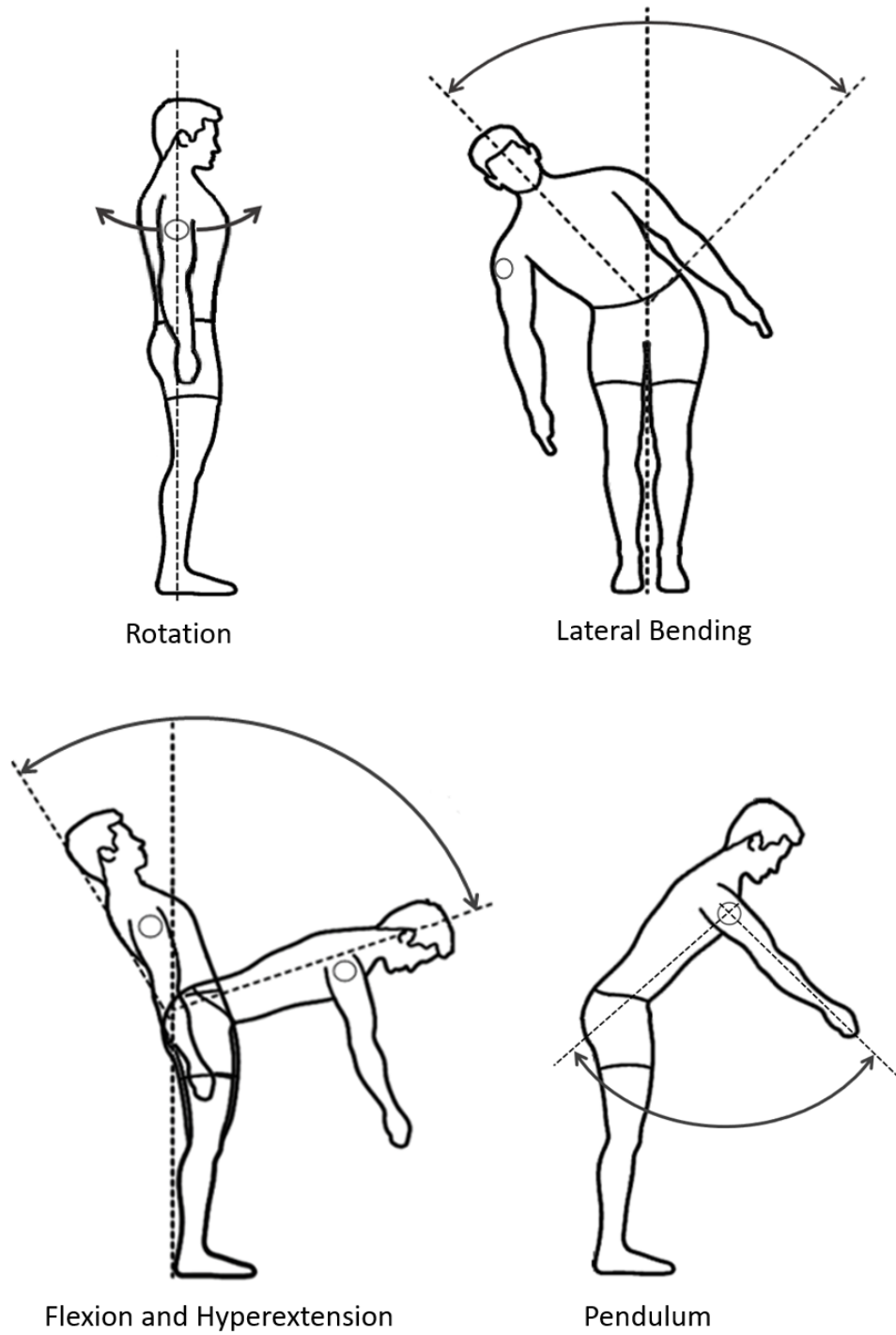Flexion and Hyperextension

Pendulum

FIGURE 3.17: Movements performed indicating the location of the DDRR antenna on the upper arm.
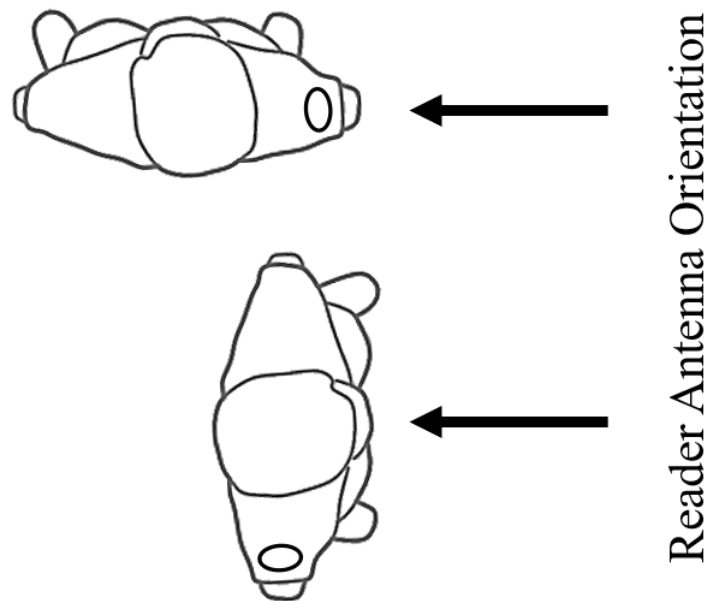
FIGURE 3.18: Relative body orientations of the measurements with the tag facing the reader antenna directly, then the body facing the reader antenna.

TABLE 3.5: Example accelerometer data from the tag.

Time	X	Y	Z	Counter	RSSI
02.36.42.829	56	243	246	136	-65
02.36.42.833	56	243	246	137	-66
02.36.42.836	56	243	246	138	-66
02.36.42.839	56	243	246	139	-65
02.36.42.845	56	243	246	140	-65
02.36.42.848	56	243	246	141	-66
02.36.42.855	56	244	246	143	-65
02.36.42.861	56	244	246	144	-65

Movements took place in a 5 s recording period, at the end of which some statistics were calculated. In the order of events taking place, the first statistic is the 'Total Tag Reads', referring to the total number of times the tag is interrogated by the reader. From which, the number of 'Reads with Data' is found, that is, the number of reads of the tag holding certifiable data, excluding empty or faulty packets. Next, each time the counter value presented did not align with the previous counter (counter $\neq$ previous counter $+ 1$) between 0-255, it is noted that packets have been dropped, thus, they were subtracted from the 'Tag Reads with Data' providing the number of 'Total Tag Reads with Data'. An example of this packet loss phenomenon can be seen in Table 3.5, whereby the counter excludes 142. Finally, the 'Data Reliability' is calculated, with the following formula: ('Total Tag Reads with Data' / 'Total Tag Reads')$\times 100\%$. The data presented is the average of three rounds of measurements of each movement, at each distance. The movement data are presented in the following: 'Lateral Bending', Table 3.6; 'Flexion and Hyperextension', Table 3.7; 'Pendulum', Table 3.8; and 'Rotation', Table 3.9. Video recording of each movement can be found in the media section of the IEEE publication [102].

TABLE 3.6: Average lateral bending data capture and reliability when the tag is facing the reader antenna, then the body facing the reader antenna.

Lateral Bending (Tag Facing Reader Antenna)					
Distance (cm)	Total Tag Reads	Reads with Data	Dropped Packets	Total Tag Reads with Data	Data Reliability
50	897	848.3	60	788.3	91.9
100	925	885.3	58.3	827	83.0
200	731.3	657	86	571	80.6
350	573	478.6	94.3	384.3	62.7
Lateral Bending (Body Facing Reader Antenna)					
50	1189.3	1150.6	68.3	1082.3	91.0
100	1185.3	1138	71.6	1066.3	89.9
200	970.6	840.3	118	722.3	74.4
350	348.3	250.6	97.6	153	43.9

TABLE 3.7: Average flexion and hyper-extension bending data capture and reliability when the tag facing the reader antenna, then the body facing the reader antenna.

Flexion to Hyperextension (Tag Facing Reader Antenna)					
Distance (cm)	Total Tag Reads	Reads with Data	Dropped Packets	Total Tag Reads with Data	Data Reliability
50	1154	1089	92	997	86.4
100	834.6	790	62.6	727.3	87.1
200	879.6	667.6	185.3	482.3	54.8
350	577.6	456	140	316	54.7
Flexion to Hyperextension (Body Facing Reader Antenna)					
50	1277	1232.6	76	1156.6	90.5
100	1090	982	107.3	874.6	80.2
200	590	463.6	110.3	353.3	59.9
350	0	0	0	0	0

TABLE 3.8: Average pendulum movement data capture and reliability with the tag facing the reader antenna.

	Pendulum				
Distance (cm)	Total Tag Reads	Reads with Data	Dropped Packets	Total Tag Reads with Data	Data Reliability
50	1189	1091.6	115	976.6	82.1
100	1188.3	1153.3	75.3	1078	90.7
200	1162.3	1079	107	972	83.6
350	918.3	783.3	155	628.3	68.4

TABLE 3.9: Average rotation movement data capture and reliability with the tag facing the reader antenna.

	Rotation				
Distance (cm)	Total Tag Reads	Reads with Data	Dropped Packets	Total Tag Reads with Data	Data Reliability
50	897	848.3	60	788.3	87.9
100	925	885.3	58.3	827	89.4
200	731.3	657	86	571	78.1
350	573	478.6	94.3	384.3	67.1

Considering the 'Total Tag Reads' of each movement, it would suggest that the biggest range of motion (RoM) can be detected at the closest distance, evident from the data rate being consistently highest. Also suggesting, that as the distance increases, the ability to transmit data consistently at high speed becomes more difficult, thus, less of the movement is communicated. However, the 'Data Reliability' percentage suggests in the measurement environment (3.8 m × 6.5 m × 2.5 m, reader antenna at tag height 1.35 m above the floor) in many cases the optimum distance for detecting maximum RoM is 1m, where fewer, but more reliable packets are received, while decaying at longer distances. Whilst it is difficult to compare the radiation pattern between the simulated pattern and the tabulated data, the measured results do indicate the main beam direction to be broadside of the antenna, however more narrow in beam width.

3.6 Data Processing

Fig. 3.19 displays the raw data seen on each axis of the accelerometer throughout the 5 second motion of the 'Pendulum', at 50 cm read distance. Each axis wraps between 0° and 360°, causing spikes to appear (Y axis: 4.2 s - 4.5 s and Z axis: 2.8 s - 3 s) where the axis value is transitioning over this threshold. Whilst the total change in each axis value is subtle, this shows the capability for accurate body movement detection, or adoption of other sensors requiring sensitivity to variation.
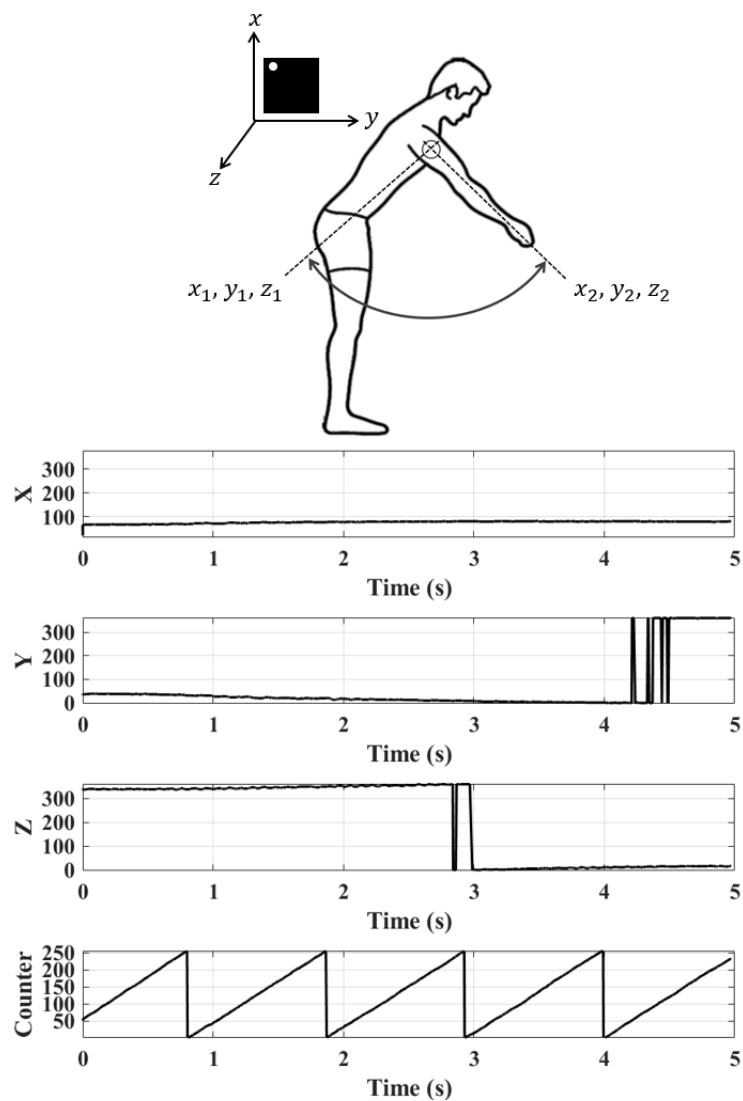
FIGURE 3.19: ADXL363 accelerometer orientation when worn on the arm and raw received accelerometer axis data (0°- 360°) and counter data (0 - 255) of the Pendulum movement at 50cm.

To quantify the range of movement that can be captured by the tag at a given read distance, the results in Tables V-VII are represented as a Range of Motion (RoM). The maximum range of each movement (averaged over 3 repetitions) between the start point $x_1, y_1, z_1 = x(t = 0), y(t = 0), z(t = 0)$ and end point $x_2, y_2, z_2 = x(t = 5 \text{ s}), y(t = 5\text{s}), z(t = 5\text{s})$ is compounded into a single value called RoM as described by (2) - (5).

$$\Delta x \equiv x_2 - x_1 \pmod{255} \tag{3.2}$$

$$\Delta y \equiv y_2 - y_1 \pmod{255} \tag{3.3}$$

$$\Delta z \equiv z_2 - z_1 \pmod{255} \tag{3.4}$$

$$RoM = \Delta x + \Delta y + \Delta z \tag{3.5}$$

The RoM value was then normalised into a percentage with respect to highest RoM value found over all distances, resulting in Fig. 3.20. 'Rotation' is excluded since this movement was a spinning motion around the torso axis maintaining the arm parallel to said axis of rotation, thus, the accelerometer axis data does not change. From the accelerometer results, it can be seen that the best range of motion data is received at either 50 cm or 100 cm, however in the movements where the motion is favourable to the antenna orientation, namely the pendulum movement as the tag is maintained well within the reader antenna beam, the performance even at the maximum ranges are reasonably reliable.

Fig. 3.19 displays each axis of the accelerometer during the motion of the 'Pendulum', at 50 cm read distance. The rotation angle is wrapped between 0 and 255 relative to a change between 0°and 360°. Whilst the change in axis data is subtle, this shows the capability for accurate body movement detection, or adoption of other sensors requiring sensitivity to variation. The full capability of the EM chip is 128 bits which is accessible without impact on the speed. The speed at which the reader antenna is interrogating the tag antenna is significantly faster than the sensor is capable of updating, therefore, the RFID platform could support higher data rate sensors.
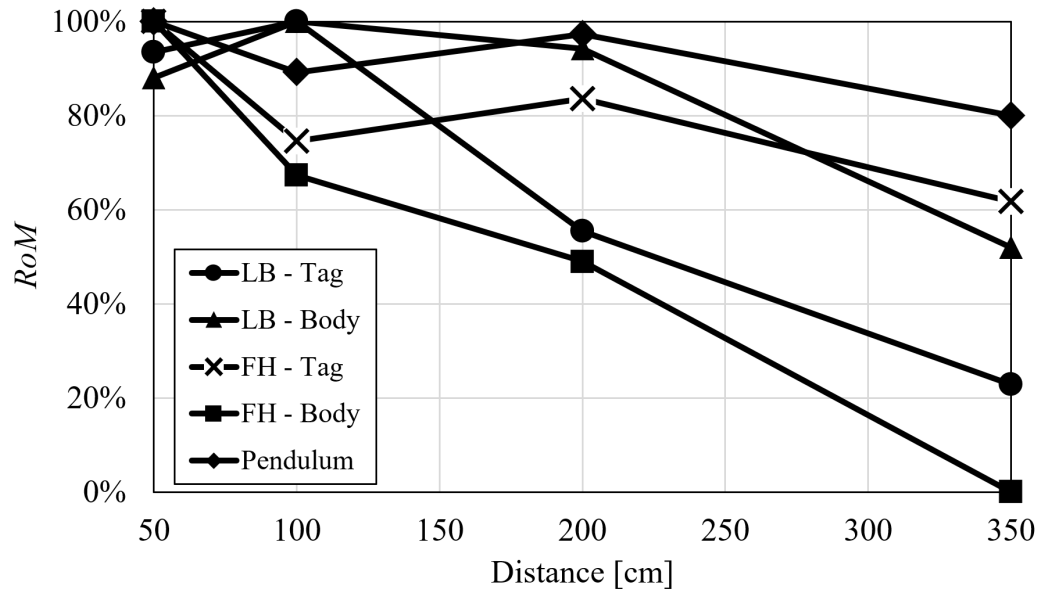
FIGURE 3.20: Relative range of motion detectable of each movement at the read distances 50cm, 100cm, 200cm, and 350cm.

3.7 Conclusion

A thin, soft, flexible UHF RFID tag vertically polarised with respect to its ground plane has been designed and fabricated for the application of on-body wireless sensing. The results presented indicate the tag is suitable for the tracking of body movements when the tag wearer is within a 1.2 m proximity of the reader antenna, with further read range achievable for data transmission under select body orientations. The speed at which the data is communicated would be suitable for real applications in the transmission of sensor data from the body, achieved with ultra-low-power operations. The antenna performance is competitive with other reputable antenna topology types, obtaining a higher efficiency and gain than those of similar size. For future development of the tag, the next suggested step is to replace the coin cell battery with a thinner, more flexible battery, to allow for a more integrated antenna, PCB, and battery tag [66]. For application, it is recommended that reader antenna diversity is adopted to account for multipath interference nulls. Whilst adding a secondary reader antenna would halve the average data rate over the communication link to a single reader, the performance capability shown in this paper is significantly above twice the minimum acceptable sample speed. Other improvements could be achieved by adopting more recent reader technology that offers higher sensitivities than the M6e [103].

Chapter 4

Soft Grid Array Antenna for RFID Communications in 5G S-Band

This chapter presents the novel application of the grid array antenna along with the simulation and prototyping of a 'Kraus' grid array antenna, at the newly allocated 5G S-band. The grid array structure will be carried forward into later chapters so this chapter will serve as an introductory explanation of the antenna operation, with an initial practical application. Since no RFID IC's exist for 5G-RFID at the time of writing, the described procedure taken for both antenna simulation and prototype take theoretical assumptions from UHF RFID technologies.

4.1 Introduction

Forthcoming fifth generation (5G) systems promise to offer the next big step forward in data communication with higher data rate, lower latencies and wider bandwidths than previously available. Many local area networks, from leisure to industry, could take advantage of 5G capabilities, thanks also to the envisaged interoperability of platforms and technologies. Among them, wearable devices and body-centric communication will significantly boost their adoption, especially backscattering-based passive radios which require neither batteries nor local power supply, and hence they will not impact on energy, waste and pollution [104]. UHF Radio frequency Identification Technology (RFID) has been identified as well suited to these applications, thanks to the absence of batteries, the minimal required electronics, sensing capabilities, and the possibility to reach read distance up to 5-7 m [105]. A particular class of RFID devices are those for Epidermal Electronics, another emerging technology aimed at turning bulk medical devices into soft, flexible and sometimes even stretchable membranes, for direct on-skin applications [34]. Preliminary studies demonstrated the potential advantage of on-skin antennas at 3.6 GHz for future 5G RFID systems. Even accounting for the higher free space attenuation, 3.6 GHz antennas are suitable to provide the same read distance of the corresponding UHF whilst boasting aforementioned advantages [94]. However, the major limitation of on-skin passive backscattering communication remains the short transmission range, especially for wearable devices operating in high frequency bands in which the path loss imposes attenuations up to 70 dB/m. To mitigate the problem and establish a robust link, an increase of the antenna gain is required, utilizing multiple antennas to form high efficiency arrays would be suitable. Currently, only arrays of patch or slot antennas, including dedicated beam forming network (BFN) have been proposed for wearable applications. However, since they are multilayered and bulky structures, concerns related to their effective usability cannot be neglected [106], hence, alternative layouts must be introduced. This chapter investigates a soft wearable/epidermal grid array for 3.6 GHz communications. The grid-array antenna (GAA) was originally proposed by

Kraus in 1964 [107], more recently exploited at mm- wave frequency for antenna-in-package technology and with great advantages in terms of high gain, bandwidth, simple feed, low profile, lightness and easy construction. Such features are also suitable for wearable antennas, since they guarantee lightweight, thin, and even highly breathable layouts. The work in this chapter was carried out at the University of Roma Tor Vergata and The University of Kent and has been published in [108].

4.2   Human Body Simulation at 3.6 GHz

For analysis of the antenna performance on the body, we must first accurately describe the body tissues numerically for the FDTD simulation tool, CST studio suite. For the following simulations in this section a 150x150 mm^2 3-layers body phantom is devised with the parameters as shown in Table.4.1. The electrical properties of the tissues have been sourced from the 'IT'IS Foundation' tissue property database [41].

TABLE 4.1: Permittivity and conductivity values for numerical body models at the 3.6 GHz 5G frequency [41].

Layers		3.6 (GHz)
Skin (1mm)	ε_r	36.92
	σ (S/m)	2.08
Fat (3mm)	ε_r	5.16
	σ (S/m)	0.16
Muscle (31mm)	ε_r	51.32
	σ (S/m)	2.65

4.3 Grid Array Antenna Rationale

The elementary structure of the wearable grid array is shown in Fig. 4.1. The topology was originally defined by John Kraus in [107], the cell vertices and horizontals of the grid array are defined by s = $\lambda/2$ and l = 2 s, respectively. The form factor of the cells is such that currents, indicated by the arrows, on vertical elements are in phase and act as radiators, while couplets of horizontal currents are in phase reversal and they hence act as transmission lines without contributing to radiation. This antenna structure was chosen for its simplicity in forming a multi-element array, creating a high gain equivalent to a patch array, without the need of a feed network. Additionally, the cell topology allows for possible ground plane reduction for a more breathable device, for more comfortable wearing on the body. Direct comparison to a patch array and ground plane reduction is explored in Chapter 5.
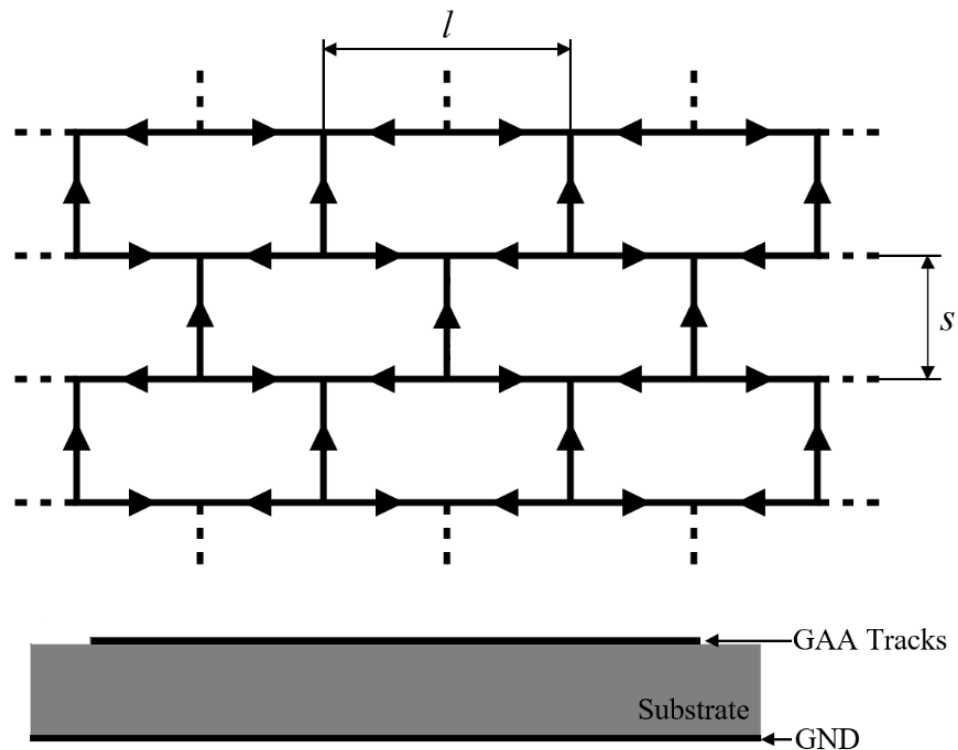
FIGURE 4.1: Multi-cell GAA structure with indication of the typical current pattern and cross-sectional view.

In the original design, the antenna structure sits 1/10th of a wavelength above a flat conducting ground plane, separated by an air gap. This iteration of the antenna was fed by way of a coaxial/pin feed at the corner of the grid, resulting in a backward-firing radiation pattern. This was later adapted to feeding the antenna centrally, still keeping with the pin feed through the ground plane, but this time providing a more useful broadside beam, finding application as a packaged automotive radar sensor at 24 GHz [109]. For the first time, this research splits the central track for a planar feed, for the possible allocation of an integrated circuit (IC) transponder connected via surface mounting, still maintaining the surface current and therefore broadside radiation pattern.

4.3.1 Substrate Thickness

In choosing the substrate, the ideal scenario would be to take maximum advantage of the dielectric effect and utilise a substrate with the highest dielectric constant that will support a working antenna, in doing so, allows for the antenna topology to be made as small as possible, since the guided wavelengths on the board would be made effectively smaller. However, increasing the dielectric constant of the substrate does come at the cost of a reduction in the bandwidth [110]. Unfortunately, for materials that would be considered affordable, the higher the dielectric constant the more inflexible the structure becomes (e.g. brittle ceramics), therefore higher dielectric constant materials would not be comfortable to wear owing to their poor flexibility. Yet again a compromise is required to be made, this time between two structural characteristics, the overall size and the flexibility. After deliberation, the substrate was settled to be silicone rubber, owing to availability and desirable structural properties, obtaining a dielectric constant value of $\epsilon_r=$ 3, $\tan\delta=1.4\cdot10^{-3}$. Using these numerical properties in CST studio, initial simulations were made into the analysing performance of a 4-cell grid array antenna over varying thicknesses of the substrate. A four cell grid was chosen as to not under-simplify the array to a single loop, or loop-pair, but not over-complicate the

system. That said, the array count and relative performance will be studied in a later section of this chapter.
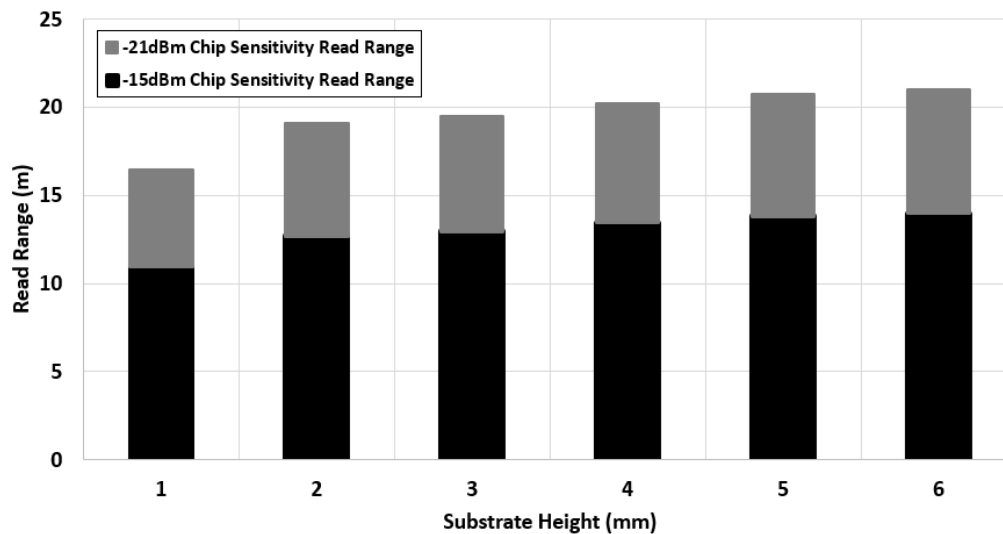

FIGURE 4.2: GAA calculated read range for each substrate height using an estimated sensitivity value for a theoretical 5G 3.6 GHz RF chip sensitivity. Firstly, a conservative -15dBm, secondly a -21 dBm sensitivity comparable to modern day UHF RFID RF chips.

In Fig. 4.2, the resultant simulated gain values are converted to a read range using the Friis equation (1), for a more relatable understanding of the outcome of the gain value. Breaking down the coefficients of the Friis equation for this case, it is assumed the future 5G regulation standards at this frequency band will be in-line with that of currently used UHF standards. The EIRP (Effective Isotropic Radiated Power) in (1) is assumed to match the European UHF regulated value at 3.2 W, G_{tag} is the simulated antenna gain, and τ is the tag antenna transmission coefficient, which for simplicity sake is assumed to have the value of 1, describing a perfect match. P_{th} is the threshold power of the RFID IC, also known as the sensitivity. Since there are no RFID IC's for this frequency, Fig. 4.2 references two sensitivities for consideration, a conservative estimate and a more likely, optimistic, performance based off the current UHF RFID IC capabilities. The resultant read range performances range from a conservative -15 dBm sensitivity, 1 mm substrate thickness equating to 11 m up to a best case 21 m in read range, with a -21 dBm sensitivity and 6 mm of substrate thickness. Between the substrate heights, a considerable performance increase is seen from 1 mm to 2 mm substrate thickness,

then a more gradual increase to the largest simulated thickness of 6 mm. For such a clear improvement in gain, the 2 mm substrate thickness was chosen for increased performance but as to not to overly compromise on the wearability of the device and the accessibility of potentially attached sensors on the skin. Whilst adjustments were made between substrate thicknesses to the antenna structure parameters, the 2 mm thickness equated to a grid array with the lengths s = 29.7 mm, l = 59.4 mm, and a track width w = 1 mm.

4.3.2 Cell Count
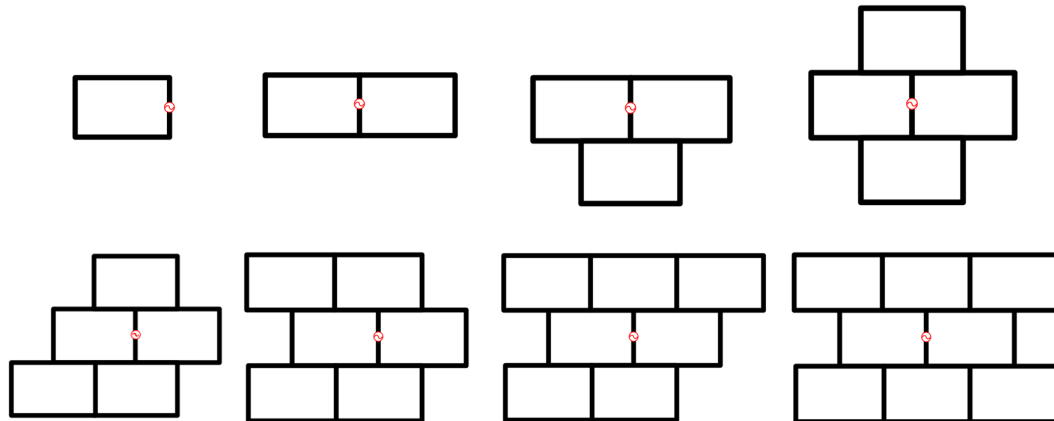
FIGURE 4.3: GAA topology for increasing cell count from 1 to 8 cells.

Once the substrate thickness had been set the array cell count was reduced down to a single cell (a loop antenna), then incrementally increased to find the performance variation. Fig. 4.3 shows the GAA topology types considered. Parameter sweeping the cell count required the dimensions of the human body model to be enlarged for the higher numbers of cells, and to keep the results consistent the body model perimeter was maintained at least one wavelength extended beyond the antenna perimeter, as shown in Fig. 4.4.

Fig. 4.5 shows the maximum radiation gain and the efficiency when moving from one cell (2 radiators) to eight cells (15 radiators) for an on-body grid-array antenna. As expected, the profile of gain and efficiency is not linear with the overall size of the antenna. The increase in gain is limited by the attenuation of currents on the microstrip lines and by the poor control over the phase synchronization in the case of large array. The increase in the efficiency and gain is mostly due to the increase in the radiation resistance, which is proportional to the number of vertical elements. Further enlargement of the grid passed this point of peak efficiency produces more intense power dissipation on the conductors and within the surrounding tissues. The optimal efficiency arises for a grid-array of four cells, thereafter the gain only increases moderately and in essence remains nearly stable due to the balance of loss of efficiency versus the relative gain improvements through additional radiators.
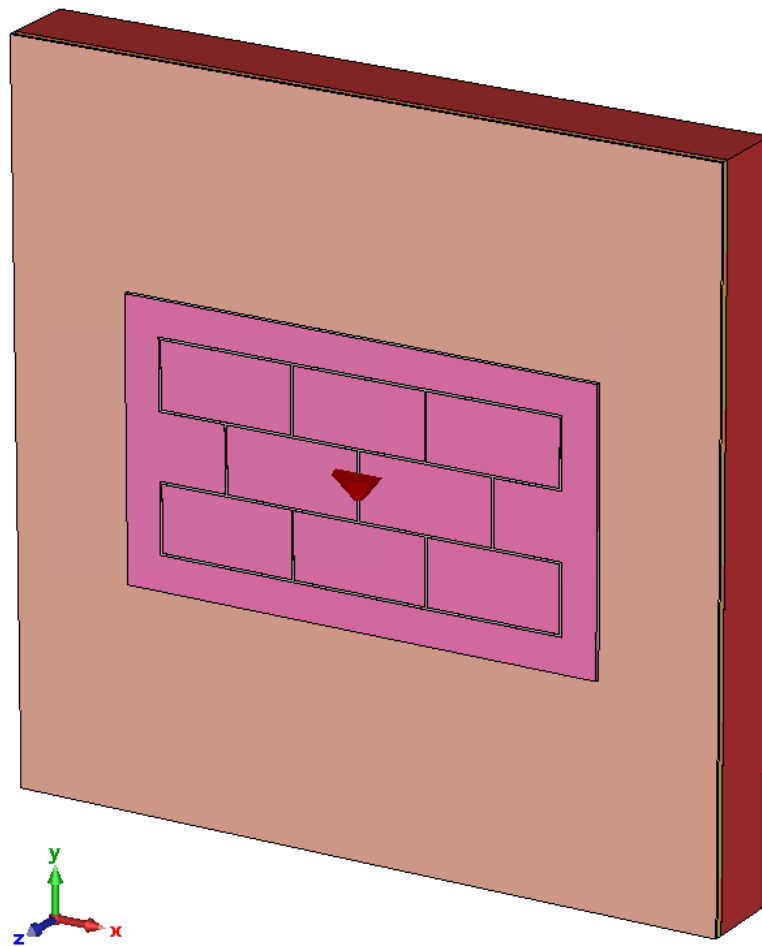
FIGURE 4.4: CST model of GAA topology with 8 cells, on biosilicone substrate and human body model.

After the optimum number of cells had been found, the relative size of the ground plane backing the GAA 'driver' topology was reconsidered. The ground plane had initially been set to a 15mm excess, referring to the extra distance the ground plane extends beyond the outer most dimensions of the grid track element perimeter, relative to the centre of the antenna. This was reduced down to 5mm excess. As expected, the larger the ground plane the more efficient the antenna, the more directive the radiation beam, resulting in a increased gain value, shown in Fig. 4.6. However, the smaller ground plane size still allowed a performance capability within 1dB of the larger plane for the 4-cell GAA. Since one of the goals of the antenna is to remain as small as possible, the relative size reduction gain to performance loss was seen as a positive for the application.
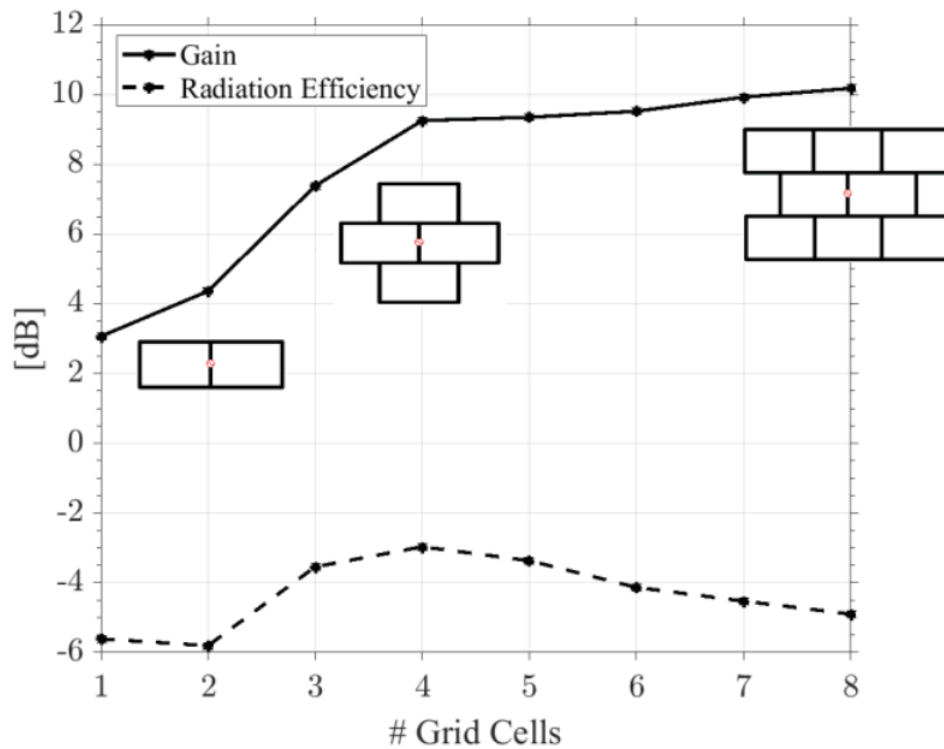
FIGURE 4.5: Simulated upper-bound gains and efficiency of wearable grids vs number of grid array cells. Maximum efficiency is achieved by a 4-cell grid with 7 radiating elements.
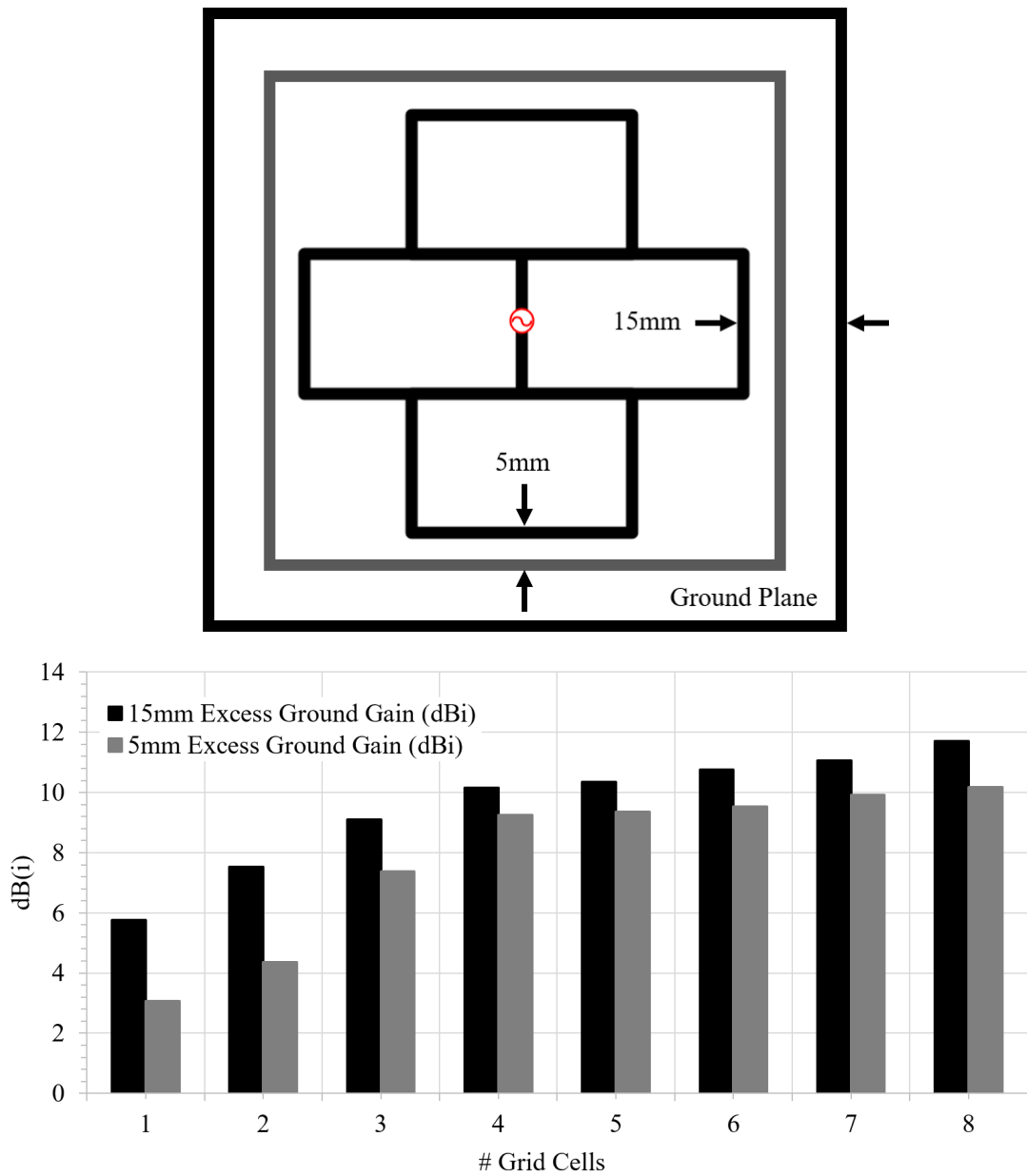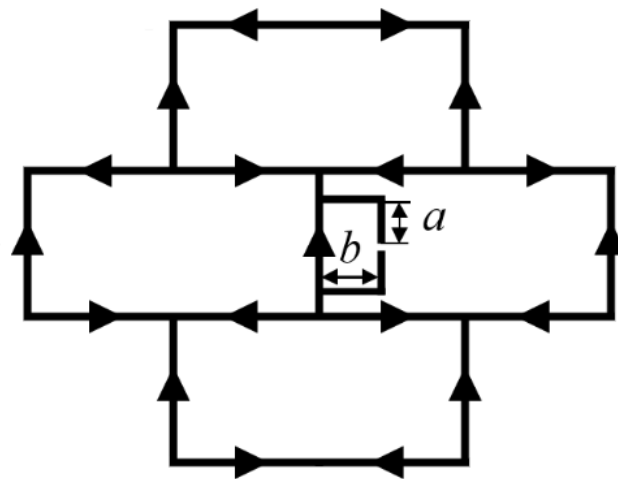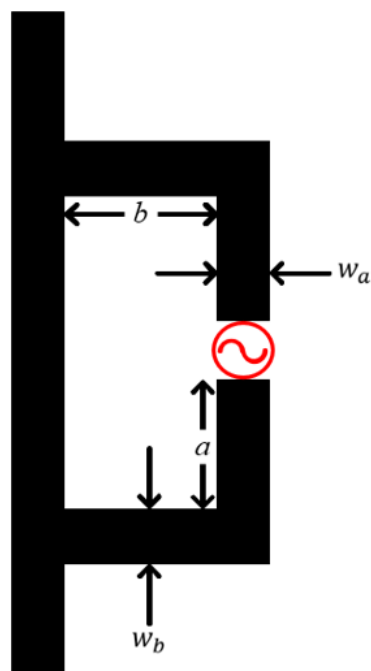
FIGURE 4.6: Comparison of simulated gain performance of a GAA with a 15mm and 5mm excess ground over the edge the outer conducting tracks.

4.3.3 T-Match

FIGURE 4.7: (A) GAA Topology with central T-Match feed network (B) T-match network tuning parameters.

Adapting to this newly proposed planar fed layout at the central element, we have allowed the addition of a T-match network [111] to finely tune the input impedance at the connection terminals to the theorised IC, shown in Fig. 4.7. The input

impedance of the GAA can be freely controlled by the use of a T-match, as made visible from simulation (Fig. 4.8) in the the matching chart, shown in Fig. 4.9. In which length a and width b have been progressively incremented respective to one another to get a wide span of values of both resistance and positive reactance as required to match an RFID IC. Having no RFID IC in the S-band to reference to, the antenna was tuned at 50 Ω to simplify the measurement.
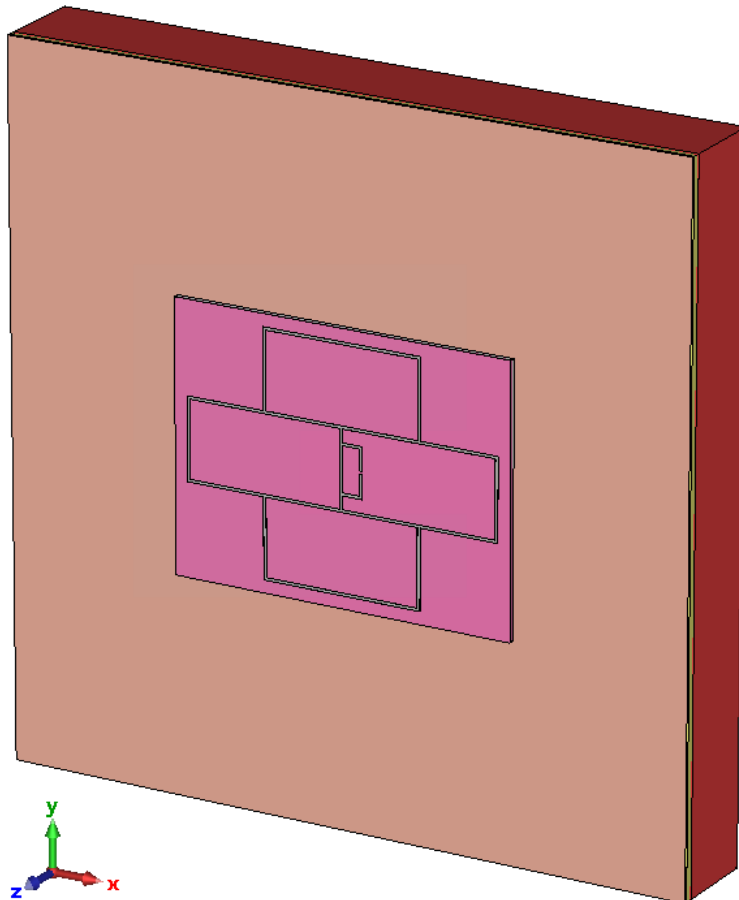

FIGURE 4.8: CST model of GAA topology with 4 cells and T-Match network, on biosilicone substrate and human body model.

It can be seen in Fig. 4.9 that after a few geometrical refinements, two 50 Ω match options are available. To choose between them a consideration of post-fabrication tuning had to be made, in that the track width labelled 'w_b' would be manipulated for fine impedance control after the prototype was constructed. Therefore, using the smaller 'a' length option allowed for the greatest possible range in 'w_b' while granting the greatest possible post-fabrication tuning capabilities, before potentially overlapping with the horizontal track length. Hence, the optimum layout

with slight adjustment for the additional track length added by the T-match was achieved with: s = 28.45 mm, l = 56.9 mm, track width w = 1 mm, a = 8 mm and b = 6.8 mm.
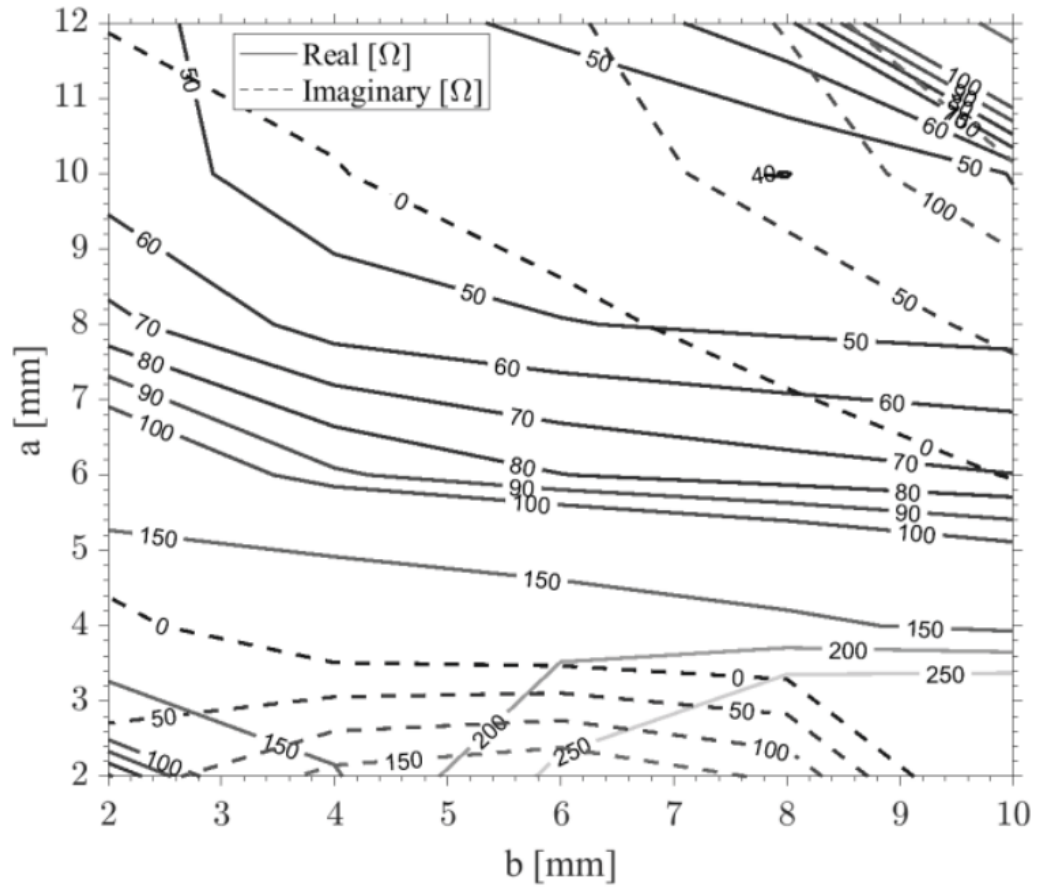

FIGURE 4.9: GAA matching chart by varying T-match shape factor a, b.

4.3.4 Initial Simulation Results

With the substrate thickness, array cell count, and T-match defined, the initial GAA simulation can now be made to find the possible performance capabilities.
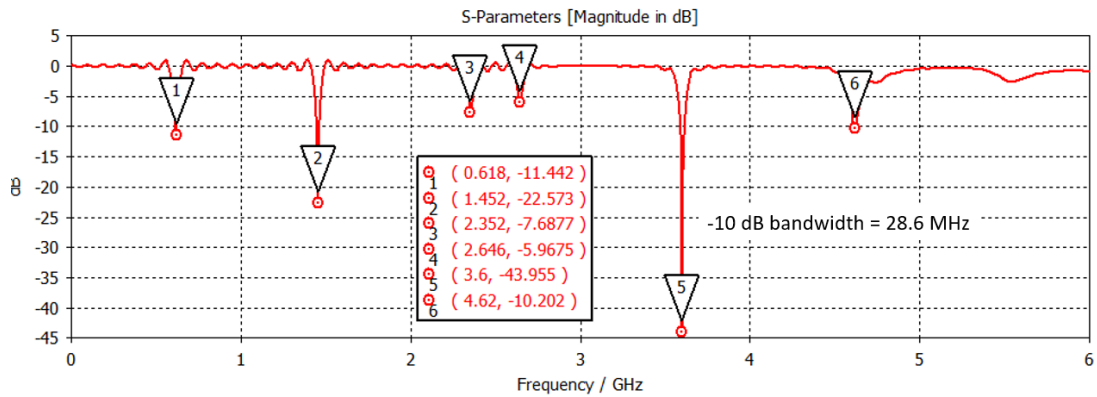

FIGURE 4.10: 4-cell GAA with T-Match initial simulation S11.

The S11 shown in Fig. 4.10 displays all the nulls for the first 6 GHz, with the best match clearly taking place at the intended 3.6 GHz, owing to the T-Match. Confirming this, the impedance parameters at 3.6 GHz are shown in Fig. 4.11, obtaining the expected 50 Ω input impedance.
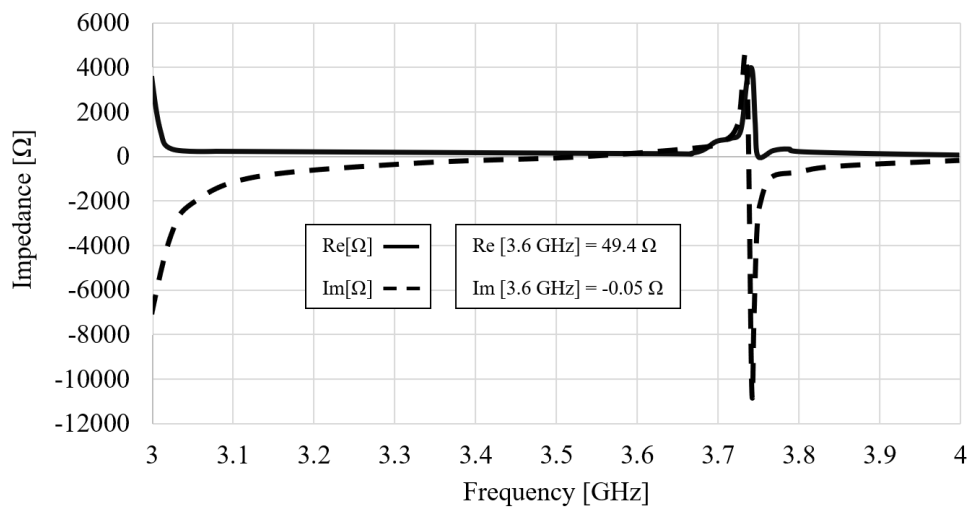

FIGURE 4.11: Impedance parameters of the simulated GAA design with T-match.

Table 4.2 shows the relative efficiency, gain and directivity performance of each frequency corresponding to an S11 null.

TABLE 4.2: GAA efficiency, gain, and directivity of S11 nulls seen between 0-6
GHz.

Frequency (GHz)	Efficiency (dB)	Gain (dBi)	Directivity (dBi)
0.618	-10.9	-15.7	-4.8
1.452	-11.2	-20.9	-9.7
2.352	-7.8	-3.8	4.0
2.646	-8.7	-6.4	2.2
3.6	**-2.8**	**9.3**	**12.2**
4.62	-3.2	7.1	10.4

The majority of nulls show negligible performance capabilities, whilst the radiation performance shown at 4.62 GHz appears almost as proficient as the intended performance at 3.6 GHz, the surface current shows no discernible pattern (shown in Fig. 4.12) and the radiation pattern is a split twin-end-firing pattern, which is impractical for our application, so is not considered a viable operating mode. Generally speaking, the proficiency of the radiation at each frequency can be gauged from the surface current pattern, shown in Fig. 4.12. At each frequency not accounted for in the design (3.6 GHz), the current phases on the vertices are opposing one another between rows.
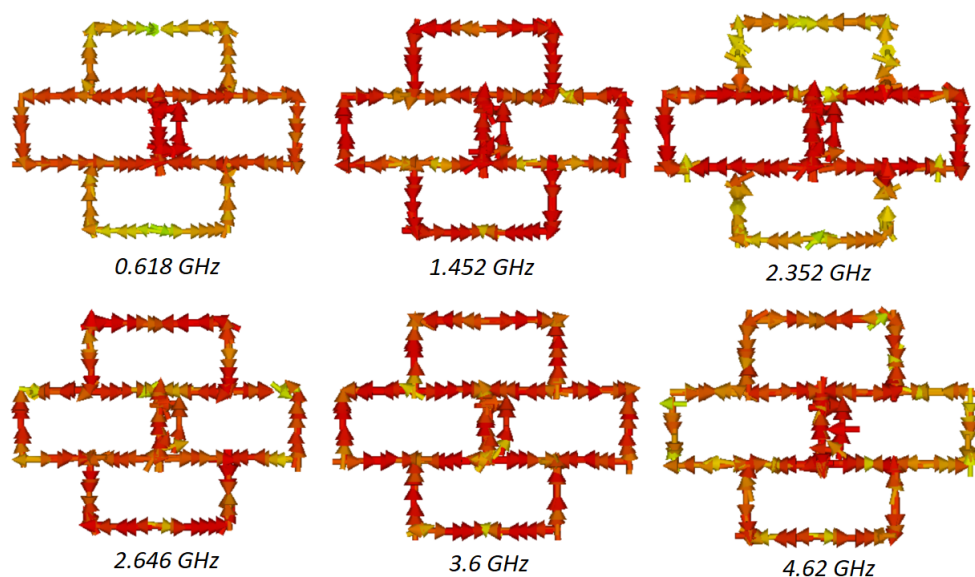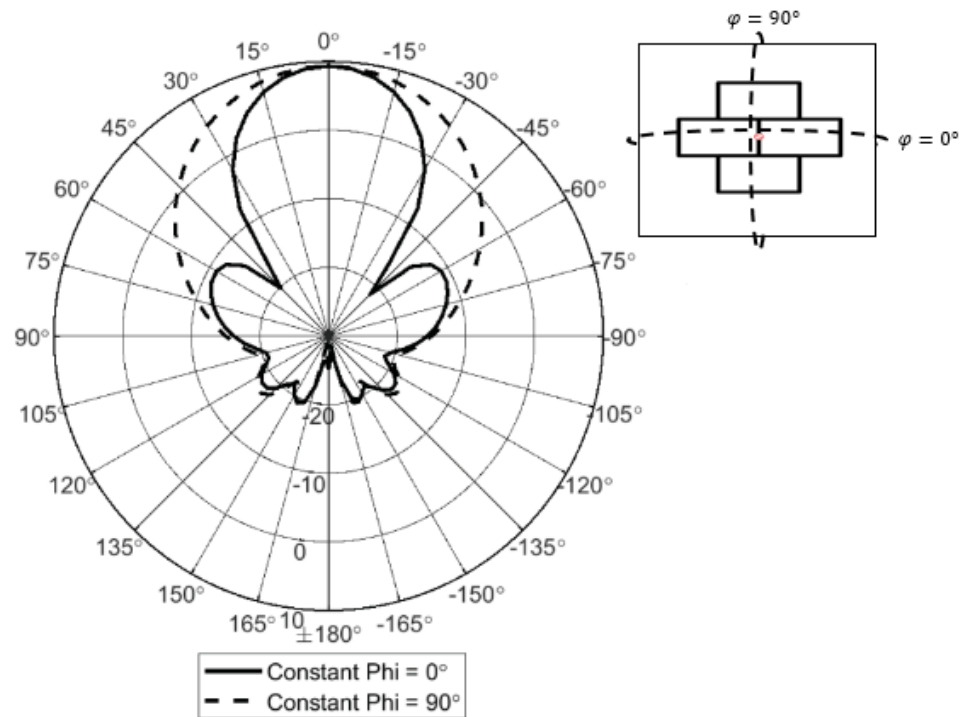

0.618 GHz   *1.452 GHz*   *2.352 GHz*

2.646 GHz   *3.6 GHz*   *4.62 GHz*

FIGURE 4.12: Surface currents of the simulated GAA design with T-match at
the S11 frequency responses described in Fig. 4.10

Figure 4.13: GAA Topology with T-Match initial simulation results.

The resultant simulation radiation pattern characteristics at 3.6 GHz are shown in Fig. 4.13, with a main lobe gain value of 9.34 dBi. The shape of the pattern being narrower more so on the phi = 0° axis than the phi = 90° axis is due to the relative spacing between radiating elements. The cross-polarization gain is -1.05 dBi, showing that the polarization is linear, as expected.

4.3.5 Prototype Simulation

Whilst the simulation serves as a representation of the complete system, the fabricated balanced antenna cannot be directly connected to a cable for measurement. With the full antenna structure, a balun would be required between the cable and antenna, but due to the small size of the antenna it is not feasible to incorporate a balun without affecting the radiation performance. Fortunately, since the antenna design is a balanced structure, the antenna performance can be accurately measured by employing image theory [112]. By halving the antenna structure, making the antenna unbalanced above a ground plane, the need for a balun can be negated and interference on the measurement will be limited.
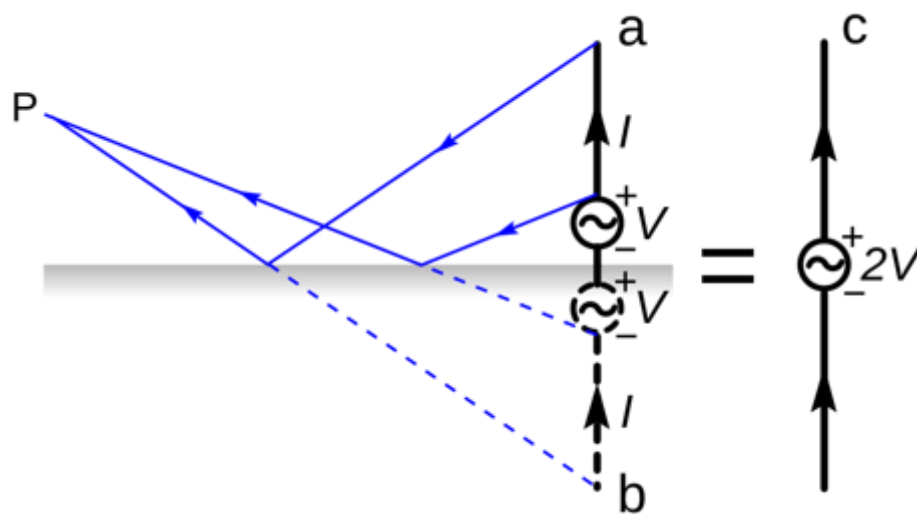

FIGURE 4.14: Monopole and dipole as described by image theory.

As shown in Fig. 4.14, a monopole shares the same electromagnetic 'image' as a dipole (a balanced antenna), achieved by constructing one half of the dipole structure over a reflective surface (ideally an infinite plane), resulting in the monopole radiation pattern from any perspective above the ground plane to look identical to that of the full dipole. As a first order approximation the input impedance of a quarter wave monopole over a large ground plane is half that of a half wave dipole. Transferring this process the the grid array antenna, the measurement setup will involve fabricating half of the structure over a reflective surface, thus, allowing for

electromagnetic 'image' of the whole structure to be analysed, with the intended planar feed to be properly represented. Additionally, the means of measuring the GAA gain performance will be done by means of gain comparison, whereby using an antenna with a known gain value, the S21 will be measured between the known antenna and the GAA allowing for a relative gain value to be found. Given the use of image theory, the most suitable antenna for comparison would hence be a monopole antenna.
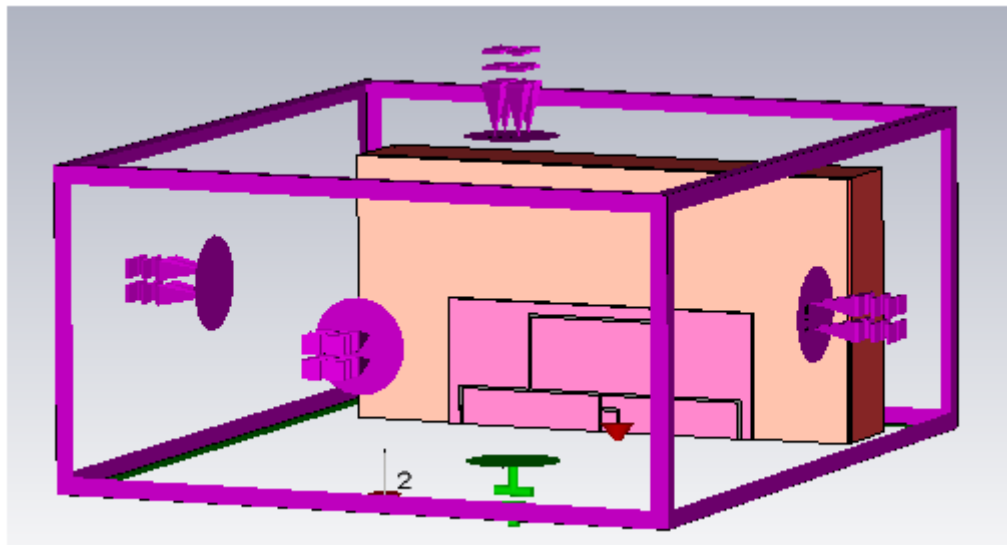

FIGURE 4.15: GAA simulation adopting image theory.

Confirming the image theory process and gauging what the eventual measurement results might show, Fig. 4.15 shows a simulation of the eventual measurement setup. The walls represented by purple describe the standard 'open space' boundary, whilst the green plane along the bottom represents an infinitely large ground plane. Opposing the GAA antenna and human tissues block is a quarter-wave monopole ($l \approx 20mm$), with a 50 Ω input impedance. The separation between the GAA and monopole feeds has been set to 13cm, the distance itself is arbitrary and only needs to be known for the gain comparison calculation later.

The resultant S-Paramaters are shown in Fig. 4.16, displaying correct frequency resonance for both the monopole and the GAA, with the monopole having an expected wide band response in contrast the the narrow band GAA. The S21 and S12 are expected to be perfectly matched in the balanced system, describing
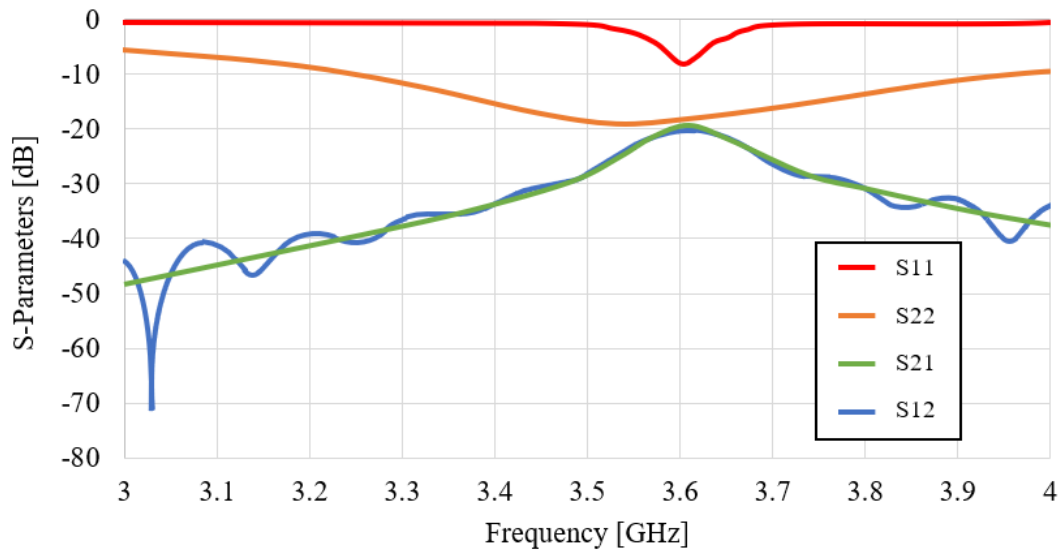
FIGURE 4.16: GAA and monopole simulated S-Parameter results.

equal power transference between the antennas, however there does appear to be a slight unexpected oscillation in the S12. This disparity is considered an artifact of the CST calculation and negligible to the system performance, thus the overall S-parameters validate the approach to gain comparison technique through image theory.
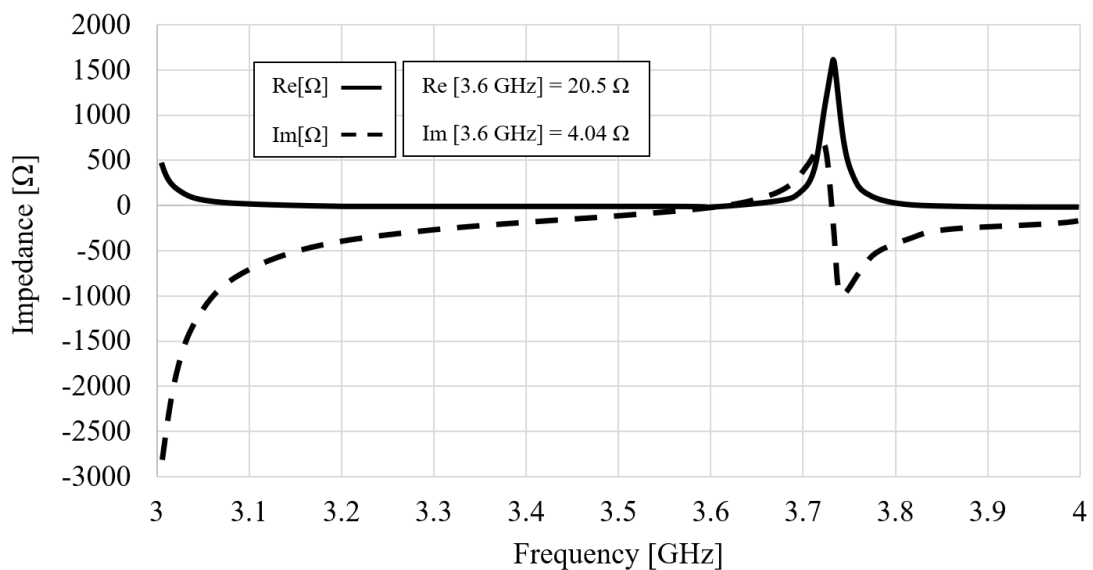

FIGURE 4.17: GAA and monopole simulated impedance parameters results.

Fig. 4.17 shows the GAA characteristic impedance of 20 Ω, whilst not exactly half of the expected 50 Ω the impedance is reasonably close, keeping in mind the additional impedance control T-match parameter w_b should this inaccuracy

need correcting for in the prototype stage. The radiation results of the GAA and monopole are presented in Table 4.3 and 4.4, and the radiation patterns shown in Figs. 4.18 and 4.19, respectively. Both antennas show inflated radiation values, a quarter-wave monopole would expect to have a gain around 5.2 dBi but appears 3dB higher, with the same unexpected effect seen with the GAA with respect to Table 4.2. This could be due to inadequate boundary conditions defined in the simulation [113]. Despite this discrepancy, the previous simulations of the full grid array indicated the actual expected gain, while this simulation portrays the measured setup with a imaging ground plane.

TABLE 4.3: GAA radiation results from image theory simulation.

GAA Radiation Characteristics at 3.6 GHz	
Radiation Efficiency (η_R)	-2.19 dB
Total Efficiency (η_T)	-3.14 dB
Gain (G)	13.20 dBi
Directivity (D)	15.39 dBi

TABLE 4.4: Monopole radiation results from image theory simulation.

Monopole Radiation Characteristics at 3.6 GHz	
Radiation Efficiency (η_R)	-0.26 dB
Total Efficiency (η_T)	-0.38 dB
Gain (G)	8.29 dBi
Directivity (D)	8.55 dBi

Farfield Gain Abs (Phi=0)

Farfield Gain Abs (Phi=90)

Theta / Degree vs. dBi
Frequency = 3.6 GHz
Main lobe magnitude =   13.2 dBi
Main lobe direction =   0.0 deg.
Angular width (3 dB) =   30.2 deg.
Side lobe level = -17.3 dB

Theta / Degree vs. dBi
Frequency = 3.6 GHz
Main lobe magnitude =   13.2 dBi
Main lobe direction =   0.0 deg.
Angular width (3 dB) =   25.0 deg.
Side lobe level = -24.7 dB
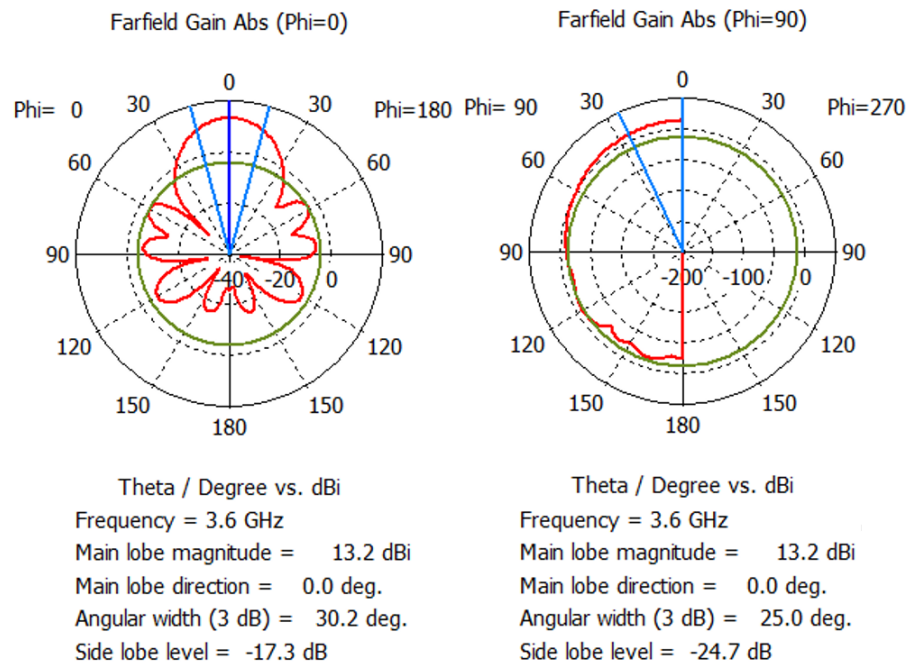
FIGURE 4.18: GAA simulated radiation pattern.

Farfield Gain Abs (Phi=90)

Farfield Gain Abs (Phi=0)

Theta / Degree vs. dBi
Frequency = 3.6 GHz
Main lobe magnitude =   7.43 dBi
Main lobe direction =   16.0 deg.
Angular width (3 dB) =   28.7 deg.
Side lobe level = -4.2 dB

Theta / Degree vs. dBi
Frequency = 3.6 GHz
Main lobe magnitude =   8.34 dBi
Main lobe direction =   18.0 deg.
Angular width (3 dB) =   58.4 deg.
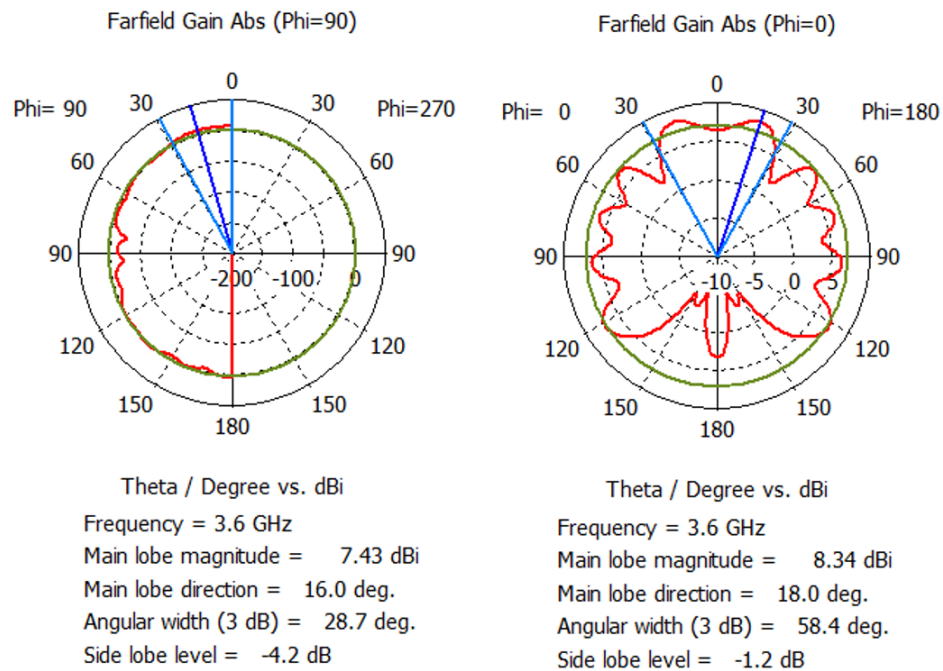Side lobe level = -1.2 dB

FIGURE 4.19: Monopole simulated radiation pattern.

4.4 Prototyping

From the GAA CST simulation, the track topology was exported to a computer-aided design (CAD) file, from which could be imported into the software of a two-axis cutter for cutting out a single-sided adhesive copper layer. The adhesive copper track was attached to the chosen substrate, silicone rubber, then the rear was also completely covered by the same adhesive copper for a ground plane. Using the imported structure as a guide, the silicone rubber and ground plane are then trimmed to size, resulting in the antenna shown in Fig. 4.20.

FIGURE 4.20: Finalised GAA Prototype.

For the full measurement setup, a thin and malleable copper plate, large enough to fit the antenna structure on, was drilled through wide enough to have an SMA pin fed through, giving ample space as to not have the SMA pin contact the copper sheet. The SMA connector was then held in place by soldering the ground terminal (the SMA pin housing) to the copper sheet, but keeping the screw threads clear of solder for the connection to the VNA. This process was then repeated, each of which being the foundation for the GAA and monopole antennas being fabricated.

For the GAA, at the locations where the GAA tracks were to meet the ground, firmer copper wires were soldered in place, acting foremost as a more reliable connection between the ground and antenna tracks, but also as a support to help keep the antenna upright when being measured. Another support structure was built on the rear of the GAA (ground plane side), again made of a more rigid copper material forming an L-bracket, to wedge the antenna firmly into the wires

connections. Once in place, more of the adhesive copper was applied in strips to secure the antenna in place, from which the wires soldered to the ground plane could now be soldered to the printed copper tracks of the GAA. To fabricate the monopole, a wire was soldered to the other SMA pin connected to copper sheet, then trimmed until a 3.6 GHz match was found on the VNA. Once the antennas had been fabricated, a much larger (1 m x 1 m, more than ten wavelengths from the radiating elements to the perimeter in each direction) copper slab 2 mm thick was used as the ground plane for the full measurement system. Holes had been drilled into this large flat copper sheet for passing through the SMA connection, holes mirrored over the center of the copper sheet separated 13 cm apart, one for the GAA and the other for the monopole. The smaller copper sheets the antennas were situated on, were then placed with their respective SMA connectors passing through the large ground plane, then sealed in place by adhesive copper strips, ensuring a flat continuous ground plane, as shown in Fig. 4.21
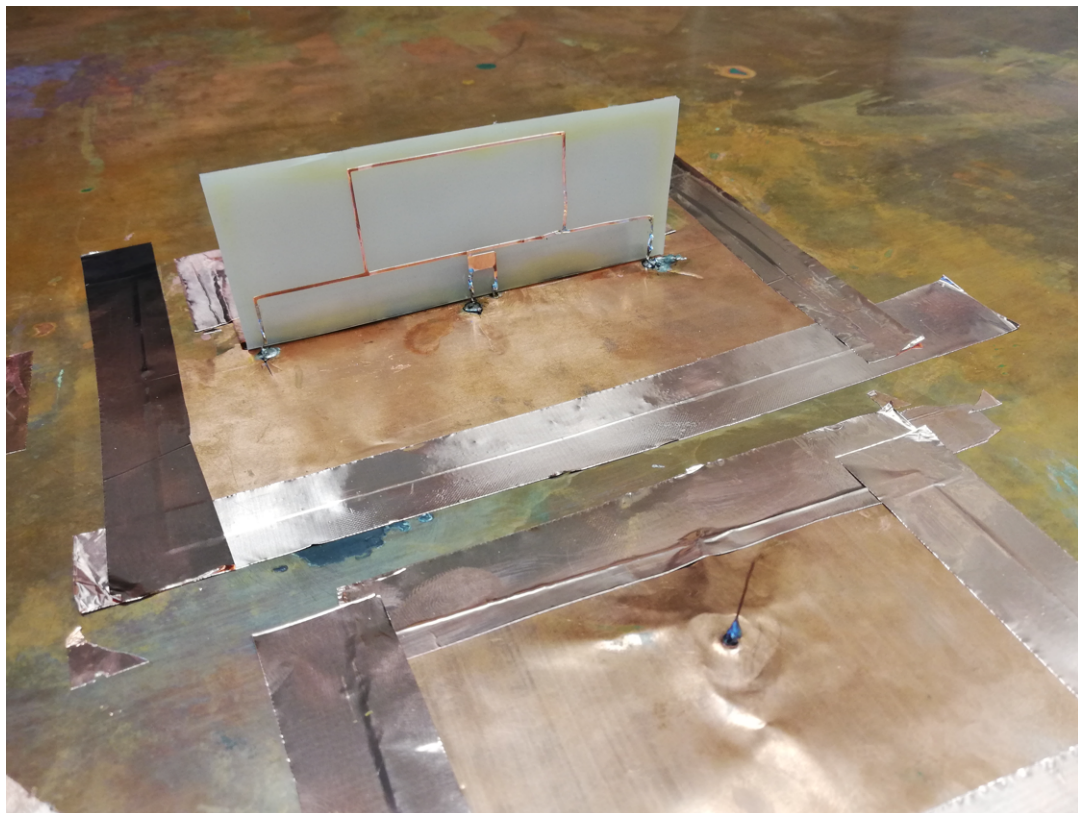

FIGURE 4.21: Finalised GAA Prototype mounted on copper sheet.

Finally, the GAA was attached onto a cubic phantom (roasted pork with estimated parameters $\epsilon_r = 40$, $\sigma = 2$ S/m) and the measurement setup was complete, as shown in Fig. 4.22 from the perspective of the monopole. VNA cables were then attached to the SMA connections under the ground plane to the GAA and monopole for the S-parameter results, Fig. 4.23.
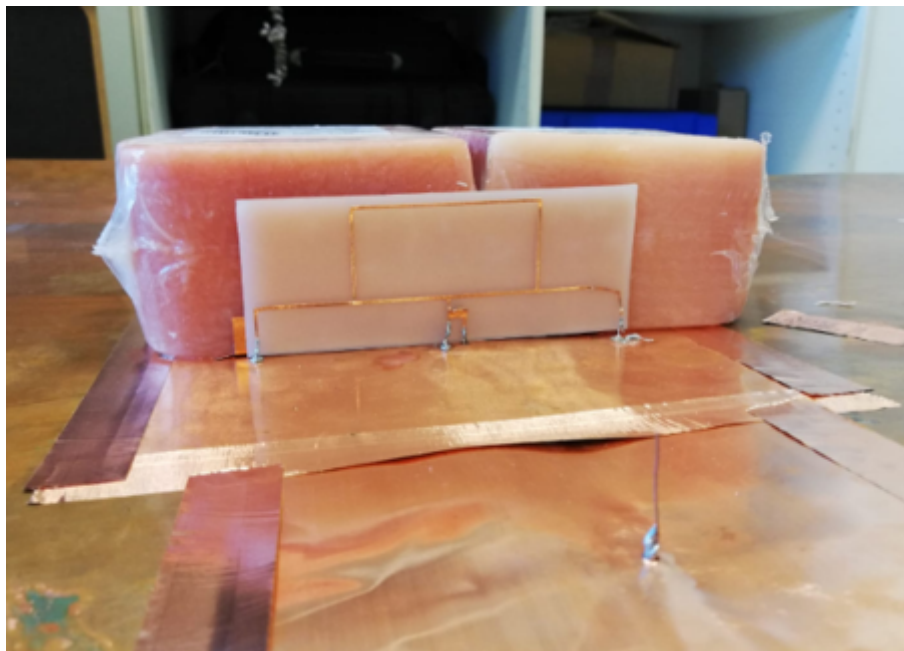

FIGURE 4.22: GAA and monopole prototype seperated by 13 cm.

FIGURE 4.23: VNA coaxial connection to SMA pin underneath the ground plane.

4.5 Grid Array Antenna Measurement Results

Initial measurements were made to test the T-Match tuning capabilities, utilizing the parameter w_b, presented in Fig. 4.7. Given the designed-in additional width to parameter w_b to compensate for uncertainties in realization, the resonant frequency was initially lower than the desired 3.6 GHz, by reducing the width of w_b the resonant frequency increased but suffered in terms of Q-factor. The optimum value for the parameter w_b showed to be 4mm, shown in Fig. 4.24.
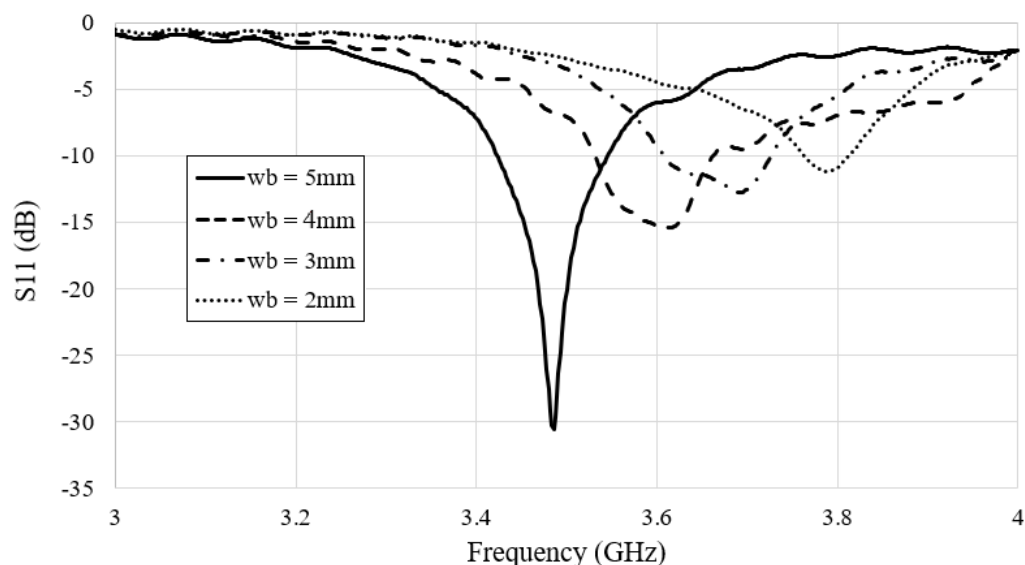

FIGURE 4.24: GAA T-Match measured reflection coefficient for varying w_b.

Fig. 4.25 shows the S11 measurement of the GAA without the monopole present, after repeating the tuning of the T-match, in comparison to the simulated versions. What can be seen is the measured S11 is it is clearly surpassing the 'Prototype Simulation' in terms of performance, and perhaps more comparable to the 'Initial Simulation', as named in their respective sections where the 'Initial' is a focus on the singular GAA, whilst the 'Prototype' incorporates the monopole into the simulation. However, in the measurement environment the GAA clearly suffers from additional losses, causing the Q-factor to be substantially diminished and the broadening of the bandwidth.
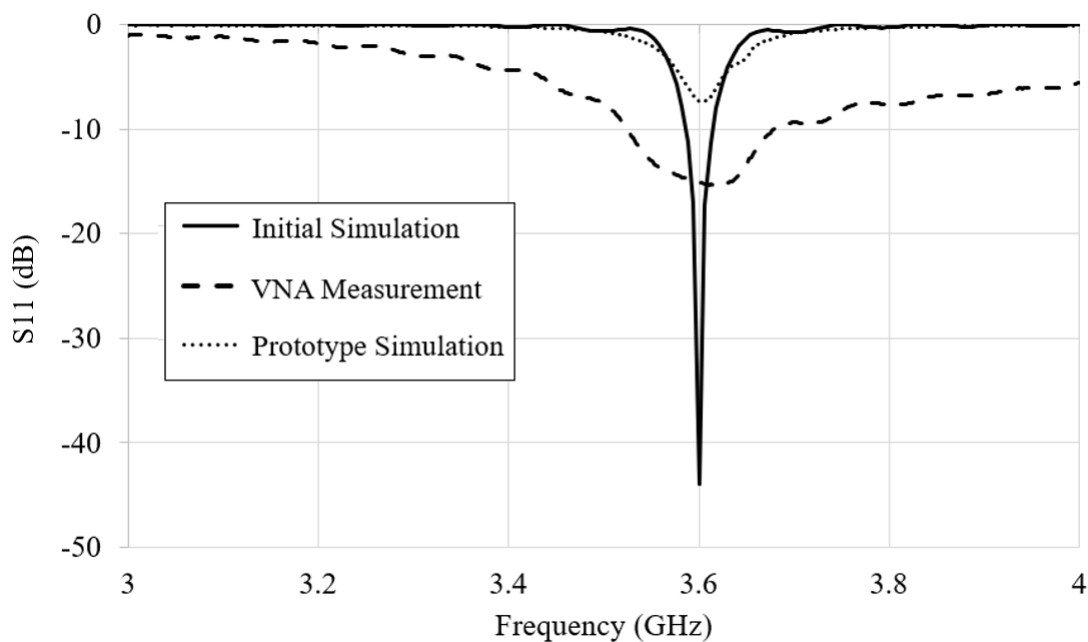
FIGURE 4.25: GAA measured S-11 results in comparison to simulations.

By assuming that the cables and the network analyzer are perfectly matched, the radiation performances of the epidermal antenna can be retrieved by measuring the S12, since $|S12|^2 \propto G$. $|S12(\phi)|^2$ measurements were taken at angles $\phi = 0°$, $+45°$, and $+90°$ relative to the monopole by carefully rotating the GAA antenna and the body phantom on the horizontal plane, with the results shown in Fig. 4.26. The S21 results indicate the GAA is radiating broadside from the feed point, decaying at the orientation changes, agreeing with the simulated gain polar plots in Fig. 4.13. The radiation pattern is symmetrical about the feed, therefore the data taken can be extrapolated to also represent the negative angles.
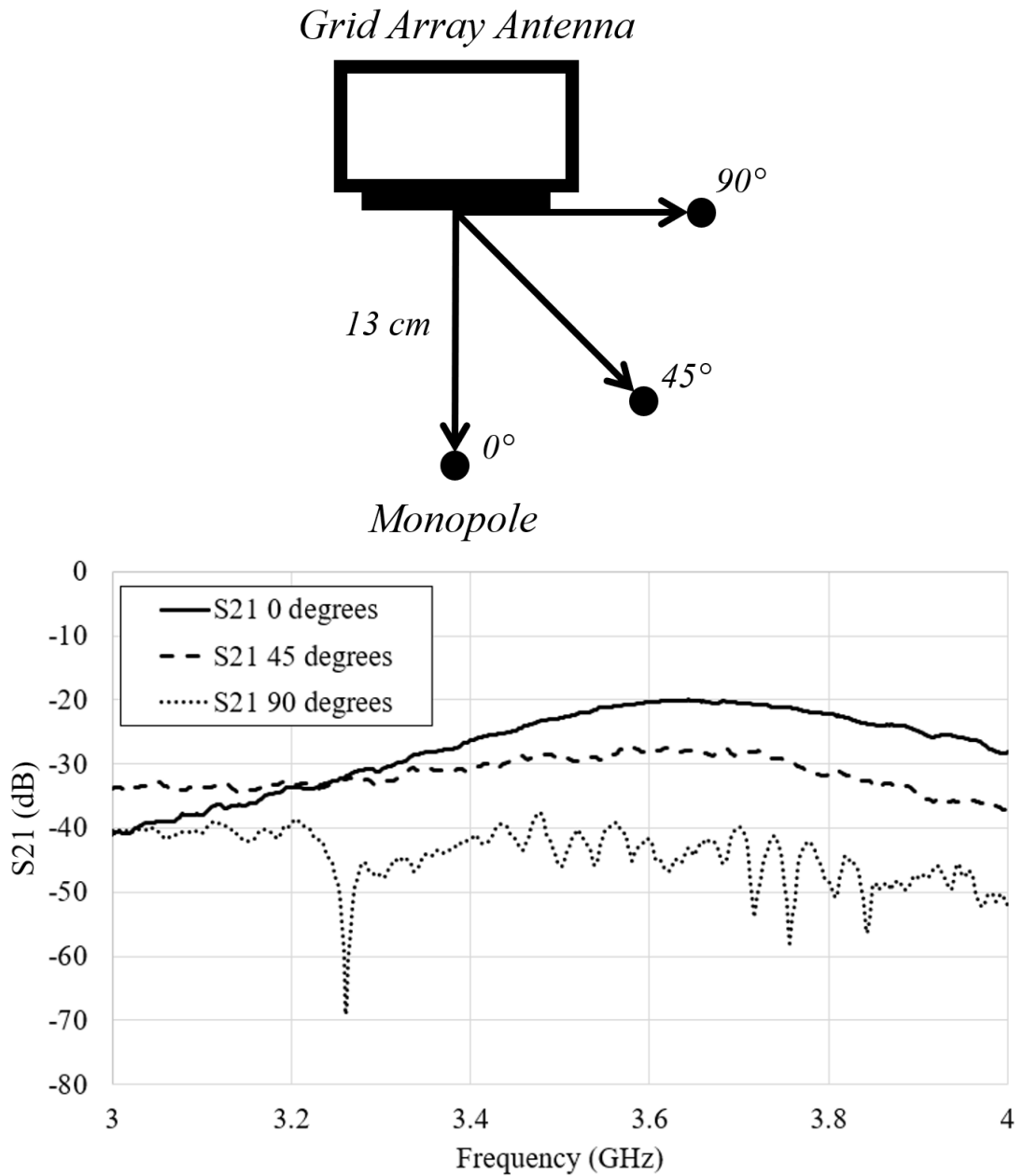
Grid Array Antenna

Monopole

FIGURE 4.26: GAA to monopole measured S21 parameter results for relative orientation angles of 0°, +45°, and +90°.
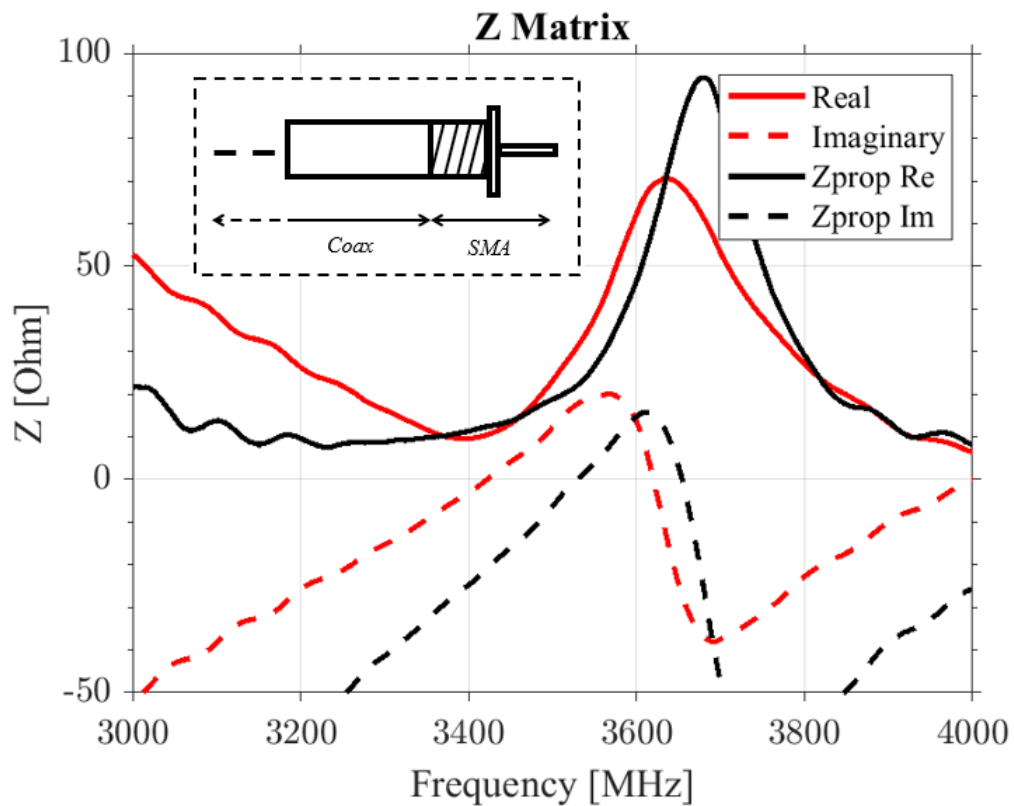
FIGURE 4.27: Measured input impedance of the antenna: (Red Line) directly extrapolated from S11, (Black Line) taking into account additional length of the SMA pin.

From the S11 data recorded on the VNA, the real and imaginary components were separated and displayed in MATLAB, shown in Fig. 4.27. The red lines represent the raw data, however the perspective of these values are taken from the point at the end of the coaxial cable, not as they should be at the tip of the SMA pin. To get a more accurate representation, the propagation delay needs to be taken into account in the additional length of the SMA pin, through the ground plane, to the connection to coaxial cable. This additional length is measured to be 4mm, which can be accounted for in the MATLAB calculations, resulting in the black lines displayed in the figure. Whilst the real part moves closer to the expected value, the impedance still remains higher than expected at 50 Ω.

4.6 Conclusion

In this chapter, the grid array antenna structure has been introduced, describing the topology and operating theory. The grid array antenna fundamentals will be carried forward into later chapters of this thesis as the antenna design evolves, including, the approach taken to the parametric analysis, prototyping, and measurement setup, with the reasoning behind such decisions limited to this chapter as to prevent repetitiveness. The 'Kraus' grid array researched in this chapter was developed into a soft, wearable antenna, simulated and fabricated for on-body applications at the 5G sub 6-GHz band. The radiation performance results of the antenna were optimistic, presenting a simple monolithic antenna with a high gain, overcoming the losses caused by the body and the free space attenuation associated with the operating frequency. The bandwidth of the antenna does appear very narrow-band in simulation, but the additional losses in measurement showed the band does considerably enlarge in real-life application. That said, should further bandwidth be required, varying designs to improve this need to be explored. The key component of the radiation results is the 9 dBi gain, which assuming reader sensitivities comparable to UHF RFID would provide a backscattered read range of over 10 m. However, the results achieved required the size of the antenna design to be considerably larger than desired, obtaining dimensions of 120 x 100 x 2 mm^3. Additionally, the antenna incorporated a substantial ground plane covering the rear of the antenna for shielding the antenna from losses arising from the body, but blocking access to the skin for the intended incorporation of sensor networks. Through this lens, the subsequent chapters will attempt to overcome these issues, improving the skin breathability, accessibility, and reducing the antenna size. However, for the proposed application, a 10 m read range would be sufficient to cover a standard room or office, and there could even be a possibility to sacrifice some efficiency by miniaturising the antenna.

Chapter 5

Soft Miniaturised Grid Array Antenna and Twin-Grid for RFID Communications in 5G S-Band

This chapter presents an evolution from the grid array antenna introduced in Chapter 4 through two variations, firstly to reduce the surface area of the overall antenna through miniaturisation, then, presenting a new variation in the 'twin-grid' array antenna for potential incorporation of sensors.

5.1 Introduction

In the emerging trend of epidermal electronics, wireless devices are envisioned to be small, soft, flexible and stretchable for direct on-skin application [114]. The antenna is often the largest component of wireless devices and research into antenna miniaturisation is common, early studies suggested the reduction in size inevitably results in decreased bandwidth, efficiency, and a lower Q-factor [115], however this is not always the case. Techniques based on manipulating geometry, current distribution, materials, and electrical dimensions of the antenna have been able to miniaturise whilst maintaining radiation performance [116]. In the previous chapter, the grid array antenna was pursued as an elegant solution for on-body communication at 3.6 GHz, offering a simple monolithic design that can be easily fabricated that produces a high gain radiation pattern. However, whilst the performance outcome met the requirement to support a 10 m read range, the structure was more cumbersome than desired. Even though 5G 3.6 GHz microwave is substantially reducing the operational wavelength relative to UHF, constructing track lengths even a couple wavelengths long is still large relative to the human body, especially for the intended device mounting locations such as on a person's appendages. To overcome this, miniaturisation of the GAA is performed on fundamental design, where non-radiating tracks are meandered to reduce the total area whilst leaving the resultant radiation performance unchanged. Additionally, the improved 'breathability' of the tag is pursued through a new array layout, where the grid array is adapted into a twin structure comprising a driver (radiating) grid and a reflector grid. The reflector grid still partially decouples the antenna from the body maintaining the broadside radiation of the Kraus grid, with the benefit of leaving most of the area uncovered by conductors and substrate. To make the device compatible with surface-mounted electronics, the antenna is fed at the middle of the central vertical element through a co-planar impedance transformer. The work in this Chapter was carried out at the University of Roma Tor Vergata and The University of Kent and has been published in [117], and [118].

5.2 Miniaturised GAA

5.2.1 Miniaturisation Technique

The grid array antenna has vertical $\lambda/2$ elements spaced by λ-length horizontal traces, making the layout inherently large compared to other antennas, e.g. the 4-cell grid is approximately $2\lambda \times 3/2\lambda$. Attempts have been made in literature to overcome this, the most prominent technique to reduce the surface area of the GAA has been outlined by Nakano through meandering, shown in Fig. 5.1 [119].
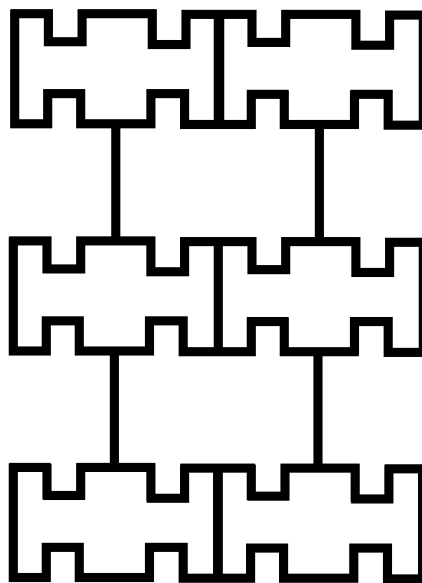

FIGURE 5.1: Nakano Miniaturised GAA

As shown in Fig. 5.2, to achieve the meandered pattern, the non-radiating sides of the grid (s) were divided into 5 equal lengths and reconstructed into the meander pattern, resulting in a layout $3/5^{th}$ of the original width. As Nakano describes, meandering each line twice mirrored from the centre allows the radiating elements to remain unaffected, as the electrical distance between the parallel vertices and vertices on adjacent rows is maintained.
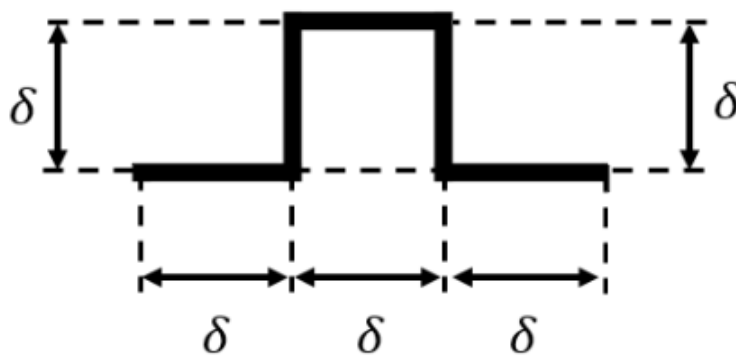
FIGURE 5.2: GAA miniaturization technique by breaking a track segment normally 1 wavelength long into 5 equal segments to be reconstructed into a meander shape.

The size of the ground plane discussed in Chapter 4 for the Kraus-grid was 5 mm in excess of the topology perimeter, in this iteration of the antenna the ground plane is further reduced to just 2 mm in excess, shown in Fig. 5.3.
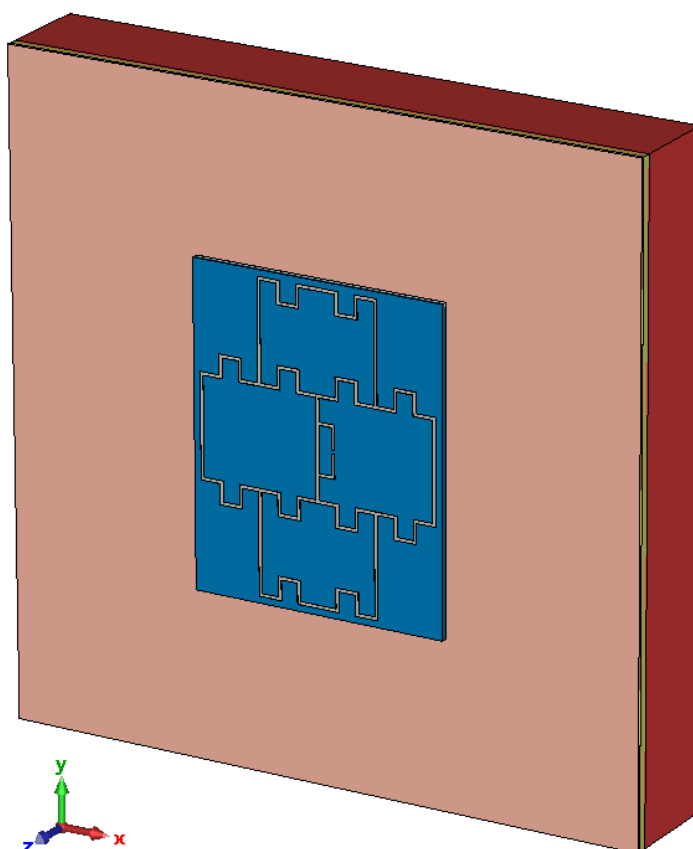

FIGURE 5.3: CST model of meandered GAA topology with 4 cells and T-Match network, on biosilicone substrate and human body model.

Extending on this technique, research was also made into the possible miniaturisation of the vertical radiating element. This miniaturisation technique would usually be avoided since the vertices are radiating elements and changing their orientation would detrimentally effect the efficiency and radiation performance. However, since size reduction is the ultimate goal, perhaps a compensation can be made on performance for structural gains. Fig. 5.5 shows the meander topology variations considered.
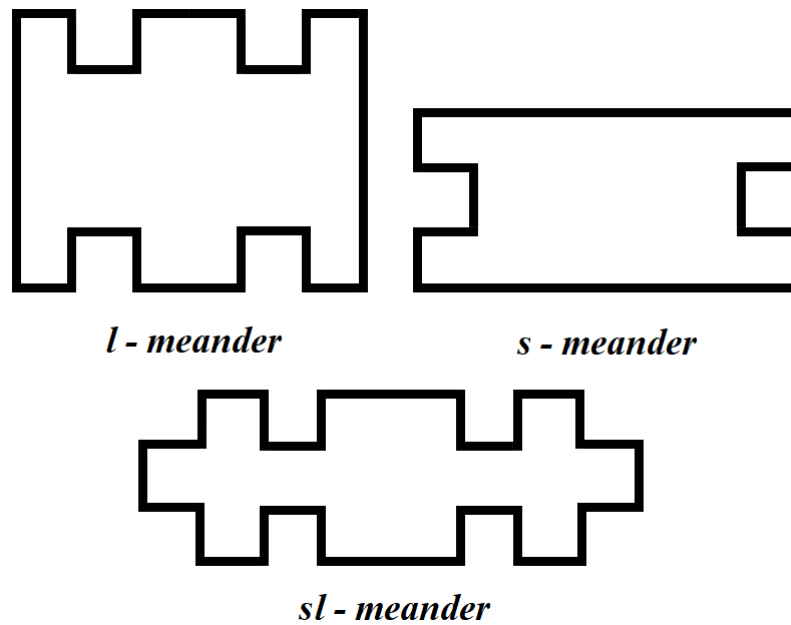

FIGURE 5.4: GAA miniaturization technique by meandering the horizontal element, the vertical element, then both simultaneously.

These structures were arrived at for being the smallest possible single-cells that allow for the meander mechanism described. Considering the layout of each in an array, they each have a cell-counterpart that needs to be oppositely meandered, as a means to connect them.
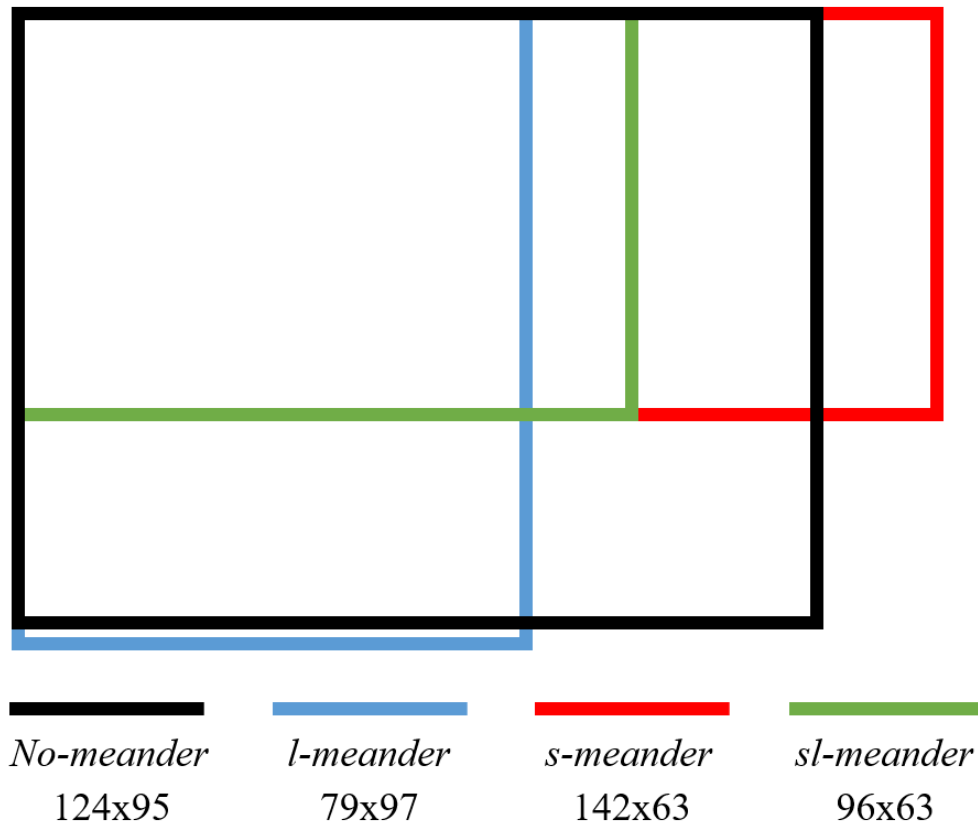
FIGURE 5.5: Total rectangular bounding area comparison of each GAA minia-
turisation technique in a 4-cell (7-radiators) topology.

In Fig. 5.5, a size comparison chart of each topology type shown in Fig. 5.4 as a
4-cell array is presented. In order of size relative to the original no-meander topol-
ogy, the *s-meander* is a 24% surface area reduction, *l-meander* a 25% reduction,
and *sl-meander* a 48% reduction. Whilst the *sl-meander* provides the greatest
miniaturisation, the relative radiation performance must be considered next to
determine whether meandering the radiating elements is a worth-while endeavour.

5.2.2 Parametric Analysis Simulations

The results of the 4-cell structures are presented in Table 5.1, as expected the manipulation of the radiating elements causes a detrimental change in radiation performance, seeing a 2 dB drop in efficiency and 3 dB drop in gain. Interestingly, the Nakano meandering appears unaffected by the change in structure and equal in radiation performance to the 'No-meander' version, though with a smaller bandwidth and wider radiation pattern. One explanation for this improvement could be due to the additional current vertices created by the meander components aligning with radiating elements, highlighted by the black arrows in Fig. 5.6.

TABLE 5.1: Simulation results of 4-cell meandered GAA topology types presented.

Meandered Grid Array Antenna					
Dimension (mm x mm)	*Gain (dBi)*	*Radiation Efficiency (dB)*	*Operating Frequency Bands*	*Fractional Bandwidth*	*HPBW (E-Plane/H-plane)*
96 x 63 (*sl-meander*)	6.454	-4.12	3.586 GHz – 3.611 GHz	0.69%	37.5°/69.1° (3.6 GHz)
79 x 97 (*l-meander*)	9.606	-2.04	3.589 GHz – 3.609 GHz	0.55%	48.2°/48.8° (3.6 GHz)
142 x 63 (*s-meander*)	7.415	-3.99	< 6 dB	n/a	35.9°/68.5° (3.6 GHz)
124 x 95 (*No-meander*)	9.342	-2.81	3.586 GHz – 3.614 GHz	0.78%	32.4°/51.7° (3.6 GHz)

A cause for concern is that the fractional bandwidth of the antenna appears very narrow-band with any given topology. However, as it will come to be seen, when the antenna is applied in a more realistic measurement environment and losses are incorporated, the bandwidth of the antenna expands considerably, making it sufficient for 5G applications. Should further bandwidth be required, tuneable or broad-bandwidth designs will need to be explored.
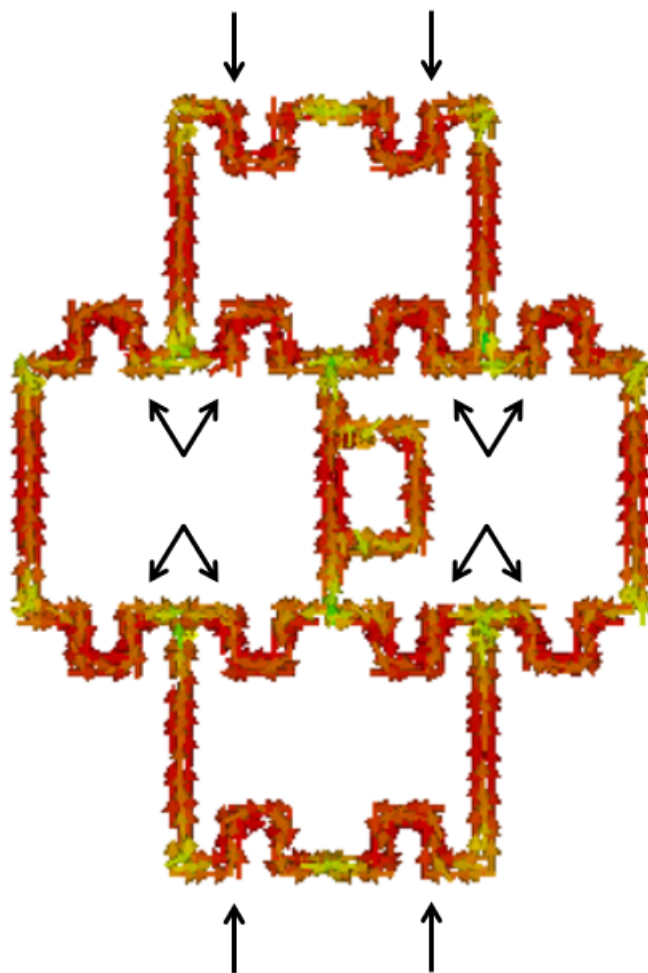
FIGURE 5.6: Surface current pattern on meandered GAA.

To gain perspective on the meandered grid-array performance, Table 5.2 presents the simulation results of a patch antenna on the body-model and subsequent array structures of the patch antenna for comparison. This comparison is weighted in favour of the patch antenna in this case, since the feed line is omitted from the design for simplicity, which especially for the on-body environment would play a significant roll in the losses. Nonetheless, the patch antenna is a well-established antenna and offers a 'gold-standard' of radiation performance for a new antenna to use as a comparative target.
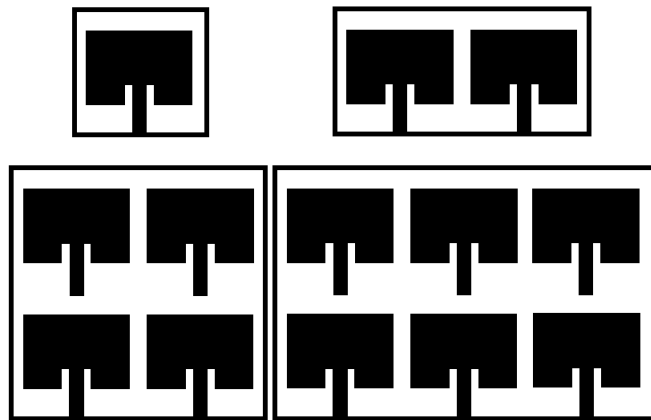
FIGURE 5.7: Single patch and patch array topology variations simulated in Table.5.2.

TABLE 5.2: Simulation results of 'perfectly-matched' patch array topology types.

Patch Array Antenna					
Dimension (mm x mm)	*Gain (dBi)*	*Radiation Efficiency (dB)*	*Operating Frequency Bands*	*Fractional Bandwidth*	*HPBW (E-Plane/H-plane)*
40 x 40 (Single)	5.115	-2.865	3.554 GHz - 3.652 GHz	2.71%	79.3°/77.7° (3.6 GHz)
80 x 40	7.359	-2.168	3.524 GHz – 3.639 GHz	3.19%	50.4°/74.8° (3.6 GHz)
80 x 80	10.98	-1.509	3.517 GHz – 3.624 GHz	3.00%	49.9°/49.0° (3.6 GHz)
120 x 80	12.02	-1.331	3.490 GHz – 3.591 GHz	2.86%	33.4°/48.8° (3.6 GHz)

In comparison, the 4-cell grid array is about equivalent to a 4-patch array 80 x 80 mm^2, obtaining gain and efficiency values 1 dB less than the patch array, with a significantly larger functional bandwidth. That said, as seen in Chapter 4, it is expected the bandwidths will be significantly larger in real-life. Plus, considering the complexity and limitation that a patch antenna suffers in incorporating to the on-body environment (need for a lossy feed network and large amount of conductor), the monolithic grid antenna array shows respectable performance.

Based on the results presented, in the aim of achieving a miniaturized topology and still have a radiation performance worthwhile for the intended applications, the decision was made to take the Nakano meander structure forward for prototyping.
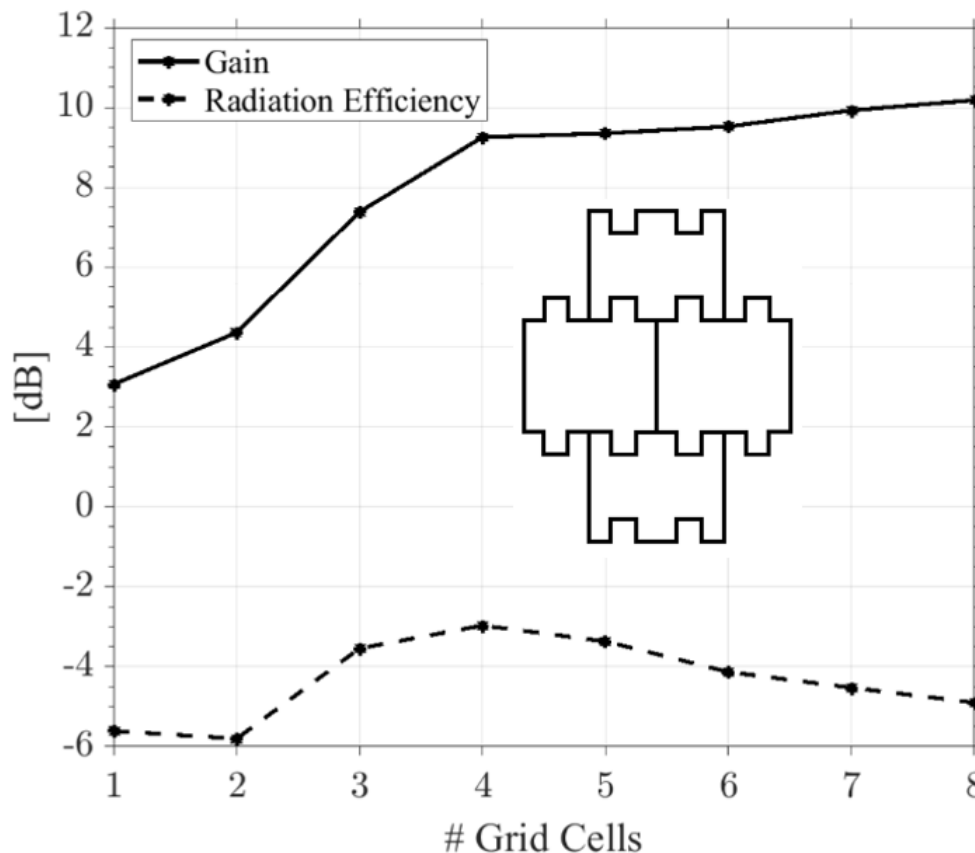

FIGURE 5.8: Simulated upper-bound gains and efficiency of wearable grids vs. number of grid array cells. Maximum efficiency is achieved by a 4-cell grid with 7 radiating elements.

As with the Kraus-grid topology, the cell count was increased from a single meandered cell to find the optimum array size for the on-body environment, Fig. 5.8. Once again, the 4-cell structure was seen as a plateauing point for the gain, appearing to be the turning point where the losses of the body overwhelm performance gain of additional array radiating elements.

5.2.3   T-Match

Once again, the T-match is being utilised for input impedance matching control, the contour map is a employed to show the changing impedance with respect to the parameters a and b (from Fig. 4.7), shown in Fig. 5.9.
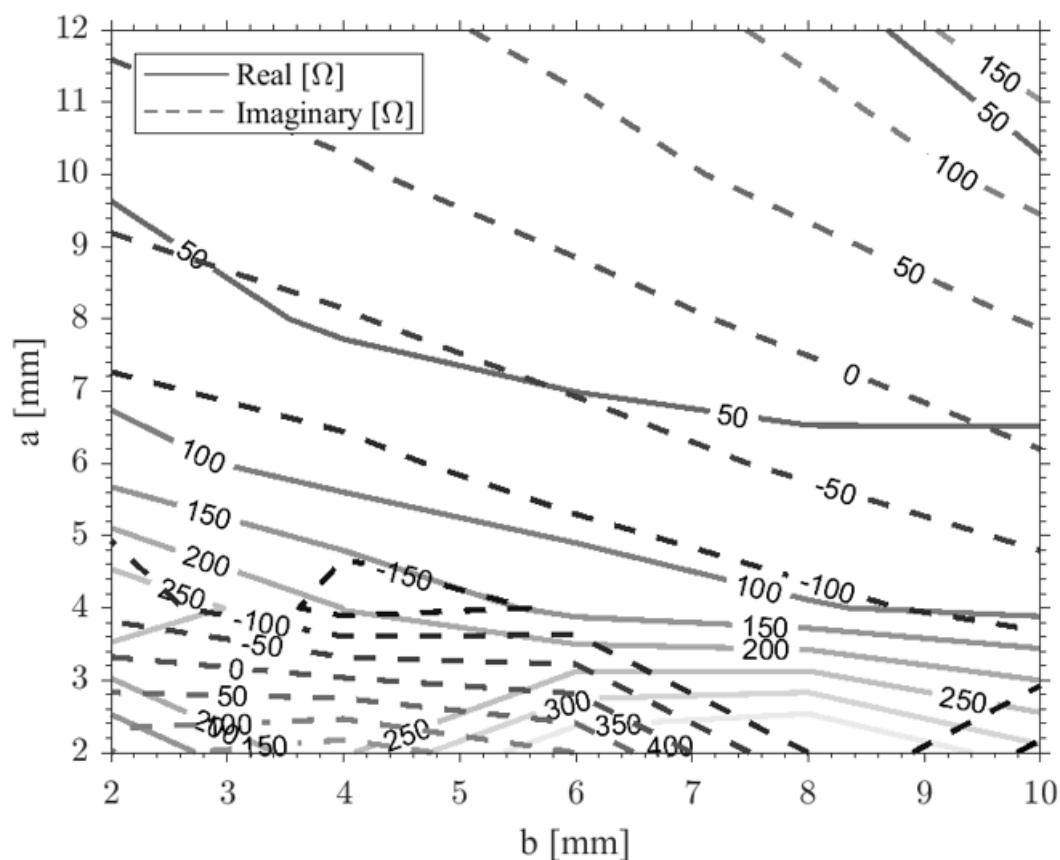

FIGURE 5.9:   Miniaturised GAA matching chart by varying T-match shape factor a, b.

For the miniaturised GAA, the T-match only has a single occurrence where the $50\,\Omega$ real component of the impedance traverses the $0\,\Omega$ imaginary component, defining the match. With the addition of the T-match, some adjustments to the antenna dimensions were required, resulting in a final structure with the parameters: s = 30.9 mm, l = 61.8 mm, track width w = 1 mm, a = 9.7 mm and b = 6.4 mm. The resultant radiation pattern is shown in Fig. 5.10.
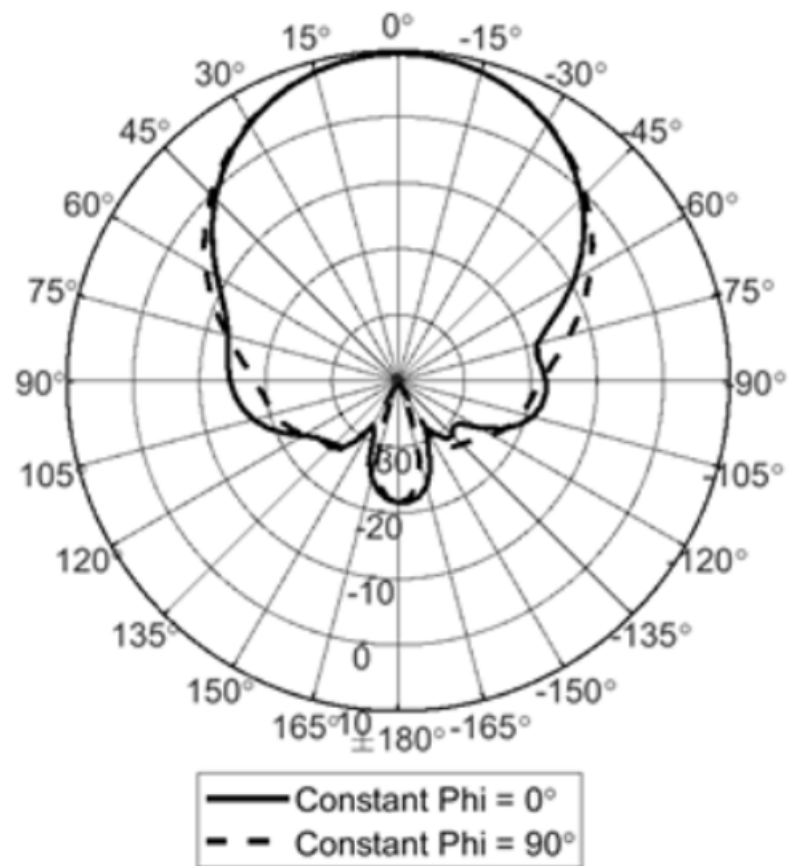
FIGURE 5.10: Miniaturised GAA simulated radiation pattern relative to the monopole.

5.2.4   Prototype Simulation

As with the Kraus grid design in Chapter 4, the full measurement setup is simulated for comparative purposes, the simulation structure is shown in Fig. 5.11. Whilst not shown in the figure, as before, the structures are mounted on an electric floor and surrounded by 'open space' boundaries.
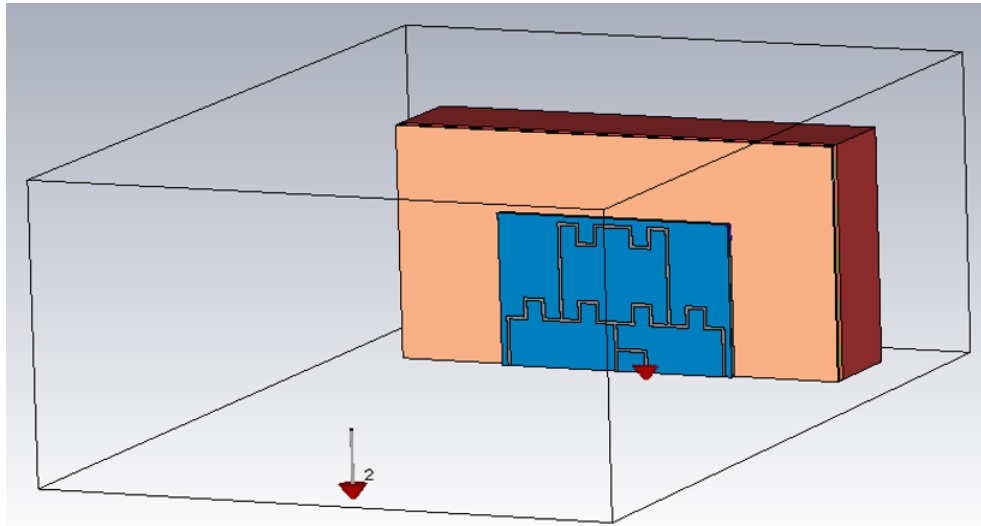

FIGURE 5.11: Miniaturised GAA simulation adopting image theory.

Fig. 5.12 shows the S-parameters to have a narrow band response from the grid array antenna and wide band response from the monopole. As with the Kraus grid, the S21 and S12 show an unexpected disparity, again this response is reasoned to be a CST calculation artifact and not of concern.
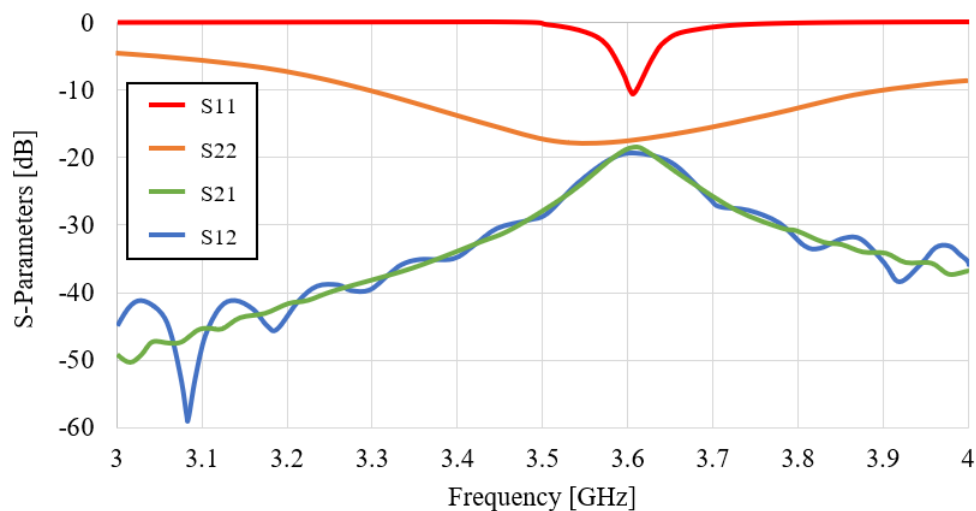

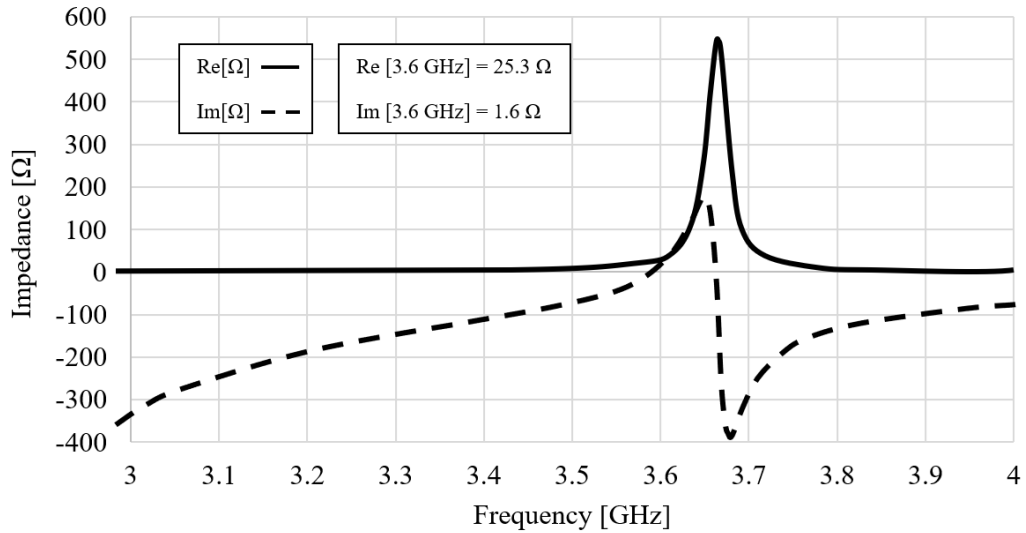FIGURE 5.12: Miniaturised GAA and monopole simulated S-Parameter results.

FIGURE 5.13: Miniaturised GAA and monopole simulated impedance parameters results.

The impedance parameters are shown in Fig. 5.13, this time the response is much closer to expected 25 Ω, half the full characteristic impedance, since the structure is halved. The radiation metrics of the GAA and monopole are presented in Fig. 5.3 and 5.4, along with the radiation patterns in 5.14 and 5.15, respectively.

TABLE 5.3: Miniaturised GAA radiation results from image theory simulation.

Miniaturized GAA Radiation Characteristics at 3.6 GHz	
Radiation Efficiency (η_R)	-2.12 dB
Total Efficiency (η_T)	-2.70 dB
Gain (G)	12.67 dBi
Directivity (D)	14.79 dBi

TABLE 5.4: Monopole radiation results from image theory simulation.

Monopole Radiation Characteristics at 3.6 GHz	
Radiation Efficiency (η_R)	-0.17 dB
Total Efficiency (η_T)	-0.30 dB
Gain (G)	7.53 dBi
Directivity (D)	7.70 dBi

Farfield Gain Abs (Phi=0)

Farfield Gain Abs (Phi=90)

Theta / Degree vs. dBi

Frequency = 3.6 GHz
Main lobe magnitude =   12.7 dBi
Main lobe direction =   0.0 deg.
Angular width (3 dB) =   43.2 deg.
Side lobe level = -17.7 dB

Theta / Degree vs. dBi

Frequency = 3.6 GHz
Main lobe magnitude =   12.7 dBi
Main lobe direction =   0.0 deg.
Angular width (3 dB) =   22.2 deg.
Side lobe level = -27.3 dB
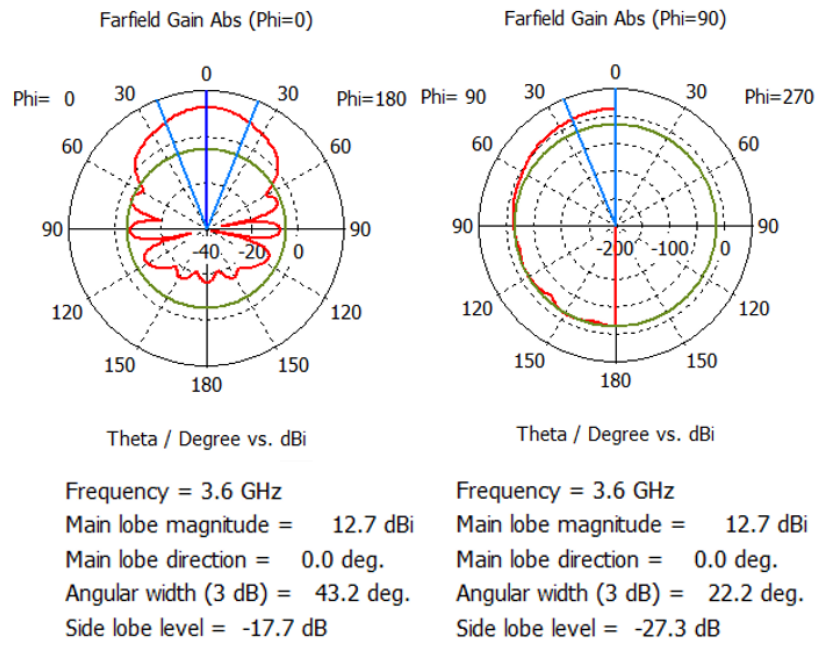
FIGURE 5.14: Miniaturised GAA simulated radiation pattern relative to the monopole.

Farfield Gain Abs (Phi=90)

Farfield Gain Abs (Phi=0)

Theta / Degree vs. dBi

Frequency = 3.6 GHz
Main lobe magnitude =   6.77 dBi
Main lobe direction =   13.0 deg.
Angular width (3 dB) =   29.1 deg.
Side lobe level =   -3.0 dB

Theta / Degree vs. dBi

Frequency = 3.6 GHz
Main lobe magnitude =   7.57 dBi
Main lobe direction =   18.0 deg.
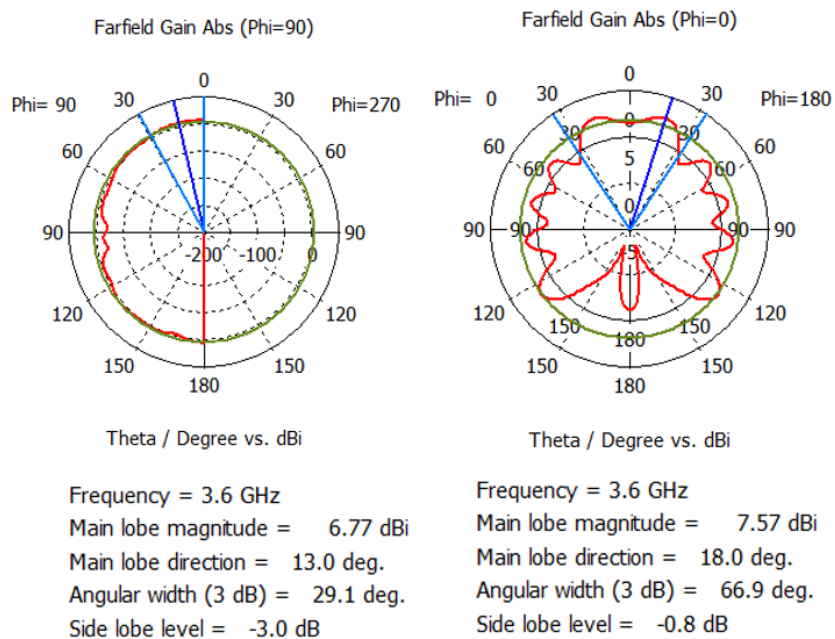Angular width (3 dB) =   66.9 deg.
Side lobe level =   -0.8 dB

FIGURE 5.15: Monopole simulated radiation pattern relative to the miniaturised GAA.

5.2.5 Measurements

Prototyping and the measurement process of the miniaturised antenna was performed in the same manner as the Kraus-grid structure, with the T-match parameter w_b given additional thickness for post-fabrication tuning capabilities. The measurement setup is shown in Fig. 5.16 and subsequently the results of the measurement process are as follows.

FIGURE 5.16: GAA miniaturisation prototype on body-phantom roasted pork.
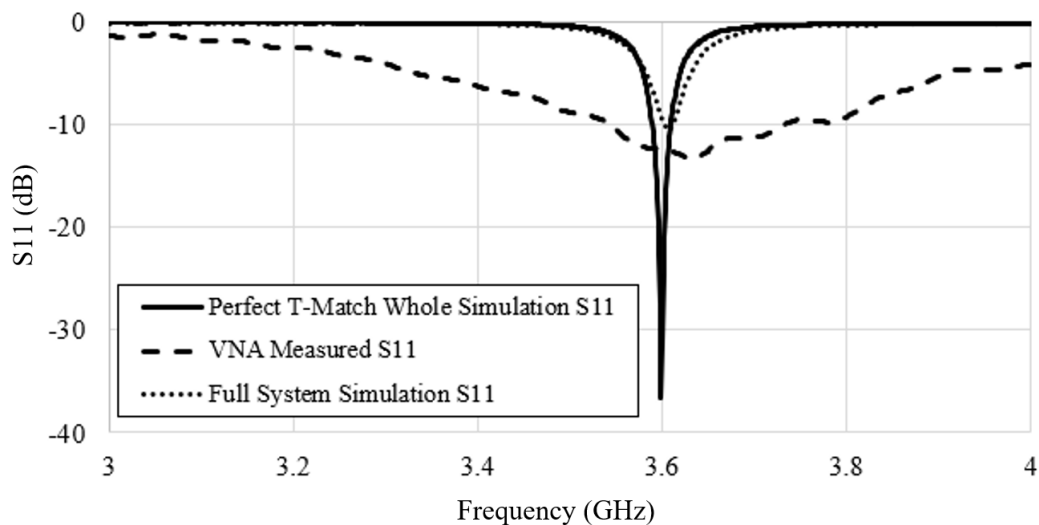

FIGURE 5.17: Simulated and Measured S11-parameters of the meandered half-grid.
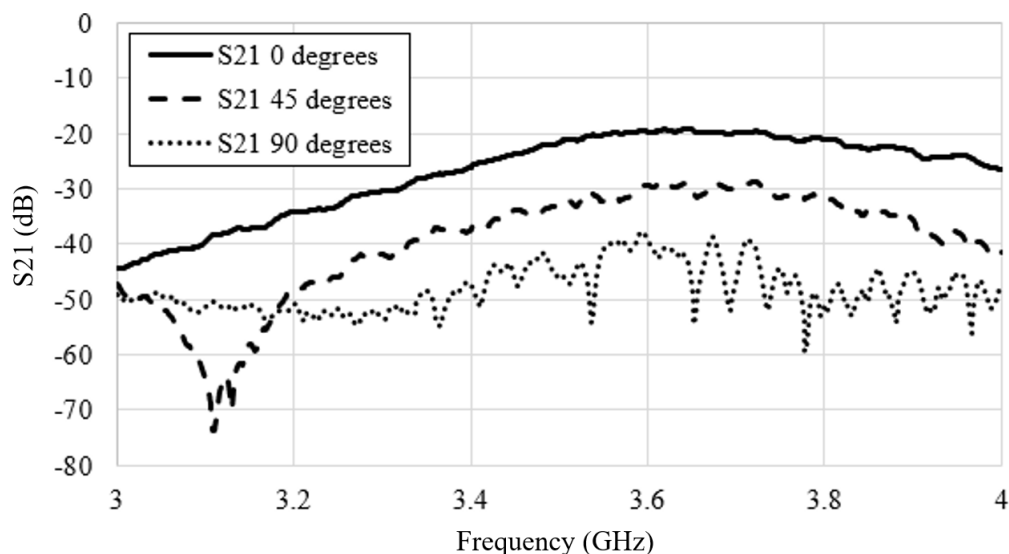
FIGURE 5.18: GAA to monopole measured S21-parameters for relative orientation angles of 0°, +45°, and +90°.
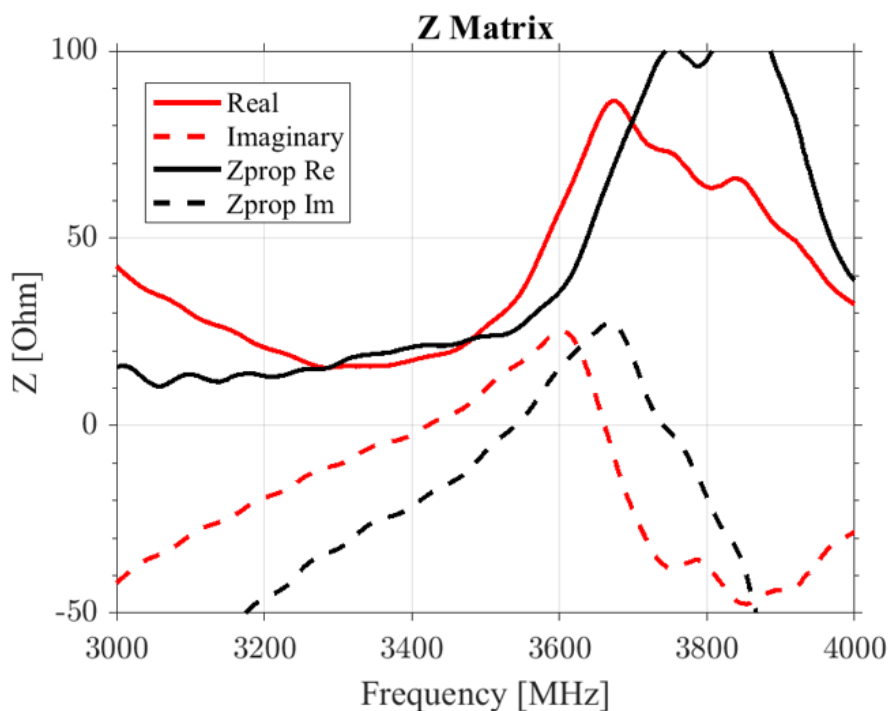

FIGURE 5.19: Measured input impedance of the miniaturised GAA antenna: (Red Line) directly extrapolated from S11, and taking into account the effect of the additional length of the SMA pin (black line).

The measurements presented in Fig. 5.17 and Fig. 5.18 fall in line with what was seen with the Kraus-grid, proving that for the on-body environment, the grid array can be miniaturised without consequence to the radiation performance.

5.3 Twin-Grid

5.3.1 Twin-Grid Rationale

Returning to the GAA topology and considering the antenna in the potential real-life application of transmitting sensor data from the body through a 5G communication link, whilst capable in terms of radiation performance, the structure does not allow for practical incorporation of sensors since the ground plane covers the body. In this iteration of the GAA, the sheet ground plane is instead replaced by a secondary grid array 'reflector' mirroring the top 'driver', allowing for direct access to the epidermis for sensor interrogation. This topology is presented in Fig. 5.20.
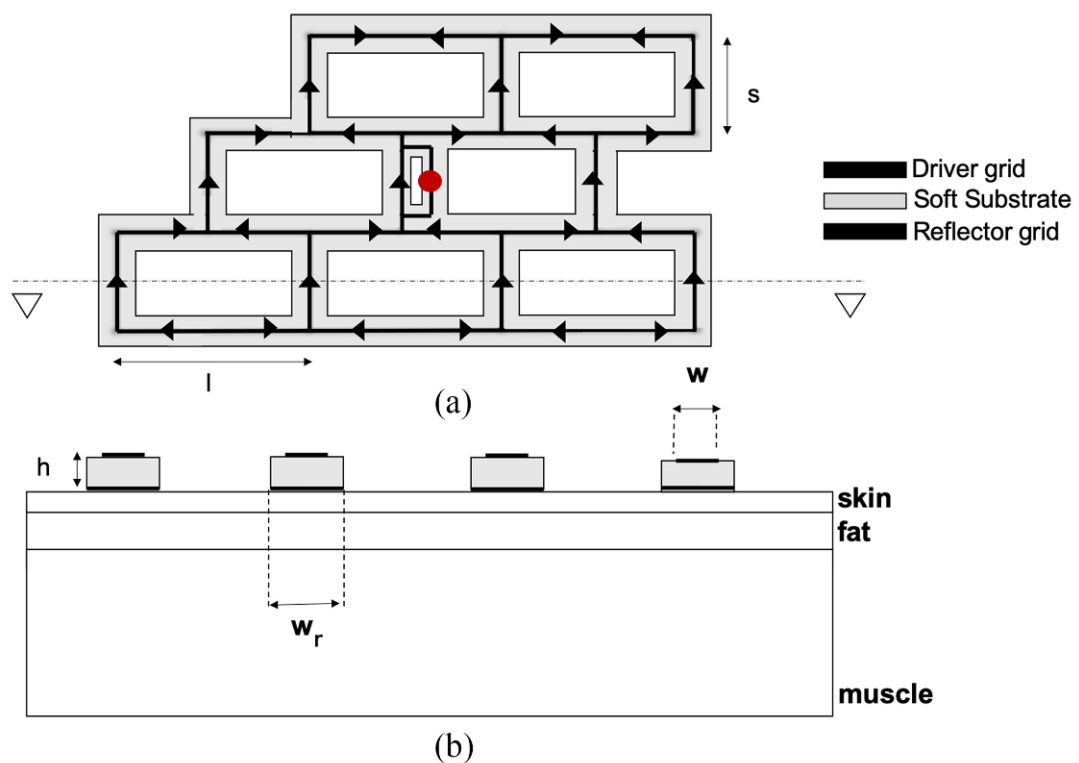

FIGURE 5.20: Schematic representation of the twin-grid antenna array and pattern of currents. Feed is planar and located on the central element through a T-+match impedance transformer. (a) Top view. (b) Section with the three-layer numerical body phantom adopted in finite-difference time-domain simulations (CST Microwave Studio).
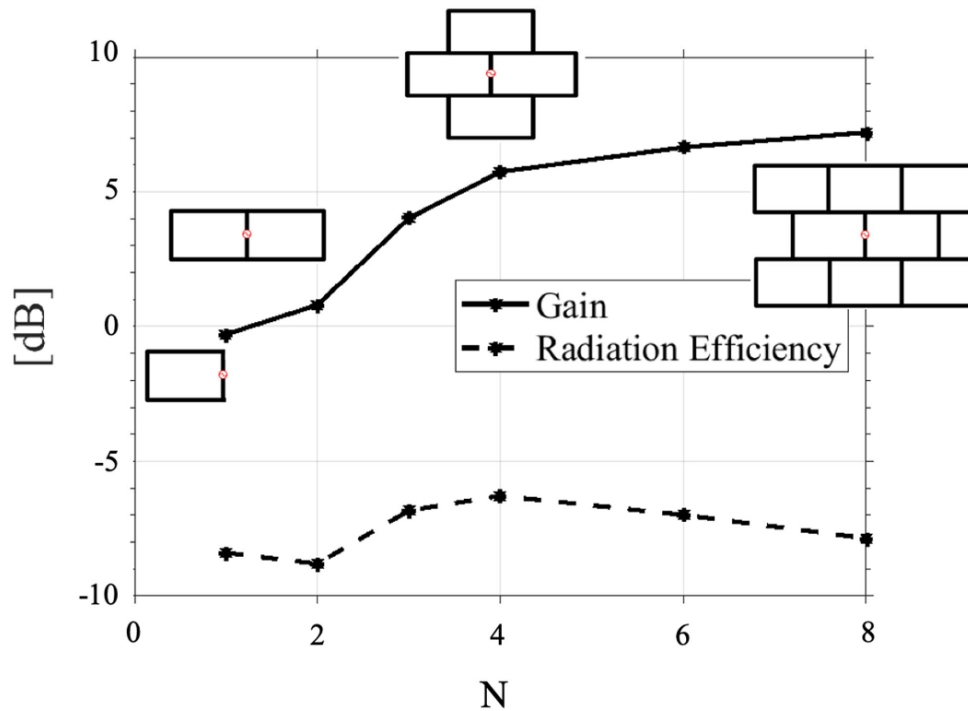
5.3.2 Parametric Analysis Simulations

FIGURE 5.21: Gain and radiation efficiency of the reference twin grid by varying the number of elements N. Efficiency is strongly affected by the radiation losses into the human body, caused by the attenuation of currents on the microstrip lines..

Once again, shown in Fig. 5.21, the array cell count is incrementally increased to find the optimum array size. The starting point is a resonant one-cell layout with parameters h = 2 mm, s = 28.45 mm, l = 56.9 mm, w = 1 mm, w_r = 8 mm, placed on the same 2 mm thick ($\sim \lambda_{wg}/25$, $\lambda_{wg} \approx 56mm$) biosilicone rubber slab. A familiar pattern emerges as the gain increases with the number of elements N (see Fig. 4.5): moving from one cell (a single loop—with two vertical radiators) to eight cells (15 radiators), an improvement of about 8 dB is obtained. Similar to standard grids with continuous ground, the G(N) profile is not linear. Again, an initial increase in the efficiency and gain caused by the increase in the radiation resistance, proportional to the number of vertical elements. Then once more, further enlargement of the grid array passed this point of peak efficiency (equating to a 6dB improvement in gain) causes power dissipation. Therefore, optimal efficiency arises for a grid array of four cells, with a maximum $\eta = 35\%$

(with corresponding gain $G_{max} = 6$ dBi); then, gain slowly improves, thanks to the more directive radiation pattern produced by a larger structure.
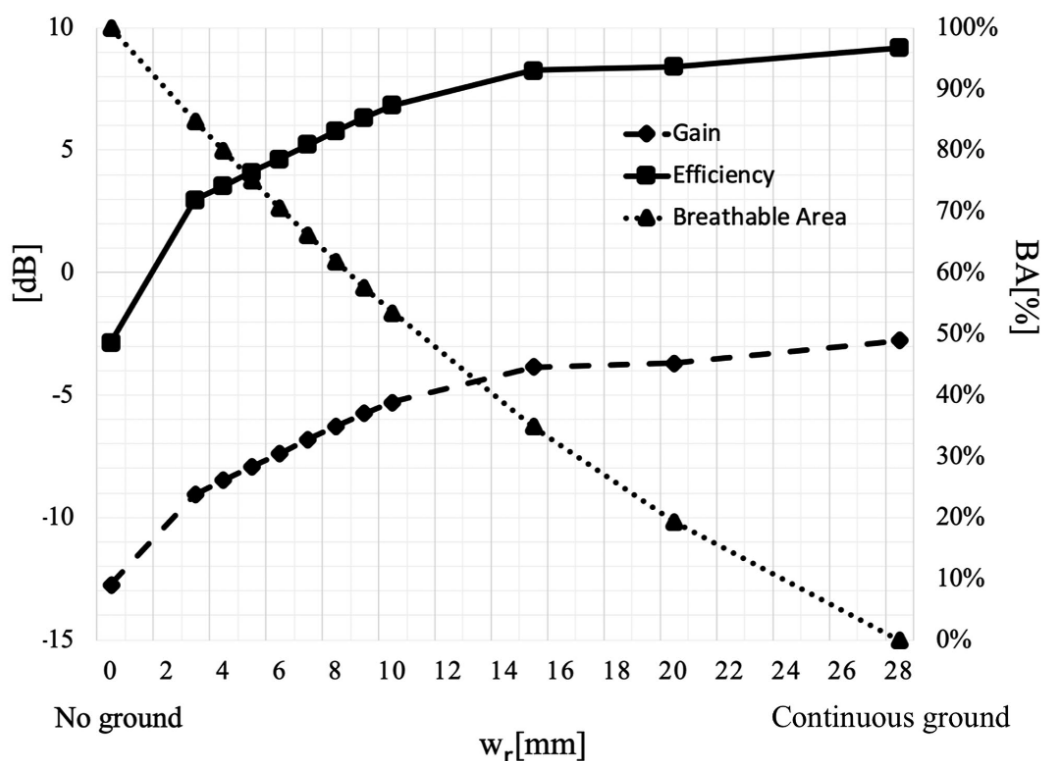

FIGURE 5.22: Gain, radiation efficiency, and breathable area of the four-element twin grid by varying the width of the reflector trace w_r.

Since the ground plane plays a critical role in the performance of any antenna, the level of reduction to apply needs careful consideration as to not too detrimentally affect the performance. Gain and efficiency of the optimal four-element twin-grid array are shown in Fig. 5.22 by varying the trace width w_r of the reflecting grid. As w_r increases, the breathable area $BA\% = [(l - w_r) \cdot (s - w_r)]/(l \cdot s)$ decreases with a better decoupling between body and array and consequently an improvement of both gain and efficiency. The size of the reflector affects the radiation performance especially in the early stages. A reduction of $\sim 15\%$ of the breathable area ($w_r = 3$ mm) with respect to the ungrounded structure (BA = 100%) corresponds to an improvement in gain and efficiency of about 6 dB (more than double read distance with respect to the ungrounded structure). By reducing BA up to 50% ($w_r = 10$ mm), performance can be further improved, with Gmax $\approx 7dBi$ and η = -5 dB. An asymptotic profile is then observed. Overall, for $w_r > 10$ mm, there

is only a modest improvement of the performances at the expenses of bulkiness of the device. Thus, a reasonable choice of the reflector parameter would be $8 \leq w_r \leq 10$ mm.

5.3.3 T-Match

The T-match is once again employed, by acting on the lengths {a, b} (from Fig. 4.7) the input impedance Z_{in} was modified such to match Z_l of 50 Ω. However, unlike the previous iterations of the GAA the T-match was incapable of making a perfect match, settling on $Z_{in} = 53.4 + 0.5 \, \Omega$. So, whilst reducing the ground plane has a manageable affect on antenna performance, consequentially the capability of the matching network is limited. That said, the impedance achieved is tolerable and the final design parameters are listed in Table.5.5.
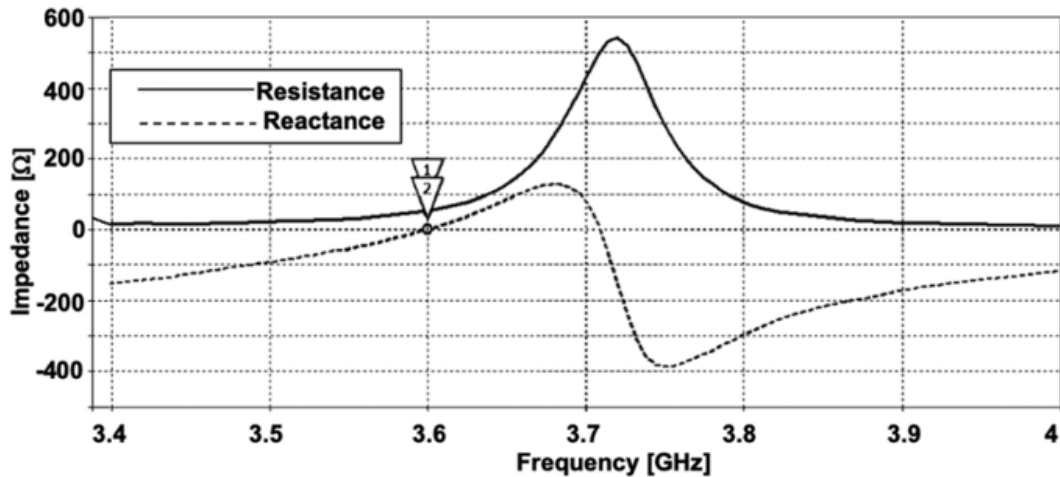
FIGURE 5.23: Simulated input impedance Z_{in} of the four-cell twin-grid array (parameters in Table 5.5). Parallel and series resonances alternate; by acting on the shape factor of the T-match, the antenna can be matched to $Z_l = 50 \, \Omega$.

TABLE 5.5: Parameters of the realized prototypes.

	s	l	h	a	b	w_r	w	w_a	w_b
Twin-grids	28.45	56.9	2	10	8	8	1	1	4
Full Ground	28.25	56.5	2	8	6.8	28	1	1	5

5.3.4 Prototype Simulation

The measurement setup for the eventual prototype was once again simulated, with the structure shown in Fig. 5.24, here the open spaces for potential sensor interrogation can be clearly seen.
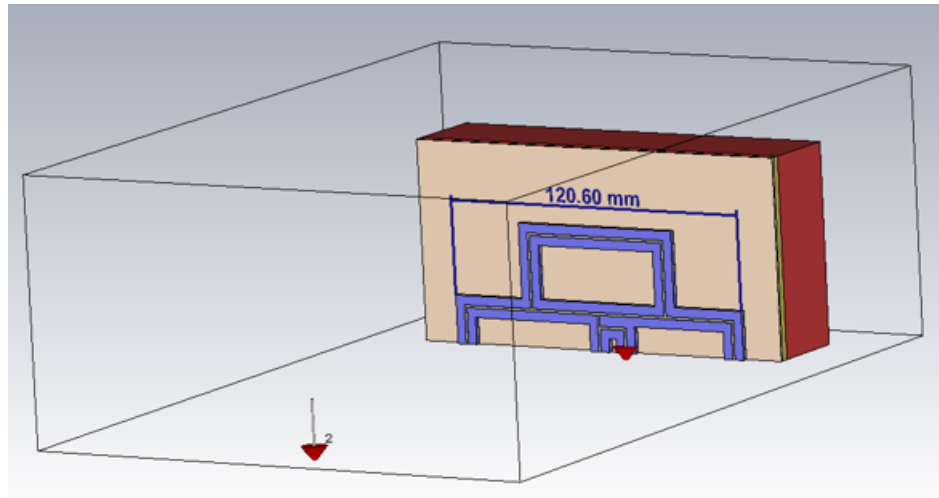

FIGURE 5.24: Twin-Grid GAA simulation adopting image theory.

The S-Parameters are shown in Fig. 5.25, appearing consistent with the previous prototype simulations. However, this simulation does not suffer from a S21, S12 disparity, showing the expected identical response between the two in a balanced system.
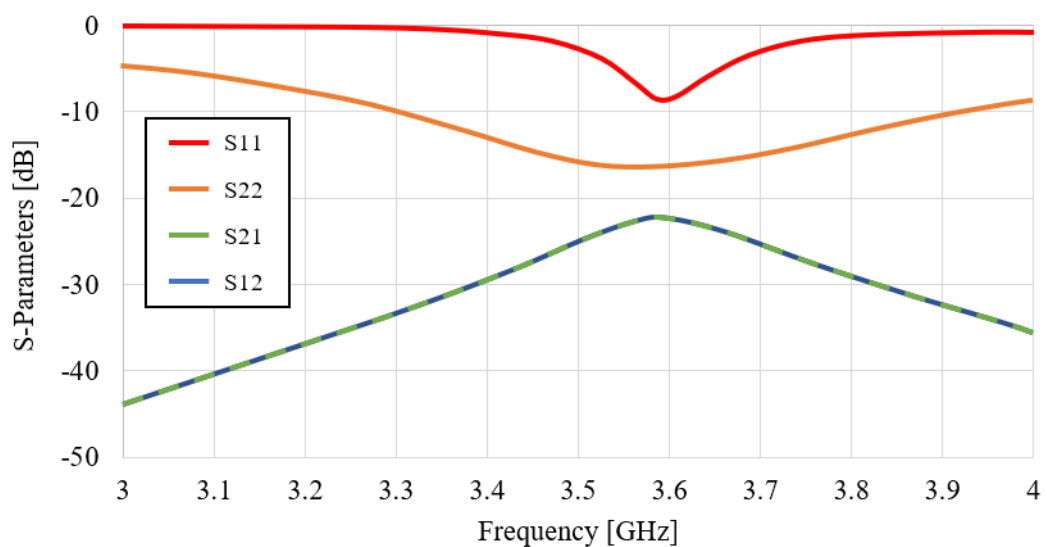

FIGURE 5.25: Twin-Grid GAA and monopole simulated S-Parameter results.

The radiation performances and the radiation patterns of the twin-grid and monopole are shown in Fig. 5.6 and Fig. 5.7, then Fig. 5.26 and Fig. 5.27, respectively.

TABLE 5.6: Twin-Grid radiation results from image theory simulation.

Twin-Grid Radiation Characteristics at 3.6 GHz	
Radiation Efficiency (η_R)	-5.52 dB
Total Efficiency (η_T)	-6.16 dB
Gain (G)	9.38 dBi
Directivity (D)	14.90 dBi

TABLE 5.7: Monopole radiation results from image theory simulation.

Monopole Radiation Characteristics at 3.6 GHz	
Radiation Efficiency (η_R)	-0.13 dB
Total Efficiency (η_T)	-0.25 dB
Gain (G)	7.64 dBi
Directivity (D)	7.77 dBi

Farfield Gain Abs (Phi=90)

Theta / Degree vs. dBi

Farfield Gain Abs (Phi=0)

Theta / Degree vs. dBi

Frequency = 3.6 GHz
Main lobe magnitude =   9.38 dBi
Main lobe direction =   0.0 deg.
Angular width (3 dB) =   25.9 deg.
Side lobe level = -21.7 dB

Frequency = 3.6 GHz
Main lobe magnitude =   9.38 dBi
Main lobe direction =   0.0 deg.
Angular width (3 dB) =   32.4 deg.
Side lobe level = -14.0 dB
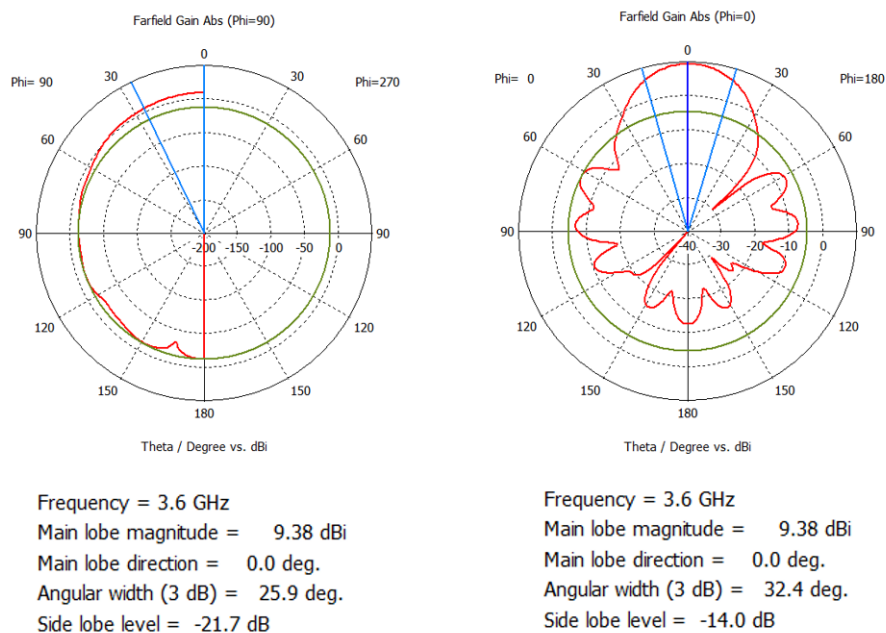
FIGURE 5.26: Miniaturised GAA simulated radiation pattern relative to the monopole.

Farfield Gain Abs (Phi=90)

Theta / Degree vs. dBi

Farfield Gain Abs (Phi=0)

Theta / Degree vs. dBi

Frequency = 3.6 GHz
Main lobe magnitude =   7.23 dBi
Main lobe direction =   10.0 deg.
Angular width (3 dB) =   27.9 deg.
Side lobe level =   -4.3 dB

Frequency = 3.6 GHz
Main lobe magnitude =   7.64 dBi
Main lobe direction =   15.0 deg.
Angular width (3 dB) =   63.8 deg.
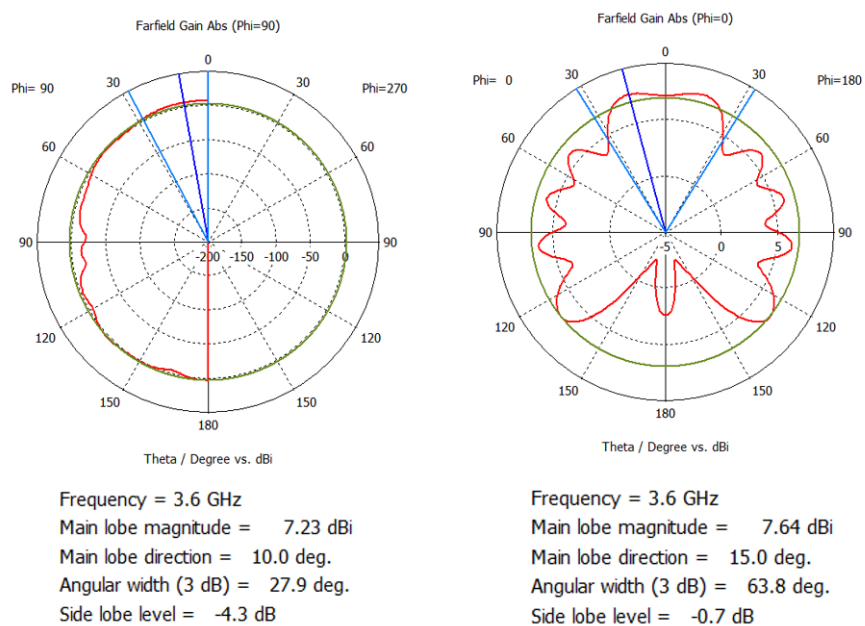Side lobe level =   -0.7 dB

FIGURE 5.27: Monopole simulated radiation pattern relative to the miniaturised GAA.
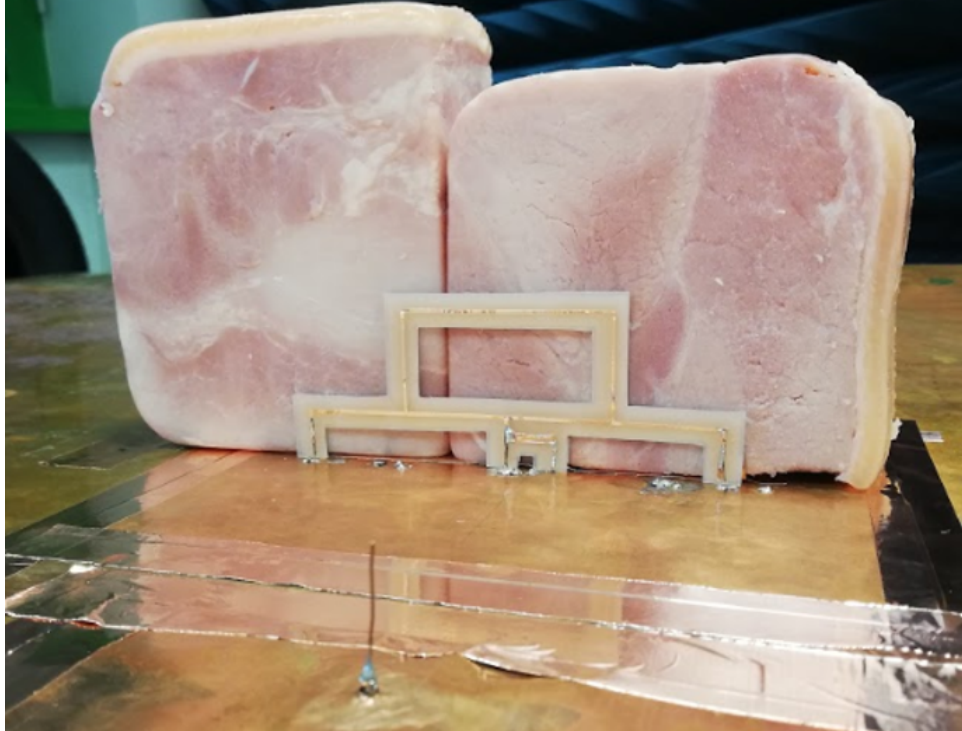
5.3.5 Measurements

FIGURE 5.28: Experimental setup for measuring the S-parameters of half-grid when attached onto a roasted pork phantom.

Once again, exploiting the image theory principle, a planar half-structure was vertically mounted on a large ground plane (1 m × 1 m) and attached onto a cubic body phantom, as shown in Fig. 5.28. The radiation performances of the epidermal antenna were again retrieved by measuring the S12 (since, $|S12|^2 \propto G$). The T-match did require slight manual tuning to 3.6 GHz by acting on the trace w_b to compensate for uncertainties in realization and phantom. Consequently, a good matching was obtained (see Fig. 5.29), in agreement with the simulations. Bandwidth BW -10dB = 8.6% is larger than the expected one, probably due to additional losses in the phantom, glue, and coaxial cables. The measured S12 of the structure with the grid reflector is approximately 3 dB lower than the one of the full ground layout. Again, rotating the grid antenna with respect to the monopole probe, $|S12(\phi)|^2$ has been evaluated also for different angles ϕ, in agreement with the simulation. The radiation pattern is shown in Fig. 5.30, a maximum broadside gain G_{max} = 6 dBi (BWV, -3dB = 54.6°, BWH, -3dB = 34.5°) and a radiation efficiency η = -5.5 dB is achieved.
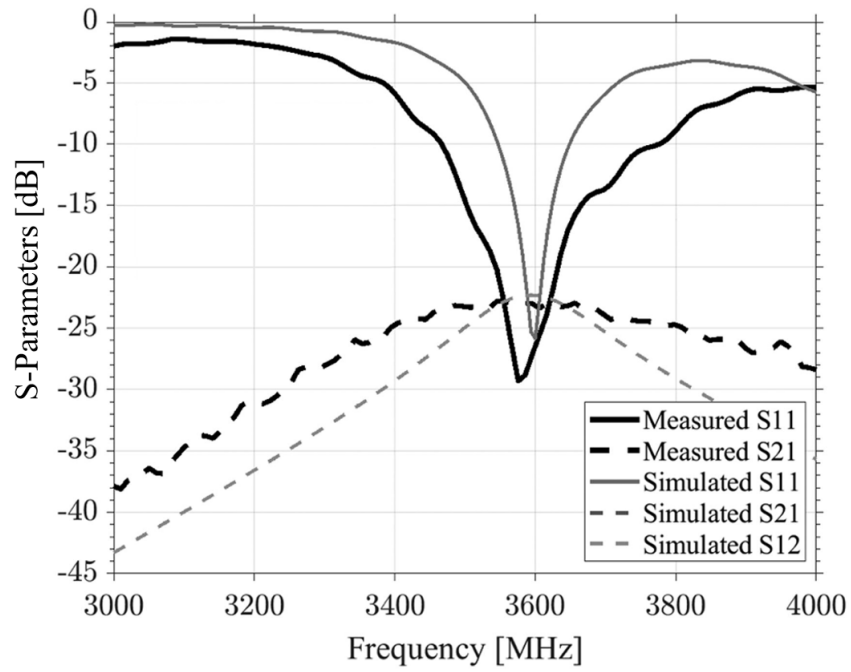
FIGURE 5.29: Simulated and measured S-parameters of the half twin-grid array sourced by a test monopole, from setup shown in Fig. 5.28.
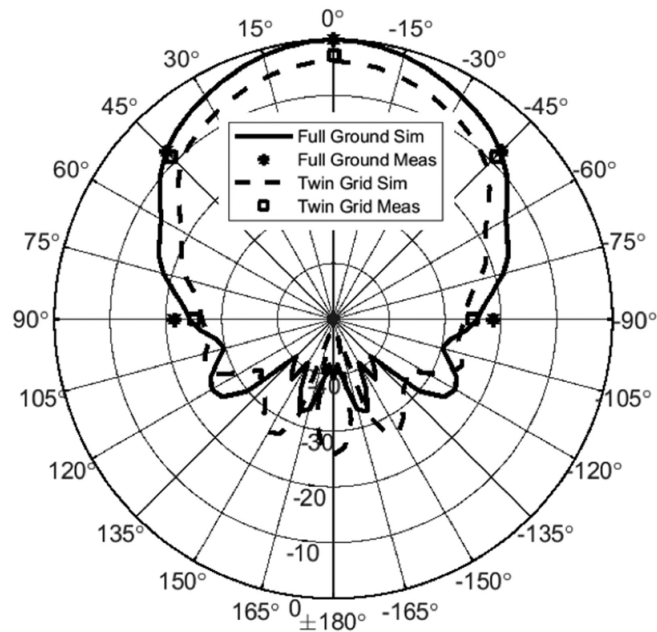

FIGURE 5.30: Measured $S12^2$ on the horizontal plane overlapped on simulated data. Data normalized with respect to the full ground maximum.

5.4   Conclusion

This chapter presented a soft, miniaturised grid-array antenna for on-body applications in the 5G S-band, achieved through adopting the technique based on the work of Nakano, meandering the non-radiating horizontal trace lines, resulting in a 25% size reduction whilst showing negligible performance differences after miniaturisation. That said, the radiation results relative to the Kraus grid were not identical, obtaining a wider radiation beam and narrower bandwidth. Next, a newly designed breathable 'twin-grid' antenna was presented, simulated and fabricated for on-body epidermal applications for the potential incorporation of sensors that directly interact with the skin. The 'twin-grid' reduction in ground area resulted in an unavoidable loss in performance relative to the Kraus grid and miniaturised versions, seeing a gain value of 6 dBi and efficiency -5.5 dBi. By assuming the current UHF RFID features (emitted power and IC sensitivities) valid in the S-band, read distances greater than 3 m are expected at a minimum, even with a thin reflector. Such distances could be suitable to continuously track the vital signs of a user within a room, thus greatly extending the current performances of UHF epidermal systems. Due to the array dimensions, even in the miniaturised case where the antenna takes up ~ 100 x 80 x 2 mm^3, the antenna would be most suitable to be applied on larger body regions such as the abdomen, shoulder, and back. Finally, it is worth noting the twin-grid array configuration is a body dependent match, that is, whilst the grounded versions of the grid array may suffer slight de-tuning when detached from the body, the twin-grid generates a broadside radiation only when it is placed on the skin, in the free space the reflector grid is ineffective and a bidirectional pattern is produced.

Chapter 6

Folded Comb-line Array for Healthcare 5G-RFID-based IoT applications

This chapter presents the folded comb-line array, a tangential antenna topology of the grid array antenna design, operating through the same fundamental current characterisation. As the name suggests, the array extends along a single axis 'line' from which the vertical radiators periodically extend. Here for the first time, the horizontal traces are folded for greater miniaturisation than in other monolithic arrays. Consequently, bringing the alignment of the horizontal traces closer to that of the radiating vertical traces improves radiation performance.

6.1 Introduction

Healthcare Internet of Things (H-IoT) is currently providing the backbone of the emerging 'Precision Medicine' initiative by means of sensors connected to our bodies linked to every-day devices such as smartphones and smart watches [120]. In recent years, Radiofrequency Identification (RFID) technology, especially in the UHF band, has been enabling this technological framework [121]. However, the limited bandwidth and bit-rate at UHF, combined with the need for devoted readers to interact with the sensors has stimulated the exploration of new backscattering-based monitoring platforms [122]. Adopting 5G into the H-IoT would hence encourage the development of innovative smart-healthcare devices [123], especially by taking advantage of the envisaged improvement in communication standards and interoperability between platforms [124]. A single loop antenna directly adhering to the skin could be readable at up to 1 m [125]. Multiple elements arranged in an array configuration could offer robust coverage in a medium-sized room [94], but at the cost of increasing complexity, with the need to host a beam forming network that could impact on size, fabrication and wearability. To simplify the layout, monolithic arrays such as the Krauss Grid [118] have been proposed for this application. In this layout, the radiating and transmission line elements are limited to a singular, easily fabricated layer and the array can be fed through only a single port. However, whilst the achieved radiation performances would be fully compliant with a medium-range body-centric communication link, the resulting size is large and cumbersome. A particular embodiment of a monolithic array is the comb-line [126]. Comb-line arrays are highly efficient radiators widely adopted for mm-wave automotive radar applications [127] and on-chip integrated architectures [128]. They can be seen as a simplified version of the Krauss' grid [126], in which the transmission lines between the top of the vertical radiating elements are removed with benefits in terms of bandwidth and cross-polarization level. Tapered radiating microstrip elements are generally adopted [129], sometimes with sequential rotation for achieving circular polarization [130], while multiple sub-array configurations can be exploited for MIMO applications

[131]. Starting from a comb-line antenna, this chapter proposes a 3.6 GHz miniaturized monolithic array for wearable body-centric communications. The work in this chapter was carried out at the University of Roma Tor Vergata and The University of Kent and has been published in [132] and [133].
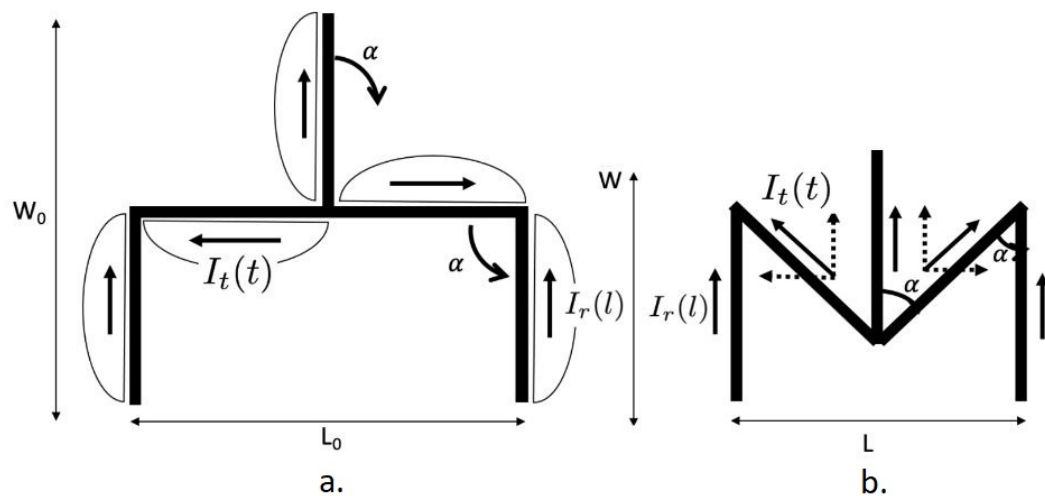
6.2 Parametric Analysis

FIGURE 6.1: Schematic representation of the folding effect on the pattern of currents and on the antenna size. Segments length $l \approx t \approx \lambda_{wg}/2$ supports standing waves. The current amplitude has a peak every half-wavelength, with nulls on the nodes and on the extremities of each element.

As described with the grid-array antenna in Chapter 4, the comb-line antenna operates the same fundamental current pattern. Radiating ($\lambda/2$) vertical components are periodically separated ($\lambda/2$) horizontal tracks. The resultant current phases on the vertices combine to produce a linearly polarized and broadside radiation beam, whilst the horizontal currents oppose each other in phase, thus cancelling. Similar to the grid array antenna (and other monolithic arrays), the main limitation of the comb-line, especially at lower frequencies and for wearable applications, is the wide surface area caused by the presence of transmission line $\lambda/2$ segments which are required to enforce the proper pattern of current to the radiating elements. Miniaturization of these monolithic antennas is typically achieved by meandering the conductors, such as to reduce the physical area of the structure while keeping

the electrical area unmodified, as explored in Chapter 5. However, meandering produces additional transmission-line segments in which currents with opposite phases are placed in close proximity. Such meandered portions do not contribute to radiation but do increase losses, especially in wearable applications due to the close proximity to the lossy human body. Hence, it is electromagnetically penalizing for the antenna efficiency to miniaturize the structure through meandering.

The proposed layout achieves a greater level of miniaturization than the 'cell' antenna topology through a better exploitation of the transmission line segments in terms of shape and current distribution, whilst maintaining high radiation efficiency. This is achieved by folding the horizontal elements with respect to the vertical elements (represented by angle α in Fig. 6.1), the transmission line current on the folded sections can be imagined as two orthogonal components (represented by $I_t(t)$) of which the vertical component is aiding the radiation performance. From this, two competing effects arise and impact on the radiation efficiency; the improved antenna-mode structure and the electromagnetic coupling between close radiating elements.

Much like the grid array antennas of the previous chapters, the comb-line comprises of a microstrip array placed on a dielectric slab, as shown in Fig. 6.2. Once again, for the on-body application, it is preferable for the dielectric substrate to be low loss, flexible, and lightweight to enable comfortable placement on the curved surfaces of the human body. Similarly to the description in Chapters 4 and 5, a comb-line array is resonant when designed such that: the currents $I_r(l)$ on the N vertical elements (with length $l \approx \lambda_{wg}/2$) are in phase, whilst the currents $I_t(t)$ on the $T = N$ - 1 guiding segments ($t \approx \lambda_{wg}/2$) are piece-wise in opposite phase (Fig. 6.1.a). The array is fed in the middle of the central vertical element through the dielectric slab and backing ground plane. λ_{wg} is the guided wavelength [134] at the centre frequency (f_0) of operation, which is evaluated by considering the microstrip width w and the thickness h of the substrate that separates the comb-line from the ground plane [128]. A proper choice of the dielectric substrate in terms of complex permittivity $\bar{\epsilon}$ and thickness h leads the microstrip lines to not have a bound field and consequently they can serve as radiating elements [135]. Radiation
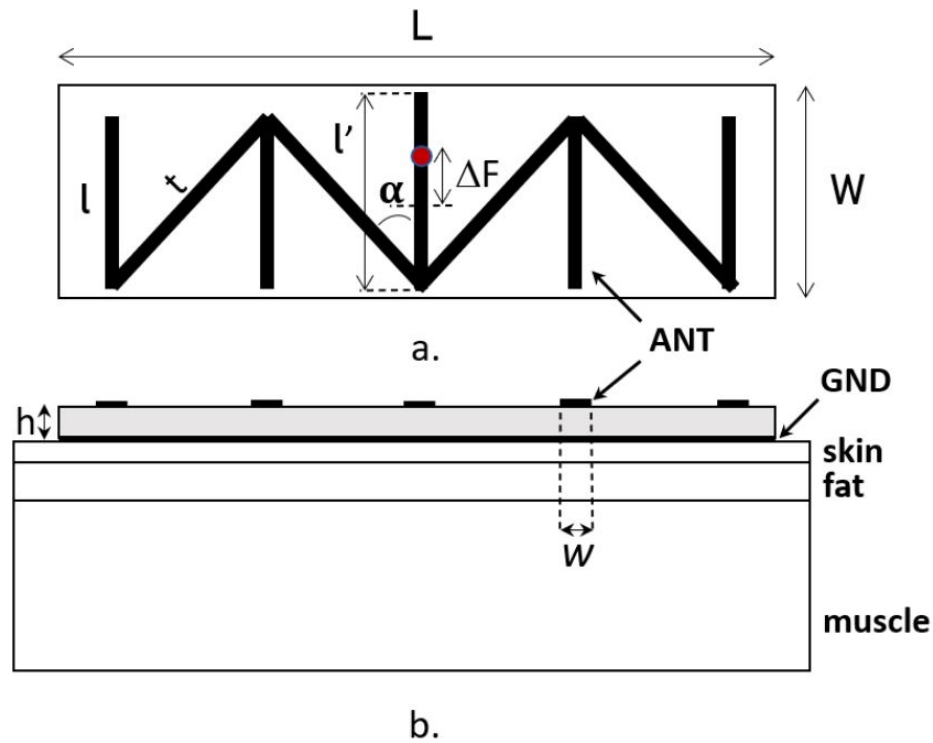
FIGURE 6.2: Schematic representation of the folded comb-line antenna. Feed is shown as a red dot located at ΔF with respect to the midpoint of the central element a) Top view; b) Side view with the three layer numerical body phantom adopted in FDTD simulations (CST Microwave Studio).

is sustained only by the vertical currents, since radiation arising from the horizontal guiding lines mutually cancel. Except for edge effects, there is no radiation in the rear direction. As such, the unfolded version (Fig. 6.1 (a)) does not efficiently exploit the available space, since almost half of the conductors $((N - 1)/(2N - 1)$, i.e. the horizontal elements) do not contribute to the radiation but instead produce resistive losses. By acting on the folding angle α the mutual position between the elements changes and consequently so does the current distribution. Bringing the orientation of the previously horizontal track more in-line with the radiating elements, a vertical current component $I_V^t(t) = I_t\cos\alpha$ is generated by these oblique elements (Fig. 6.1 (b)). Thus, depending on the folding angle α, additional current elements will sum in phase and the radiation will be enhanced and the efficiency improved. Furthermore, the folding of the horizontal strips produces miniaturization of both external sizes $L = L_0\sin\alpha$ and $W = W_0(1 - 1/2\cos\alpha)$, where W_0 and L_0 are the width and length of the unfolded structure

($\alpha = 90°$), respectively, therefore a better exploitation of conductors and available area is achieved.

The proposed folded comb-line (Fig. 6.2 (a)) offers two degrees of freedom for optimizing size and radiation performances and two additional independent parameters for tuning the input impedance. The former are the number N of radiating elements and the folding angle α, whilst input impedance can be modified by acting on the length of the central segment l' and on the position ΔF of the feeding point with respect to the middle of the central element. The folded array is hereafter parametrically investigated. Analysis has been carried out through the FDTD method (CST Microwave Studio). Simulations include a $150\times150\times h$ mm^3 3-layers planar body phantom [94] (Skin $h = 1$ mm, $\epsilon_r = 36.92$, $\tan \delta = 2.08$ - Fat $h = 3$ mm, $\epsilon_r = 5.16$, $\tan \delta = 0.16$ - Muscle $h = 31$ mm, $\epsilon_r = 51.32$, $\tan \delta = 2.65$ shown in Fig. 6.2.b).
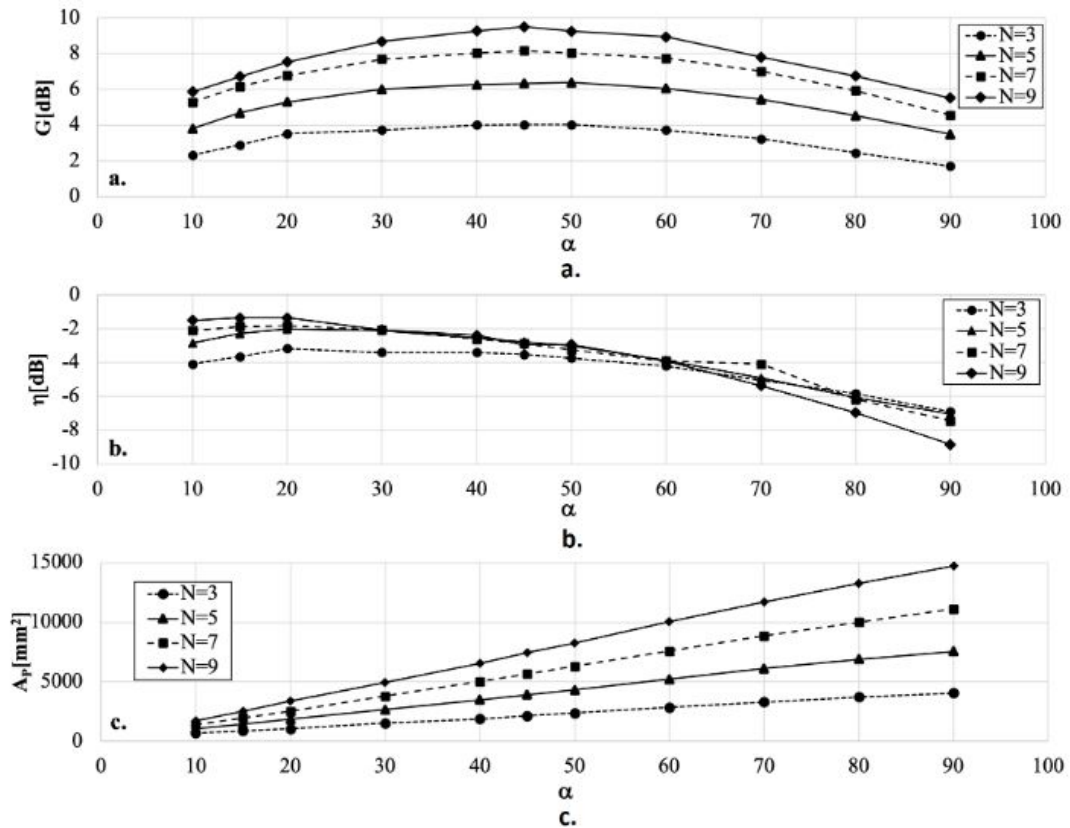

FIGURE 6.3: Gain (a), radiation efficiency (b) and physical area (c) of the folded comb-line by varying the folding angle α and the number of elements N. Here $t = l = 28.55$ mm, $w = 1$ mm, $h = 1$ mm, as defined in Fig. 6.2.b.

Starting from the 3-element unfolded layout, the number of vertical elements N and the folding angle α were progressively modified. Maximum gain G, radiation efficiency η and physical area $A_p = \text{W} \cdot \text{L}$ are shown in Fig. 6.3. As the number of elements in the array increases, so does the gain (Fig. 6.3 (a)). A maximum exists, regardless of the number of elements when $\alpha = 45°$. However, since efficiencies remain almost constant (shown by overlapping curves in Fig. 6.3 (b), in the $\alpha = 30°$- $60°$ range), this effect is attributed to an increase in directivity caused by the enlargement of the antennas physical area with N, as visible in Fig. 6.3 (c).

The study found that the folding angle affects the radiation performance. Highly folded layouts compensate for the detrimental effect of the coupling with the benefits produced by the additional vertical current elements, causing efficiency to increase. An optimum $\eta \sim$ -2 dB exists for $\alpha = [15°$- $40°]$, corresponding to a spacing $s = t \cdot \sin(\alpha)$ between vertical elements, ranging between 7.38 mm and 18.3 mm. Further enlargements of the angle α reduces the vertical current components and increases the distance between the radiating elements, hence resulting in a reduction of the overall radiation efficiency and in an increase of overall size.
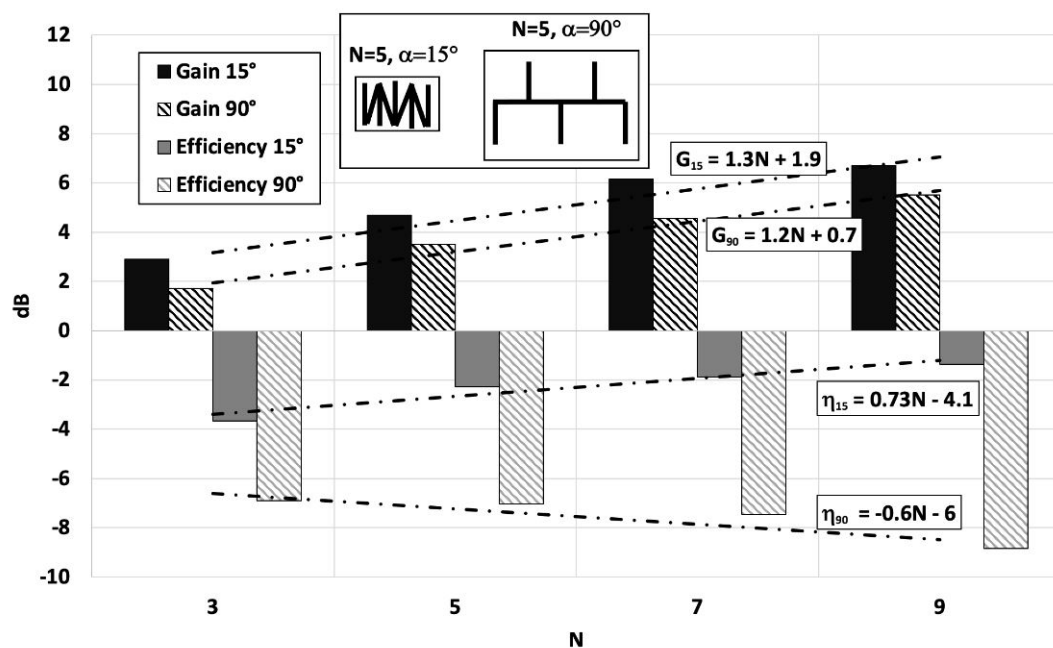

FIGURE 6.4: Gain and radiation efficiency of the folded and the unfolded comb-line arrays ($\alpha = 15°$, $90°$) by varying the number of radiating elements. Dashed lines indicate the linear regressions. The area of the folded array is approximately 20% of the unfolded one, as in the inset.

The beneficial effects of the folding on the radiation performance are visible in Fig. 6.4, where the unfolded conventional layout ($\alpha = 90°$) is compared with a highly folded layout ($\alpha = 15°$). Regardless of the number of elements, the gain and efficiency of the folded array are higher than the unfolded version. Furthermore, the folded layout better exploits the radiating elements since its efficiency increases at $0.73N$. On the contrary, the unfolded layout suffers with the increase in radiating dipoles, with a decreasing trend in efficiency (scaling factor of $\eta_{90} \propto$ -0.6N).
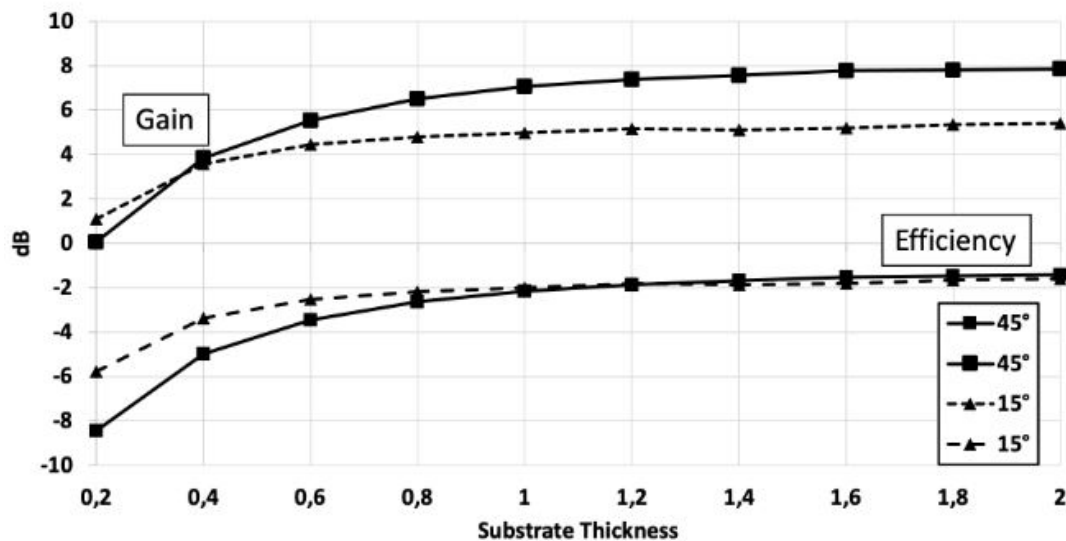

FIGURE 6.5: Gain and radiation efficiency of the optimal folded comb-line array ($\alpha =15°$) over varying substrate thicknesses.

From folding angles considered in Fig. 6.3, two possible optimum configurations can be defined: i) $\alpha = 45°$ offers the maximum gain, ii) $\alpha = 15°$ has maximum efficiency and minimal physical area. For these configurations, the effect of the substrate thickness h is numerically investigated in Fig. 6.5. Regardless of the folding angle α, gain and efficiency improve with an increasing h before reaching a state of insensitivity to the substrate thickness, from about $h > 0.5$ mm.
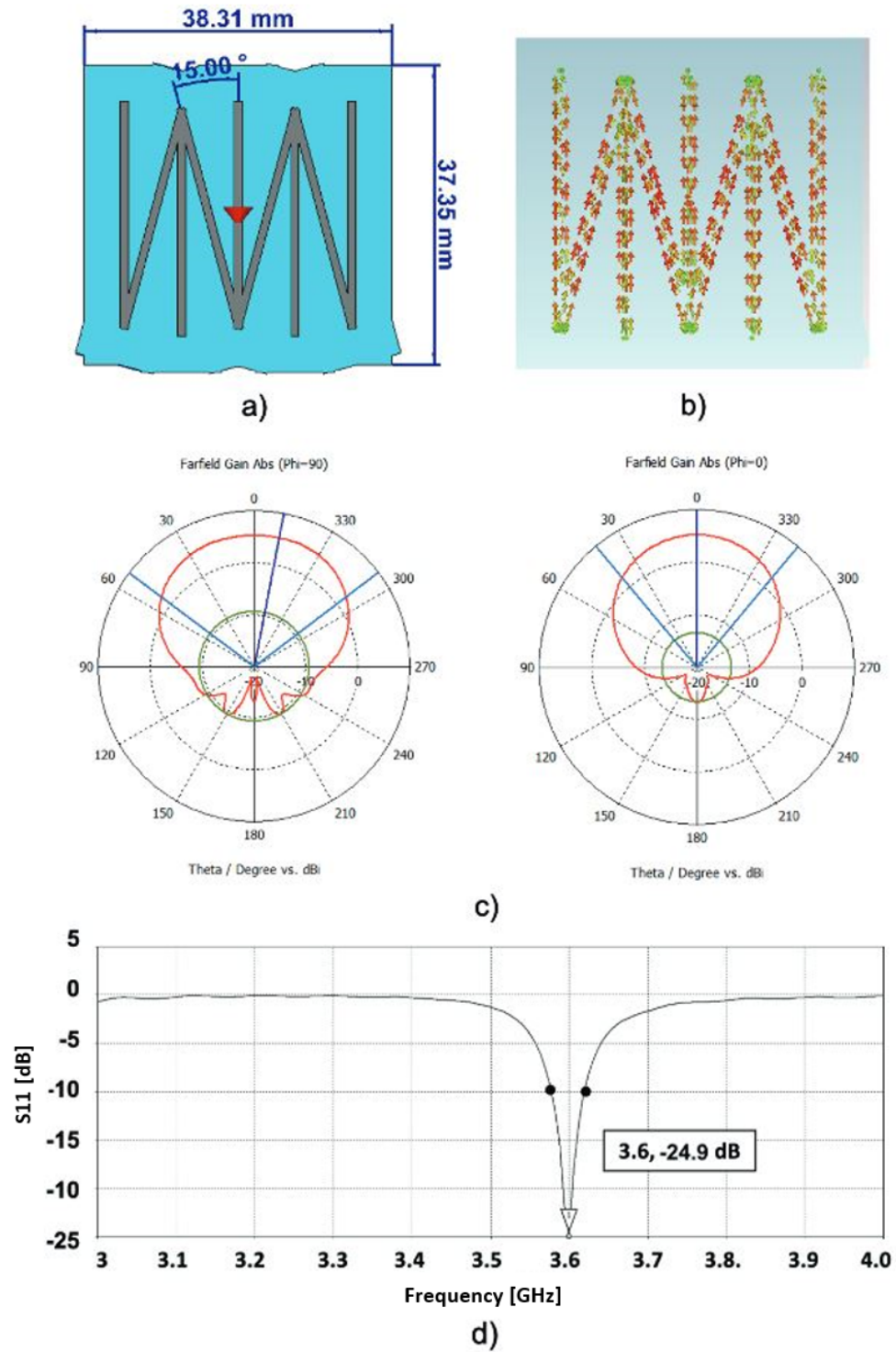
FIGURE 6.6: a) Layout of the optimal folded comb-line array. b) Pattern of current at resonance, c) Radiation pattern, d) Return Loss S_{11}.

Of the two antenna configurations, $\alpha = 15°$ is seen to be a good compromise between miniaturization and activation distance, corresponding to $[L,\ W] = [38, 37]$ mm. The layout is visible in Fig. 6.6 (a), together with the pattern of currents 6.6 (b), the radiation pattern 6.6 (c) at the operative frequency $f_0 = 3.6$ GHz and the reflection coefficient 6.6 (d). The antenna is well matched to 50 Ω, with a bandwidth of 42 MHz. Polarization is linear and vertically oriented. A read distance d $\approx$ 4 m is compliant with typical room size and can be achieved thanks to a broadside maximum gain of 5.5 dB.

As a benchmark, a 40×40 mm^2 microstrip-fed patch has been simulated in the same conditions (1 mm Eccostock® FlexK as substrate and same body phantom, as described for Fig. 6.2). Results are summarized in Table 6.1, together with a 3.6 GHz groundless loop antenna [136] and the twin-grid from Chapter 5. The radiation performances ($G_{max} = 5.5$ dB and $\eta = $ -1.8 dB) are similar to the ones offered by the patch, and sensibly better than the twin-grid array, although with extremely reduced size and halved thickness. Perceptible improvements in terms of wearability are hence expected. The proposed antenna is then larger than the groundless loop (loop presented in Table 6.1) when placed in direct contact with the skin (through a thin bio-compatible membrane of 0.135 mm), but with almost 10 dB better gain.

TABLE 6.1: Parameters and performance of the optimal layout compared with other 3.6 GHz antennas

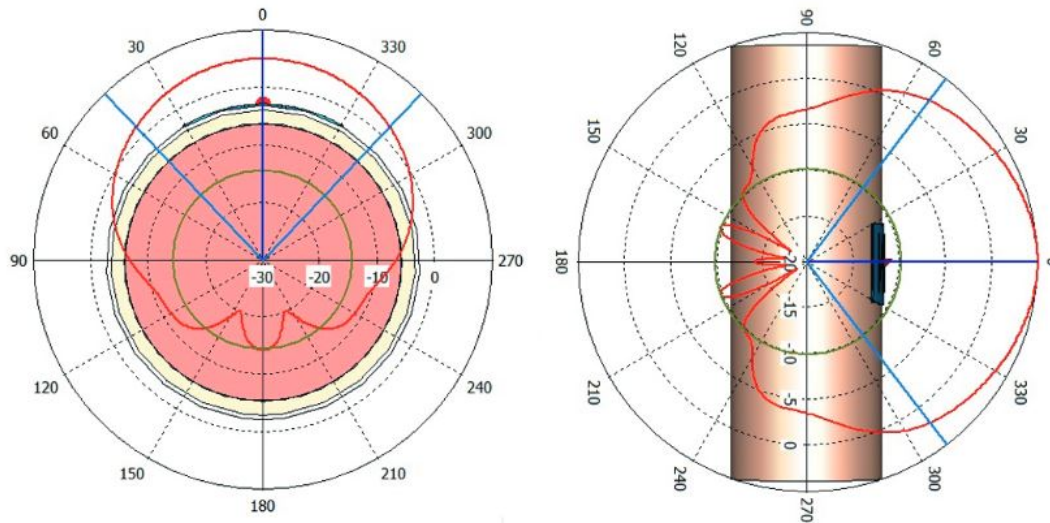|	Topology	Substrate	Thickness (mm)	Dimensions (mm × mm)	G_{max} (dBi)	η (dBi)
This Work	$\alpha = 15°$	Eccostock® FlexK	1	39×38	5.5	-1.8
This Work	Patch	Eccostock® FlexK	1	40×40	5.4	-2
[131]	Loop	PET	0.135	20×20	-5	-11
Chapter 5	Twin-Grid	Bio-Silicone	2	120×100	6	-5.5

FIGURE 6.7: Simulated radiation pattern of the antenna bent over a human arm with radius 40 cm.

Finally, a preliminary evaluation of the radiation performance when the antenna is bent over an arm was conducted, with the results visible in Fig. 6.7. Despite the array configuration, the radiation pattern appears uniform in the entire half space, with a vertical beamwidth of 107° and a horizontal one of almost 90° , hence assuring a robust communication link regardless the body orientation.

6.2.1 Input Impedance

Starting from $[l,\ t] = \lambda_{wg}/2$, the length of the segments can be changed such to make the antenna resonant and to obtain the proper pattern of current as in Fig. 6.1. To tune the antenna to a particular input impedance, two additional parameters are considered; the length of the central vertical dipole l' and the position of the feeding point ΔF with respect to the center of the dipole. Especially for small variations of the length, the former mainly impacts on the resonant frequency and hence on the imaginary part of the input impedance, while the latter acts on the real part (Fig. 6.8 and Fig. 6.9).
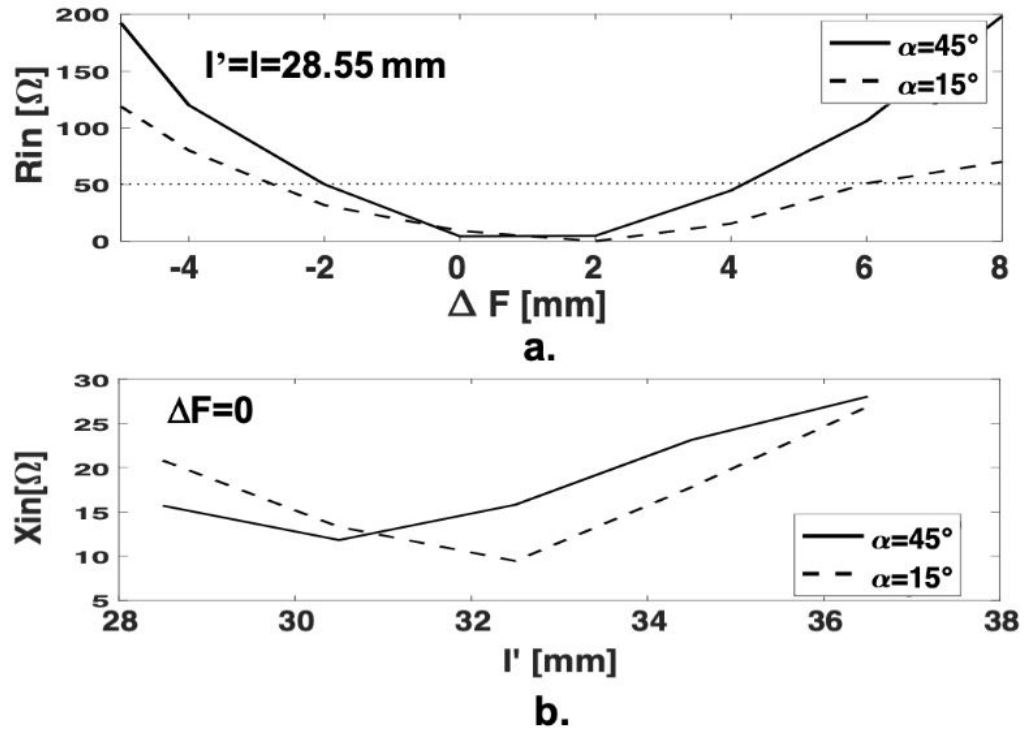
FIGURE 6.8: Input impedance Z_{in} versus the feeding position ΔF (a) and the length of the central element l' (b) $N = 5$ array.
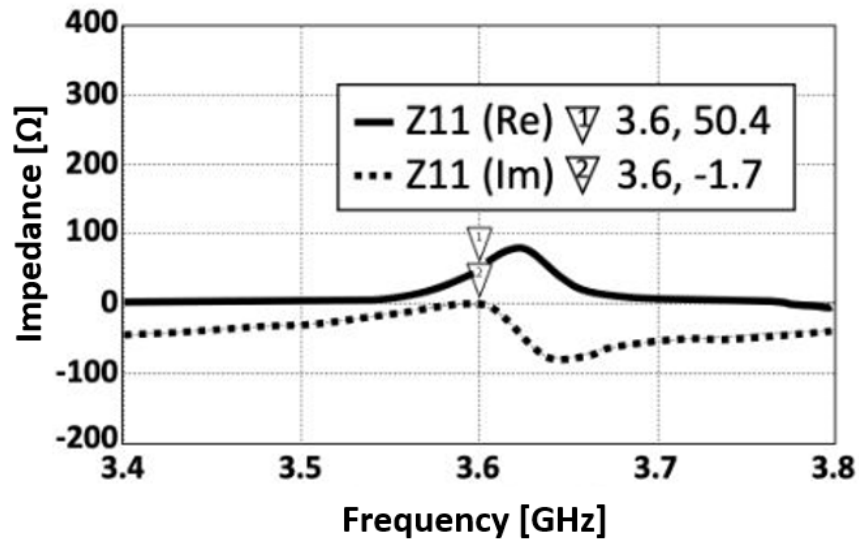

FIGURE 6.9: Simulated input impedance of the $N = 5$, $\alpha = 15°$ folded combline. Standing waves on each segment are clearly visible.

6.3 Prototyping and Measurements

The folded comb-line structure was fabricated by exporting the CST topology for copper etching on the chosen substrate of AstraMT77, shown in Fig. 6.10.

FIGURE 6.10: Folded comb-line prototype, copper etched on to AstraMT77 substrate.

Using the simulation as guide, a hole was drilled through the ground plane 8 mm from the end of the central element to allow the SMA pin to be passed through and soldered either side, as shown in Fig. 6.11.
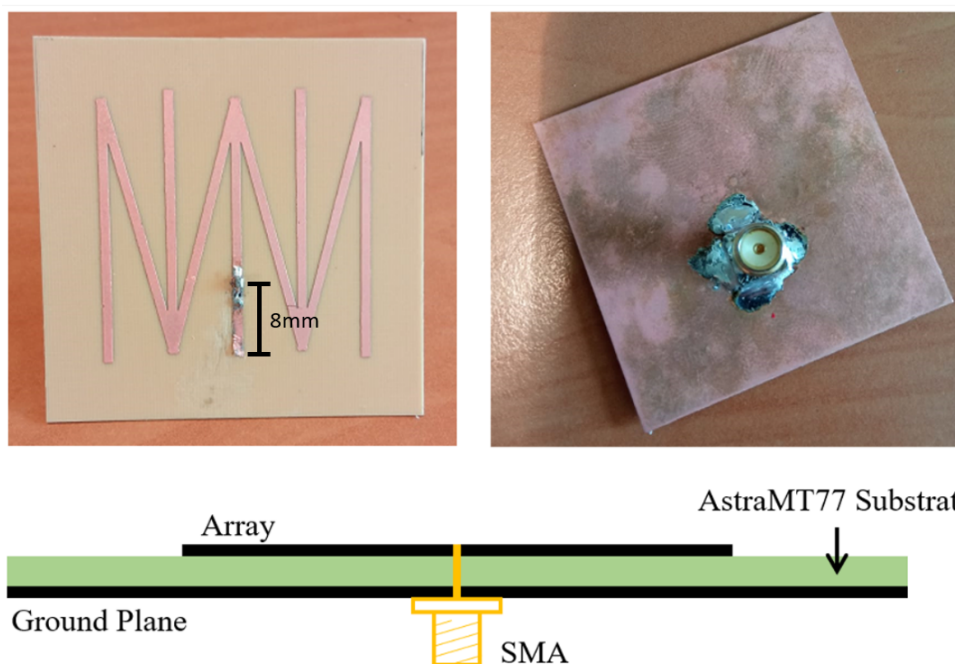

FIGURE 6.11: Folded comb-line with SMA attached.

The S_{11} was measured by a vector network analyzer (HP 8517A) with the antenna attached onto a cubic body phantom (cooked pork with estimated parameters ϵ_r = 40 and σ = 2 S/m). To reduce the impact of the cable, it was passed through the phantom and then connected to the VNA behind. The full measurement set up is shown in Fig. 6.12.
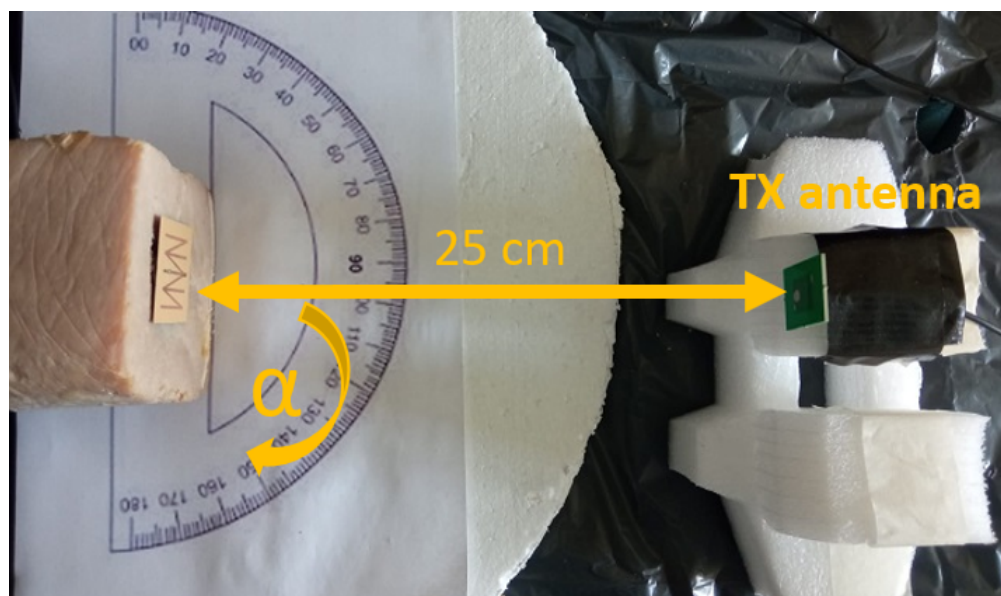

FIGURE 6.12: Measurement Setup, with FCL antenna hosted on body phantom (roasted pork).

The initial S_{11} measurement showed a deviation from the intended frequency by 0.66 GHz, shown in Fig. 6.13. This difference from the simulation is likely due to the variation in the body-phantom material properties and additional losses in the cables.

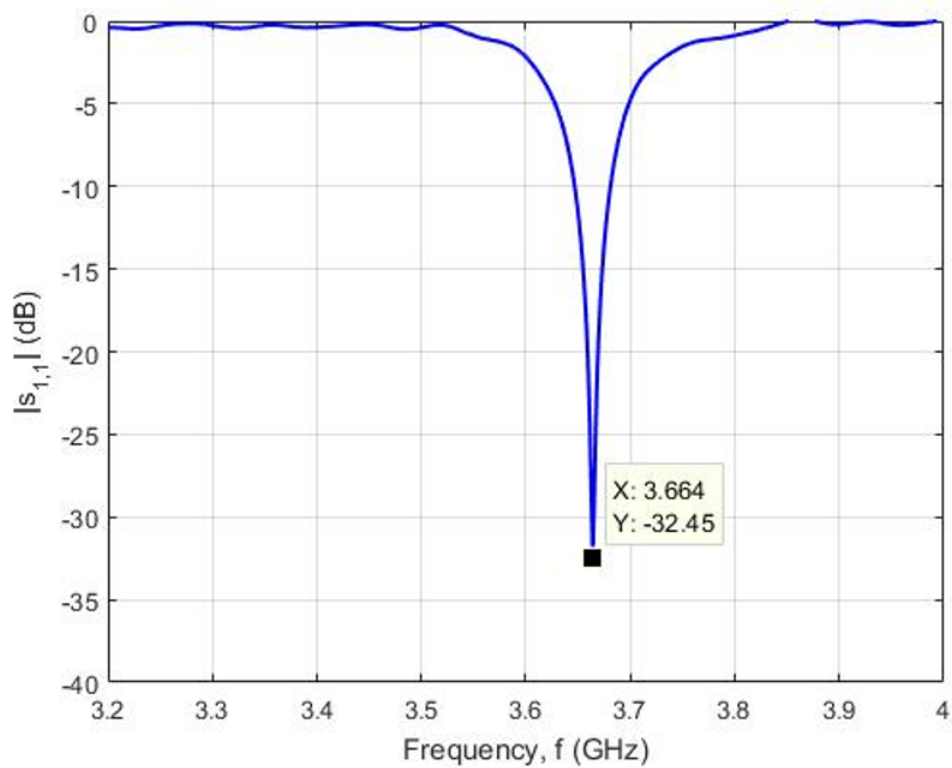FIGURE 6.13: Initial FCL prototype measurement

To correct the operational frequency, instead of adjusting the SMA pin attachment location (feeding point ΔF), the length of the central track (l') was used to influence the frequency of resonance. Fig. 6.14 shows 4 mm of additional adhesive copper tape attached to the central component.

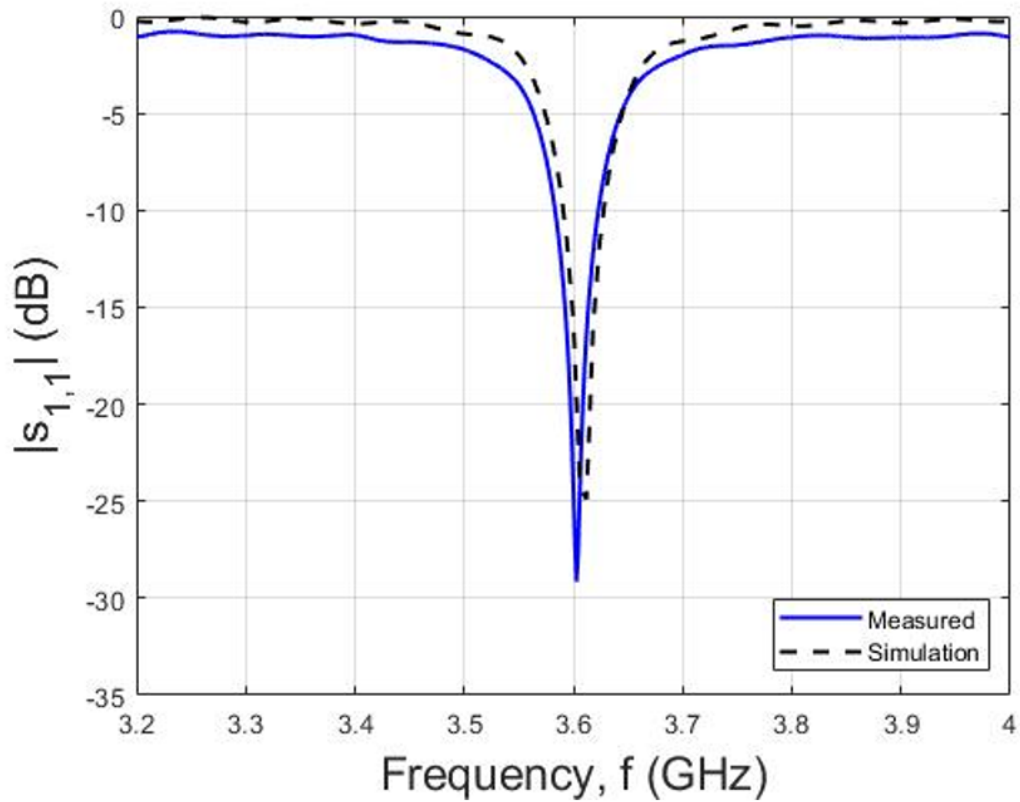FIGURE 6.14: Adjusted folded comb-line prototype

FIGURE 6.15: Simulated and measured S_{11} on body phantom. Parameters l, l', t, f, N, w, h, L, W = 28, 30, 28.25, 5.75, 5, 1, 0.762, 40, 40 mm, $\alpha = 15°$.

Through adjustment of the centre length l', a match approaching -30 dB was obtained (Fig. 6.15), in agreement with the simulations. The bandwidth is BW_{-10dB} $\sim 1.1\% \approx 40$ MHz for both simulation and measurements. Thanks to the decoupling ground plane and the path of the VNA cable through the phantom, measurements were repeatable.

As with the grid arrays in Chapter 5, radiation performance of the antenna was obtained by applying the gain-comparison method [137]. A reference patch antenna with known gain ($G_0 = 2.2$ dB) [138] was measured on the same body phantom and in the same geometrical arrangement of the array under test (Fig. 6.12 and 6.17). A $G_{max} \sim 3.7$ dB with BW_{-3dB} (0°, 90°) = 67.5°, 135° was measured and is fully in line with the simulations ($|G_{max-sym}$ - $G_{max-meas}| \approx 0.9$ dB) on both vertical and horizontal planes (Fig. 6.16).
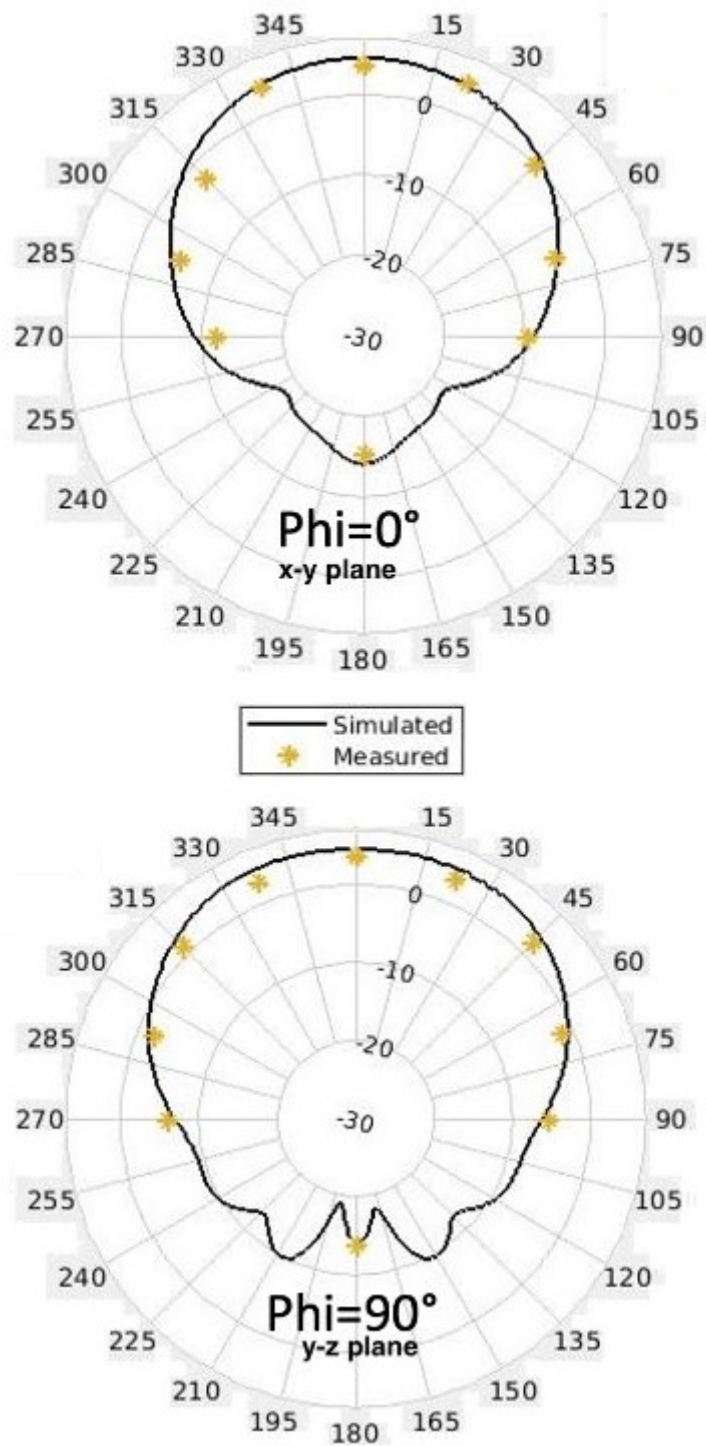
FIGURE 6.16: Simulated and measured radiation pattern on the horizontal (Phi = 0°) and vertical plane (Phi = 90°).
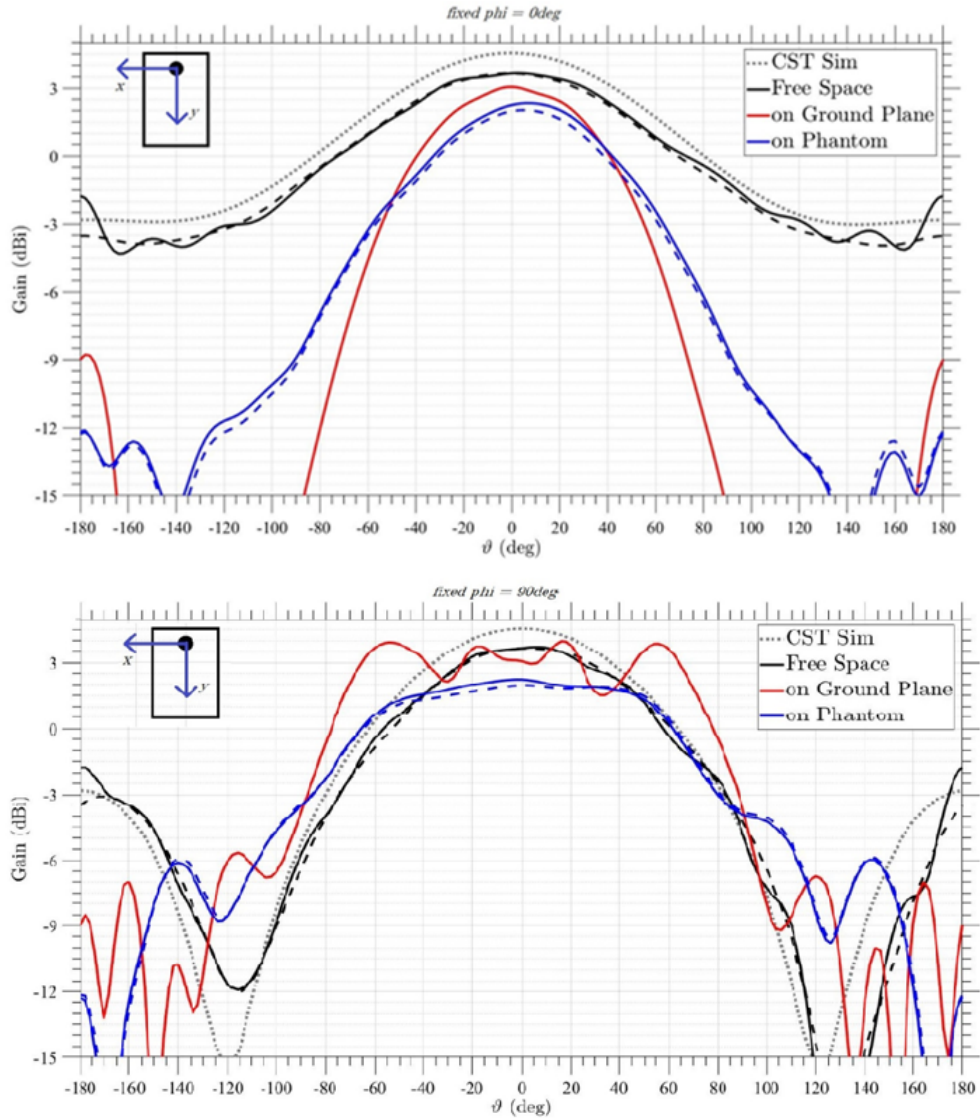
FIGURE 6.17: Cartesian gain plots of the reference patch antenna in simulation and measurement used for gain comparison.

The prototype was also characterized in a real scenario. S_{11} and broadside gain were measured on a male volunteer when the device was placed in different body positions (Fig. 6.18 (a)), namely at the armpit, knee, palm, back of the hand, and elbow. To reduce the impact of the cable, it was passed through gaps around the arm, leg, and fingers so that it was hidden by the body and then connected to the VNA behind. The decoupling ground makes the antenna insensitive to the body, with S_{11} (see Fig. 6.18 (b)) appearing stable and in good agreement with simulations, regardless of the position.
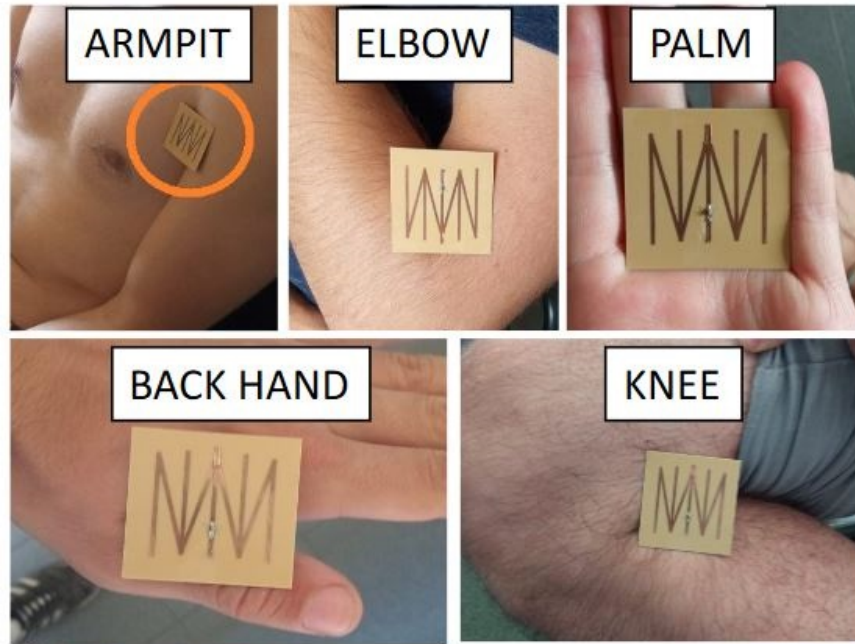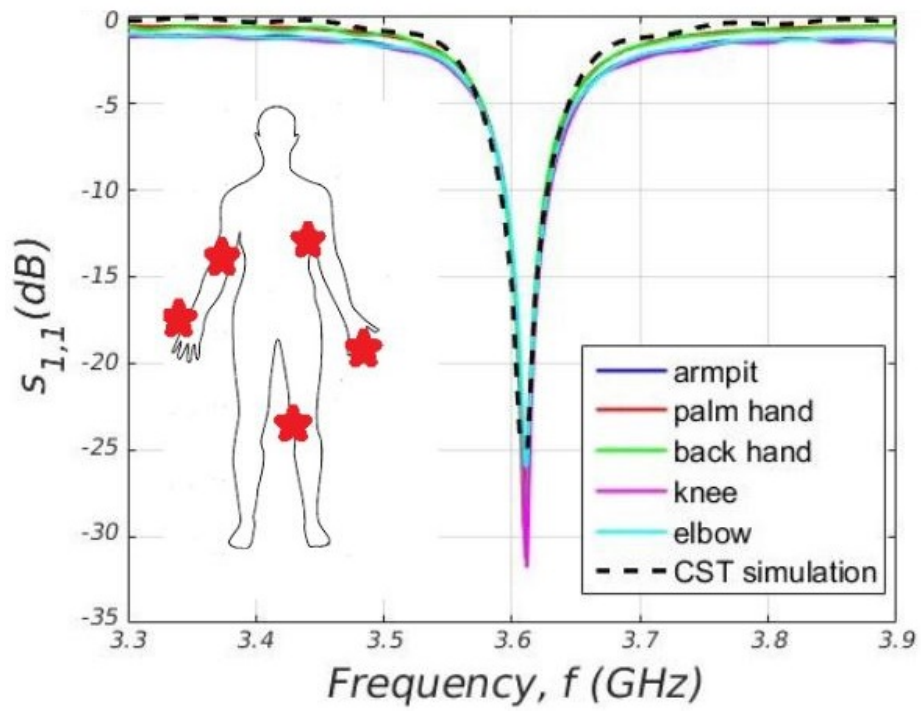
FIGURE 6.18: Measured S_{11} of the antenna placed on different body regions of a male volunteer.
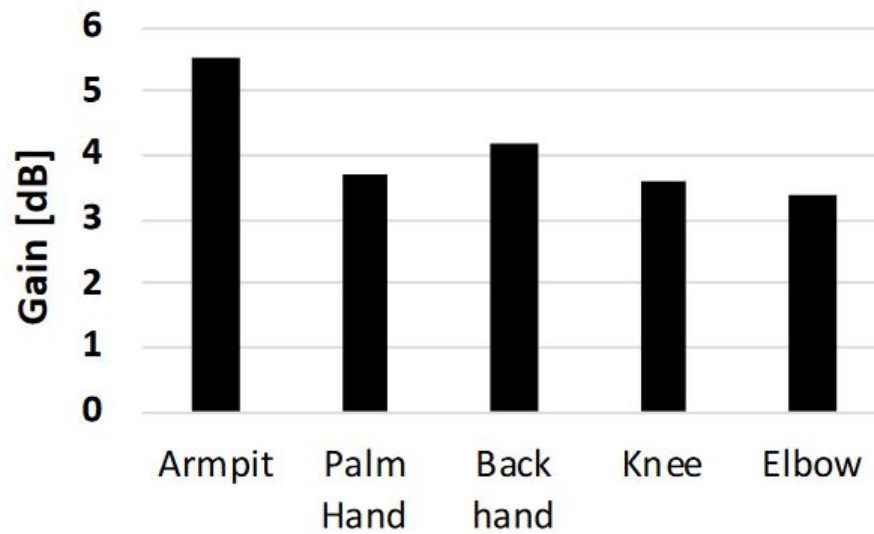
FIGURE 6.19: Measured broadside gain of the antenna (peak values) placed on different body regions of a male volunteer.

A similar consideration can be performed for the gain (see Fig. 6.19). With the exception of the armpit region (where the presence of a larger area of the body increases the array directivity) the maximum gain in the broadside direction ranges was between 3 and 4 dBi, in agreement with the measurements on the phantom. By considering the UHF RFID features (i.e. a reader emitting EIRP = 3.2W and a sensing-oriented chip with sensitivity p_{chip} = -15 dBm) to be valid in the n78-band [139], read distances up to 5 m [138] are expected in realistic conditions. This distance is similar to what could be achieved by wearable UHF tags (4.9 m) of comparable surface area (4.5 cm × 3.5 cm × 0.3 cm) [140] but at a third of the thickness. In comparison with the 3.6 GHz epidermal twin-grid array from Chapter 5, the same radiation performances can be achieved but with only 13% of the physical area and half the thickness.

To evaluate the conformability of the array to curved body regions, the antenna was bent over a cardboard cylindrical tube of diameter $D = 8.5$cm emulating arms or legs (Fig. 6.20). S_{11} and the maximum gain were measured for the flat configuration and for the two bends, over the E-plane and over the H-plane respectively (Fig. 6.21 and 6.22). Since the prototype is semi-rigid, bending over the cylinder was forced through adhesive tape. Despite the different measurement conditions (the cylinder is an empty cardboard tube), S_{11} and broadside gain are in-line with the flat configurations. Bending produces minimal variations of the input impedance, however $S_{11} < -12$ dB at 3.6 GHz regardless of the configuration. The gain appears stable, showing bending had a negligible impact (< 0.5 dB), confirming the conformability of the miniaturized device.
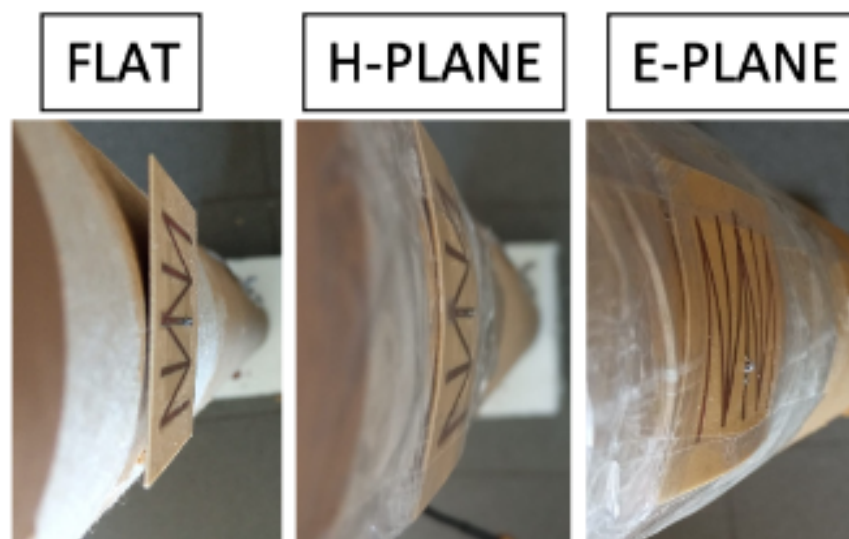

FIGURE 6.20: Conformability analysis, array bent over a cylindrical cardboard tube with a radius of 4.25 cm on the E and H planes.
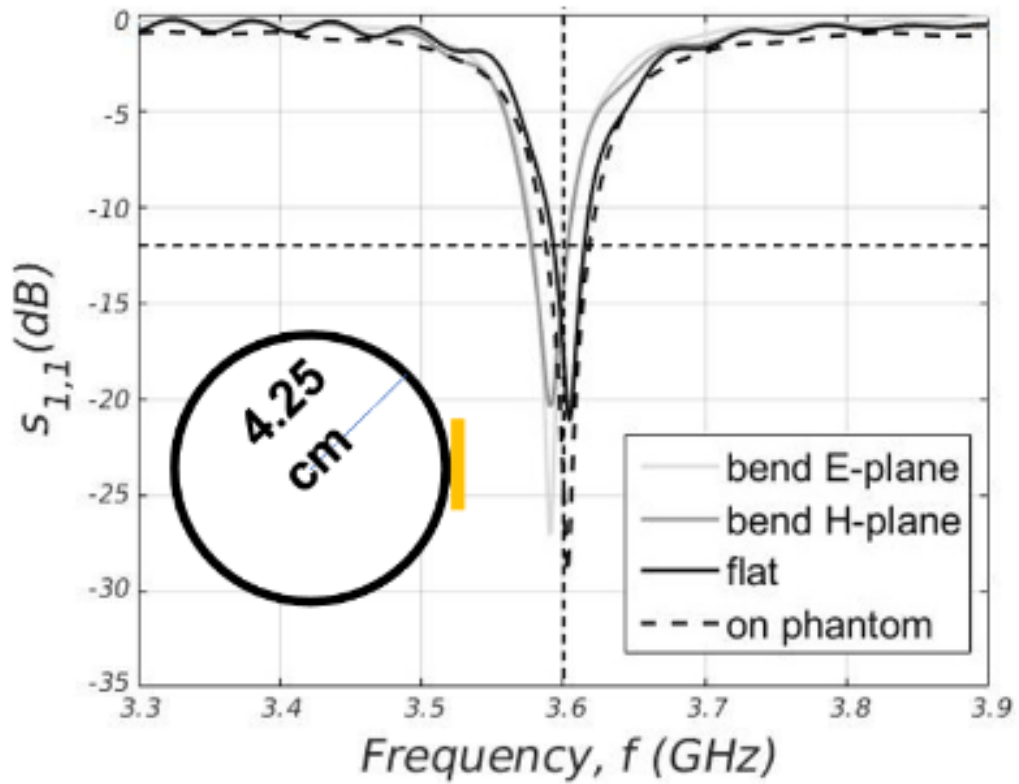
FIGURE 6.21: Conformability analysis, measured S_{11}.
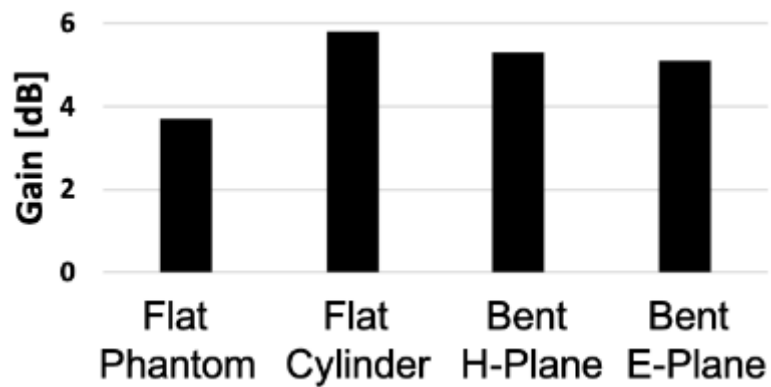
FIGURE 6.22: Conformability analysis, measured broadside gain (peak values).

6.4 Conclusion

A thin monolithic antenna array has been proposed for on-body applications at the 5G sub 6 GHz band of 3.6 GHz as an evolution of the traditional comb-line array. The proposed layout offers better performance in terms of both efficiency and gain as well as a miniaturized footprint. The antenna is robust against positioning over the body. Furthermore, the smallest 4 cm $\times$ 4 cm $\times$ 0.1 cm configuration proved to be conformable to curved surfaces, with almost invariable input impedance and gain. The achieved size is compliant with typical epidermal plaster-like UHF tag antennas. Expected read distances are similar to what could be achieved by wearable UHF tags of comparable surface area, but with the additional benefits of the 5G frequencies. Such distances could be suitable for Personal Area Network (PAN) applications or to continuously track the vital signs of a user within a room, thus greatly extending on the current performances of UHF body-centric systems. Furthermore, since flexible elastomeric substrates capable of conforming to the different body regions can be adopted, the layout is suitable to be worn on different body areas, such as shoulders, abdomen, arms and even on the head. Finally, to reduce the impact on the body and hence improve the wearability of the device, the ground can be trimmed around the comb-line profile or replaced by conductive fabrics.

Chapter 7

24 GHz Grid Array Antenna for 5G-RFID-based IoT applications

This chapter presents the design and fabrication of an on-body grid array antenna for the 5G K-band at 24 GHz. Attempting to utilise the reflective properties of the body in an aim to remove the ground plane, thus allowing potential incorporated sensor networks to have direct access to the skin.

7.1 Introduction

Chapters 4 and 5 focused on the Kraus grid into a 5G, wearable, grid array antenna (GAA) for the C-band at 3.6 GHz. What was found is the GAA at 3.6 GHz falls victim to the same structural shortcomings as UHF antennas, ultimately larger than desired and requiring a ground plane for proper function. However, the GAA still remains an attractive antenna for on-body application, owing to the monolithic, planar, continuous, wire structure that is fed at a singular location capable of achieving high gain. One potential solution to overcome the issues seen at 3.6 GHz is to increase the operational frequency. Studies have shown that for on-body antennas, at high operational frequencies, the skin presents more reflective properties, potentially serving as a functional replacement for a ground plane [141]. In this chapter, the grid array antenna is designed and fabricated for the 5G K-band frequency of 24 GHz. This frequency band is analyzed to determine whether it is suitably high enough as to achieve the reflective properties of the skin, thus, allowing there to be an absence of any ground plane, but relatively low enough as to keep the wavelength practical for fabrication. The feasibility of this reflective property can be determined by the performance of grid-array antenna. Since the antenna relies on the ground plane for proper performance, if the skin cannot duplicate this effect, the normal lossyness of the skin will become apparent. That is, the electric field of the antenna will penetrate the body, causing the aqueous properties of the tissues to absorb the RF energy away from the antenna, hence causing the performance of the antenna to be significantly hampered. Losses that will be exacerbated by the additional path-loss, associated with this higher frequency. Whilst the GAA has shown capability of increasing gain with increased radiating elements, this chapter presents the same topology as shown in Chapter 4, as an initial performance check. Another challenge by virtue of the reduced wavelength, whilst favourable for the desired application of being worn on the body, limits the space for necessary matching network components. This chapter will describe the design through CST simulation, including matching network parameters, then prototyping and measurement of the simulated design.

7.2 Antenna design and parametric analysis

The GAA topology is as described in Chapter 4, whereby the vertical, $\lambda_g/2$ length, radiating elements are separated by $\lambda_g/2$ horizontal tracks on alternating rows. In this arrangement, the phase on the vertical elements align constructively producing the radiation, whilst the phase on the horizontal elements are in opposite phase, thus cancelling, acting only as transmission line. As with the earlier work, simulations took place using CST studio suite, employing a skin properties at 24 GHz ($\epsilon_r = 19$, $\sigma = 22.8$ S/m) described by IT'IS foundation [41]. For this case, the fat and muscle blocks body-model components are omitted since the radiation penetration depth is reduced with the high frequency [136], with the added benefit of simplifying the simulation, decreasing the simulators calculation time. Previous work into the GAA at 3.6 GHz showed most efficient grid-array antenna topology obtained seven radiating elements, hence this was used as the starting structure, utilising the low-loss substrate Rogers 4003c ($\epsilon_r = 3.38$, $\tan\delta = 5\cdot10^{-3}$, t = 0.2 mm). Unlike the work at 3.6 GHz, the smaller physical wavelength at 24 GHz and consequently tighter grid perimeters prevent a practical feed network from being constructed over the central radiating element, instead, requiring the feed network adjacent to the antenna connecting to the edge, thus, the resultant starting topology is shown in Fig. 7.1.
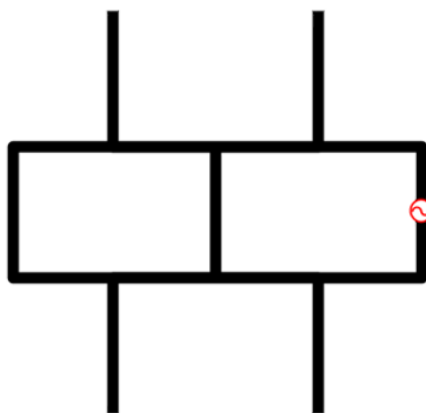
FIGURE 7.1: 7-radiating element grid array antenna with edge-feed.

In a first step to controlling the input impedance, an additional strip of track is placed in close proximity to the feed to imbue a capacitive affect, thus allowing

control over the complex impedance (Im component) through the dimensions of the capacitive strip length ($l_{cs} + (2 \times e_{cs})$), width ($w_{cs}$), and proximity to the feed (p_{cs}) (Fig. 7.2). The parameters for the GAA dimensions, as well as the capacitive strip dimensions, are given in Table 7.1.
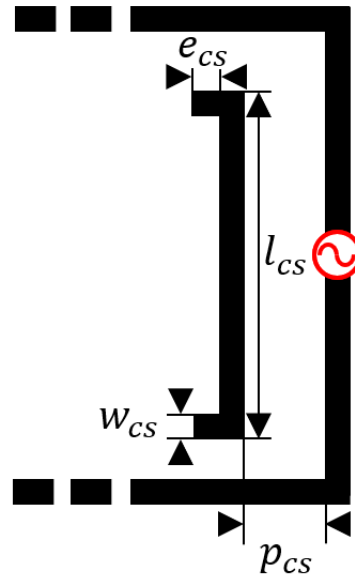
FIGURE 7.2: Capacitive strip dimensions for input impedance control.

TABLE 7.1: GAA simulated dimensions (in mm).

l	s	l_{cs}	w_{cs}	p_{cs}	e_{cs}
7	3.5	2.8	0.2	0.2	0.23

In nullifying the complex part of the impedance, the remaining real impedance was 106 Ω. Since no 5G RFID IC's exist for 24 GHz, the practical measurement feed is required to be matched to 50 Ω. To achieve this on the split vertical track, groundless microstrip coupled lines are employed.
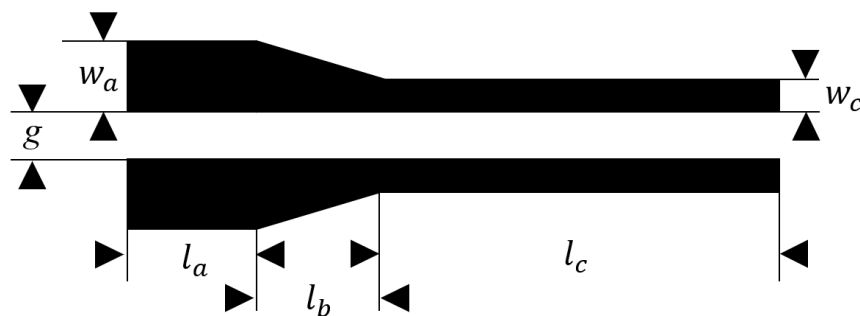
FIGURE 7.3: Groundless microstrip coupled feed line dimensions.

The microstrip coupled lines are the formation of three sections a 106 Ω characteristic impedance line ($l_a \times w_a$), a 50 Ω characteristic impedance line ($l_c \times w_c$), and a tapering section linking the two sections ($l_b \times \frac{1}{2}(w_a + w_c)$), as shown in Fig. 7.3. However, for practical measurement, the edge connector being utilized has a mounting mechanism that bolts on either side of the feed lines, which with a short feed line would cause the mounting elements to overlap with the antenna track. Consequently, the feed lines have been lengthened to allow for the antenna and the mounting system to remain unimpeded. In extending the feed lines, the capcitive strip required adjusted for tuning the operational frequency back to 24 GHz.

TABLE 7.2: GAA simulated design including feed network dimensions (in mm).

l	s	l_{cs}	w_{cs}	p_{cs}	e_{cs}
7	3.5	2.3	0.2	0.2	0
l_a	w_a	l_b	l_c	w_c	g
1.2	0.5	1.2	4.5	0.2	0.2
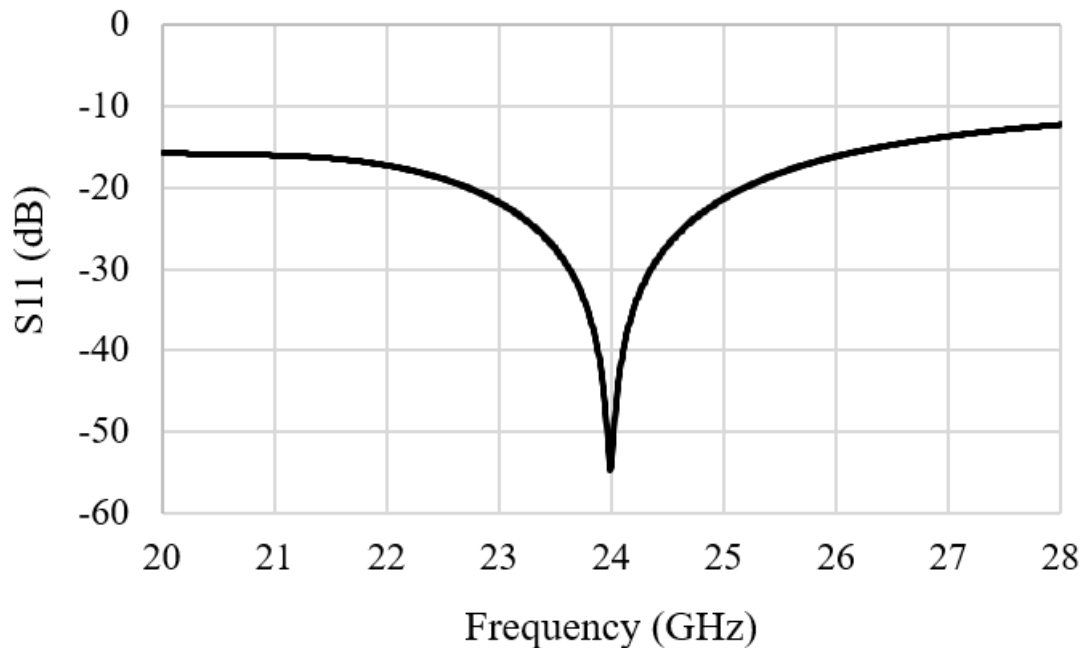
FIGURE 7.4: Simulated S_{11}.

The simulated radiation performance has a gain of -8.8 dBi and an efficiency of -16.6 dBi, the surface current is presented in Fig. 7.5 and radiation pattern described by Fig 7.6, 7.7 and 7.8. Whilst the current pattern on the GAA is as expected, it is clear a large proportion of the energy is dispersing on the feed lines before arriving at the radiating elements, this, in addition to the removal of the ground plane, are the main cause for loss in the system.
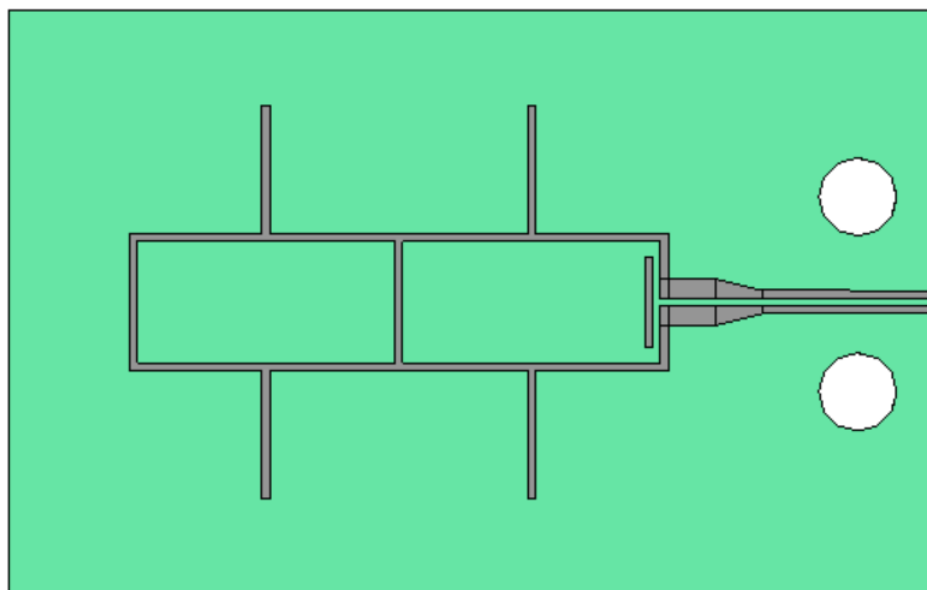
a.
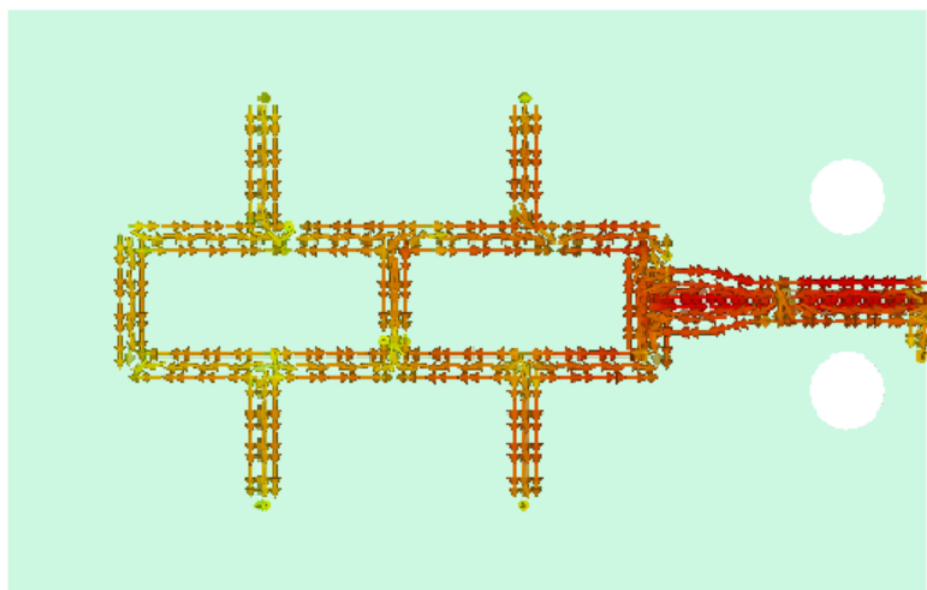
b.

FIGURE 7.5: Simulated: (a) final structure, (b) surface current.
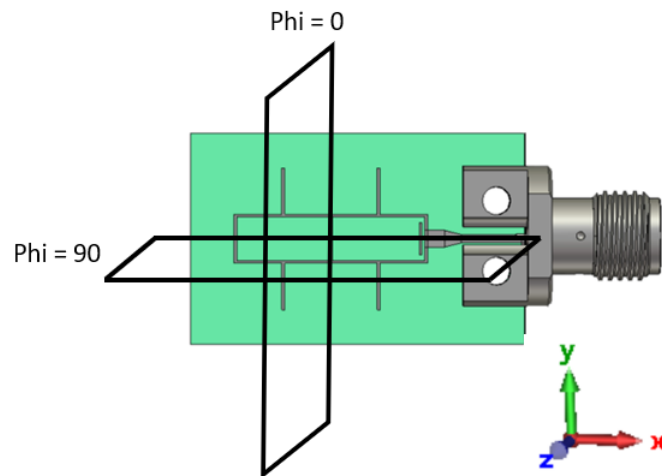
FIGURE 7.6: Respective antenna radiation planes.
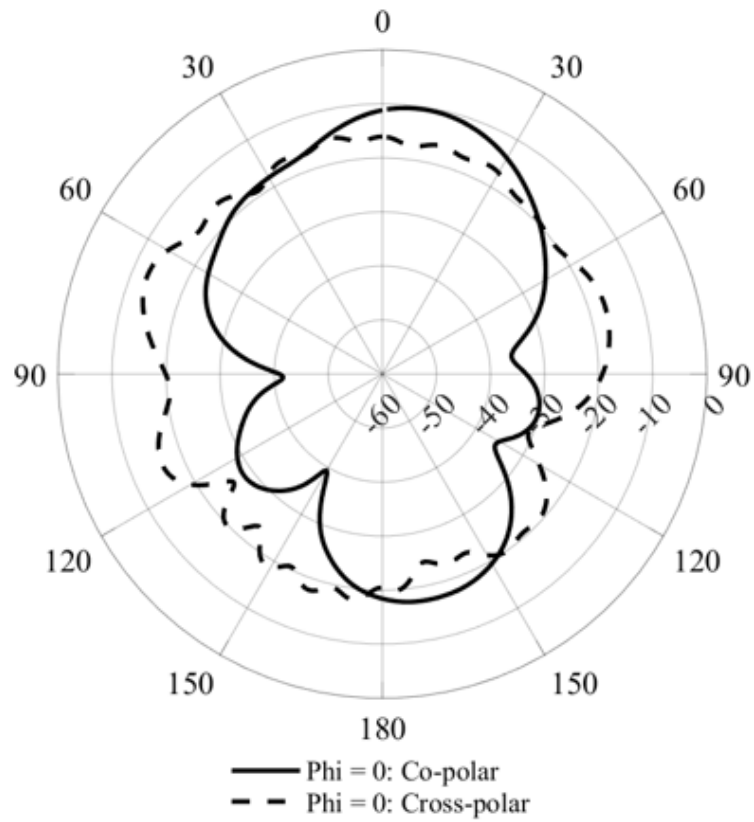
FIGURE 7.7: Simulated radiation pattern respective to Phi = 0, copolar and crosspolar.
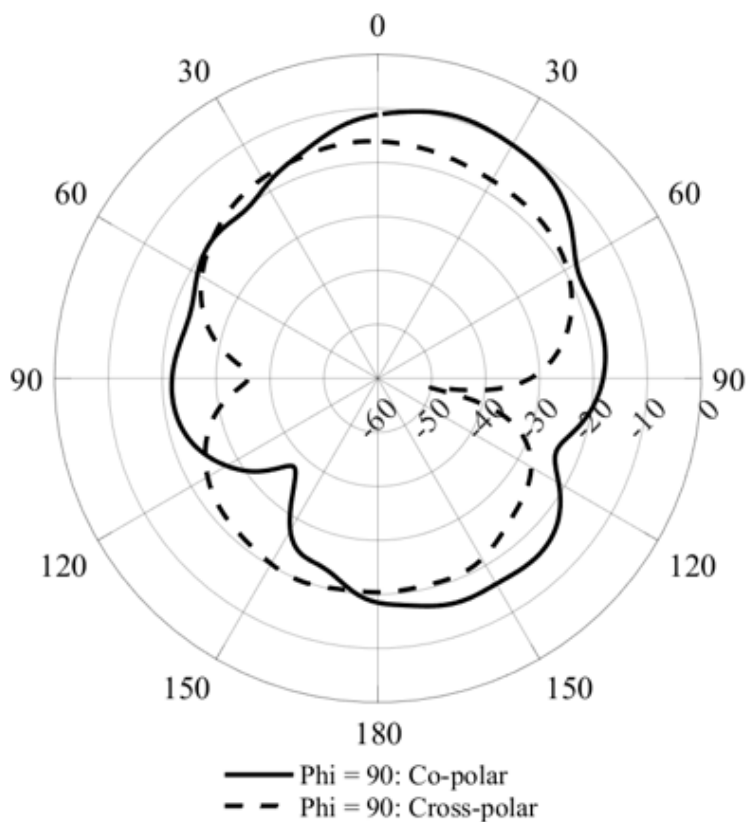
FIGURE 7.8: Simulated radiation pattern respective to Phi = 90, copolar and crosspolar.

Whilst the antenna is designed to be vertically polarized, owing to the alignment of currents on the vertical components being the source of the radiation, the radiation pattern instead describes an antenna radiating equally in both planes. This could be due to the majority of the energy output from the antenna occurring on the feed lines, which are horizontal. The pattern does also suggest a significant backward beam in both planes, however this is likely amplified due to the restricted simulator body-model in favour of a simpler skin-only model for a faster calculating simulation.

7.3 Prototype Measurements

The GAA was prototyped on Rogers4003c using copper etching, to which the connector attached via nuts and bolts, shown in Fig 7.9 and 7.10.
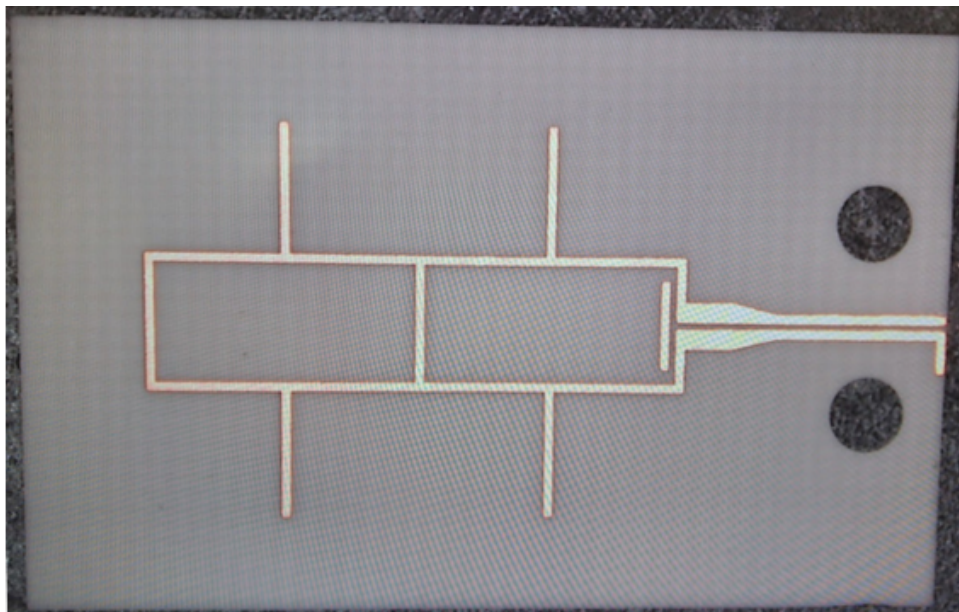
FIGURE 7.9: GAA Prototype.
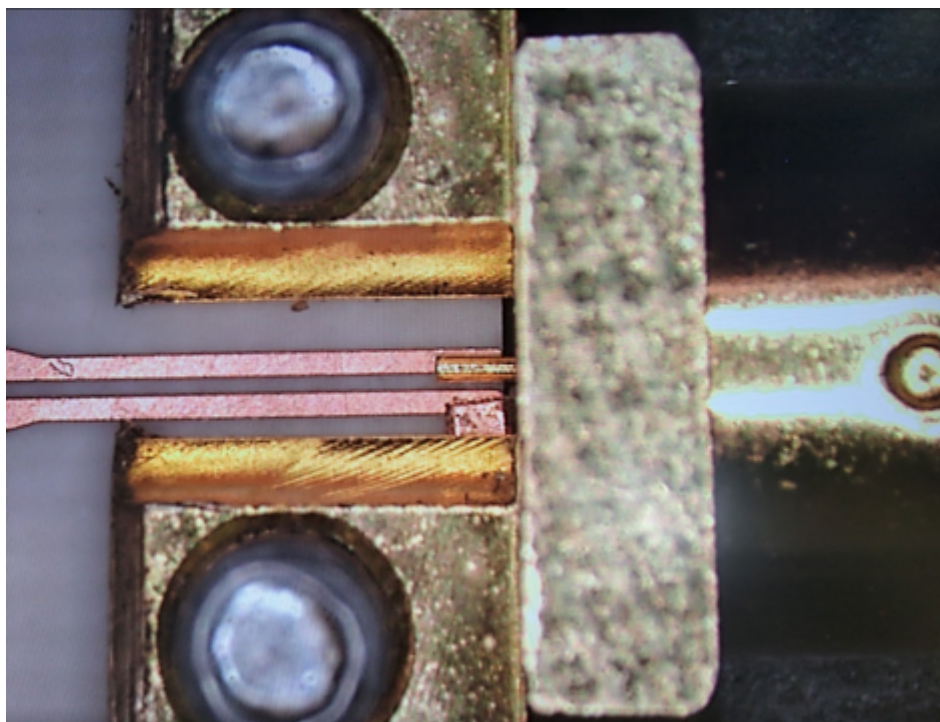
FIGURE 7.10: Prototype feed connection.

As the antenna is matched to the body, pork was employed as a body-phantom for a more controlled measurement environment (Fig. 7.11). The antenna was then connected to a VNA for measurement of the reflection coefficient, showing a null at 20.5 GHz, 3.5 GHz lower in frequency than intended, as shown in Fig. 7.12. Due to the small size of the antenna, it is difficult to re-tune the frequency response as attaching any additional conducting material to the system, however small, can significantly influence the response. Therefore, the antenna was carried forward with measurements without correction to the frequency response.
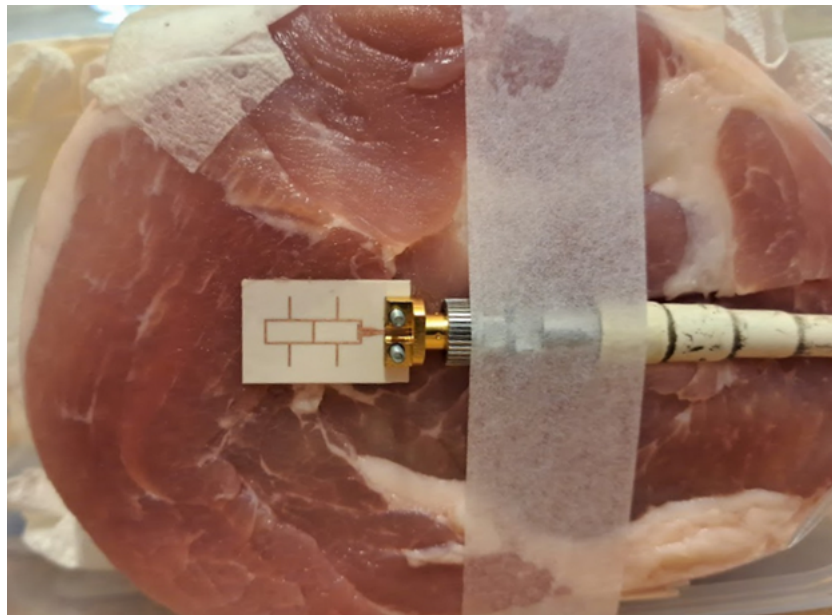
FIGURE 7.11: GAA reflection coefficient measurement setup.

Next, the antenna was measured in the anechoic chamber for the gain response and radiation pattern in the vertical and horizontal planes with respect to the probe antenna (horn), the measurement setup for the antenna in horizontal polarisation is shown in Fig. 7.13. Due to health and safety concerns, the meat was kept wrapped in a thin plastic sheet to prevent contamination of the chamber. The gain response in each polarisation could then be used to perform the gain comparison technique to normalise the radiation pattern, resulting in the Fig. 7.14 and 7.15 describing the antenna in vertical polarity, then Fig. 7.16 and 7.15, describing the antenna in horizontal polarity.
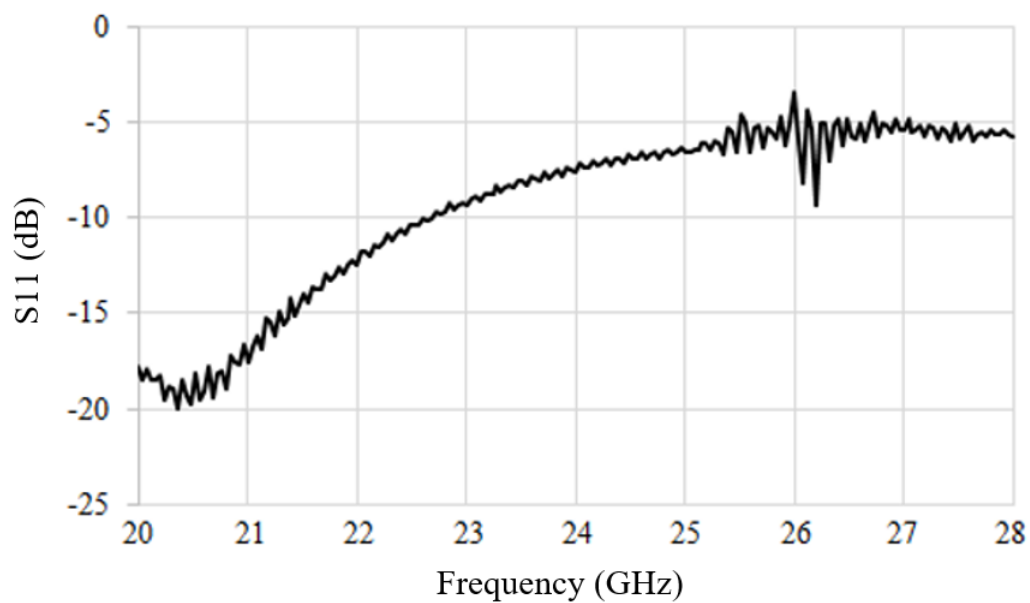
FIGURE 7.12: GAA reflection coefficient.
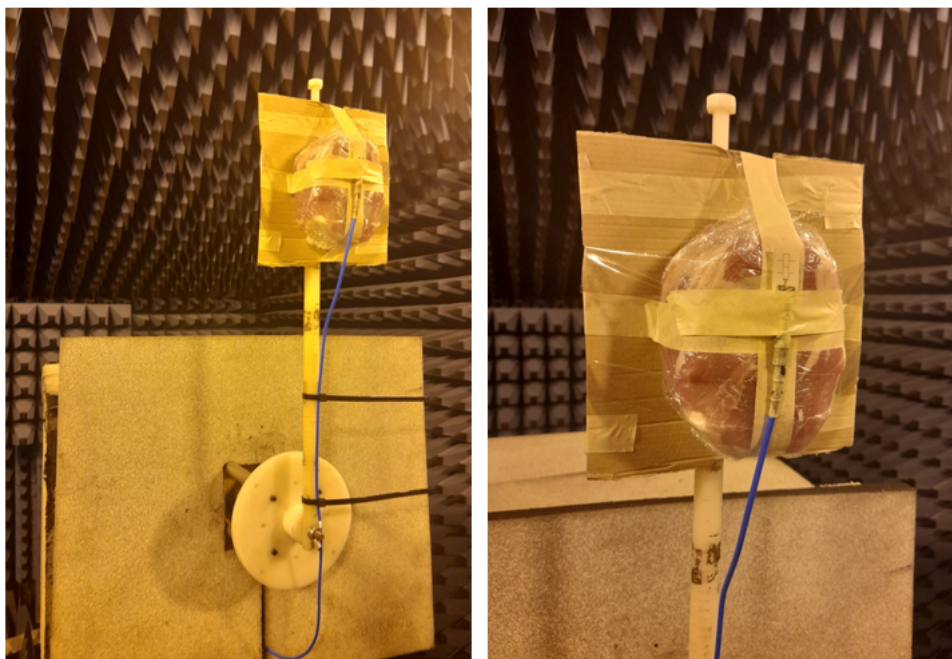
FIGURE 7.13: Measurement setup of GAA within the anechoic chamber.
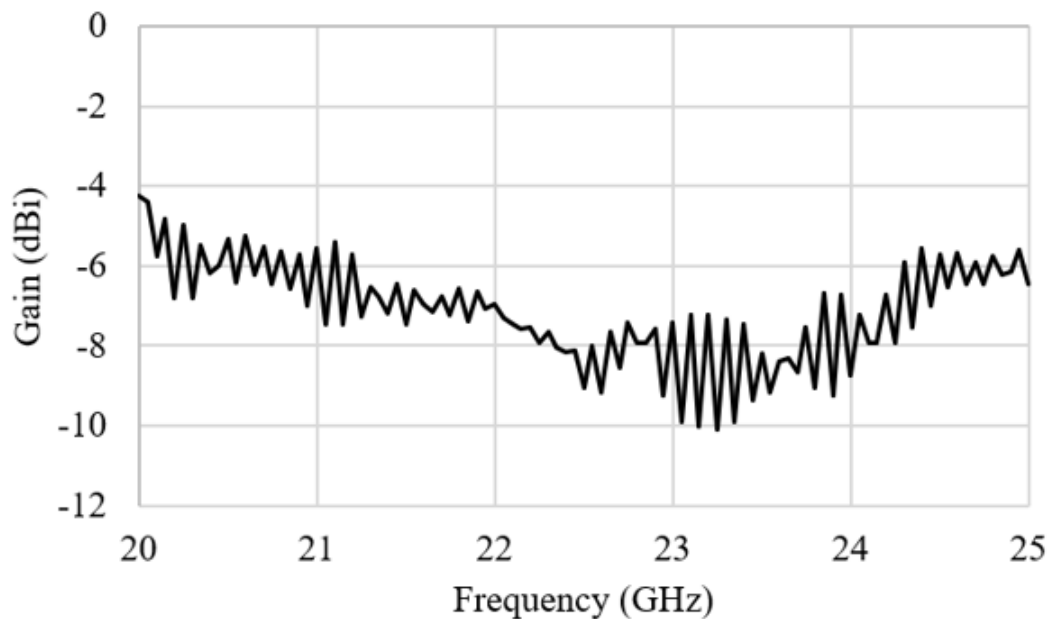
FIGURE 7.14: Gain response of a vertically orientated GAA antenna with respect to a vertically orientated horn antenna.
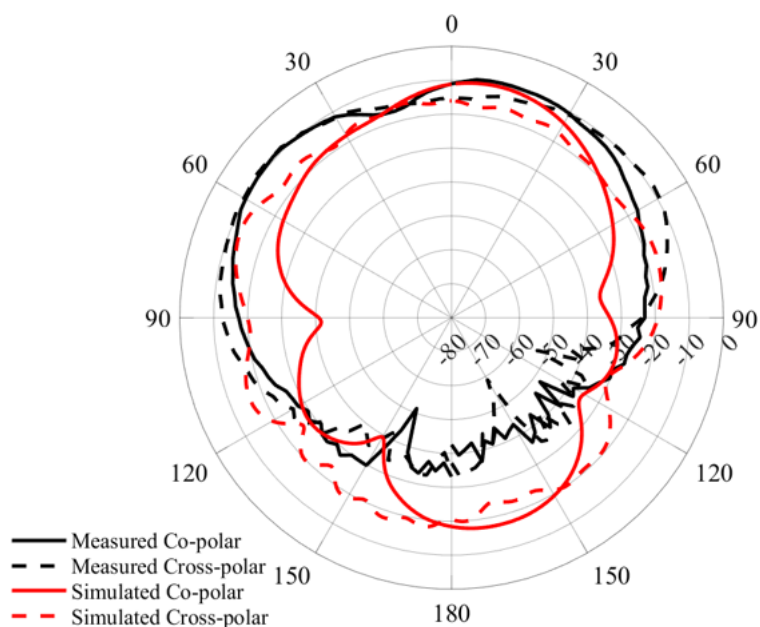
FIGURE 7.15: Measured and simulated radiation pattern of a vertically polarized GAA, equivalent to Phi = 0 simulation.

In the vertically polarised orientation (Phi = 0), the simulated and measured patterns share many features in both the copolar and crosspolar pattern shape, with the measured response appearing wider in beam width, likely owing to the increased directivity thanks to the thicker (hence more opaque) body-phantom.
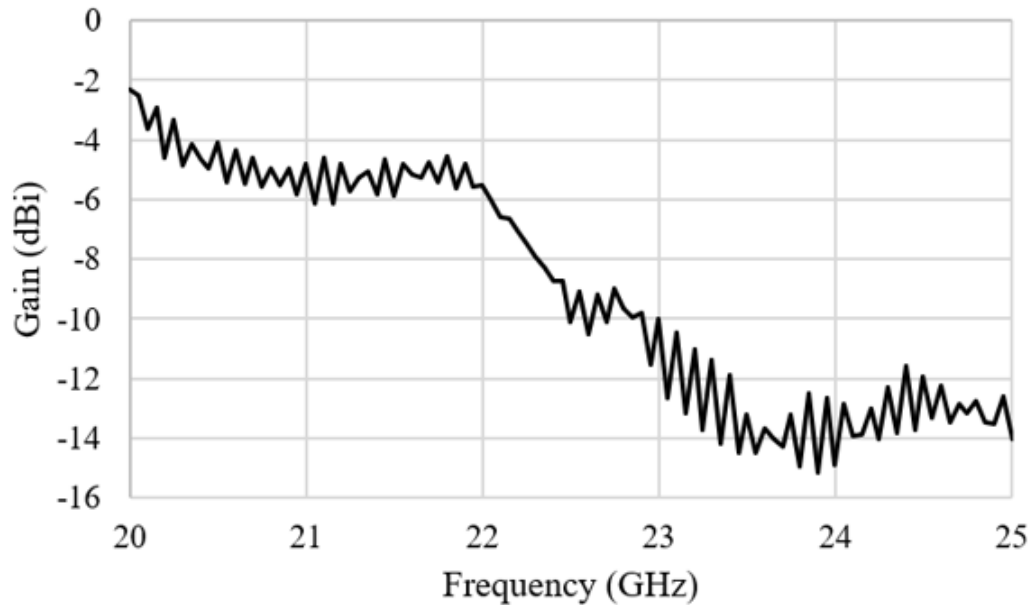
FIGURE 7.16: Gain response of a horizontally orientated GAA antenna with respect to a vertically orientated horn antenna.
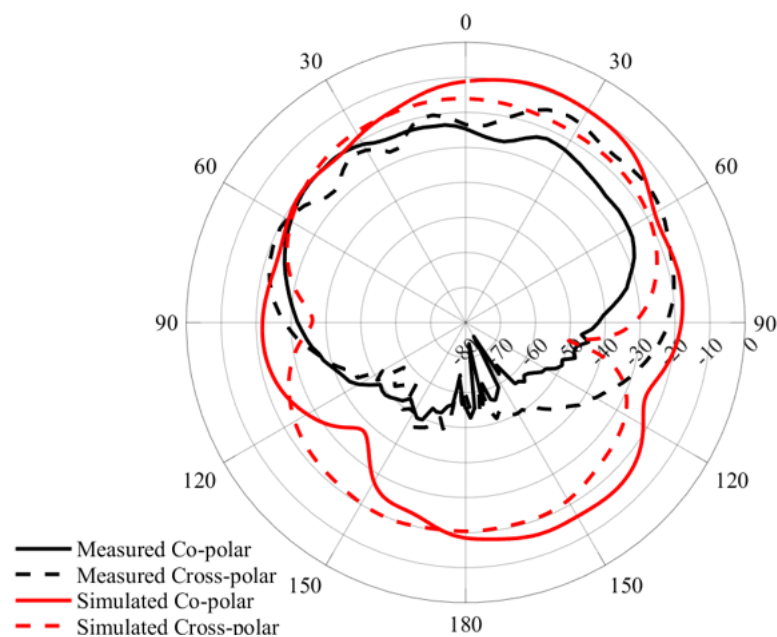
FIGURE 7.17: Measured and simulated radiation pattern of a horizontally polarized GAA, equivalent to Phi = 90 simulation.

In the horizontally polarized orientation (Phi = 90), the measured pattern is somewhat lower in gain than the simulated pattern, even with the more directive response, implying the simulator may be over evaluating the performance of the antenna in the horizontal plane, which was previously stated as higher in gain than expected and hypothesised being due to the feed lines.

As described in Chapter 4, the Friss equation can be used to calculate the theoretical read range at a given frequency. Once again, current UHF standards are required to be assumed to carry over to this higher frequency, specifically the regulated EIRP of 3.2 W and an RFID IC chip sensitivity of -21 dBm. The measured gain performance of the antenna, in the intended vertically polarized orientation at 24 GHz, was -8 dBi. These values equate to a theoretical read range of just 25 cm. However, measurement saw the antenna was better operational at the frequency 20 GHz, with a gain performance in the vertical polarization of -4 dBi, then -2dBi for the horizontal polarization. Which in turn equate to read range performances of 40 cm and 50 cm, respectively. Therefore, it could be seen the antenna performance could be improved at the intended frequency with furrther study.

7.4   Conclusion

In this chapter, early research has been made into an on-body grid array antenna for the 5G K-band at 24 GHz. The topology was unlike previous GAA iterations in removing the ground plane, a desirable structural trait for the potential incorporation of a sensor network without blocking access to the skin. An additional difference over previous iterations was employing an edge-feed over a central-feed, a necessary requirement to incorporate a matching network that no longer fit within the grid cells due to the small wavelengths. The resultant structure measurements confirmed simulation radiation performance, describing a gain of -9 dBi and an efficiency of -17 dB. However, there were notable differences between the simulation and measurement, foremost being the frequency of resonance and radiation pattern. Both of these effects could be explained by inaccurate modelling of the body in the simulation, since the measurement environment featured a much more significant meat block than just the skin model in simulation. Further research would require a more accurate body model for 24 GHz. To increase antenna performance, investigation needs to be made into whether increasing the number of radiating elements has a substantial affect, though, based on the work in Chapter 4, it is likely that this will only be detrimental to the antenna efficiency and achieving the desired performance requires the re-introduction of the ground plane. As described in Chapter 5 with the twin-grid antenna, investigation into a partial ground plane may be pertinent with regards to future research. Measurements showed when the GAA is in vertical polarisation, the measured radiation pattern showed a wider beam pattern than the simulation in both copolar and crosspolar, with a more directive beam. However, the antenna in horizontal polarisation was relatively poor performance, that said, the antenna is intended to be vertically polarised so the radiation performance lost was only an unexpected improvement in simulation. Overall, the performance could be seen as better than expected, considering the return loss frequency mismatch, however this appears to be accounted for with slight separation between the antenna and body phantom in the measurement process.

Chapter 8

Conclusion and Future Work

The research presented in this thesis has investigated the design of on-body antennas as passive UHF and 5G RFID tags. Introducing a novel package device for UHF potential healthcare applications, as well as an early pursuit to find an achievable 5G antenna for an RFID communication band that does not yet exist. This chapter provides a summary of the research work described and concludes the thesis, then goes on to give recommendations for related future research.

8.1 Conclusions

This thesis has discussed the possible application of RFID in healthcare, seen for the potential to produce a low-cost, rugged, long-lasting, passive RFID tags that could be adopted in medical facilities, or even for people to use within their own homes. However, the antenna aspect of these systems, and the primary focus of this thesis, remains limited by fundamental challenges when placing an antenna on the body. An example being the effect the placement has on the tag, the difference in body make up at the same location between two individuals, and how that area is effected by movement. Thus, as described by the comparative literature in Chapter 2, the most successful antenna performances have occurred through adopting large ground planes, rigid substrates, or substantially thicker substrates. Consequently, these solutions are in conflict with the desirable tag structure that is low-profile, flexible, and allows direct access for sensor networks to interrogate the skin. Therefore, ultimately (for UHF RFID, the current RFID standard), the options for antenna designers are as follows: maximise the structural performances in terms of comfort; consequently deal with the relatively poor radiation performance by maintaining functionality to only short-read ranges, or maximise the antenna radiation performance by sacrificing the comfort of the tag; consequently granting long read-range performance but only for short application, or finally, finding a middle ground between the two ideals of radiation and structural performance.

Chapter 3 took the latter approach, presenting the design and fabrication of a UHF RFID tag with DDRR antenna for live data streaming applications. The DDRR antenna was thought of as an attractive option, owing to the vertical polarisation, in an attempt to negate the losses the body would normally inflict on horizontal/planar antenna running parallel to the skin. The resultant antenna was a 4 cm diameter and 1 mm thick cylinder, so not in the realm of 'epidermal' classified antennas, but still reasonably small. The DDRR was capable of reasonable bending, with measurements obtained through placement on the upper arm. In combination with the circuitry, the system was able to achieve data transfer at a speed of 1 kB/s consistently up to 1.2 m from the reader antenna, then sporadically up

to 3.6 m, due to what is assumed to be channel effects including constructive and destructive interference in a complex echoic environment. It is recommended that until the data dropouts are resolved, whether through reader antenna diversity or improvement to the antenna performance, application of this system should be kept to less than 1.2 m distance from the reader.

The next prospect discussed in this paper was the possible adoption of 5G for RFID. Suggesting that by reducing the operational wavelength, the limitations on the antenna structure may be reduced, whilst the antenna performance could be improved through employment of antenna arrays.

Chapter 4 offered the first step in using the 'grid array antenna' (GAA) at 5G frequencies, with this chapter initially introducing the original topology designed by Kraus, with adaption to function on the body and to incorporate a hypothetical RFID IC. This chapter laid the foundation for the methodological approach taken in designing an RFID antenna considering the unknowns of 5G, by assuming standards at UHF will carry over to future 5G technologies. The resultant antenna design in this chapter showed promising radiation performance in a simulated gain value of 9 dBi and efficiency of -3 dBi, however suffering the expected structural necessities to achieve the radiation performance, owing to a large topology entirely shielding the body with a ground plane. Consequently, it was difficult to imagine the GAA seeing application in this format.

Chapter 5 sought to overcome the challenges faced in Chapter 4, presenting two GAA variations in the meandered GAA and the Twin-Grid. The meandered GAA was designed in an attempt to miniaturise the topology, without having a detrimental effect on the radiation performance. Several meander variations were considered in the meandering of the GAA tracks, whether meandering the horizontal tracks, vertical tracks, or a combination of the two. The simulation results were clear, when meandering the radiating tracks there are significant consequences on the radiation performance, thus the only acceptable miniaturisation was with horizontal meandering, which saw an unchanged radiation performance to the Kraus grid with a 25% size reduction. Which, whilst a substantial reduction

without detriment to the radiation, it did remain larger than desired. The next iteration of the GAA was the 'twin-grid', designed to tackle the obtrusive ground plane preventing access of potential sensor networks to the skin. By mirroring the 'driver' topology as a 'reflector', skin access spaces were revealed at the centre of each grid. The resultant antenna design saw a simulated gain value of 6 dBi and efficiency -5.5 dBi, hence a sacrifice in radiation performance compared to that of the Kraus grid and miniaturised version. For future on-body antenna designers looking to integrate sensors into a system, investigation into a possible reduction of the ground plane is a valuable consideration. Ultimately, regardless of the GAA variation, the topology remained relatively large for application on the body, achieving no real benefit over the more reliable antenna topology types, such as a patch or slot antenna, with the same drawbacks being identified.

In Chapter 6 a tangential antenna design to the GAA was considered in the comb-line antenna, an antenna operating under the same fundamental current patterns, but geometrically constructed along a single horizontal track instead of spreading into grids. Adopting this antenna topology allowed the antenna to undergo a greater level of miniaturisation, whilst also improving radiation performance. This result was achieved by folding the 'horizontal' tracks into closer alignment with the 'vertical' tracks, hence increasing the vertical energy of the folded tracks orthogonal current components, adding to the radiation, whilst reducing the entire topology to a smaller surface area. This antenna is much more realistic for real application than the GAA with regards to the overall size, however should be replaced with a more flexible substrate. After further consideration, this antenna topology could be seen as a centrally fed and reduced conductor patch antenna, owing to the similar current pattern traits these antennas share.

Chapter 7 saw the final iteration of the grid array antenna, increasing the operational frequency to 24 GHz. The attraction of this frequency is the body characteristic, where at the higher frequency the skin appears more reflective instead of absorbing. In addition to the reduction in the operational wavelength, which opens up the structural limitations the lower frequency version of the antenna suffered. With a simulated performance of -9 dBi and efficiency of -17 dB, confirmed by

measurement, the antenna lacks the radiation characteristics required for practical application. It may however be necessary for the ground plane to be reintroduced, though it is recommended to do so such as with the Twin-Grid, requiring further investigation of a partial ground plane.

In conclusion, this thesis has outlined the challenges of on-body RFID antenna design and attempted to overcome them through a review of current literature, further research, and applied testing. This has allowed for the identification of the limitations of typically used planar and horizontally polarised antennas on the body, therefore attempting a low-profile vertical polarised antenna in the DDRR. Then simultaneously recognising the limitations of UHF RFID and potential for 5G RFID, going on to present possible 5G antennas in the grid-array antenna and its variations.

8.2 Future Work

8.2.1 DDRR Antenna

The DDRR antenna saw a promising performance with maximum data transfers up to 3.6 m away from the reader antenna, however the reading of the data up to this distance was inconsistent, seeing the most significant data dropout between 2.1 m and 3 m. This is believed to be due to channel effects including constructive and destructive interference in a complex echoic environment, a confirmation of which requires additional investigation using reader antenna diversity to provide a full understanding. Recommended steps would include changing the measurement environment, such as using an anechoic chamber, or an area with radar absorbing material (RAM) on the floors to prevent the most prominent reflection, then incriminating the reader antenna distance closer to the worn tag (instead of the tag away from the reader).

An aspect intended for development was the replacement of the coin cell battery with a custom ultra-thin battery that could be discretely layered with the antenna and PCB, such as described by Caccami in [66], shown in Fig. 8.1. Thus, a singular system package encapsulated within the 4 cm diameter of the antenna would be achieved, instead of the separate antenna and PCB. That said, this process would also require an investigation into the effects of elongating the feed line.
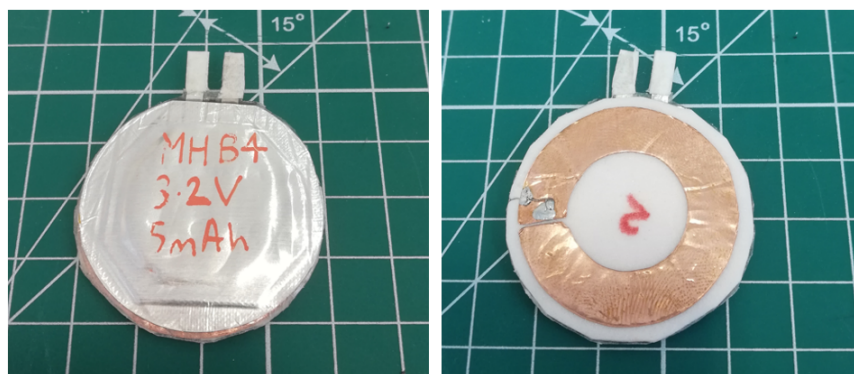
FIGURE 8.1: Custom ultra-thin battery for DDRR tag system.

8.2.2 Grid Array Antenna

Unfortunately, due to study limitations the cross-over between the miniaturised GAA and the twin-grid was not pursued, instead opting to invest time into the next adaption of the array antenna. Reflecting further on the study, an adaptation that would improve the miniaturisation of the GAA would be adopting the technique described by Zhang in [142].
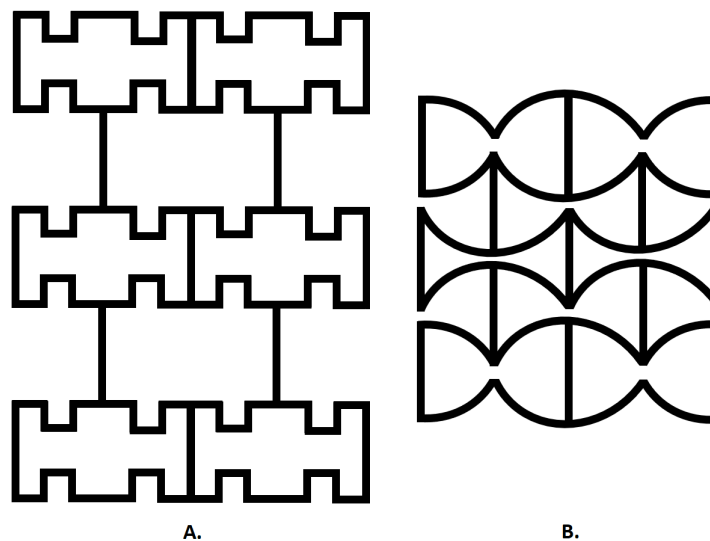
FIGURE 8.2: A. Nakano meandered GAA researched, B. Zhang alternative miniaturisation technique.

Fig.8.2 shows two 8-cell GAA topology variations with relative sizes. As can be seen, the bent horizontal lines greatly reduces the overall size of the antenna relative to the meandered version. Whilst the technique does impede on the possible T-match space, the area in which the central vertical element is interlinked by two convex horizontal traces, which should allow for ample matching network space, though the T-match horizontal lines may also need to be bent.

Additionally, an error was found post-publication in the accuracy of the quoted bio-silicone loss tangent. This had been accidentally miss-entered into the CST simulation as $1.4 \cdot 10^{-4}$. Whilst this does have implications about the antenna operation on this particular substrate, the overall capabilities of the antenna remains unaffected. Future renditions of this antenna would need to be on a lower loss substrate for high performance such as the Eccostock FlexK by Laird [143].

8.2.3 Folded Comb-Line

Due to study-limitations, the prototype and simulation differ in the substrate material utilized, for improved flexibility to conform with the body it would be recommended to employ the Eccostock® FlexK, by Laird. With improved material flexibility a comb-line array could feasibly be adapted into a wearable bracelet/strap for a wider radiation pattern. That said, it would require increasing the number of elements in the array structure. A prominent feature in larger monolithic arrays, be it the grid or comb structure, is the current dissipation the further away from the port you look. Sun [109] explores potential solutions for this through the use of multi-feed structures, an avenue which could be pursued for the wearable application.

8.2.4 24 GHz GAA

The final iteration of the grid array antenna designed for 24 GHz saw only early stages of progress, with an initial design, fabrication and measurement. The fabricated antenna was poorly tuned, showing a reflection coefficient response at 20.5 GHz. The cause of this could be due to the omission of the connector bolts in the simulation, however regardless of this, an improvement in measured performance will occur with a better matched antenna. As with the previous version of the GAA, parametric analysis into increasing the array size and substrate thickness in an effort to optimise the antenna gain would be beneficial. Further, it would also be interesting to reduce the substrate, treating the space inside the cells much like the twin-grid in Chapter 5, with the aim of revealing the skin for sensor access.

Bibliography

[1] R. Want, "An introduction to RFID technology," *IEEE Pervasive Computing*, vol. 5, no. 1, pp. 25–33, 2006.

[2] R. Weinstein, "RFID: a technical overview and its application to the enterprise," *IT Professional*, vol. 7, no. 3, pp. 27–33, 2005.

[3] M. D. Raghu Das, Yu-Han Chang, "RFID forecasts, players and opportunities 2022-2032," *IDTechEx Research*, 2022.

[4] M. J. McGrath and C. N. Scanaill, "Sensor technologies," *Apress Open*, 2013.

[5] S. Passke, A. Bauer, T. Moser, and C. Seckman, "The benefits and barriers to RFID technology in healthcare," *Online Journal of Nursing Informatics (OJNI)*, vol. 21, 2017.

[6] H. Stockman, "Communication by means of reflected power," *Proceedings of the IRE*, vol. 36, no. 10, pp. 454–455, 1963.

[7] R. Harrington, "Field measurements using active scatterers (correspondence)," *IEEE Transactions on Microwave Theory and Techniques*, vol. 11, no. 5, pp. 454–455, 1963.

[8] D. B. Harris, "Radio transmission systems with modulatable passive responder," *US Patent*, vol. 2927312, 1960.

[9] R. F. Harrington, "Theory of loaded scatterers," *Proceeding IEE*, vol. 111, no. 4, pp. 617–623, 1964.

[10] A. Koelle, S. Depp, and R. Freyman, "Short-range radio-telemetry for electronic identification, using modulated rf backscatter," *Proceedings of the IEEE*, vol. 63, no. 8, pp. 1260–1261, 1975.

[11] National Museum of American History, "Electronic cow tag." `https://americanhistory.si.edu/collections/search/object/nmah_1437998`. Accessed: 2022-08-09.

[12] IBM, "RFID - T.J watson research center." `https://researcher.watson.ibm.com/researcher/view_group.php?id=7064`. Accessed: 2022-08-09.

[13] RAIN alliance, "Rain RFID." `https://rain{RFID}.org/`. Accessed: 2022-08-09.

[14] Ofcom, "Office of communications." `www.ofcom.org.uk`. Accessed: 2022-08-09.

[15] FCC, "Federal communications commission." `www.fcc.gov`. Accessed: 2022-08-09.

[16] GS1, "Overview of UHF frequency allocations (860 to 960 MHz) for RAIN RFID," 2022.

[17] GS1 *EPC Radio-Frequency Identity Protocols*, 2013.

[18] M. C. O'Connor, "Gen 2 EPC protocol approved as ISO 18000-6C," *RFID Journal*, 2006.

[19] P. Pursula, "Analysis and design of UHF and millimetre wave radio frequency identification: Dissertation," *Espoo: VTT Technical Research Centre of Finland*, 2009.

[20] K. Witrisal, S. Hinteregger, J. Kulmer, E. Leitinger, and P. Meissner, "High-accuracy positioning for indoor applications: RFID, UWB, 5G, and beyond," in *2016 IEEE International Conference on RFID (RFID)*, pp. 1–7, 2016.

[21] B. Unhelkar, S. Joshi, M. Sharma, S. Prakash, A. K. Mani, and M. Prasad, "Enhancing supply chain performance using RFID technology and decision support systems in the industry 4.0–a systematic literature review," *International Journal of Information Management Data Insights*, vol. 2, no. 2, p. 100084, 2022.

[22] J. Uddin, M. B. I. Reaz, M. Hasan, A. Nordin, M. Ibrahimy, and M. Ali, "UHF RFID antenna architectures and applications," *Scientific Research and Essays*, vol. 5, 05 2010.

[23] D. M. Pozar, *Microwave engineering; 3rd ed.* Hoboken, NJ: Wiley, 2005.

[24] C. Propper, G. Stoye, and B. Zaranko, "The wider impacts of the coronavirus pandemic on the NHS," *Fiscal Studies*, vol. 41, no. 2, pp. 345–356, 2020.

[25] B. Riegel, S. B. Dunbar, D. Fitzsimons, K. E. Freedland, C. S. Lee, S. Middleton, A. Stromberg, E. Vellone, D. E. Webber, and T. Jaarsma, "Self-care research: Where are we now? where are we going?," *International Journal of Nursing Studies*, vol. 116, p. 103402, 2021. Self-care in long term conditions.

[26] P. Mukherjee and A. Mukherjee, "Chapter 1 - advanced processing techniques and secure architecture for sensor networks in ubiquitous healthcare systems," in *Sensors for Health Monitoring* (N. Dey, J. Chaki, and R. Kumar, eds.), vol. 5 of *Advances in ubiquitous sensing applications for healthcare*, pp. 3–29, Academic Press, 2019.

[27] N. Thammasan, I. V. Stuldreher, E. Schreuders, M. Giletta, and A.-M. Brouwer, "A usability study of physiological measurement in school using wearable sensors," *Sensors*, vol. 20, no. 18, 2020.

[28] Y. Liu, M. Pharr, and G. A. Salvatore, "Lab-on-skin: A review of flexible and stretchable electronics for wearable health monitoring," *ACS Nano*, vol. 11, pp. 9614–9635, 2017.

[29] H. Dillon, J. Day, S. Bant, and K. J. Munro, "Adoption, use and non-use of hearing aids: a robust estimate based on welsh national survey statistics," *International Journal of Audiology*, vol. 59, no. 8, pp. 567–573, 2020. PMID: 32530329.

[30] L. Yin, J. Lv, and J. Wang, "Structural innovations in printed, flexible, and stretchable electronics," *Advanced Materials Technologies*, vol. 5, 11 2020.

[31] A. M. Hussain and M. M. Hussain, "CMOS-technology-enabled flexible and stretchable electronics for internet of everything applications," *Advanced Materials*, vol. 28, pp. 4219–4249, 6 2016.

[32] R. Kashyap, *Applications of Wireless Sensor Networks in Healthcare*, pp. 8–40. IGI Global, 01 2020.

[33] J. Wan, C. Zou, S. Ullah, C.-F. Lai, M. Zhou, and X. Wang, "Cloud-enabled wireless body area networks for pervasive healthcare," *IEEE Network*, vol. 27, no. 5, pp. 56–61, 2013.

[34] D. H. Kim, N. Lu, R. Ma, Y. S. Kim, R. H. Kim, S. Wang, J. Wu, S. M. Won, H. Tao, A. Islam, K. J. Yu, T. I. Kim, R. Chowdhury, M. Ying, L. Xu, M. Li, H. J. Chung, H. Keum, M. McCormick, P. Liu, Y. W. Zhang, F. G. Omenetto, Y. Huang, T. Coleman, and J. A. Rogers, "Epidermal electronics," *Science*, vol. 333, pp. 838–843, 2011.

[35] Z. Krupka, "The effect of the human body on radiation properties of small-sized communication systems," *IEEE Transactions on Antennas and Propagation*, vol. 16, pp. 154–163, 1968.

[36] H. E. King, "Characteristics of body-mounted antennas for personal radio sets," *IEEE Transactions on Antennas and Propagation*, vol. 23, pp. 242–244, 1975.

[37] H. King and J. Wong, "Effects of a human body on a dipole antenna at 450 and 900 MHz," *IEEE Transactions on Antennas and Propagation*, vol. 25, no. 3, pp. 376–379, 1977.

[38] M. H. Lin and C. W. Chiu, "Human-body effects on the design of card-type UHF RFID tag antennas," *IEEE Antennas and Propagation Society, AP-S International Symposium (Digest)*, pp. 521–524, 2011.

[39] M. Ramzan, X. Fang, Q. Wang, and D. Plettemeier, "Study of a dipole antenna in the vicinity of lossless and lossy medium for on-body antenna analysis," *Internet of Things*, pp. 371–385, 2019.

[40] R. M. Mäkinen and T. Kellomäki, "Body effects on thin single-layer slot, self-complementary, and wire antennas," *IEEE Transactions on Antennas and Propagation*, vol. 62, pp. 385–392, 2014.

[41] "IT'IS foundation: Tissue properties database." `https://itis.swiss/virtual-population/tissue-properties/database/dielectric-properties/`. Accessed: 2022-03-25.

[42] D. O. Oyeka, J. C. Batchelor, and A. M. Ziai, "Effect of skin dielectric properties on the read range of epidermal ultra-high frequency radio-frequency identification tags," *Healthcare Technology Letters*, vol. 4, pp. 78–81, 2017.

[43] R. Bancroft, *Microstrip and Printed Antenna Design*. Electromagnetic Waves, Institution of Engineering and Technology, 2009.

[44] C. Miozzi, S. Nappi, S. Amendola, C. Occhiuzzi, and G. Marrocco, "A general-purpose configurable RFID epidermal board with a two-way discrete impedance tuning," *IEEE Antennas and Wireless Propagation Letters*, vol. 18, pp. 1–1, 2019.

[45] V. Makarovaite, C. Gourlay, A. J. Hillier, J. C. Batchelor, and S. J. Holder, "Adjustable passive RFID skin mounted sticker," *2019 IEEE 16th International Conference on Wearable and Implantable Body Sensor Networks (BSN)*, pp. 0–3, 2019.

[46] K. Xu, L. Xie, S. Xue, K. Xue, and G. Wan, "Influence of transverse deformation on resonant frequency of patch antenna," *2018 IEEE Sensors Applications Symposium (SAS)*, pp. 1–6, 2018.

[47] L. Song and Y. Rahmat-Samii, "A systematic investigation of rectangular patch antenna bending effects for wearable applications," *IEEE Transactions on Antennas and Propagation*, vol. 66, pp. 2219–2228, 2018.

[48] M. A. Ziai and J. C. Batchelor, "Temporary on-skin passive UHF RFID transfer tag," *IEEE Transactions on Antennas and Propagation*, vol. 59, pp. 3565–3571, 2011.

[49] C. Miozzi, S. Nappi, S. Amendola, and G. Marrocco, "A general-purpose small RFID epidermal datalogger for continuous human skin monitoring

in mobility," *IEEE MTT-S International Microwave Symposium Digest*, vol. 2018-June, pp. 371–373, 2018.

[50] C. Miozzi, F. Amato, and G. Marrocco, "Performance and durability of thread antennas as stretchable epidermal UHF RFID tags," *IEEE Journal of Radio Frequency Identification*, vol. 4, no. 4, pp. 398–405, 2020.

[51] L.-Y. Ma and N. Soin, "Recent progress in printed physical sensing electronics for wearable health-monitoring devices: A review," *IEEE Sensors Journal*, vol. 22, no. 5, pp. 3844–3859, 2022.

[52] Y. Khan, A. Thielens, S. Muin, J. Ting, C. Baumbauer, and A. C. Arias, "A new frontier of printed electronics: Flexible hybrid electronics," *Advanced Materials*, vol. 32, no. 15, p. 1905279, 2020.

[53] S. F. Kamarudin, M. Mustapha, and J.-K. Kim, "Green strategies to printed sensors for healthcare applications," *Polymer Reviews*, vol. 61, no. 1, pp. 116–156, 2021.

[54] A. Sharif, J. Ouyang, Y. Yan, A. Raza, M. A. Imran, and Q. H. Abbasi, "Low-cost inkjet-printed ¡sc¿RFID¡/sc¿ tag antenna design for remote healthcare applications," *IEEE Journal of Electromagnetics, RF and Microwaves in Medicine and Biology*, vol. 3, no. 4, pp. 261–268, 2019.

[55] S. Amendola, A. Palombi, and G. Marrocco, "Inkjet printing of epidermal RFID antennas by self-sintering conductive ink," *IEEE Transactions on Microwave Theory and Techniques*, vol. 66, pp. 1561–1569, 2018.

[56] Y. Yao, S. Chakraborty, A. Dhar, C. B. Sangani, Y. Duan, B. R. Pansuriya, and R. L. Vekariya, "Graphene, an epoch-making material in RFID technology: a detailed overview," *New J. Chem.*, vol. 45, pp. 18700–18721, 2021.

[57] T. Leng, X. Huang, K. Chang, J. Chen, M. A. Abdalla, and Z. Hu, "Graphene nanoflakes printed flexible meandered-line dipole antenna on paper substrate for low-cost RFID and sensing applications," *IEEE Antennas and Wireless Propagation Letters*, vol. 15, pp. 1565–1568, 2016.

[58] N. K. Jacob, E. Balaban, R. Saunders, J. C. Batchelor, S. Member, S. G. Yeates, A. J. Casson, and S. Member, "An exploration of behind-the-ear ecg signals from a single ear using inkjet printed conformal tattoo electrodes," *IEEE EMBC*, pp. 1283–1286, 2018. On-Body sensor.

[59] J. S. Chang and T. Ge, "A fully additive low-temperature all-air low-variation printed/flexible electronics with self-compensation for bending: Codesign from materials, design, fabrication, and applications," *Proceedings of the IEEE*, vol. 107, no. 10, pp. 2106–2117, 2019.

[60] Y. Dong, X. Min, and W. S. Kim, "A 3-d-printed integrated pcb-based electrochemical sensor system," *IEEE Sensors Journal*, vol. 18, no. 7, pp. 2959–2966, 2018.

[61] E. Ragonese, M. Fattori, and E. Cantatore, "Printed organic electronics on flexible foil: Circuit design and emerging applications," *IEEE Transactions on Circuits and Systems II: Express Briefs*, vol. 68, no. 1, pp. 42–48, 2021.

[62] J. Willmann, D. Stocker, and E. Dörsam, "Characteristics and evaluation criteria of substrate-based manufacturing. is roll-to-roll the best solution for printed electronics?," *Organic Electronics*, vol. 15, no. 7, pp. 1631–1640, 2014.

[63] A. Dubok and A. B. Smolders, "Miniaturization of robust UHF RFID antennas for use on perishable goods and human bodies," *IEEE Antennas and Wireless Propagation Letters*, vol. 13, pp. 1321–1324, 2014.

[64] G. A. Casula, G. Montisci, G. Valente, and G. Gatto, "A robust printed antenna for UHF wearable applications," *IEEE Transactions on Antennas and Propagation*, vol. 66, no. 8, pp. 4337–4342, 2018.

[65] P. S. Taylor, J. C. Batchelor, and S. Member, "Finger-worn UHF far-field RFID tag antenna," *IEEE Antennas and Wireless Propagation Letters*, vol. 18, pp. 2513–2517, 2019.

[66] M. C. Caccami, M. P. Hogan, M. Alfredsson, G. Marrocco, and J. C. Batchelor, "A tightly integrated multilayer battery antenna for RFID epidermal applications," *IEEE Transactions on Antennas and Propagation*, vol. 66, pp. 609–617, 2018.

[67] D. Le, S. Member, S. Ahmed, S. Member, and L. Ukkonen, "A small all-corners-truncated circularly polarized microstrip patch antenna on textile substrate for wearable passive UHF RFID tags," *IEEE Journal of Radio Frequency Identification*, vol. 7281, 2021.

[68] J. Zhang, G. Y. Tian, A. M. J. Marindra, A. I. Sunny, and A. B. Zhao, "A review of passive RFID tag antenna-based sensors and systems for structural health monitoring applications," *Sensors*, vol. 17, no. 2, 2017.

[69] M. H. Zarifi, S. Deif, and M. Daneshmand, "Wireless passive RFID sensor for pipeline integrity monitoring," *Sensors and Actuators A: Physical*, vol. 261, pp. 24–29, 2017.

[70] S. Johann, C. Strangfeld, M. Müller, B. Mieller, and M. Bartholmai, "RFID sensor systems embedded in concrete – requirements for long–term operation," *Materials Today: Proceedings*, vol. 4, no. 5, Part 1, pp. 5827–5832, 2017. 33rd Danubia Adria Symposium on Advances in Experimental Mechanics, 20-23 September 2016.

[71] I. Ullah, R. Horne, B. Sanz-Izquierdo, and J. C. Batchelor, "RFID ac current sensing technique," *IEEE Sensors Journal*, vol. 20, no. 4, pp. 2197–2204, 2020.

[72] J. Zhang, G. Y. Tian, and A. B. Zhao, "Passive RFID sensor systems for crack detection & characterization," *NDT & E International*, vol. 86, pp. 89–99, 2017.

[73] A. Rennane, A. Abdelnour, D. Kaddour, R. Touhami, and S. Tedjini, "Design of passive UHF RFID sensor on flexible foil for sports balls pressure monitoring," *IET Microwaves, Antennas & Propagation*, vol. 12, no. 14, pp. 2154–2160, 2018.

[74] C. Occhiuzzi, C. Paggi, and G. Marrocco, "Passive RFID strain-sensor based on meander-line antennas," *Antennas and Propagation, IEEE Transactions on*, vol. 59, pp. 4836 – 4840, 01 2012.

[75] A. Oprea, N. Barsan, U. Weimar, M.-L. Bauersfeld, D. Ebling, and J. Wollenstein, "Capacitive humidity sensors on flexible RFID labels," in *TRANSDUCERS 2007 - 2007 International Solid-State Sensors, Actuators and Microsystems Conference*, pp. 2039–2042, 2007.

[76] B. SAGGIN, Y. Belaizi, A. Vena, B. Sorli, V. Guillard, and I. Dedieu, "A flexible biopolymer based UHF RFID-sensor for food quality monitoring," in *2019 IEEE International Conference on RFID Technology and Applications (RFID-TA)*, pp. 484–487, 2019.

[77] M. Caldara, B. Nodari, V. Re, and B. Bonandrini, "Miniaturized and low-power blood pressure telemetry system with RFID interface," *Procedia Engineering*, vol. 87, pp. 344–347, 12 2014.

[78] Z. Xiao, X. Tan, X. Chen, S. Chen, Z. Zhang, H. Zhang, J. Wang, Y. Huang, P. Zhang, L. Zheng, and H. Min, "An implantable RFID sensor tag toward continuous glucose monitoring," *IEEE Journal of Biomedical and Health Informatics*, vol. 19, no. 3, pp. 910–919, 2015.

[79] R. Horne, P. Jones, P. Taylor, J. Batchelor, and C. Holt, "An on body accelerometer system for streaming therapy data using COTS UHF RFID," *IEEE International Conference on RFID Technology and Applications (RFID-TA)*, pp. 301–305, 2019.

[80] R. Horne and J. C. Batchelor, "A framework for a low power on body real-time sensor system using UHF RFID," *IEEE Journal of Radio Frequency Identification*, vol. 4, pp. 391–397, 2020.

[81] R. Colella, M. R. Tumolo, S. Sabina, C. G. Leo, P. Mincarone, R. Guarino, and L. Catarinucci, "Design of UHF RFID sensor-tags for the biomechanical analysis of human body movements," *IEEE Sensors Journal*, vol. 21, no. 13, pp. 14090–14098, 2021.

[82] C. Occhiuzzi, C. Caccami, S. Amendola, and G. Marrocco, "Breath-monitoring by means of epidermal temperature RFID sensors," *2018 3rd International Conference on Smart and Sustainable Technologies (SpliTech)*, pp. 1–4, 2018.

[83] M. C. Caccami, M. Y. Mulla, C. Occhiuzzi, C. D. Natale, and G. Marrocco, "Design and experimentation of a batteryless on-skin RFID graphene-oxide sensor for the monitoring and discrimination of breath anomalies," *IEEE Sensors Journal*, vol. 18, pp. 8893–8901, 2018.

[84] S. K. Behera, "Chipless RFID sensors for wearable applications: A review," *IEEE Sensors Journal*, vol. 22, no. 2, pp. 1105–1120, 2022.

[85] P. Fathi, N. C. Karmakar, M. Bhattacharya, and S. Bhattacharya, "Potential chipless RFID sensors for food packaging applications: A review," *IEEE Sensors Journal*, vol. 20, no. 17, pp. 9618–9636, 2020.

[86] M. Agiwal, A. Roy, and N. Saxena, "Next generation 5G wireless networks: A comprehensive survey," *IEEE Communications Surveys Tutorials*, vol. 18, no. 3, pp. 1617–1655, 2016.

[87] M. H. Adnan and Z. Ahmad Zukarnain, "Device-to-device communication in 5G environment: Issues, solutions, and challenges," *Symmetry*, vol. 12, no. 11, 2020.

[88] Apple, "Apple watch: Helping identify early warning signs." `https://www.apple.com/uk/healthcare/apple-watch/`. Accessed: 2022-03-11.

[89] Garmin, "Garmin watch - health science." `https://www.garmin.com/en-GB/garmin-technology/health-science/`. Accessed: 2022-03-11.

[90] A. Jo, B. D. Coronel, C. E. Coakes, and A. G. Mainous, "Is there a benefit to patients using wearable devices such as fitbit or health apps on mobiles? a systematic review," *The American Journal of Medicine*, vol. 132, no. 12, pp. 1394–1400.e1, 2019.

[91] M. Weenk, H. van Goor, B. Frietman, L. J. Engelen, C. J. van Laarhoven, J. Smit, S. J. H. Bredie, and T. H. van de Belt, "Continuous monitoring of vital signs using wearable devices on the general ward: Pilot study," *JMIR mHealth and uHealth*, vol. 5, 2017.

[92] O. Kwon, J. Jeong, H. Kim, I. H. Kwon, S. Park, J. Kim, and Y. Choi, "Electrocardiogram sampling frequency range acceptable for heart rate variability analysis," *Healthcare Informatics Research*, vol. 24, p. 198, 07 2018.

[93] H. G. Espinosa, D. V. Thiel, M. Sorell, and D. Rowlands, "Can we trust inertial and heart rate sensor data from an apple watch device?," *Proceedings*, vol. 49, no. 1, 2020.

[94] F. Amato, S. Amendola, and G. Marrocco, "Upper-bound performances of RFID epidermal sensor networks at 5G frequencies," *2019 IEEE 16th International Conference on Wearable and Implantable Body Sensor Networks, BSN 2019 - Proceedings*, pp. 2019–2022, 2019.

[95] D. Soldani and M. Innocenti, *5G Communication Systems and Connected Healthcare*, ch. 7, pp. 149–177. John Wiley & Sons, Ltd, 2019.

[96] G. M. Bianco, C. Occhiuzzi, N. Panunzio, and G. Marrocco, "5G NR base station (BS) radio transmission and reception," *IEEE Journal of Radio Frequency Identification*, vol. 6, pp. 77–96, 2022.

[97] C. Occhiuzzi, S. Parrella, F. Camera, S. Nappi, and G. Marrocco, "RFID-based dual-chip epidermal sensing platform for human skin monitoring," *IEEE Sensors Journal*, vol. 4, pp. 5359–5367, 2021.

[98] X. Li, G. Gao, H. Zhu, Q. Li, N. Zhang, and Z. Qi, "UHF RFID tag antenna based on the dls-ebg structure for metallic objects," *IET Microwaves, Antennas and Propagation*, vol. 14, p. 567–572, 2019.

[99] S. Chowdhury and K. Ali, "Effects of human body on antenna performance: A quantitative study," pp. 108–112, 12 2016.

[100] R. C. Hansen and R. E. Collin, "Clever physics, but bad numbers," *Small Antenna Handbook*, vol. 14, p. 135–145, 2019.

[101] ROHACELL, "Rohacell hf foam material." `https://www.rohacell.com/en/products-services/rohacell-hf'`. Accessed: 2022-08-09.

[102] J. D. Hughes, R. Horne, N. Brabon, and J. Batchelor, "An on-body UHF RFID tag with ddrr antenna for healthcare data streaming applications," *IEEE Journal of Radio Frequency Identification*, vol. 6, pp. 680–687, 2022.

[103] Impinj, "Impinj R700 RAIN RFID reader." `https://www.impinj.com/products/readers/impinj-r700`. Accessed: 2022-08-09.

[104] N. F. M. Aun, P. J. Soh, A. A. Al-Hadi, M. F. Jamlos, G. A. Vandenbosch, and D. Schreurs, "Revolutionizing wearables for 5G: 5G technologies: Recent developments and future perspectives for wearable devices and antennas," *IEEE Microwave Magazine*, vol. 18, no. 3, pp. 108–124, 2017.

[105] S. Manzari, C. Occhiuzzi, and G. Marrocco, "Feasibility of body-centric systems using passive textile RFID tags," *IEEE Antennas and Propagation Magazine*, vol. 54, pp. 49–62, 2012.

[106] A. Pellegrini, A. Brizzi, L. Zhang, K. Ali, Y. Hao, X. Wu, C. C. Constantinou, Y. Nechayev, P. S. Hall, N. Chahat, M. Zhadobov, and R. Sauleau, "Antennas and propagation for body-centric wireless communications at millimeter-wave frequencies: A review [wireless corner]," *IEEE Antennas and Propagation Magazine*, vol. 55, no. 4, pp. 262–287, 2013.

[107] J. Kraus, "A backward angle-fire array antenna," *IEEE Transactions on Antennas and Propagation*, vol. 12, no. 1, pp. 48–50, 1964.

[108] J. D. Hughes, C. Occhiuzzi, J. Batchelor, and G. Marrocco, "Wearable soft grid array antenna for S-band 5G communication," in *2020 XXXIIIrd General Assembly and Scientific Symposium of the International Union of Radio Science*, pp. 1–4, 2020.

[109] M. Sun and Y. P. Zhang, *Grid Antenna Arrays*, pp. 1249–1277. Singapore: Springer Singapore, 2016.

[110] L. Zhang, Q. Zhang, and C. Hu, "The influence of dielectric constant on bandwidth of u-notch microstrip patch antenna," *2010 IEEE International Conference on Ultra-Wideband*, vol. 1, pp. 1–4, 2010.

[111] G. Marrocco, "The art of UHF RFID antenna design: impedance-matching and size-reduction techniques," *IEEE Antennas and Propagation Magazine*, vol. 50, no. 1, pp. 66–79, 2008.

[112] C. Balanis, "Antenna theory: a review," *Proceedings of the IEEE*, vol. 80, no. 1, pp. 7–23, 1992.

[113] T. M. Macnamara, "Introduction to antenna placement and installation," *The Aeronautical Journal (1968)*, vol. 115, no. 1172, p. 650–650, 2011.

[114] Z. Xie, R. Avila, Y. Huang, and J. A. Rogers, "Flexible and stretchable antennas for biointegrated electronics," *Advanced Materials*, vol. 32, no. 15, p. 1902767, 2020.

[115] H. Wheeler, "Fundamental limitations of small antennas," *Proceedings of the IRE*, vol. 35, no. 12, pp. 1479–1484, 1947.

[116] M. Fallahpour and R. Zoughi, "Antenna miniaturization techniques: A review of topology- and material-based methods," *IEEE Antennas and Propagation Magazine*, vol. 60, no. 1, pp. 38–50, 2018.

[117] J. D. Hughes, C. Occhiuzzi, J. Batchelor, and G. Marrocco, "Miniaturized grid array antenna for body-centric RFID communications in 5g s-band," in *2020 50th European Microwave Conference (EuMC)*, pp. 796–799, 2021.

[118] J. D. Hughes, C. Occhiuzzi, J. Batchelor, and G. Marrocco, "Twin-grid array as 3.6 GHz epidermal antenna for potential backscattering 5G communication," *IEEE Antennas and Wireless Propagation Letters*, vol. 19, no. 12, pp. 2092–2096, 2020.

[119] J. Y. H Nakano, T Kawano, "Meander-line grid-array antenna," *IEE Proceedings - Microwaves, Antennas and Propagation*, vol. 145, pp. 309–312(3), August 1998.

[120] H. Habibzadeh, K. Dinesh, O. Rajabi Shishvan, A. Boggio-Dandry, G. Sharma, and T. Soyata, "A survey of healthcare internet of things (HIoT): A clinical perspective," *IEEE Internet of Things Journal*, vol. 7, no. 1, pp. 53–71, 2020.

[121] J. Batchelor, R. Horne, P. Taylor, and M. Sobhy, "RFID monitoring for assistive technologies beyond the clinic," in *12th European Conference on Antennas and Propagation (EuCAP 2018)*, pp. 1–4, 2018.

[122] C. Yao, Y. Liu, X. Wei, G. Wang, and F. Gao, "Backscatter technologies and the future of internet of things: Challenges and opportunities," *Intelligent and Converged Networks*, vol. 1, no. 2, pp. 170–180, 2020.

[123] N. F. M. Aun, P. J. Soh, A. A. Al-Hadi, M. F. Jamlos, G. A. Vandenbosch, and D. Schreurs, "Revolutionizing wearables for 5G: 5G technologies: Recent developments and future perspectives for wearable devices and antennas," *IEEE Microwave Magazine*, vol. 18, no. 3, pp. 108–124, 2017.

[124] H. Ullah, N. Gopalakrishnan Nair, A. Moore, C. Nugent, P. Muschamp, and M. Cuevas, "5G communication: An overview of vehicle-to-everything, drones, and healthcare use-cases," *IEEE Access*, vol. 7, pp. 37251–37268, 2019.

[125] C. Occhiuzzi, F. R. Venturi, F. Amato, A. Di Carlofelice, P. Tognolatti, and G. Marrocco, "Design and experimental characterization of on-skin loop antenna for next 5G backscattering-based communications," *IEEE Journal of Radio Frequency Identification*, pp. 1–1, 2022.

[126] B. Zhang and Y. Zhang, "Analysis and synthesis of millimeter-wave microstrip grid-array antennas," *IEEE Antennas and Propagation Magazine*, vol. 53, no. 6, pp. 42–55, 2011.

[127] Y. Hayashi, K. Sakakibara, M. Nanjo, S. Sugawa, N. Kikuma, and H. Hirayama, "Millimeter-wave microstrip comb-line antenna using reflection-canceling slit structure," *IEEE Transactions on Antennas and Propagation*, vol. 59, no. 2, pp. 398–406, 2011.

[128] M. Sun, Y. P. Zhang, Y. X. Guo, K. M. Chua, and L. L. Wai, "Integration of grid array antenna in chip package for highly integrated 60-GHz radios," *IEEE Antennas and Wireless Propagation Letters*, vol. 8, pp. 1364–1366, 2009.

[129] D.-H. Shin, J.-W. Ahn, S.-O. Park, S.-J. Park, and K.-W. Han, "Design of shorted parasitic rhombic array antenna for 24 GHz rear and side detection system," *IET Microwaves, Antennas and Propagation*, vol. 9, 08 2015.

[130] K. Hirose, K. Shinozaki, and H. Nakano, "A comb-line antenna modified for wideband circular polarization," *IEEE Antennas and Wireless Propagation Letters*, vol. 14, pp. 1–1, 01 2015.

[131] M. Mosalanejad, I. Ocket, C. Soens, and G. A. E. Vandenbosch, "Multilayer compact grid antenna array for 79 GHz automotive radar applications," *IEEE Antennas and Wireless Propagation Letters*, vol. 17, no. 9, pp. 1677–1681, 2018.

[132] J. D. Hughes, C. Occhiuzzi, J. Batchelor, and G. Marrocco, "Folded comb-line array for healthcare 5G-RFID-based IoT applications," in *2021 IEEE International Conference on RFID (RFID)*, pp. 1–5, 2021.

[133] C. Occhiuzzi, J. D. Hughes, F. R. Venturi, J. Batchelor, and G. Marrocco, "Folded comb-line array for backscattering-based bodycentric communications in the 5G sub-6 GHz band," *IEEE Transactions on Antennas and Propagation*, pp. 1–1, 2022.

[134] S. J. Orfanidis, *Electromagnetic Waves and Antennas*. 2010.

[135] N. Uzunoglu, N. Alexopoulos, and J. Fikioris, "Radiation properties of microstrip dipoles," *IEEE Transactions on Antennas and Propagation*, vol. 27, no. 6, pp. 853–858, 1979.

[136] F. Amato, C. Occhiuzzi, and G. Marrocco, "Epidermal backscattering antennas in the 5G framework: Performance and perspectives," *IEEE Journal of Radio Frequency Identification*, vol. 4, no. 3, pp. 176–185, 2020.

[137] F. Amato, A. D. Carlofelice, C. Occhiuzzi, P. Tognolatti, and G. Marrocco, "S-band testbed for 5G epidermal RFIDs," in *2020 XXXIIIrd General Assembly and Scientific Symposium of the International Union of Radio Science*, pp. 1–3, 2020.

[138] K. Finkenzeller, "RFID handbook: Fundamentals and applications in contactless smart cards and identification," 01 2005.

[139] ETSI, "5G NR base station (BS) radio transmission and reception," *3GPP TS 38.104 version 16.4.0 Release 16*, 2020.

[140] S. Manzari, S. Pettinari, and G. Marrocco, "Miniaturised wearable UHF-RFID tag with tuning capability," *Electronics Letters*, vol. 48, pp. 1325–1326, 10 2012.

[141] C. Occhiuzzi and G. Marrocco, "Monolithic antenna array for epidermal 5G backscattering communications," *2020 14th European Conference on Antennas and Propagation (EuCAP)*, pp. 1–3, 2020.

[142] J. P. Zhang and J. J. Mao, "A Miniaturized Ka-Band High-Gain Planar Grid Antenna," *2020 IEEE Asia-Pacific Conference on Antennas and Propagation, APCAP 2020 - Proceedings*, pp. 2–3, 2020.

[143] Laird, "Eccostock flexk:flexible dielectric elastomer." `https://www.laird.com/products/microwave-absorbers/low-lossdielectrics/eccostock-flexk`. Accessed: 2022-03-25.